2013

Cytochrome P450-mediated drug metabolizing activity in the nasal mucosa

Varsha Sudhir Dhamankar
University of Iowa

CYTOCHROME P450-MEDIATED DRUG METABOLIZING ACTIVITY IN THE NASAL MUCOSA

by

Varsha Sudhir Dhamankar

An Abstract

Of a thesis submitted in partial fulfillment
of the requirements for the Doctor of
Philosophy degree in Pharmacy (Pharmaceutics)
in the Graduate College of
The University of Iowa

May 2013

Thesis Supervisor: Professor Maureen D. Donovan

ABSTRACT

Pre-systemic elimination by local enzymatic degradation can play a key role in limiting the bioavailability of intranasally administered drugs. Despite remarkable advancement in the characterization of the nasal biotransformative enzymes, knowledge of the role of the nasal mucosa in limiting bioavailability of therapeutic agents is still inadequate. The aim of this work was to evaluate the expression and substrate biotransformation activity of cytochrome P450 enzymes in the nasal mucosa using bovine olfactory and respiratory explants as *in vitro* models.

Gene expression and localization of major CYP450 isoforms in the nasal mucosa were examined using RT-PCR and immunohistochemistry. The bovine nasal mucosa showed abundant expression of CYP2A6 and 3A4 genes whereas 1A1, 1A2, 2C9, and 2C19 isoforms were expressed at much lower levels. The CYP450 proteins were observed to be present in the epithelial layer and in submucosal glandular cells.

The diffusion of melatonin, a CYP1A2 substrate, and the appearance of 6-hydroxymelatonin, its primary metabolite, across bovine olfactory and respiratory explants was measured, and nasal olfactory and respiratory microsomal preparations were used to quantify the kinetic parameters for melatonin 6-hydroxylation. Results indicated that bovine olfactory and respiratory CYP450 isoforms were metabolically active towards melatonin metabolism, and the respiratory mucosa demonstrated the greatest melatonin 6-hydroxylation activity.

Numerical simulations were used to probe the effects of the relative magnitudes of the permeability coefficient and enzymatic parameters on net substrate mass transfer across nasal mucosal tissues. The simulations indicated that the concentration gradient of

the drug coupled with its permeability coefficient were the most significant factors controlling the transport of drugs across the mucosal tissue. Enzymatic degradation decreased the flux of drugs across the mucosa and had the greatest impact on low permeability compounds.

The results from these studies show that the bovine nasal mucosa possesses significant metabolic activity, and the flux of a metabolically labile substrate across the nasal mucosa can be significantly reduced by its enzymatic degradation within the tissue. Use of kinetic modeling to characterize of the extent of biotransformation in the nasal mucosa enables the identification of metabolism-limited bioavailability of intranasally administered drug compounds.

Abstract Approved: _____
Thesis Supervisor

_____
Title and Department

_____
Date

CYTOCHROME P450-MEDIATED DRUG METABOLIZING ACTIVITY IN THE NASAL MUCOSA

by

Varsha Sudhir Dhamankar

A thesis submitted in partial fulfillment
of the requirements for the Doctor of
Philosophy degree in Pharmacy (Pharmaceutics)
in the Graduate College of
The University of Iowa

May 2013

Thesis Supervisor: Professor Maureen D. Donovan

Graduate College
The University of Iowa
Iowa City, Iowa

CERTIFICATE OF APPROVAL

_____

PH.D. THESIS

_____

This is to certify that the Ph.D. thesis of

Varsha Sudhir Dhamankar

has been approved by the Examining Committee
for the thesis requirement for the Doctor of Philosophy
degree in Pharmacy (Pharmaceutics) at the May 2013 graduation.

Thesis Committee: _____
Maureen D. Donovan, Thesis Supervisor

_____
Michael Duffel

_____
Jennifer Fiegel

_____
Douglas Flanagan

_____
Lee Kirsch

To my family

ACKNOWLEDGMENTS

I would like to express my sincere and deepest gratitude to my advisor Prof. Maureen Donovan for her invaluable guidance, support, and patience throughout my graduate career. Her enthusiasm, encouragement, and constructive feedback constantly steered me in the right direction and led me towards the completion of my dissertation research.

I would like to express my sincere appreciation to my thesis committee members, Prof. Douglas Flanagan, Prof. Lee Kirsch, Prof. Jennifer Fiegel, and Prof. Michael Duffel for their interest in my research, and for their time and vital inputs on my thesis. I would like to thank Prof. Vijay Kumar for his help and feedback on my comprehensive examination proposal. I would also like to express my gratefulness to Dr. Steven Stamatis for sharing his interest, knowledge, and expertise in diffusion modeling. In addition, I would like to thank Prof. Flanagan and Prof. Kirsch for providing me with valuable guidance and discussions on drug diffusion and transport modeling. I would like to thank Prof. Daryl J. Murry and Dr. Mark Schmidt for their help during the development of the solid phase extraction and LCMS detection methods for quantification of melatonin and its metabolites. I would like to thank Prof. Michael Duffel for providing essential knowledge on microsomal metabolism studies. I am extremely grateful to all the following professors for letting me use their lab facilities: Prof. Murry for the LCMS, Prof. Duffel for the ultra-centrifuge, Prof. Assem for the PCR instruments, and Prof. Salem for the UV-fluorescence absorbance reader. I am very appreciative of the central microscopy research facility at the University of Iowa, especially Kathy Walters and Chantal Allamargot for their constant help and assistance towards the completion of my research. I would also like to thank the DNA Core Facility and DNA Sequencing Facility at the University of Iowa for providing us with the excellent research facility on campus. I would like to thank Prof. Todd Scheetz and Manar Al-Ghabeish for their help

in generating the microarray data. Furthermore, I am extremely grateful to all the faculty and staff members of the Division of Pharmaceutics and Translational Therapeutics, College of Pharmacy, for their help and support during the course of my graduate studies. I would also like to express utmost appreciation to my labmates Dr. Hefei Zhang, Dr. Chen-Ming Lee, Dr. Joanne Reiland-Wakeman and Dr. Nag Chemuturi for their help in getting me started with my research.

I would like to thank Bud's Custom Meats, Iowa for providing me with bovine nasal turbinates, and University of Iowa Pharmaceuticals and the College of Pharmacy for providing me with means of transportation for the collection of tissue samples.

Special thanks to the University of Iowa campus recreation and wellness services (especially the yoga and zumba crew) for motivating me to maintain a healthy and active lifestyle.

This work could not have been completed without the love and support from my family and friends. I would like to thank my mom, dad, and brother for their unconditional love and encouragement. Also, sincere thanks to Bhakti and all my friends in Iowa City for making the graduate study an awesome experience. Finally, I would like to thank Girish for making this journey a memorable one!

ABSTRACT

Pre-systemic elimination by local enzymatic degradation can play a key role in limiting the bioavailability of intranasally administered drugs. Despite remarkable advancement in the characterization of the nasal biotransformative enzymes, knowledge of the role of the nasal mucosa in limiting bioavailability of therapeutic agents is still inadequate. The aim of this work was to evaluate the expression and substrate biotransformation activity of cytochrome P450 enzymes in the nasal mucosa using bovine olfactory and respiratory explants as *in vitro* models.

Gene expression and localization of major CYP450 isoforms in the nasal mucosa were examined using RT-PCR and immunohistochemistry. The bovine nasal mucosa showed abundant expression of CYP2A6 and 3A4 genes whereas 1A1, 1A2, 2C9, and 2C19 isoforms were expressed at much lower levels. The CYP450 proteins were observed to be present in the epithelial layer and in submucosal glandular cells.

The diffusion of melatonin, a CYP1A2 substrate, and the appearance of 6-hydroxymelatonin, its primary metabolite, across bovine olfactory and respiratory explants was measured, and nasal olfactory and respiratory microsomal preparations were used to quantify the kinetic parameters for melatonin 6-hydroxylation. Results indicated that bovine olfactory and respiratory CYP450 isoforms were metabolically active towards melatonin metabolism, and the respiratory mucosa demonstrated the greatest melatonin 6-hydroxylation activity.

Numerical simulations were used to probe the effects of the relative magnitudes of the permeability coefficient and enzymatic parameters on net substrate mass transfer across nasal mucosal tissues. The simulations indicated that the concentration gradient of

the drug coupled with its permeability coefficient were the most significant factors controlling the transport of drugs across the mucosal tissue. Enzymatic degradation decreased the flux of drugs across the mucosa and had the greatest impact on low permeability compounds.

The results from these studies show that the bovine nasal mucosa possesses significant metabolic activity, and the flux of a metabolically labile substrate across the nasal mucosa can be significantly reduced by its enzymatic degradation within the tissue. Use of kinetic modeling to characterize of the extent of biotransformation in the nasal mucosa enables the identification of metabolism-limited bioavailability of intranasally administered drug compounds.

TABLE OF CONTENTS

LIST OF TABLES

LIST OF FIGURES

CHAPTER 1

INTRODUCTION

Intranasal administration has gained popularity in the past two decades as an alternative for rapid and non-invasive delivery of therapeutic agents into the systemic circulation[1–5]. In addition to alleviating local disorders, such as nasal congestion and allergic rhinitis, the nasal route is being extensively investigated to systemically deliver medications for the treatment of migraine[6], osteoporosis[7], vitamin B_{12} deficiency[8], nocturnal enuresis[9], and smoking cessation[10]. Examples of marketed intranasal preparations for treating systemic disorders include Imitrex® (sumatriptan) by GlaxoSmithKline, Nicotrol® (nicotine) by Pfizer, Zomig® (zolmitriptan) by AstraZeneca, Miacalcin® (calcitonin) by Novartis Pharmaceuticals, and Nascobal® (cyanocobalamin) by Par Pharmaceuticals. The US market report on intranasal drug delivery, published by Global Industry Analysts Inc. in 2012 has predicted the US intranasal drug delivery products market to reach $5.2 billion by 2017, primarily owing to expansion in nasal product differentiation and additional therapeutic applications[11].

The nasal route is suitable for acute or chronic delivery of a large variety of compounds because the nasal mucosa offers several advantages as an alternate site of drug administration. It possesses a relatively large absorptive surface area (150-180 cm^2) due to the presence of microvilli on the epithelial surface, a porous endothelial membrane and a highly vascularized epithelium[12]. Absorption from the nasal cavity avoids hepatic first pass metabolism in addition to circumventing the acidic environment of the stomach and the enzymes in the intestinal lumen, enabling rapid absorption and quick onset of drugs that are susceptible to degradation upon oral administration. Intranasal administration has also been recognized to be a viable option for targeted delivery of drugs directly to the brain via the olfactory neuronal pathway[13–16].

Despite these advantages, nasal administration can still be associated with low systemic bioavailability. The major contributors to the pre-systemic losses responsible for reducing the bioavailability of intranasally administered drugs are rapid mucociliary clearance and enzymatic degradation of the drug molecule in the nasal cavity[3,17]. Mucociliary clearance is the primary protective function in the nose which eradicates foreign particles and microbes from the nasal cavity and prevents them from reaching the lower airways. Enzymatic degradation is the second key barrier to the transfer of materials across the nasal mucosa. The technique of administration, the site of deposition, the physicochemical properties of the materials, and the pathological condition of the nasal mucosa are also other factors that affect the nasal bioavailability.

Anatomy and physiology of the nose

The primary functions of the nose are olfaction and filtering and conditioning of the inhaled air. The anatomical organization of the nasal cavity is shown in Figure 1-1. The external portion of the nose, called the nostril regions, open to the exterior environment and enables breathing. The nostril region is sustained and shaped by a framework of bone and cartilage[12,18]. The nostrils internally form the nasal vestibules, which perform the function of filtering the inhaled air through the hair lining the surfaces of the region. The vestibular epithelium is composed of stratified, squamous, keratinized cells and sebaceous glands. The vestibules possess a low surface area with limited drug permeability and thus are not an efficient site for drug absorption. The innermost region of the nose is called the nasal cavity, which extends from the nostrils to the posterior tips of the choanae (turbinates). The nasal cavity is lined with a mucosal membrane and is divided into two halves by the nasal septum. The lateral wall of the cavity is anatomically segregated into three scroll-shaped protrusions, the superior, medial and inferior turbinates. These turbinates assist in regulating the airflow path through the nose which

results in the modification of the temperature of the inspired air. The roof of the nasal cavity is lined by the cribriform plate of the ethmoid bone.

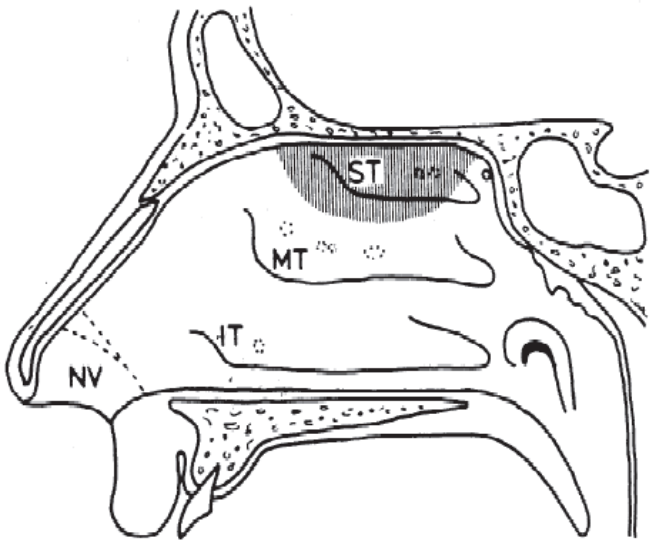

Figure 1-1 Anatomy of the nasal cavity showing the nasal vestibules (NV) along with the three turbinates, namely inferior turbinate (IT, respiratory mucosa), middle turbinate (MT, respiratory mucosa) and the superior turbinates (ST, olfactory mucosa)[12]; reproduced with permission.

The epithelial layer of the middle and inferior turbinates of the nasal cavity is part of the nasal respiratory mucosa. The olfactory mucosa, responsible for the sense of smell, lines portions of the superior turbinates and the roof of the nasal cavity. Posteriorly, the nasal cavity leads into the nasopharynx. In adult humans, the total surface area of the nasal cavity is about 150 cm^2 and its volume is about 20 ml[12]. It is covered by a 2 to 5 μm thick mucus layer produced by submucosal glands and epithelial goblet cells[18,19]. Mucus is a thick, viscoelastic aqueous fluid consisting of glycoproteins, secretory proteins, proteolytic enzymes and electrolytes. It enhances the wettability of the ciliated epithelial layer and maintains a physical barrier against the entry of foreign particles and pathogens.

Histologically, the respiratory and the olfactory mucosa possess an apical epithelial layer and underlying submucosal layer organization[12,18]. The respiratory epithelium (Figure 1-2) is composed of ciliated, pseudostratified columnar cells along with mucus secreting goblet cells. Basal cells (progenitor cells) form and begin their maturation process on the surface of the basement membrane. The epithelial cells are joined by tight junctions which regulate the transport of small, hydrophilic, or charged molecules across the intercellular spaces between the epithelial cells. The apical surfaces of the epithelial cells possess numerous microvilli which increase the surface area available for nasal absorption and facilitate the exchange of gases and water between the mucosal cells and the external environment. Underneath the basement membrane lies the lamina propria and the submucosal layer, which contain large populations of blood vessels, respiratory serous glands and lymphatic vessels interspersed within a connective tissue matrix. The histology of the olfactory epithelial layer (Figure 1-3) is essentially the same as the respiratory epithelium with a few functional differences due to the olfactory neurons. The olfactory epithelium is devoid of goblet cells and contains neurons projecting from the olfactory bulb. The neurons traverse the region in fascicules (bundles) in the olfactory submucosa and terminate as individual olfactory receptor cells on the epithelial surface. The olfactory receptors are exposed to the external environment in the nasal cavity and are surrounded by supporting or sustentacular cells. The axons penetrate the cribriform plate and synapse with second-order neurons in the olfactory bulb. The submucosal region of the olfactory epithelium is populated with Bowman's glands which provide mucus-like secretions to the epithelial surface. Humans have a weakly developed sense of smell (microsmatic), as their olfactory epithelium covers less than 10% of the total nasal mucosa[20]. Other examples of microsmatic animals include cows, sheeps, monkeys, and other primates. Animals belonging to the families Canidae (dogs) and Rodentia (rats, hamsters) are macrosmatic, possess a much greater fraction of olfactory epithelium, and thus possess an intense sense of olfaction[20].

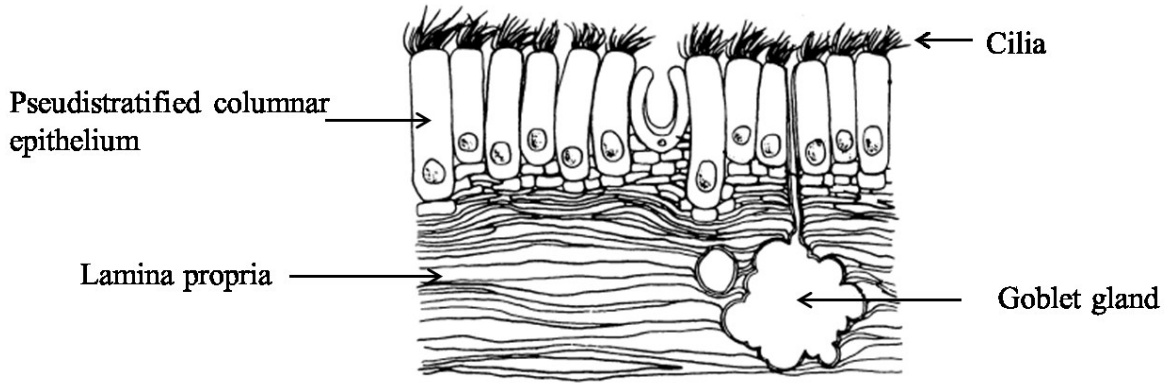

Figure 1-2 Schematic representation of the respiratory mucosa. Respiratory mucosa is characterized by a ciliated, pseudostratified, columnar epithelial layer containing dispersed Goblet glands that secrete mucus to the nasal cavity. Underlying the epithelial layer is the lamina propria and the submucosal layer which contains blood vessels and lymphatic vessels in a connective tissue matrix[21]; reproduced with permission.

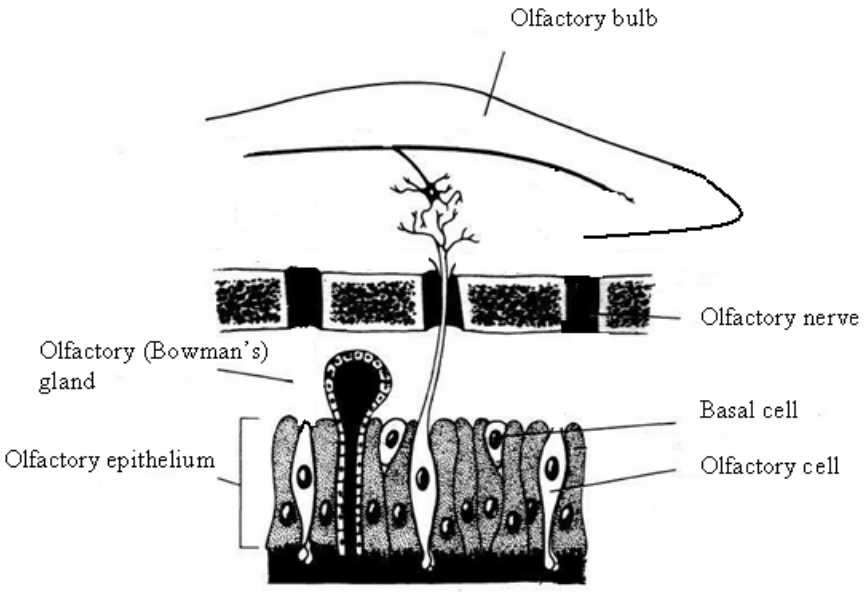

Figure 1-3 Schematic representation of the olfactory epithelium and its nerve connections to the olfactory bulb. The olfactory epithelium contains pseudostratified columnar cells along with specialized olfactory and sustentacular cells. Neurons projecting from the olfactory bulb terminate in the nasal cavity as olfactory receptor cells. Sustentacular cells surround and protect the olfactory neurons on the olfactory epithelial surface[21]; reproduced with permission.

Drug absorption and elimination from the nasal cavity

Following intranasal administration, drug molecules must permeate across the nasal mucosal epithelium and lamina propria in order to reach the blood vessels in the submucosal region. Drug molecules can cross the mucosal barrier either by passive diffusion or carrier-mediated transport, including facilitated or active transport[17,22]. Poor nasal absorption of a drug can be associated either with the physicochemical properties of the drug limiting its transport across the nasal membrane, reduced retention time in the nasal cavity due to mucociliary clearance and/or biotransformation by the enzymes in the nasal mucosa.

Mucociliary clearance is the primary cause of presystemic drug loss from the nasal cavity[23]. The ciliary beating clears mucus as well as substances adhering to the nasal mucosa (bacteria, allergens) and drains them into the nasopharnyx for eventual transfer to the gastrointestinal tract. The human nasal cilia exhibit an average beat frequency of 10 Hz[23]. Normal mucociliary transit time (turbinate to nasopharynx) in humans has been recorded to be 12 to 15 minutes[23]. For nasal sprays, biphasic clearance kinetics has been observed[24]. The first phase lasts for about 15-20 minutes during which about 50% of the administered dose is cleared. It is followed by a slower second phase, which removes the fraction of the nasal spray deposited in the anterior regions of the turbinates and the non-ciliated vestibular region.

Enzymatic degradation is the second key barrier to the efficient transport of xenobiotics across the nasal mucosa. Biotransformation in the nasal cavity or the nasal mucosa can significantly reduce the fraction of the parent drug available for absorption, and results in the creation of a ‘pseudo-first-pass’ effect[21]. The flux of an intact substrate, susceptible to enzymatic degradation in the nasal mucosa, can thus be influenced by both diffusion and metabolism parameters.

Drug metabolizing enzymes

Enzymes are highly substrate-specific biological catalysts. They accelerate the rates of biochemical reactions by lowering the energy of activation required for one or more reaction steps. The main purpose of drug metabolism in the body is to convert lipophilic xenobiotics into hydrophilic compounds to favor their excretion in the urine[25,26]. This is brought about by either oxidizing one or more functional groups on the molecule or by conjugating the compound with an endogenous hydrophilic moiety. Drug metabolizing enzymes are broadly divided into two major categories: phase I or oxidative enzymes and phase II or conjugative enzymes[27]. Phase I reactions are the most common metabolic reactions and include oxidative, hydrolytic and sometimes reductive reactions. These reactions generally precede the phase II reactions. The phase I reactions are also called functionalization reactions because during phase I metabolism, a polar functional group (-OH, -COOH, $-NH_2$, -SH etc.) is either introduced into a lipophilic substrate or is unmasked if it is already present in the substrate. A polar metabolite can then undergo phase II metabolism or may be directly excreted in the urine. Examples of phase I enzymes include: cytochrome P450 (CYP450) monooxygenases, flavin-containing monooxygenases, aldehyde dehydrogenase, epoxide hydrolases, monoamine oxidases, esterases, and amidases.

Phase II reactions involve covalent attachment of small polar endogenous molecules such as glucuronic acid, glycine, sulfate etc. to the parent drug or its phase I metabolite. The resulting water-soluble conjugates can be readily excreted in urine or bile. Examples of enzymes catalyzing phase II reactions include: uridine diphosphate glucuronosyltransferases (UGT), glutathione S-transferases, and sulfotransferases (SULT). The major oxidative and conjugative drug metabolizing enzymes and their reactions are listed in Table 1-1.

Table 1-1 Major oxidative and conjugative drug-metabolizing enzymes and their reactions[28].

Enzyme	Overall reaction	Chemical Reaction
Oxidative (phase I) enzymes:		
Cytochrome P450	Monooxygenase	$RH + O_2 + NADPH + H^+ \rightarrow ROH + H_2O + NADP^+$
Flavin-containing monooxygenase	Oxidation of heteroatoms N (or S) oxidation	$R\text{-}NH\text{-}R' + O_2 + NADPH + H^+ \rightarrow R\text{-}NOH\text{-}R' + H_2O + NADP^+$
Monoamine oxidase	Oxidative deamination	$R\text{-}CH_2NH_2 + O_2 + H_2O \rightarrow R\text{-}CHO + H_2O_2 + NH_3$
Alcohol dehydrogenase	Alcohol oxidation	$R\text{-}CH_2OH + NAD^+ \rightarrow R\text{-}CHO + NADH + H^+$
Aldehyde dehydrogenase	Aldehyde oxidation	$R\text{-}CHO + NAD(P)^+ + H_2O \rightarrow R\text{-}COOH + NAD(P)H + H^+$
Conjugative (phase II) enzymes:		
UDP-glucuronosyltransferase	Glucuronidation	R + UDP-glucuronic acid → R-glucuronide + UDP
Glutathione S-transferase	Glutathione conjugation	$R + GSH \rightarrow GS\text{-}R$ $R\text{-}X + GSH \rightarrow GS\text{-}R + HX$
Sulfotransferase	Sulfation	$R\text{-}XH + PAPS \rightarrow R\text{-}X\text{-}SO_3 + PAP + H^+$

R, xenobiotics; NADP, β-nicotinamide adenine dinucleotide phosphate; NAD, β-nicotinamide adenine dinucleotide; UDP, uridine-5′-diphosphate; GSH, glutathione; PAPS, 3′-phosphoadenosine 5′-phosphosulfate.

The liver is the primary site of metabolism and detoxication for both endogenous chemicals (e.g., cholesterol, steroid hormones, fatty acids, and proteins) and xenobiotics[29]. Upon oral administration, a drug has to pass through the gastrointestinal tract and the liver before reaching the systemic circulation. Enzymatic activity in the small intestine and the intestinal lumen is responsible for the initial metabolic degradation of many orally administered drugs prior to their transfer to the liver via the portal circulation[30–32]. A large fraction of the orally administered dose can thus be eliminated due to pre-systemic metabolism by enzymes located in the gut wall, gastrointestinal fluids and the liver, resulting in reduced bioavailability.

Extra-hepatic metabolism, that is metabolism by organs other than liver, also plays a significant role in metabolizing a large fraction of a drug dose. Extra-hepatic organs that contain significant xenobiotic-metabolizing enzymes include the lungs[33–35], kidneys[36], intestine[30,31], nose[21,37], skin[38,39], and placenta[40]. Organs that are ports for entry of foreign chemicals (xenobiotics) into the body, like the nose, skin or the mucosal membranes like the buccal or vaginal mucosa have a protective barrier function against the entry of foreign compounds in the body, and are reported to be populated with a large variety of drug metabolizing enzymes[21,39,41–44]. Pre-systemic metabolic degradation of administered drugs in these extra-hepatic organs can significantly reduce their bioavailability. Local metabolism can also have toxicological consequences as the metabolites formed could be potentially harmful or irritating to the underlying tissues.

Cytochrome P450 superfamily of enzymes

The most significant phase I drug-metabolizing enzymes belong to the cytochrome P450 (CYP450) superfamily, which is sub-classified into families (≥ 40% amino acid sequence identity), subfamilies (≥ 55% amino acid sequence identity), and specific enzymes referred to as isoforms. CYP450 enzymes metabolize a number of endogenous substances and xenobiotics, including more than 90% of all clinical

medications[45]. Approximately 75% of all the biotransformative reactions that take place in a human body are catalyzed by the CYP450 superfamily[46]. Fifty-seven functional genes and 58 pseudogenes of the CYP450 superfamily have been identified in humans[47]. Cytochromes P450 in humans and most vertebrates are divided into 18 families. CYP1, 2, and 3 are the three main families catalyzing the metabolism of more than 90% of clinical drugs. The metabolic capacity of these families can be attributed to the following isoforms[48,49]: 1A2 (4%), 2A6 (2%), 2C9 (10%), 2C19 (2%), 2E1 (2%), 2D6 (30%), and 3A4 (50%). The other families (e.g., CYPs 4, 7, 11, 17, 19, and 21) are involved in oxidation of endogenous substrates including steroids, bile acids, leukotrienes, and eicosanoids[46,50].

The cytochrome P450 isoforms are heme containing membrane proteins found primarily in the endoplasmic reticulum or mitochondrial inner membrane. These enzymes, also known as mixed-function oxidases, catalyze incorporation of one atom of molecular oxygen into the substrate to give product while the other oxygen atom is reduced by two electrons to give water. A representative substrate oxidation reaction catalyzed by CYP450 is shown in Equation 1-1[51].

$$RH+O_2+2H^++2e^- \xrightarrow[\text{NADPH}]{\text{CYP450 reductase}}^{\text{CYP450}} ROH+H_2O \qquad \text{Equation 1-1}$$

Reduced nicotinamide adenine dinucleotide phosphate (NADPH), NADPH-cytochrome P450 reductase or cytochrome b5, and molecular oxygen (O_2) are required as cofactors for the CYP450 catalytic cycle. The catalytic mechanism of CYP450 is illustrated in Figure 1-4.

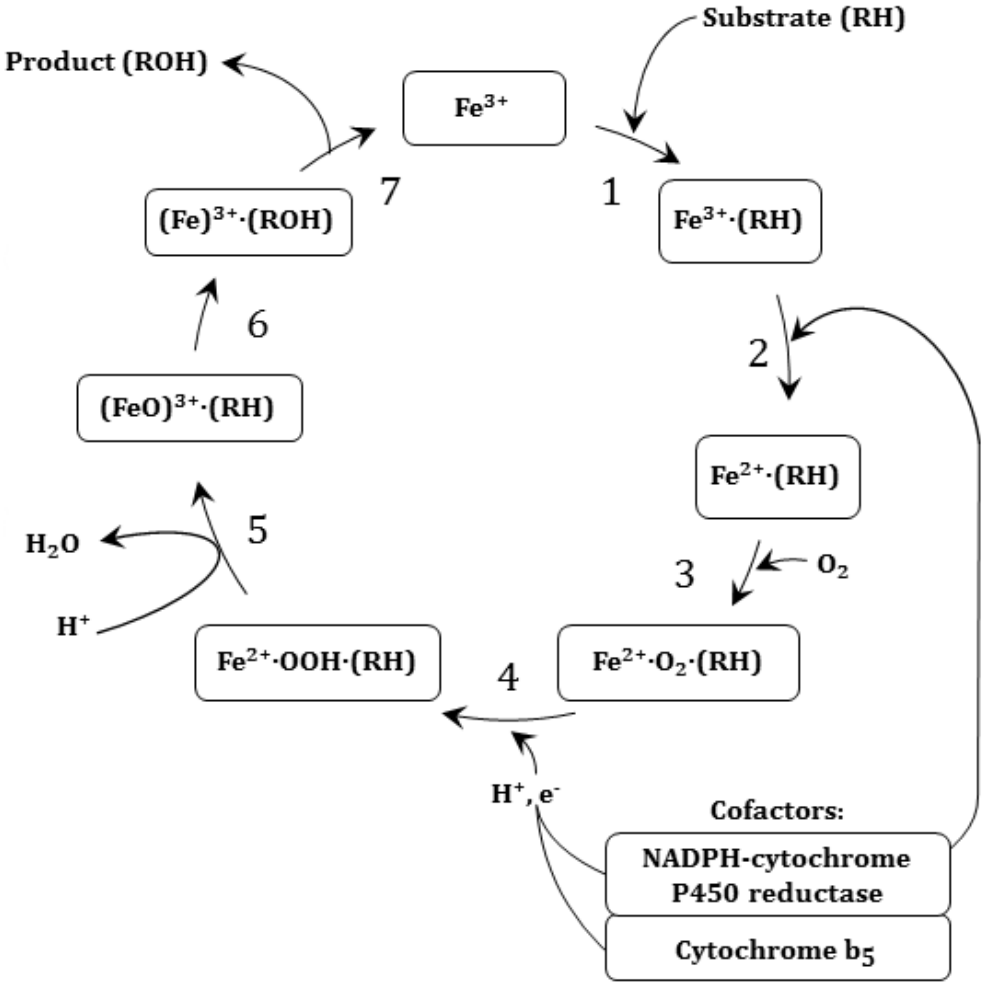

Figure 1-4 Catalytic cycle of cytochrome P450 enzymes[51].

The steps involved in the catalytic mechanism can be briefly summarized as follows: Step 1: The substrate (RH) binds to the oxidized form (ferric, Fe^{3+}) of the enzyme, in close proximity to the heme porphyrin group. Step 2: This step involves reduction of the ferric heme iron to the ferrous (Fe^{2+}) state due to the transfer of an electron from NADPH-cytochrome P450 reductase. Step 3: Oxygen binding: Molecular oxygen binds rapidly to the heme iron in ferrous (Fe^{2+}) state. Step 4: A second electron is transferred via the electron-transport system (NADPH CYP450 reductase or cytochrome b5) reducing the dioxygen adduct to a negatively charged peroxo group (Rate limiting step). Step 5: Oxygen cleavage: Molecular oxygen is broken down to form water and $(FeO)^{3+}$ complex. Step 6: Product formation: Substrate is oxidized by incorporation of an oxygen atom. Step 7: Product (ROH) is released and the enzyme returns to its initial active state.

Nasal drug metabolism

CYP450 mediated

Preliminary evidence of the presence of enzymatic activity in the nasal mucosa came from work of Dahl and Briner who were examining the deposition and disposition of inhaled 59Fe-labeled ferrocene[52]. They witnessed release of free iron in the nasal cavity, suggestive of CYP450 catalyzed oxidation. Shortly thereafter, Brittebo et al. detected the presence of accumulated radioactivity in nasal and tracheal mucosa following administration of radioactively labeled N-nitrosamines in rats, indicative of in situ metabolism[53]. High levels of CYP450 monooxygenases in all regions of the nasal mucosa were first reported by Dahl et al. in a dog model[54]. An increasing number of reports on induction of nasal tumors or lesions in laboratory animals following inhalation of compounds capable of generating toxic metabolites fueled interest in the area of enzymatic barrier properties of the nasal mucosa[42,55]. Since then, the expression and activity of nasal mucosal phase I and phase II drug metabolizing enzymes has been investigated by various researchers.

Tissue selective forms of several CYP450 isoforms have been identified in the nasal mucosa of a number of species including rabbits, guinea pigs, rats, mice, hamsters, dogs and humans[21,42,56–59]. The catalytic activity of the CYP450 enzymes in the nasal mucosa was observed to be much higher than that of liver, on a per mg of protein basis[21,37,60,61]. Ding et. al. showed that rabbit nasal microsomes had exceptionally high levels of CYP450 reductases when compared to the levels in hepatic or renal microsomes[56]. Reed et al. demonstrated the olfactory epithelium of rats, mice, and hamsters possessed higher NADPH-CYP450 reductase activity than that of the liver[62]. The ratio of CYP450 reductase to CYP450 content was obtained to be 1:11 to 1:15 in liver, whereas in the olfactory epithelium the ratio was 1:2 to 1:3. NADPH-CYP450 reductase mediates the rate limiting electron transfer represents the rate limiting step in

the catalytic cycle of CYP450[63]. Thus, their findings confirmed that the higher reductase to CYP450 ratio in the olfactory epithelium considerably increased its CYP450-mediated catalytic activity.

Rats and rabbits are the two most thoroughly studied species with regard to nasal CYP450 expression and activity[15,42]. Minn et al. examined mRNA expression of 19 CYP450 isoforms in rat olfactory mucosa and liver and measured their microsomal activities towards specific substrates[57]. Considerable quantitative difference in the mRNA expression levels was detected between the two tissues for several isoforms (CYP1A2, 2A1, 2A3, 2B2, 2D1, 2D4, 2E1, 2J4, and 3A9), while some isoforms (CYP2C6, 2C11, 2D2, 3A1, 3A2, and 4A1) were preferentially expressed in liver whereas others (CYP1A1, 2G1, 2B21, and 4B1) were exclusively expressed in the olfactory mucosa. Microsomal metabolism studies indicated that the CYP450-mediated catalytic activity of rat olfactory mucosa exceeded that of rat liver for phenacetin, chlorzoxazone, and dextromethorphan. The metabolism of lauric acid and testosterone occurred to a similar extent in both tissues, and the olfactory mucosa was almost incapable of metabolizing tolbutamide. Immunohistochemical characterization of rabbit olfactory mucosa was performed by Ding et al.[64]. These investigators isolated two unique forms of CYP450, designated as NMa and NMb, from olfactory microsomes of rabbits. NMa was also detected in the liver but NMb was expressed exclusively in the olfactory mucosa. Other CYP450 hepatic isoforms belonging to families 2, 3A, and 4 were also reported to be detected in the olfactory mucosa by immunochemical characterization. The specific occurrence of NMb in the olfactory mucosa was further confirmed by the detection and specific inhibition of NMb-dependent metabolism of testosterone in olfactory microsomes but not in hepatic microsomes.

It is now well established that the nasal mucosa contains significant levels and unique forms of microsomal CYP450 enzymes. The olfactory mucosae of rats, mice, hamsters, and rabbits exhibit maximum CYP450 expression amongst all extrahepatic

tissues[62,65]. Levels of CYP450 in the nasal mucosa of rats and dogs have been shown to be comparable[54,62]. Rabbit nasal tissues have 6-fold higher CYP450 levels than those observed in rats and dogs[42,56,57]. Pigs, cows, horses and monkeys are among a few additional species which have been employed to study nasal biotransformation. These models are at times preferred for studying nasal metabolism because of their larger nasal cavities enable the collection of more mucosal tissue for *in vitro* mechanistic studies and the distinction between the olfactory and respiratory nasal mucosa is better defined, as is seen in humans. Several isoforms of CYP450 monooxygenases were identified in the porcine nasal olfactory and respiratory mucosa, and the olfactory mucosa was observed to exhibit significantly higher CYP2A-mediated catalytic activities than those in the liver[66] (pig nasal and hepatic enzymes). Longo et al. isolated three constitutive forms of CYP450 from olfactory microsomes of cattle and evaluated their catalytic activity with respect to oxidation of various substrates including testosterone, progesterone, 7-ethoxycoumarin, aniline, 7-ethoxyresorufin, hexamethylphosphoramide etc[67]. They observed that the bovine nasal microsomes were more active in the metabolism of xenobiotic compounds (7-ethoxycoumarin, aniline, and hexamethylphosphoramide) than towards endogenous substrates (testosterone and progesterone). Metabolic activation of aflatoxin B by CYP3A4 and 2A6/2B6 in horse olfactory and respiratory mucosa was examined by Larsson et al.[68] Their studies revealed covalent binding of aflatoxin B metabolites in the respiratory epithelium, the sustentacular cells and cells of Bowman's glands in the olfactory mucosa, which correlated with the immunohistochemical localization of the specific isoforms in the olfactory and respiratory tissues in the horse. Characterization of nasal enzymes in cynomolgus monkeys demonstrated CYP450, NADPH-cytochrome P450 reductase and ethoxycoumarin O-deethylase activity[69].

Due to the lack of availability of human nasal tissues, studies available on CYP450 mediated metabolic activities in the human nasal mucosa are limited. Gervasi et al. reported that the amount of CYP450 enzymes in human respiratory mucosa was

around 5% of that of liver (on a per mg of protein basis) but the NADPH CYP450 reductase activity was comparable to that of liver[70]. The human nasal microsomes exhibited CYP450-mediated monooxygenase activities on substrates such as ethoxycoumarin, ethoxyresorufin and dimethylnitrosamine, however, the extent of metabolism was lower than that obtained with human hepatic microsomes[70]. On the contrary, in another study conducted by Longo et. al., the diethylnitrosamine metabolizing capacity of human nasal mucosa was found to be 10–25 times higher than that of the liver[71]. Various researchers have examined the expression and activity of specific CYP450 isoforms in the human nasal mucosa[59]. Since the development of the first whole-genome assembly of the human genome[72], considerable attention is being directed towards unfolding quantitative expression of specific CYP450 genes in the human olfactory and respiratory mucosa. The adult human olfactory and respiratory mucosa have been shown to possess gene transcripts for CYP2A6[73,74], 2A13[74], and isoforms of the subfamilies CYP 2C[75], 2E[76], 2F[76] 2G[77], 2S[78], and 3A[75]. The isoforms identified in human fetal nasal mucosa were CYP2A6[79], 2A13[79], 2B6[79], 2E1[76], 2F1[76], and 2J2[79].

Non-CYP450 mediated

Apart from CYP450 enzymes, the nasal mucosa has been reported to possess a number of additional phase I metabolizing enzymes, along with phase II and proteolytic enzymes, which together form a strong protective barrier against the entry of xenobiotics into the systemic circulation. Expression of aldehyde dehydrogenase, flavin containing monooxygenase, glutathione S-transferase and uridine diphosphate glucuronosyltransferase has been demonstrated in the human nasal mucosa by Zhang et al.[76]. Nasal carboxylesterases have been reported to significantly metabolize drugs containing carboxylic acid esters as functional groups[80,81]. The importance of nasal esterases in modulating pharmacokinetics and pharmacological response of drugs was

illustrated by ciclesonide, which is activated by nasal mucosal carboxylesterases and cholinesterases to active metabolite desisobutyryl-ciclesonide[82,83]. The fatty acid conjugates of the metabolite are retained inside the nasal cells and maintain its pharmacological action for a longer duration of time, hence allowing a once-a-day dosing. Expression of monoamine oxidase and its involvement in dopamine metabolism has also been documented in the nasal mucosa[84]. Other phase I enzymes such as epoxide hydrolase, alcohol dehydrogenases, and quinone reductase have been shown to be present in the nasal mucosa[61,76,79].

The biotransformation of peptides upon intranasal administration has been reviewed by several investigators in humans[85–87]. Enzymatic degradation is one of the key barriers for efficient nasal delivery of peptides and proteins. The presence of both exopeptidase (aminopeptidases, carboxypeptidases) and endopeptidases has been demonstrated in the human nasal epithelium[88–90]. A large fraction of the model peptide compounds leucine enkephalin and methionine enkephalin have been demonstrated to be hydrolyzed during transport across the nasal mucosa[49]. Nasal secretions also contain a variety of enzymes including lactate dehydrogenase, creatinin kinase, leucine aminopeptidase, angiotensin converting enzyme, and acid and alkaline phosphatases[91,92].

In vitro models for studying nasal metabolic clearance

Nasal *in vitro* models have been widely used to elucidate mechanistic information regarding transport, metabolism and absorption of drugs across the nasal mucosa. They provide relatively inexpensive and quicker alternatives to *in vivo* studies for studying nasal drug uptake by separating nasal mucosal permeation from the subsequent systemic absorption involving local blood flow, protein binding, systemic distribution, metabolism, and elimination. Although *in vivo* experiments permit characterization of physiological response and pharmacokinetic-pharmacodynamic assessments of intranasal

formulations, *in vitro* tests using excised nasal mucosa or cell culture models enable researchers to identify various factors influencing intranasal bioavailability.

Obtaining human olfactory and respiratory mucosal tissues from nasal biopsies is troublesome and expensive. Therefore, most *in vitro* studies are performed with the nasal mucosa excised from different animal species including sheep, pigs, dogs, rabbits and cows[93–95]. Some investigators have also used nasal cell cultures to study mechanistic functions or pathology of the upper airway. These cell cultures originated from hamster tracheal cells[96], rat, rabbit or human turbinate cells[97], human nasal epithelial tumors[98] or the commercially available human tracheal-bronchial epithelial cell culture epi-Airway™ (MatTek Corp., Ashland, MA)[99]. Excised nasal mucosa has been demonstrated to yield better *in vivo* correlations with respect to nasal drug absorption and metabolism than the cell cultures[93]. In the available cell culture models, only one or two cell types are predominant, and many heterotypic interactions arising from the complex cellular organization of the olfactory and respiratory mucosa are lost. Another limitation to the reproducible use of cell cultures for nasal mechanistic studies is the lack of an immortalized nasal cell line.

When comparing CYP450 mediated catalytic capacity of the nasal mucosa, species differences in the expression and activity of the P450 isoforms between the model animals and human nasal mucosa become a significant factor in estimating the extent of substrate degradation. Even within a single population, CYP450 activity can drastically vary leading to intra-species differences, which can have a significant impact on the metabolic fate, efficacy and potential adverse effects of administered drugs. Most CYP450 isoforms exhibit significant variability in enzyme activity due to enzyme induction, inhibition, genetic mutation and polymorphism. Alterations in enzyme activity can considerably affect the extent of drug metabolism leading to differences in drugs' physiological and toxicological effects[50,100–102]. Nevertheless, the permeation and metabolic activity of excised nasal mucosa obtained from the model animals provide

initial information about the potential human nasal absorption and metabolism, and assist in the determination of the kinetic impact of the factors involved, including the drug diffusion coefficient, concentration, mechanism of drug uptake and maximum metabolic rate (V_{max}), on drug permeation across the nasal mucosa. The extensive knowledge gained from characterization of nasal CYP450s and the role of CYP450s in metabolic activation and/or degradation of intranasally administered drugs in the animal models thus forms an excellent platform for screening of drug candidates for nasal delivery.

In our experiments, bovine nasal mucosal tissue has been used as the model membrane for studying nasal metabolism, mainly because of its ready and economic availability in large quantities with reproducible quality. The use of bovine tissues for studying the enzymatic activity of various organs like the liver, lungs, intestinal mucosa, kidneys, coronary arteries and tongue has become increasingly popular in the recent years[103–106]. This model has been shown to be well suited for studies on nasal permeation and metabolism of therapeutic peptides[94]. Bovine and human nasal mucosa have also been shown to exhibit comparable aminopeptidase activity[94]. Previous researchers have studied CYP450 monooxygenase activity in the bovine olfactory mucosa[67]. However, literature reports characterizing the CYP450 isoforms in cattle nasal mucosa are still scarce and an extensive knowledge of expression and activity of the biotransformative enzymes in bovine olfactory and respiratory mucosae is critically needed for efficiently evaluating the role of this model in predicting the extent of nasal metabolism in humans.

Melatonin as a model drug to investigate nasal CYP450 activity

Introduction

Melatonin (N-acetyl-5-methoxytryptamine) is an endogeneous indole amide neurohormone. It is biosynthesized primarily by the pineal gland from the amino acid tryptophan and the neurotransmitter serotonin[107–109]. Melatonin has also been detected in

retina, thymus, bone marrow, respiratory epithelium, skin, intestine, and to a very small extent at other sites in humans[109,110].

In mammals, melatonin is secreted in a circadian fashion in the hours of darkness and plays an important role as a regulator of sleep. The circadian pattern of endogenous melatonin production in humans is characterized by low plasma levels during the day (<30 pg/ml) and higher constant values (50–200 pg/ml) for over 8 hours at night[111,112]. Disturbances in melatonin circadian rhythm may lead to a disrupted sleep-wake cycle. Melatonin is responsible for maintaining homeostasis in humans, due to its ability to affect a variety of physiological conditions including the diurnal rhythm, sleep, mood, immunity, reproduction, intestinal motility, and metabolism[110,113–115]. Melatonin also possesses antioxidant, anticancer, neuroprotective, and cardioprotective properties due to the presence of an electron rich aromatic center[113,114,116–118].

Melatonin receptors

The actions of melatonin are mediated by membrane receptors and nuclear sites belonging to the nuclear receptor superfamily RZR/ROR[119]. Three specific melatonin receptors have been identified, and named as MT1, MT2, and the putative MT3 binding site[114,120]. MT1 and MT2 receptors are members of the 7-transmembrane G-protein coupled receptor family and are classified as unique subtypes owing to their molecular structure and chromosomal localization of their encoding gene. They perform signal transduction by altering cyclic AMP formation and protein kinase A activity, and interacting with phospholipase A2 and C, calcium and potassium channels[121].

Metabolism of melatonin

Melatonin, upon oral administration, undergoes extensive first pass metabolism. The half-life of intravenously administered melatonin in rats and dogs is about 20 minutes[122], whereas in humans, following exogenous administration, melatonin half-life ranges between 20-50 minutes[123,124]. The major degradation pathways of

melatonin are shown in Figure 1-5. Approximately 75% of the oral dose of melatonin is inactivated by hepatic microsomal CYP450-mediated hydroxylation, yielding 6-hydroxymelatonin[123,125,126]. 6-Hydroxylation of melatonin is principally catalyzed by CYP1A2[127–132], with a minor contribution from CYP1A1[132], CYP1B1[127], and CYP2C19[129,133]. The primary metabolite, 6-hydroxymelatonin, is further conjugated with sulfuric (~75%) or glucuronic (~25%) acid[134]. Melatonin is a potent substrate for CYP1A2, and acts as an inhibitor, affecting the metabolism of most CYP1A2 substrates, including caffeine and theophylline[129,135]. Fluvoxamine has been shown to competitively inhibit melatonin metabolism, with a K_i of 0.02 μM for the formation of 6-hydroxymelatonin in human liver microsomes[129,136]. Melatonin is also metabolized by O-demethylation, to a relatively smaller extent, producing N-acetyl-5-hydroxytryptamine (N-acetylserotonin)[127,134]. This reaction is catalyzed by CYP2C19. CYP1A2 has also been shown to catalyze O-demethylation of melatonin, though its relative contribution to this reaction is negligible, compared to the 6-hydroxylation reaction. Other minor metabolic pathways of melatonin include 2-hydroxylation to 2-hydroxymelatonin, or deacetylation by the action of amidase to 5-methoxytryptamine, which can be further conjugated or excreted unchanged in the urine.

The metabolic pathway of melatonin in the central nervous system is different from that in the liver[138]. In addition to 6-hydroxylation and demethylation by CYP450 isoforms, enzyme indoleamine-2,3-dioxygenase cleaves the pyrrole ring of melatonin to produce N-acetyl-5-N-methoxykynurenamine, which is further hydrolyzed to N-acetyl-5-methoxykynurenine.

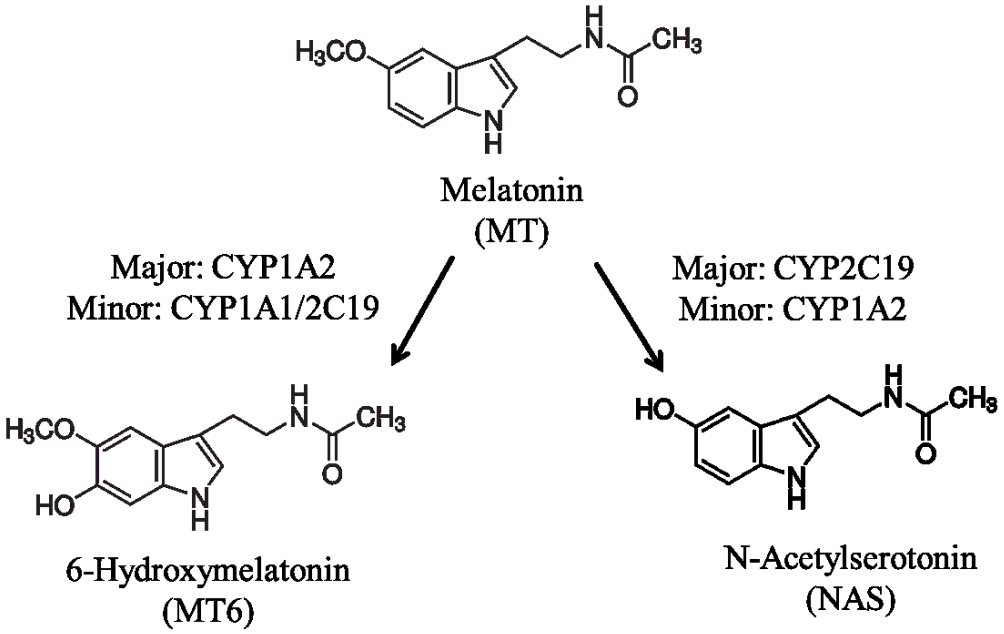

Figure 1-5 Principle metabolites of melatonin and major CYP450 isoforms involved in melatonin metabolism in human liver[50,129,137].

Limitations of oral melatonin delivery

The administration of melatonin during the daytime, out of the phase of its endogeneous secretion, aids in sleep induction[107,112]. Additionally, it is shown to improve sleep quality and latency especially in the elderly, without affecting REM sleep[111,139]. The sleep inducing effects of melatonin have advantages over conventional hypnotics. Unlike the synthetic hypnotics, melatonin merely induces a state of sleepiness without the adverse side effects of the conventional hypnotics. Melatonin has also been indicated in the treatment of Parkinson's disease, depression, epilepsy, dementia, and metastatic cancer[119,140–143] due to its radical scavenging and behavior altering properties.

Administration of melatonin in oral immediate release formulations has been shown to decrease sleep disturbances in patients suffering from some types of delayed sleep phase syndromes[111,112,139]. However, oral melatonin administration fails to maintain sleep for 8 hours, owing to its extensive first pass metabolism and variable oral

absorption. The bioavailability of orally administered melatonin is low and varies widely (20-40%)[123,124,144]. Because of its short elimination half-life, melatonin plasma levels are at a minimum level when the sleep-promoting effect is needed most (around 4-5 hours after the onset of sleep) when the circadian wake drive is increasing due to a decrease in sleep pressure. As a result, melatonin is not a good candidate for conventional, oral, immediate-release formulations.

In order to mimic the physiologic melatonin plasma concentration profile, a relatively high oral dose of melatonin could be administered, but this leads to desensitization of the melatonin receptors, resulting in tolerance[145]. As a consequence, a controlled release oral melatonin delivery system with rapid onset and rapid offset is essential to mimic the nocturnal endogenous plasma melatonin profiles. Several investigators have developed oral sustained release formulations of melatonin[145–147]. However, studies in human volunteers with some of these preparations have indicated a large intersubject variability in the plasma concentration profiles and poor oral bioavailability owing first-pass hepatic metabolism and variable absorption.

Alternative routes of melatonin delivery

To overcome the limitations of oral melatonin delivery, transdermal, intranasal, and buccal routes of administration are currently being investigated. Intranasal administration offers a viable option for systemic delivery of melatonin because the nasal mucosa can provide a rapid onset of action, avoidance of hepatic first-pass metabolism and non-invasiveness; all of which may maximize patient comfort and compliance. Using *in vitro* studies with Caco-2 cells, the permeability coefficient of melatonin was calculated to be 1.26×10^{-6} cm/s[139]. The high permeability of melatonin across Caco-2 cells is consistent with the observations of Costa et al., who showed that melatonin can easily pass through multilamellar lipid vesicles[148]. Melatonin permeates the biomembranes by transcellular passive diffusion, and no evidence of facilitated or

carrier-mediated transport of melatonin has been reported. Melatonin's low molecular weight, good lipophilicity arising from an unionizable indole amide moiety, and relatively nontoxic nature make it an attractive candidate for transmucosal delivery. However, the low solubility of melatonin in water (100 μg/ml at room temperature) complicates formulation development involving high dose melatonin formulations.

Several researchers have investigated melatonin absorption following intranasal delivery, however, insufficient data exists on the characterization of the bioavailability limitations resulting from pre-systemic metabolism of melatonin by the nasal CYP450 enzymes. Bechgaard et al. studied the intranasal absorption and bioavailability of melatonin in a 40% PEG 300 solution in rabbits[149]. Intranasal administration resulted in fast absorption of melatonin into the systemic circulation (T_{max}: 5 min), and the bioavailability was reported to be 55%, significantly higher than that obtained after oral administration (~20%). Incorporation of melatonin into starch microparticles has also been shown to result in a rapid absorption rate (T_{max}: 7.8 min) and high bioavailability (~80%) in rabbits[150]. Merkus has patented several melatonin formulations for intranasal administration comprising of cyclodextrins or glycerol[151,152]. He demonstrated that melatonin can be administered as a nasal spray, drop, solution, suspension, gel, ointment, cream, or powder by varying the choice of excipients, and all these formulations resulted in significantly higher bioavailability of melatonin than that obtained after oral administration in healthy human volunteers.

The nose-to-brain transport of melatonin has also been investigated by some researchers, although there is no evidence of any transporter mediating the direct transport of melatonin from the nasal olfactory region to the brain. Merkus et al. studied the uptake of melatonin in blood and CSF after nasal and intravenous delivery in healthy human volunteers[153]. Van der Berg et al. investigated melatonin uptake in blood and CSF upon intranasal administration to rats[154]. The results in rats and human subjects were comparable, and indicated that melatonin entered the CSF from the blood crossing the

blood-brain barrier and there was no additional nose-to-brain or nose-to-CSF transport of melatonin. Babu et al. examined nose-to-brain transport of melatonin incorporated in a polymer gel suspension in rats[155]. From the data obtained during their microdialysis study, the authors concluded that the polymeric vehicle (carbopol, CMC, or PEG 400) increased the mean residence time of melatonin in the nasal cavity, which, coupled with melatonin's lipophilicity, enhanced its penetration into the olfactory neuronal and respiratory trigeminal pathways to yield higher brain melatonin concentrations than those obtained after intravenous delivery.

As evident from these literature reports, interest in melatonin as a sleep-inducer and an antioxidant, homeostasis-regulating drug has increased tremendously in the past few years. A significant amount of research is being put into developing alternate dosage forms of melatonin, to improve its pharmacokinetic profile and correspondingly, its physiologic effects. A few examples of melatonin formulations under investigation are transdermal patches[145], topical creams[156], bioadhesives[145], solid lipid nanoparticles[157], liposomes[158,159], and starch microparticles[150]. A prolonged-release, oral solid melatonin formulation, Circadin®, has recently been launched in European and Asian countries for inducing natural sleep for patients with primary insomnia[160]. The consumption of melatonin as an antioxidant supplement and for sleep induction has increased tremendously in the past few years, now exceeding the sale of vitamin C in the US[161]. An intranasal melatonin delivery system is expected to result in rapid absorption of melatonin into the systemic circulation with increased bioavailability compared to the oral route. Hence, an estimation of the proportion of administered melatonin dose lost due to pre-systemic intranasal metabolism is currently needed to better understand the dosage requirements for melatonin following nasal administration and to serve as an example of a drug compound which undergoes metabolism-associated loss in the nasal cavity prior to systemic absorption.

CHAPTER 2

OBJECTIVES

Despite extensive research and literature reports characterizing the expression and activity of nasal enzymes, our knowledge of the role of these enzymes in limiting the bioavailability of intranasally administered drugs is still limited. Our central hypothesis is that the nasal mucosa is highly populated by several CYP450 isoforms which metabolize drug compounds as they diffuse through the nasal tissue and significantly reduce the fraction of parent compound available for systemic absorption. The principal objective of the current project is to evaluate the expression and drug metabolizing activity of major CYP450 isoforms in the nasal olfactory and respiratory mucosa in order to estimate the extent of biotransformation of metabolically-susceptible drugs during their transport across the nasal mucosa into the systemic circulation.

Specific Aims

1. Characterization of expression of major CYP450 isoforms in the nasal mucosa
   a. Examine and compare the expression of cytochrome P450 genes belonging to subfamilies 1A, 2A, 2C, and 3A in bovine respiratory and olfactory mucosa and liver using real time RT-PCR.
   b. Identify the cellular location of the major CYP450 isoforms in the bovine nasal mucosa using immunohistochemistry.
2. Analysis of melatonin metabolizing activity of bovine nasal CYP450 enzymes
   a. Examine and compare melatonin metabolizing activity of bovine respiratory, olfactory, and hepatic microsomes.
   b. Perform *in vitro* transport experiments to measure flux and concurrent metabolism of melatonin across bovine nasal respiratory and olfactory explants.

c. Evaluate the effects of CYP450 inhibitors on melatonin transport and metabolism.

d. Compare melatonin diffusion and metabolism across full thickness and de-epithelized mucosal explants to correlate the enzyme activity with enzyme distribution patterns in nasal epithelial and submucosal layers.

3. Estimation of mass transport of metabolically-susceptible drugs across the nasal mucosa

a. To develop a simulation model to evaluate passive diffusion of drugs coupled with saturable enzymatic metabolism to predict net drug transfer across the nasal mucosa.

b. To illustrate the relative kinetic contributions of drug permeability and metabolic susceptibility on nasal mucosal permeation.

c. To test the ability of the model to predict melatonin flux and metabolism across the nasal mucosal tissues.

CHAPTER 3

EXPRESSION AND LOCALIZATION OF MAJOR CYTOCHROME P450 ISOFORMS IN BOVINE NASAL MUCOSA

Introduction

Unlike the extensive literature that exists on the characterization of expression of CYP450 enzymes in major body organs including liver, kidney, and small intestine; our knowledge of the expression and localization of various CYP450 isoforms in the human nasal mucosa is still limited, primarily due to the lack of a sufficient supply of human nasal tissues. As a result, *in vitro* animal models have been extensively used to characterize the tissue specific expression and localization of CYP450 isoforms in the nasal mucosa[42,93]. The gene expression of CYP450 enzymes has now been well established in the olfactory mucosa of rats and rabbits[56,60,97,162,163]. The nasal mucosa of cattle, however, has not yet been well characterized with respect to CYP450 expression or activity. Cows are inexpensive and easily accessible sources of nasal tissues in the United States. Unlike rodents or rabbits, cattle are microsmatic, and thus their mucosal tissues better resemble the structural and histological organization of the human nose where the respiratory epithelium covers more than 90% of the total surface area of the nasal cavity[20]. The use of bovine tissues for studying the enzymatic activity of various organs like the liver, lungs, intestinal mucosa, kidneys, coronary arteries and tongue has become increasingly popular in the recent years[103,106,164]. The proteolytic capacity of the bovine nasal mucosa has also been widely studied, and bovine nasal explants are also one of the most common models for investigating peptide transport and metabolism across the olfactory and respiratory mucosa[94]. Characterization of bovine nasal mucosa for its oxidative and conjugative drug metabolizing enzymes would provide researchers with a convenient screening tool for studying biotransformation of xenobiotics during transport across the nasal mucosa.

The aim of the present study was to evaluate the gene expression and tissue-specific protein localization of major CYP450 isoforms in the bovine nasal mucosa. The specific isoforms of the CYP450 superfamily investigated in these studies were selected based on the data published by Williams et al., which reported that the enzymes belonging to CYP450 subfamilies 1A, 2A, 2C, and 3A contribute to the metabolism of more than 75% of the top 200 clinically administered drug compounds in the US in 2002[165].

Fluorescence based real time reverse transcriptase polymerase chain reaction (RT-PCR) has now become an indispensable tool for quantification of mRNA levels coding for specific proteins in the body. The technique of amplifying mRNA with RT-PCR is extremely sensitive and permits the use of minute quantities (as little as one cell) of sample. It can be used to compare the levels of mRNA expression and structure in different samples or different organs. However, a direct correspondence between the mRNA expression levels and protein concentrations within the tissues cannot always be established[166,167]. RT-PCR does not provide information about the tissue-specific cellular expression of nucleic acids, corresponding proteins, or protein activity. We thus used a combination of RT-PCR and immunohistochemical staining to investigate the CYP450 enzyme expression in bovine olfactory and respiratory mucosa. Using the quantitative reverse transcriptase-polymerase chain reaction, we determined the relative gene expression levels of major CYP450 isoforms in the olfactory and respiratory mucosa, and compared them with the expression in bovine hepatic tissues for relative comparison of the metabolic barrier properties of the nasal mucosa and liver. Tissue-specific localization of major CYP450 isoforms in bovine olfactory and respiratory explants was examined using immunohistochemistry. To enable inter-species comparisons of the nasal mucosal CYP450 gene expression levels, a complimentary DNA (cDNA) microarray analysis was performed on the mRNA extracted from bovine nasal olfactory and respiratory mucosal

samples. The CYP450 isoform expression levels were compared to the corresponding gene expression levels reported previously in the nasal mucosa of humans, rats, and mice.

Polymerase chain reaction

The polymerase chain reaction (PCR) is a process which amplifies specific DNA fragments for sensitive detection and quantification of nucleic acids[168,169]. A basic PCR run can be broken up into three steps. The first step involves denaturation of double stranded (ds) DNA by heating at high temperature (usually 95ºC) to separate the individual strands. The second step is annealing, in which the reaction mixture is cooled and target-specific primers are added to bind to complementary nucleotides on the target gene of interest. This results in the formation of a double strand between the primer and the complementary nucleotide sequence on the target gene. In the final extension step, the enzyme DNA polymerase synthesizes a new DNA strand by extending the primers in the 5' to 3' direction by adding complementary nucleotides on the target gene of interest.

The cycle of denaturation, annealing and extension is repeated over and over, stimulating the primers to bind to the original sequences and to newly synthesized sequences. Every cycle exponentially increases the copies (number) of required DNA transcripts (DNA segments), thereby improving the sensitivity of the detection. Depending on the quantity produced and the size of the amplified fragment, the reaction products can be separated using agarose gel electrophoresis and visualized directly by staining the gel with ethidium bromide.

Reverse transcriptase-PCR (RT-PCR) is a technique used for analysis of RNA expression using a PCR reaction. In RT-PCR, the specific mRNA strand is first reverse transcribed into its complementary DNA (cDNA) by the action of enzyme reverse transcriptase, which is then used in a regular PCR reaction for amplification.

The traditional PCR technique (regular or reverse-transcriptase) is also called 'end-point' PCR since the amplification product of a specific gene is detected at the end

of the final cycle. The end point detects transcripts at the plateau phase of the PCR reaction, where the reaction has stopped and no more products are being made; and if left long enough, the PCR products will begin to degrade. Thus, the end-point PCR analysis is associated with high variability. The results are based on size discrimination, possess low sensitivity, and allow only for qualitative or semi-quantitative analysis of target genes. Real time PCR involves data collection throughout the PCR amplification process rather than only at the end[170,171]. It enables real time detection of products formed at each cycle during transcript amplification in the exponential phase. In the exponential phase of a PCR reaction, the exact doubling of product is occurring at every cycle, resulting in 100% reaction efficiency. Thus, real time PCR quantification is very specific.

Intercalation of a fluorescent dye into the dsDNA is one of the most common techniques used to perform real-time PCR analyses. This detection method utilizes a DNA-intercalating dye that fluoresces once it binds to dsDNA. The most commonly used intercalating dye is SYBR® Green I which binds to the minor groove of dsDNA[172]. The real-time PCR instrument measures the fluorescence emitted at each cycle when the dye binds to dsDNA products synthesized during PCR amplification. From measurements of the fluorescence intensity plotted versus cycle number, amplification plots can be drawn. The DNA contents in each sample are characterized by the time point during cycling when the fluorescence signal generated exceeds a threshold value. Therefore, the higher the starting gene expression level of a target gene, the sooner the threshold level is exceeded. After completion of cycling, the real time PCR instrument can be set to perform a melting (dissociation) curve analysis to determine the melting temperature (T_m) of the amplified DNA, to confirm the specificity of the amplified PCR products.

The fluorescent signal is quantified as an R_n number, which is the reporter signal (SYBR® Green I) normalized to the internal standard fluorescence dye, ROX. ROX is a reference dye which is inert to the real time PCR reaction. Its fluorescence is stable throughout the PCR cycles. It thus acts as an internal standard in the real time PCR

reactions to correct for any pipetting or instrumental errors. The R_n numbers are monitored for each cycle. A fixed fluorescence threshold is set significantly above the baseline fluorescence level but within the exponential growth region of the amplification curve. This is then used to determine the threshold cycle value (C_T) which is the cycle number at which the fluorescence emission exceeds the fixed threshold level[173]. The C_T value is a relative measure of the concentration of target in the PCR reaction and is inversely proportional to amount of starting template. The gene expression level of a target gene (L) can be calculated from the corresponding C_T value using Equation 3-1.

$$L= 2^{-C_T} \qquad \text{Equation 3-1}$$

The expression level of the target gene can be normalized to the expression level of an endogeneous control or housekeeping gene. Housekeeping genes are constitutive genes that are required for the maintenance of basic cellular function. They are expressed in uniform levels in most cell types. Examples of some housekeeping genes include: glyceraldehyde 3-phosphate dehydrogenase (GAPDH), beta-2-microglobulin, hypoxanthine phosphoribosyltransferase 1, β-actin etc[174,175]. Following normalization with the housekeeping gene expression, a quantitative comparison of mRNA or gene expression levels can be performed in different sample populations.

Immunohistochemistry

Immunohistochemistry (IHC) is a method for identifying the cellular location and spatial resolution of tissue constituents (particularly antigens) in animal tissues or cell culture[176]. An antigen could be a protein, lipopolysaccharide, or any other constituent capable of generating an immune response. The process of imaging proteins by immunohistochemistry can be divided in three broad sections: tissue fixation and sectioning, immunostaining, and microsocopic examination. The aim of fixation is to

inhibit autolysis or self-degradation of excised tissues in an attempt to preserve them in a "life-like" state. Chemical cross-linking of proteins is the most common method of fixing biological tissues, and common preservatives used for this purpose include formaldehyde, glutaraldehyde, and acrolein. Upon fixation, the tissue is embedded in paraffin blocks, or is cryofrozen to enable thin sectioning (> 2 μm thickness). During the process of immunostaining, an initial antigen retrieval step is usually performed to break/open the methylene bridges formed during tissue fixation, which can mask antigenic sites on proteins. Antigen retrieval can be induced by heating the sections at controlled temperature and pressure or by chemically digesting the methylene bonds by proteolytic enzymes. Non-specific binding of the primary antibody to other tissue proteins is minimized by incubating the sections in blocking buffer (pH 7.4) containing species-matched serum proteins. Immunohistochemical staining is performed by incubating the tissue section with a primary antibody targeted against a specific antigen on the protein of interest. In order to visualize the antigen localization, a secondary antibody containing a visible marker is conjugated to the antigen-primary antibody complex. Depending on the chemical nature of the conjugated marker, the antigen-antibody complex can be visualized by light microscopy, confocal microscopy, or electron microscopy.

DNA microarray

The DNA microarray technology refers to the fabrication and use of arrays containing a collection of DNA fragments immobilized on a 'chip', such as a glass microscope slide or a silicon wafer[177,178]. Each array can contain tens of thousands of DNA probes with specific nucleotide sequences representing specific genes identified from the genome of the species of interest. Such 'genomes on a chip' then serve as a target to which fluorescently labeled nucleic acid probes can be applied for quantification of the gene expressions levels in the sample. The technique of DNA microarray for gene

expression analysis involves the following steps: RNA extraction from the sample of interest (organism, tissue, or cell culture), reverse transcription to convert RNA to complementary DNA (cDNA), labeling of the cDNA samples with specific fluorescent dyes, hybridization of the fluorescent cDNA samples on the microarray chip, and quantification of the relative fluorescence at each probe site to measure the relative abundance of the gene of interest with respect to an internal control, usually a housekeeping gene. By using a single reference sample as an internal control, the gene expression levels among several different genomic samples can be compared simultaneously. In addition to analyzing gene expression levels in multiple sample populations, the technique of microarray has gained popularity in the areas of biomarker determination, analysis of genes correlating with disease progression, toxicogenomics, pharmacogenomics, and personalized medicine.

Materials and Methods

Materials

Thin-walled, frosted lid, RNase-free PCR tubes (0.5 ml), TRIzol® reagent for RNA extraction, 10 mM dNTP Mix (2′-deoxynucleoside 5′-triphosphates) and SuperScript® III reverse transcriptase for cDNA synthesis reactions were purchased from Invitrogen (Life Technologies™, Carlsbad, CA). Oligonucleotide primers were obtained from IDT (Integrated DNA Technologies Inc., Coralville, IA). Real-time qPCR Master Mix SYBR® Advantage® was purchased from Clontech Laboratories (Clontech Laboratories, Inc., Mountain View, CA). The MicroAmp® Fast optical 48-well reaction plate was obtained from Applied Biosystems® (Life Technologies™, Carlsbad, CA). The thermal seal adhesive sealing film to cover the PCR plates was purchased from RPI (Research Products International Corp., Mount Prospect, IL). RNase free water and QIAquick gel extraction kit were purchased from Qiagen (Qiagen Inc., Valencia, CA). Primary antibodies, including mouse monoclonal anti-human CYP2A6, mouse

monoclonal anti-human CYP1A2, and rabbit polyclonal anti-human neuron-specific enolase (NSE) were obtained from Abcam (Abcam Inc., Cambridge, MA). Rabbit polyclonal anti-human antibody to CYP 2C8, 2C9, 2C19; and rabbit monoclonal anti-human antibody to CYP3A4 were obtained from Biomol International LP (Plymouth Meeting, PA). Alexa fluor 488 conjugated secondary antibodies: goat anti-mouse IgG, goat anti-rabbit IgG as well as horse-radish peroxidase (HRP)-conjugated goat anti-mouse IgG, and the nuclear stain ToPro3, Dulbecco's phosphate buffered saline (PBS) were obtained from Molecular Probes® (Life Technologies™, Carlsbad, CA). Other chemicals and stains used in microscopy were obtained from the Central Microscopy Research Facility, University of Iowa. All other reagents were obtained from Sigma-Aldrich® (Sigma-Aldrich® Co. LLC, St. Louis, MO).

Preparation of animal tissues

Bovine (*Bos taurus*) (six animals, average two years old) nasal explants and liver specimens were obtained from Bud's Custom Meats Co. (Riverside, IA). The nasal respiratory and olfactory mucosae were collected by making incisions along the lateral walls of the nasal cavity and a horizontal incision along the ocular plane. The ethmoturbinates, covered by the olfactory mucosa, and the maxilloturbinates, covered by the respiratory mucosa, as well as liver tissue were excised immediately after death. For histological and immunofluorescence examinations, the excised olfactory and respiratory mucosal sections were fixed immediately in zinc formalin (1% zinc sulfate in 3.7% unbuffered formalin, prepared from a 37-40% concentrated formaldehyde solution) for 36 hours. For RNA extraction, the nasal and liver tissues were frozen in liquid nitrogen immediately after dissection and transferred to the lab. They were kept frozen at -80 ºC until use.

RNA extraction

Total RNA was isolated from frozen tissues using TRIzol® reagent according to the manufacturer's instructions. Briefly, 1 mL of TRIzol® was added to a small piece of frozen tissue and homogenized at 4 ºC to release the nucleic acids. The RNA was isolated using a phenol-chloroform extraction method provided in the TRIzol® kit. The concentration and purity of RNA was checked by absorbance spectroscopy using a Nanodrop 2000 spectrophotometer (Thermo Scientific, Wilmington, DE). The concentration of RNA was measured by the absorbance at 260 nm. The integrity of the RNA samples was assessed by denaturing electrophoretic analysis on agarose gels. Contamination of the RNA with proteins and genomic DNA was examined by measuring the UV absorbance at 260 nm and 280 nm. The ratio of absorbance of the RNA sample at 260 nm and 280 nm (A260/A280) should be greater than 1.8 to ensure the absence of genomic DNA and proteins such as RNases in the RNA sample.

Reverse transcription

Complementary DNA (cDNA) was synthesized from RNA samples using a SuperScript® III reverse transcriptase kit in a Bio-Rad MyCycler™ thermal cycler (Bio-Rad Laboratories Inc., Hercules, CA). The reaction was initiated by mixing 2.5 µg of total RNA and 2.5 µM oligo(dT) primer in a total volume of 13 µL in an autoclaved RNase-free PCR tube (0.5 ml capacity). Oligo(dT) primers are a short sequence of deoxy-thymine nucleotides that bind to the poly-A tail of the mRNA. This results in the formation of a free 3-hydroxy end that is required for the activity of the reverse transcriptase enzyme to synthesize the cDNA strand on the mRNA strand. The tubes were maintained at 65 °C for 8 minutes in the thermal cycler. After the 8 minute incubation, the tubes were placed in an ice bath (4 °C) for 2 minutes. The reverse transcription reaction was performed at 50 °C for 90 minutes with the use of 200 units of SuperScript® III reverse transcriptase enzyme, 10 mM dithiothreitol, 0.5 mM dNTP

(2′-deoxynucleoside 5′-triphosphates containing 0.5 mM each dATP, dGTP, dCTP, and dTTP) and 50 mM Tris-HCl buffer (pH 8.3) containing 75 mM KCl and 3 mM $MgCl_2$ in a total volume of 20 µl. The reverse transcriptase was inactivated by heating to 70 ºC for 15 minutes. The quality of the synthesized cDNA samples was confirmed by denaturing agarose gel electrophoresis. The cDNA samples were maintained at -20 ºC until further use.

Real time RT-PCR

Bos taurus primer pairs used for quantitative real time PCR are given in Table 3-1. Primer pairs for CYP1A1-like, 1A2-like, 2C9-like, 2C19-like, and 3A4-like genes have been described previously[179]. The primers for the remaining genes and for glyceraldehyde 3-phosphate dehydrogenase (GAPDH) were designed according to the sequences in GenBank with the help of Primer-3. Specificity of the primers used was confirmed by BLAST analysis of the GenBank database of NCBI.

One microlitre of the reverse transcription product (cDNA) was added to the PCR mixture containing 5 µl of SYBR® Advantage® premix, 1 µM each of the sense and antisense primers (Table 3-1) in a final volume of 10 µl made with RNase free water in the wells of the MicroAmp® Fast optical 48-well reaction plate placed on ice (4 ºC). The wells were sealed with the thermal seal adhesive film and the plate was centrifuged at 250×g for 30 seconds at 4 ºC using an Eppendorf 5804R centrifuge (Eppendorf, Hauppauge, NY). The real time PCR reactions were performed in a StepOne PCR machine, version 1.0 from Applied Biosystems® (Life Technologies™, Carlsbad, CA).

The PCR run was initiated with one 5-minute cycle at 95 ºC. A three step cycling program was used to monitor amplification for 40 cycles with a 30 second denaturating step at 95 ºC, a 30 second annealing step at a specific annealing temperature and a 30 second elongation step at 72 ºC. At the end of the PCR cycles, a melting (dissociation) curve analysis was performed to verify the amplification of a single amplicon. Melting

Table 3-1 Primers used for quantitative real time RT-PCR

Gene	Primers	Sequence (5'-3')	Product size (bp)	Annealing temp (°C)	Position (5')	Accession number
CYP1A1-like (Bovine CYP1A1)	Sense	GACCTGAATCAGAGGTTCTACGTCT	81	60	861	XM_588298
	Antisense	CCGGATGTGACCCTTCTCAA			941	
CYP1A2-like (Bovine CYP1A2)	Sense	ACCATGACCCGAAGCTGTG	78	60	1301	NM_001099364
	Antisense	CAATGGTGGTGCCATCAGAC			1378	
CYP2A6-like (Bovine CYP2A6)	Sense	CCAGAATGGAGCTCTTCCTCT	195	58	26	DQ114539
	Antisense	CTATTTGCTCCTCCCACCAG			220	
CYP2C9-like (Bovine CYP2C87)	Sense	TCCCTGGACATGAACAACCC	71	60	760	XM_612374
	Antisense	TTGTGCTTTTCCTGTTCCATCTT			830	
CYP2C19-like (Bovine CYP2C21)	Sense	TCCCAAGGGCACAACCATA	56	60	1146	XM_600421
	Antisense	CCTTGCCATCGTGCAGG			1201	
CYP3A4-like (Bovine CYP3A28)	Sense	GCCAGAGCCCGAGGAGTT	77	60	1309	NM_174531
	Antisense	GCAGGTAGACGTAAGGATTTATGCT			1385	
CYP3A4 (Bovine CYP3A4)	Sense	GGAAACCTGGGTTCTCCTGGCT	308	58	114	NM_001099367
	Antisense	CCGATGGACCAAAAACCCTCCG			421	
GAPDH	Sense	ATGGAGAAGGCTGGGGCTCACT	209	58	379	NM_001034034
	Antisense	AGTCCCTCCACGATGCCAAAGT			587	

For the nomenclature of bovine specific primers, the bovine CYP450 isoform sequences were identified with name of the human sequence sharing the highest percentage of homogeneity, based on protein sequence alignment, followed by the suffix ‘-like’.

curves were run immediately after the cycling program and first derivative dissociation curves were generated for each well. Wells in which more than one peak appeared above 80 ºC were discarded. Negative control reactions with no added reverse transcriptase product were performed for each PCR run to monitor potential contamination of reagents. Electrophoretic analysis of the PCR products was performed by separating the products on ethidium bromide-stained 2% agarose gels. The separated products were visualized by transillumination with ultraviolet light. The absence of non-specific amplification was verified by electrophoresis on agarose gels & melt curve analysis.

Multiple PCR products formed during RT-PCR amplifying CYP1A2-like genes from bovine nasal respiratory mucosa were isolated using the QIAquick gel extraction kit (Qiagen Inc., Valencia, CA). The kit contains a silica membrane assembly for binding of double-stranded DNA fragments. It enables the isolation of the the DNA from the gel by dissolving the agarose gel in acidic extraction buffer. The portion of the agarose gel containing each DNA fragment was cut using an autoclaved scalpel (Cole-Parmer, Vernon Hills, IL) in an autoclaved, RNase-free microcentrifuge tube (RPI, Research Products International Corp., Mount Prospect, IL). The extraction buffer (Buffer QG provided with the kit) was added (3 times the volume of the sliced gel) to each tube, and the tubes were incubated at 50 °C for 10 minutes to dissolve the gel completely. Isopropanol (one third the volume of extraction buffer) was added to tubes and the contents of the tubes were mixed by gentle shaking. The solution from the microcentrifuge tube was then added to the QIAquick spin column placed in the collection tube provided with the kit. The collection tubes were centrifuged for 1 minute at 10000 ×g using an Eppendorf Minispin® centrifuge (Eppendorf, Hauppauge, NY). The column was washed using 1 ml of buffer PE provided with the kit and the collection tubes were again centrifuged for 1 minute at 10000 ×g. For elution of the DNA fragment from each column, the QIAquick column was placed into an autoclaved 1.5 ml microcentrifuge tube and 25 µl of the elution buffer (Buffer EB provided with the kit,

10 mM TrisHCl, pH 8.5) was added to the column. The tubes were centrifuged for 2 minutes at 10000 ×g. After centrifugation, the QIAquick column was discarded and the microcentrifuge tubes were submitted to the DNA Sequencing Facility of the University of Iowa to confirm the nucleotide sequence and gene specificity of the PCR products.

Calculations and statistical analysis

For real time PCR, the relative expression level (L) for each gene was calculated from the C_T values using Equation 3-1. Normalization of expression level of each CYP450 genes to the endogenous control (housekeeping gene, GAPDH) was performed by dividing the expression levels of each gene of interest by the expression level of GAPDH. The tissue expression of mRNA for each CYP450 isoform was expressed as mean ± standard deviation of six animals. Statistically significant difference between expression levels of CYP450 isoforms within the nasal olfactory and respiratory mucosa and the liver was evaluated using the Student's t-test with a Bonferroni correction. A p-value of less than 0.05 was considered to be significant.

Histological examination of bovine nasal mucosa

Fixed nasal mucosal explants were dehydrated and embedded in low temperature melting paraffin using an RMC paraffin tissue processor, model 1530 (Kroslak Enterprises Inc., Midland, ON, Canada). For morphological examination, 5 µm thick sections were cut using a Leica UC6 ultramicrotome (Leica Microsystems Inc., Bannockburn, IL) and mounted onto Superfrost® Plus microscope slides (Fisher Scientific Inc., Pittsburgh, PA). The mounted sections were dehydrated overnight and deparaffinized by placing them in an oven maintained at 60 ºC to melt the paraffin followed by rinsing the slides in xylene. Staining of the sections with hematoxylin and eosin was carried out using DRS-601 Sakura Diversified Stainer (GMI Inc., Ramsey, MN). Finally, the sections were coverslipped and examined using an Olympus BX-51

light microscope (Olympus America Inc., Center Valley, PA) equipped with a DP-71 digital camera.

Neuron-specific enolase (NSE) immunohistochemistry

The olfactory mucosa consists of a pseudostratified epithelial layer containing neurons projecting from the olfactory bulb and an underlying submucosal layer. The presence of a nervous system-specific protein enolase in bovine olfactory mucosa was verified using immunohistochemical staining. Bovine respiratory and olfactory mucosal sections (5 μm thick) were deparaffinized and hydrated using a DRS-601 Sakura Diversified Stainer (GMI Inc., Ramsey, MN). Heat-induced epitope retrieval of the sections immersed in citrate buffer was carried out in a microwave (Pelco-Biowave, Ted-Pella Inc., Redding, CA) set at 650 watts at 95ºC (5 minutes warm, 5 minutes rest, 5 minutes warm). Non-specific binding was minimized by incubating the sections in blocking buffer (10% normal goat serum, 1% bovine serum albumin in PBS, pH 7.4) for 20 minutes at room temperature. The sections were incubated with the primary antibody solution (rabbit polyclonal anti-human neuron-specific enolase, 1:200 dilution of the manufacturer's stock with blocking buffer, pH 7.4) for 90 minutes at room temperature. Negative control sections were incubated instead with rabbit immunoglobulin G (IgG) at concentrations identical to those of the primary antibodies. After rinsing in PBS, the tissues were exposed to secondary antibody solution (goat anti-rabbit Alexa 488, 1:500 dilution of the manufacturer's stock with PBS, pH 7.4) for 30 minutes at room temperature. Following washing, the sections were incubated with the nuclear stain, To-Pro3, and mounted in Vectashield (Vector Laboratories, Burlingame, CA). Examination took place with a BioRad 1024 confocal laser-scanning microscope (BioRad, Carl Zeiss, Germany) equipped with a krypton/argon laser at excitation wavelengths of 488 nm and 647 nm. Digital image processing was performed using ImageJ software[180,181] (U.S. National Institutes of Health, Bethesda, MD).

Cytochrome P450 immunohistochemistry

For CYP450 immunofluorescence imaging, respiratory and olfactory mucosal sections (5 μm thick) were mounted on slides, deparaffinized, and hydrated using a DRS-601 Sakura Diversified Stainer (GMI Inc., Ramsey, MN). To optimize the process of antigen retrieval of formalin-fixed bovine nasal explants, enzymatic and heat-induced epitope retrieval methods were individually tested. During preliminary method optimization, enzymatic epitope retrieval was performed using trypsin or proteinase K. Tissue sections were incubated with 0.1% trypsin dissolved in PBS (pH 7.4) at 37 ºC for 20 minutes or with proteinase K (1.5 units/ml) dissolved in PBS (pH 7.4) at room temperature for 15 minutes. Heat-induced epitope retrieval of the sections immersed in citrate buffer was carried out in a laboratory microwave (Pelco-Biowave, Ted-Pella Inc., Redding, CA) set at 650 watts, at 95ºC, (5 minutes warm, 5 minutes rest, 5 minutes warm). After heat-induced epitope retrieval, the tissues and citrate buffer were allowed to cool for 20 minutes before removing the slides. This allowed the slides to cool sufficiently so that they may be handled and the antigenic site could re-form after being exposed to high temperature. It was observed with CYP2A6 immunofluorescence staining that epitope retrieval performed with the enzymatic treatment, either with trypsin or proteinase K, did not retrieve the antigenic sites and the sections did not demonstrate any immunofluorescence signal. Sections treated with heat-induced epitope retrieval exhibited immunofluorescence. Hence, heat-induced epitope retrieval in the microwave was performed on bovine nasal sections for all the CYP450 immunohistochemical analyses.

Following epitope retrieval, non-specific binding was minimized by incubating the sections in blocking buffer (10% normal goat serum, 1% bovine serum albumin in PBS, pH 7.4) for 20 minutes at room temperature. The sections were incubated with the different dilutions of primary antibody solutions (1:250, 1:350, 1:500, 1:1000 dilutions in blocking buffer, pH 7.4) for 90 minutes at room temperature. The dilutions were

performed to choose the optimal concentration of primary antibody that yielded the strongest immunofluorescence signal with minimal background staining on bovine nasal sections. The final dilutions of the primary antibodies used for immunofluorescence imaging were: mouse anti-human CYP1A2 (1:100 dilution of the manufacturer's stock with blocking buffer, pH 7.4), mouse anti-human CYP2A6 (1:350 dilution of the manufacturer's stock with blocking buffer, pH 7.4, 1.5 μg/ml), rabbit anti-human CYP2C (1:1000 dilution of the manufacturer's stock with blocking buffer, pH 7.4) and rabbit anti-human CYP3A4 (1:1000 dilution of the manufacturer's stock with blocking buffer, pH 7.4). Negative control sections were incubated with species-matched, non-specific immunoglobulins at concentrations identical to those of the primary antibodies. After rinsing in PBS, the tissues were exposed to secondary antibody solutions: goat anti-mouse Alexa 488 (1:500 dilution of the manufacturer's stock with PBS, pH 7.4) for CYP1A2 and CYP2A6, or goat anti-rabbit Alexa 488 (1:500 dilution of the manufacturer's stock with PBS, pH 7.4) for CYP2C and CYP3A4. These tissues were incubated for 30 minutes at room temperature. Following a washing step, the sections were incubated with the nuclear stain, To-Pro3, and mounted in Vectashield (Vector Laboratories, Burlingame, CA). Examination took place with a BioRad 1024 confocal laser-scanning microscope (BioRad, Carl Zeiss, Germany) equipped with a krypton/argon laser at excitation wavelengths of 488 nm and 647 nm. Digital image processing was performed using ImageJ software[180,181] (U.S. National Institutes of Health, Bethesda, MD).

cDNA microarray

The cDNA microarray analysis on bovine nasal olfactory and respiratory mRNA samples and inter-species comparison of nasal CYP450 expression was performed with the assistance of Professor Todd Scheetz, Department of Ophthalmology and Visual Sciences, College of Engineering, and Center for Bioinformatics and Computational

Biology at the University of Iowa. Microarray expression data from nasal samples were identified and collected from NCBI's Gene Expression Omnibus[182]. Only samples from normal (non-diseased, non-treated) tissues were used. A total of 71 samples from human (GSE11348, GSE2395, GSE8987, GSE9150), 15 samples from mouse (GSE1680, GSE2437, GSE3455, GSE4915, GSE4927), and 34 samples from rat (GSE5019, GSE5349, GSE7002) were used for data analysis. These samples were all run on Affymetrix 3' IVT arrays from which selected CYP450 isoform expression present/absent calls were obtained using the Affymetrix MAS 5.0 expression summary algorithm[183].

For analysis of bovine nasal mucosal CYP450 enzyme expression, RNA extraction was performed by Manar Al-Ghabeish, College of Pharmacy, the University of Iowa. Nasal olfactory and respiratory mucosal tissues were extracted from 3 different animals, and immediately frozen in liquid nitrogen. RNA was extracted from the frozen tissues using TRIzol® reagent and purified by DNase treatment. Examination of the quality of the RNA samples, reverse transcription to synthesize complementary DNA (cDNA), and gene expression microarray analysis was performed by the DNA Core Facility at the University of Iowa. To ensure the purity of extracted RNA, the ratio of absorbance of RNA samples at 260 nm and 280 nm was maintained greater than 1.8 and the RNA integrity number (RIN) generated by the Agilent QC (Agilent Technologies, Inc., Santa Clara, CA) was maintained above 7. The complementary DNA (cDNA) was synthesized from the total RNA and the CYP450 gene expression was evaluated using the Affymetrix GeneChip® Bovine Genome Array (Affymetrix Inc., Santa Clara, CA) with normalization and gene-level expression values obtained using Partek Genomics Suite (Partek Inc., St. Louis, MO). Genes expressed above the 50^{th} percentile were defined as expressed, while expression values between the 15^{th} and 50^{th} percentile were classified as weakly expressed. Orthologs of the genes of interest were identified using Ensembl's BioMart resource[184] to examine the sequence homology and/or differences in CYP450 genes in the four species studies (humans, rats, mice, and cattle).

Results

The technique of immunoblotting for identifying the location of CYP450 proteins in bovine tissues can suffer from false immunopositive signals arising due to antibody cross-reactivity, as bovine specific antibodies to specific CYP450 isoforms have not yet been commercialized. With the advancement in the bovine genome sequencing, it was possible to design bovine-specific primers for quantitative analysis of gene expression of various CYP450 isoforms. A definitive nomenclature for bovine CYP450 isoforms is not yet available. Hence, we followed a nomenclature system reported in several previous studies[164,179], where the bovine CYP450 isoform sequences were identified with name of the human sequence sharing the highest percentage of homogeneity, based on protein sequence alignment, followed by the suffix '-like'.

The data obtained with RT-PCR confirmed the expression of several CYP450-like genes in the bovine olfactory and respiratory mucosa. As seen in gel electrophoresis images (Figure 3-1), transcripts of each of the isoforms selected were detected in the real time PCR products amplified from bovine hepatic mRNA. Bovine hepatic tissue exhibited significantly higher gene expression levels of all the CYP450 isoforms examined (CYP1A1-like, CYP1A2-like, CYP2A6-like, CYP2C9-like, CYP2C19-like, CYP3A4-like, CYP3A4), than the corresponding mRNA levels in the olfactory and respiratory mucosa (Figure 3-2). The graph has been plotted on logarithmic scale to enable simultaneous visualization of mRNA expression levels of all the genes studied. The negative controls included in each run yielded either an undeterminate C_T value or a C_T value of greater than 38 indicating that the sample did not meet the threshold value, confirming the absence of any DNA contamination. No statistically significant difference was observed between the mRNA expression levels obtained in the olfactory and the respiratory mucosa for any of the genes studied. Although all of the isoforms were expressed in the bovine olfactory and respiratory mucosa, there were significant differences in the expression levels observed for the different CYP450 genes. Both the

nasal tissues exhibited abundant expression of three genes, CYP2A6-like, CYP3A4-like and bovine CYP3A4. Remaining isoforms, including CYP1A1-like, CYP2C9-like, and CYP2C19-like were expressed in both bovine olfactory and respiratory mucosa, but exhibited extremely low expression levels (<1%) compared to those obtained in bovine hepatic tissues. Greater inter-animal variability was observed in the olfactory and respiratory expression levels of CYP450 isoforms as compared to the hepatic expression levels.

Amplification of the CYP1A2-like gene from mRNA extracted from bovine respiratory mucosal tissues resulted in multiple PCR products, yielding multiple peaks on melting curve analysis and bands on electrophoretic analysis (Figure 3-3 and Figure 3-4). To identify the sequences of the fragments amplified during real time RT-PCR, the individual DNA fragments were individually extracted from the agarose gel and sequenced to identify possible sequence homology with the bovine CYP1A2-like genes (NCBI accession number NM_001099364). The sequence of the amplified products partially aligned with the nucleotide sequence of bovine CYP1A2 mRNA, indicating the possible expression of a spliced variant of CYP1A2-like genes in the bovine olfactory and respiratory mucosa. Spliced variants for a gene are mRNA sequences that exhibit different nucleotide sequences resulting from alternative splicing of pre-mRNA to mRNA, however, they code for the same protein. Sequencing of the PCR products showed matched nucleotide sequences for CYP1A2-like genes, and the full sequences are provided in Appendix A.

The histological organization of the bovine olfactory mucosa, located in the superior region of the nasal cavity, is shown in Figure 3-5. The olfactory mucosa consists of a pseudostratified columnar epithelial layer (seen as columnar lining of cells on the exterior side of the explant in cross-section) and the underlying highly cellular lamina propria (seen as granulated light pink cell layer). The basement membrane separates the epithelial layer from the lamina propria. The submucosal region contains of the cells of

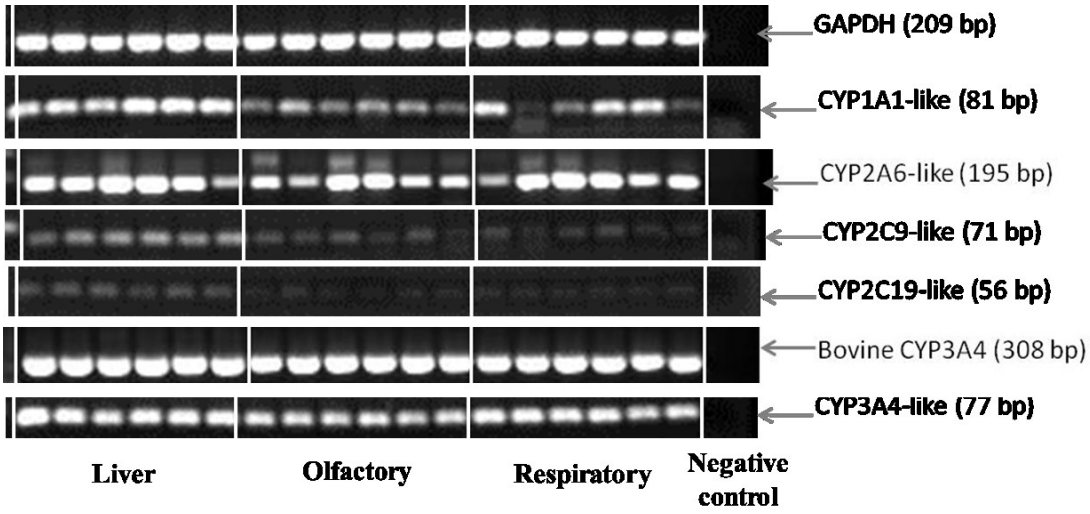

Figure 3-1 Gel electrophoretic analysis of RT-PCR products obtained during amplification of the selected CYP450 genes in bovine hepatic, olfactory, and respiratory tissues. RT-PCR for GAPDH and each CYP450 isoform was performed with primer pairs and annealing temperatures shown in Table 3-1. PCR products (10 µl each) were analyzed on agarose gels and were visualized by staining with ethidium bromide. Each lane represents mRNA extracted from an individual cow.

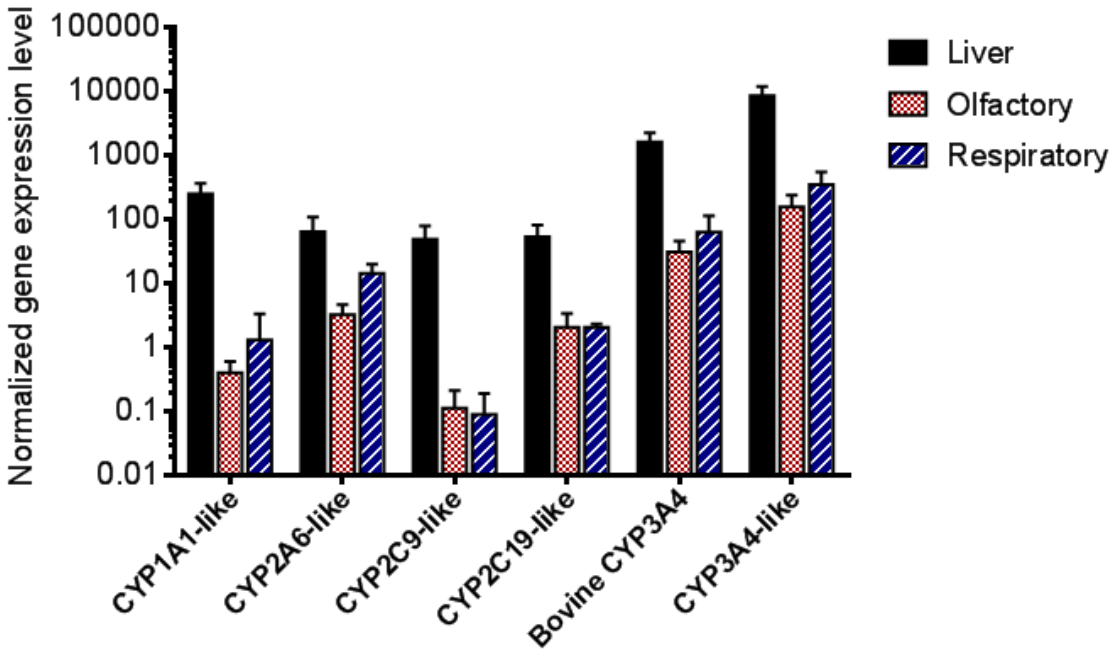

Figure 3-2 Gene expression levels of the selected CYP450 isoforms normalized with respect to GAPDH expression in bovine hepatic, olfactory, and respiratory tissues analyzed using real time RT-PCR. The graph has been plotted on logarithmic scale to enable simultaneous visualization of gene expression levels in the three tissues studied. The relative expression level (L) for each gene was calculated from the C_T values using equation $L = 2^{-C_T}$. The gene expression level for each CYP450 isoform was expressed as mean ± standard deviation of six animals. The gene expression levels of all the CYP450 isoforms studied were significantly higher samples (p-value < 0.05) in the hepatic tissues than the olfactory or respiratory mucosal samples. No statistically significant difference was observed between the gene expression levels in bovine olfactory and respiratory tissues for any of the isoforms studied.

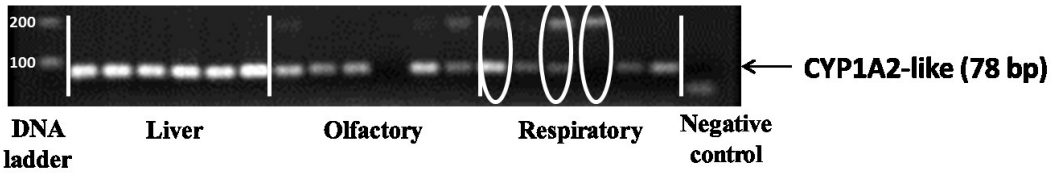

Figure 3-3 Gel electrophoretic analysis of RT-PCR products from amplification of CYP1A2-like gene in bovine hepatic, olfactory, and respiratory tissues. Amplification of CYP1A2-like gene from mRNA extracted from some of the bovine respiratory and olfactory mucosal tissues resulted in multiple PCR products. Each lane represents mRNA extracted from an individual cow. Lanes showing multiple bands following amplification are highlighted with oval circles.

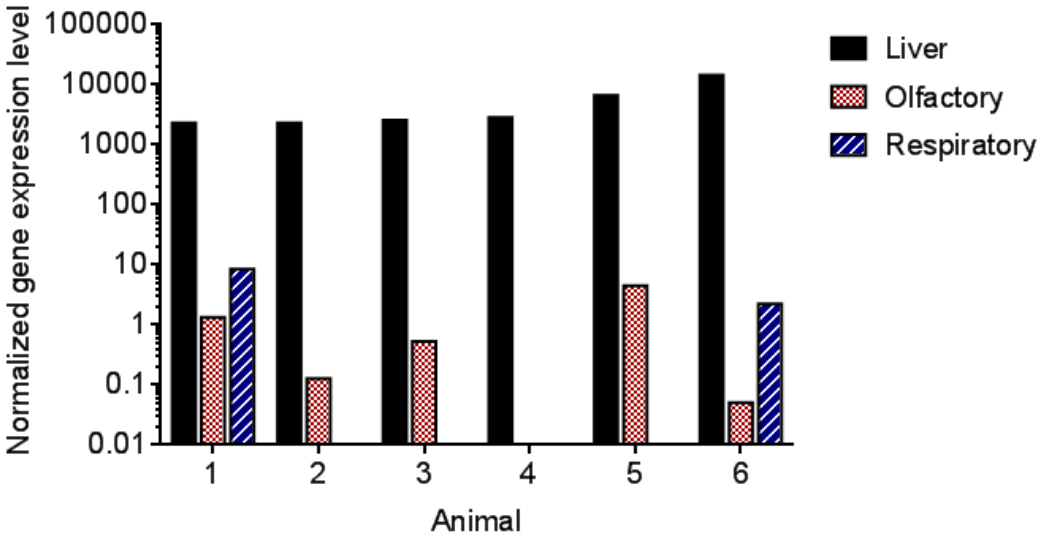

Figure 3-4 Gene expression levels of the CYP1A2-like gene normalized with respect to GAPDH expression in bovine hepatic, olfactory, and respiratory tissues analyzed using real time RT-PCR. The graph has been plotted on logarithmic scale to enable simultaneous visualization of mRNA expression levels of all the genes studied. Real time PCR monitoring of one of six olfactory tissues and four of six respiratory tissues resulted in an indeterminate C_T value for the desired transcript of CYP1A2.

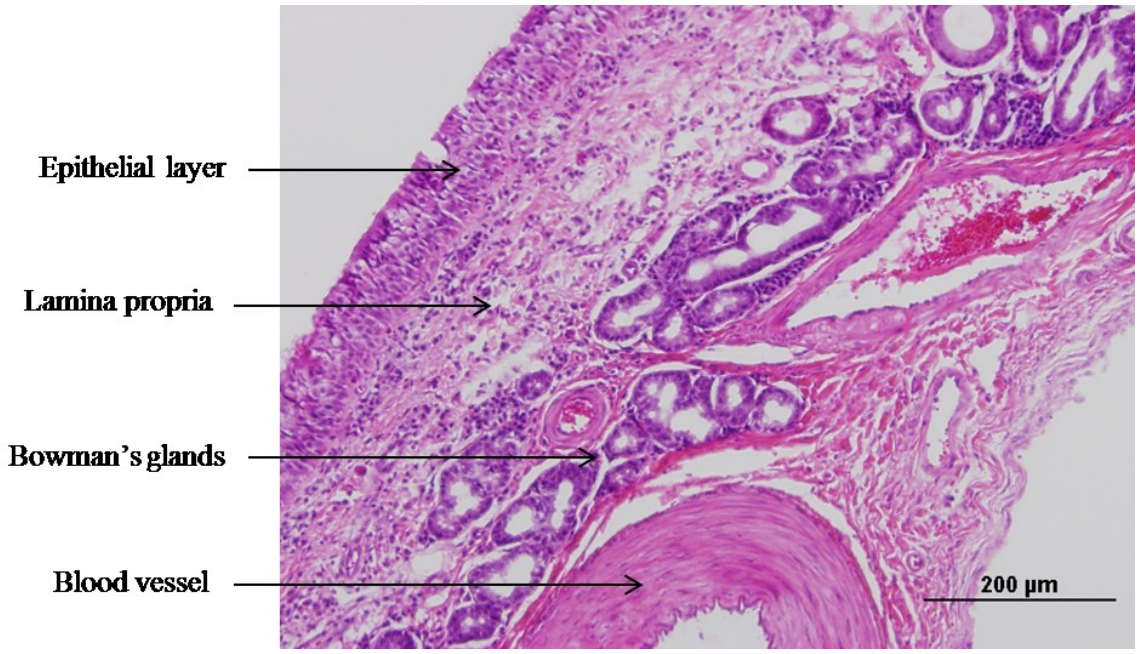

Figure 3-5 Brightfield image of a formalin-fixed, paraffin-embedded, and hematoxylin and eosin stained section of bovine olfactory mucosa. The bovine olfactory mucosa consists of a pseudostratified columnar epithelial layer and an underlying lamina propria. The submucosal region includes the cells of Bowman's glands and blood vessels surrounded by connective tissue. Section thickness: 5 µm.

Bowman's glands, blood vessels and lymphatic vessels surrounded by nerves and connective tissue.

The respiratory mucosa, shown in Figure 3-6, has a similar cellular organization. It is lined by the pseudostratified columnar epithelial layer interspersed with mucus producing goblet glands as seen in the micrograph. The lamina propria contains respiratory serous glands, blood vessels and connective tissue in the submucosal layer.

Immunofluorescence imaging of neuron-specific enolase (NSE) in bovine respiratory and olfactory explants along with the corresponding negative control sections are shown in Figure 3-7 and Figure 3-8 respectively. Bovine olfactory mucosa demonstrated a stonger immunofluorescence signal, and the immunoreactivity (indicated by green fluorescence) was intersperced throughout the epithelial layer, in parts of lamina propria and in the submucosal glandular region. The respiratory mucosal section did not exhibit significant immunoreactivity, however, some immunofluorescence signal was obtained in the epithelial layer (Figure 3-7). The distribution of the NSE protein in the bovine olfactory mucosa visualized using immunofluorescence studies correlated well with the reported NSE localization patterns in human fetus[185] and adult Wistar rats[186] where strong NSE immunoreactivity was detected in the olfactory mucosa.

Immunohistochemical analyses (Figures 3-9 to 3-16) showed that the isoforms belonging to CYP450 subfamilies 1A, 2A, 2C, and 3A were expressed in the bovine nasal mucosa. Positive immunoreactivity is indicated by green fluorescence. ToPro3 was used to stain the nuclei red, which helped distinguish the cytoplasmic green fluorescence signal obtained from the cellular immunostaining from that of the autofluorescent red blood cells. In the olfactory mucosal sections, CYP 3A4, 2C8/9/19, and 2A6 protein immunoreactivity was confined to the pseudostratified columnar epithelial layer and the acinar cells of Bowman's glands in the submucosal layer. In the immunopositive tissues, immunofluorescence was mainly confined to the cytoplasm. Submucosal endothelial cells did not exhibit significant immunoreactivity. Replacement of the primary antibody with

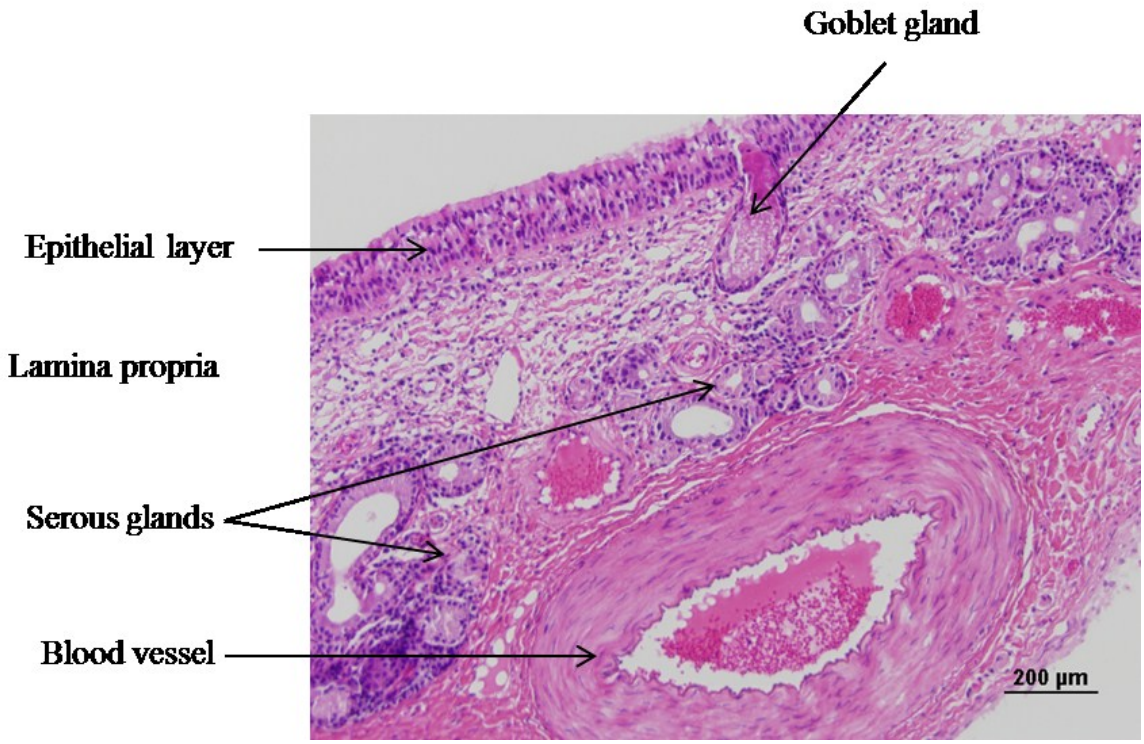

Figure 3-6 Brightfield image of a formalin-fixed, paraffin-embedded, and hematoxylin and eosin stained section of bovine respiratory mucosa. The bovine respiratory mucosa consists of a pseudostratified columnar epithelial layer containing mucus secreting goblet glands and an underlying lamina propria. The submucosal region includes serous glands and blood vessels surrounded by connective tissue. Section thickness: 5 µm.

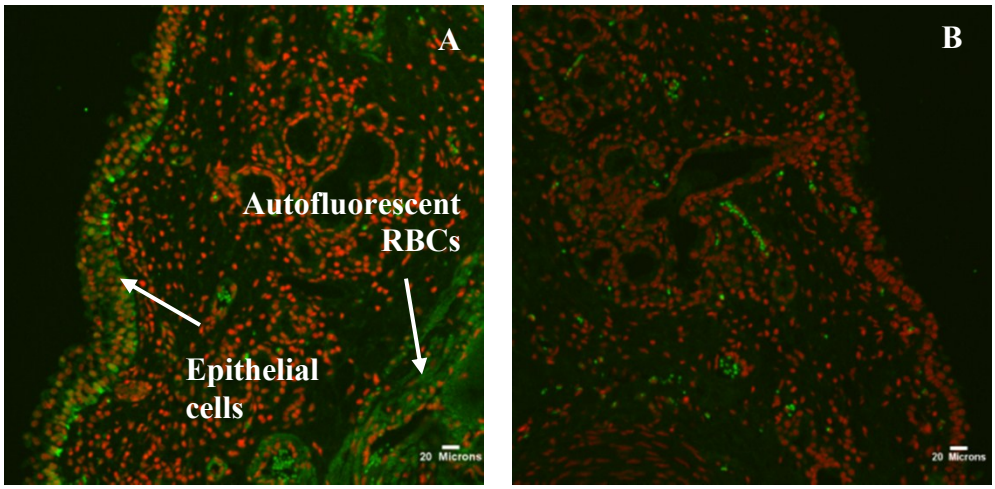

Figure 3-7 Immunohistochemical staining of neuron-specific enolase (NSE) in bovine respiratory mucosa. Weak immunofluorescence signal (indicated by green fluorescence) was obtained in the pseudostratified columnar epithelial layer. Within the immunopositive tissues, the cellular signal was entirely cytoplasmic, with no immunostaining of the nucleus (seen as To-Pro3 stained red dots). Scale bar: 20 µm. Section thickness: 5 µm.

A: Specimen incubated with the primary antibody: Rabbit polyclonal anti-human NSE

B: Negative control: Specimen incubated with rabbit IgG

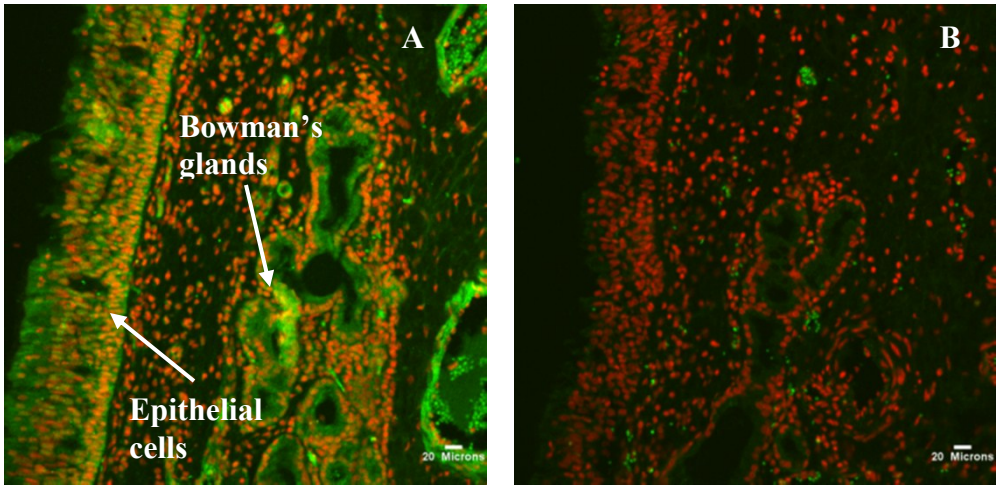

Figure 3-8 Immunohistochemical staining of neuron-specific enolase (NSE) in bovine olfactory mucosa. Enzyme immunoreactivity (indicated by green fluorescence) was detected in the pseudostratified columnar epithelial layer and the glandular cells in the submucosal layer. Within the immunopositive tissues, the cellular signal was entirely cytoplasmic, with no immunostaining of the nucleus (seen as To-Pro3 stained red dots). Scale bar: 20 µm. Section thickness: 5 µm.

A: Specimen incubated with the primary antibody: Rabbit polyclonal anti-human NSE

B: Negative control: Specimen incubated with rabbit IgG

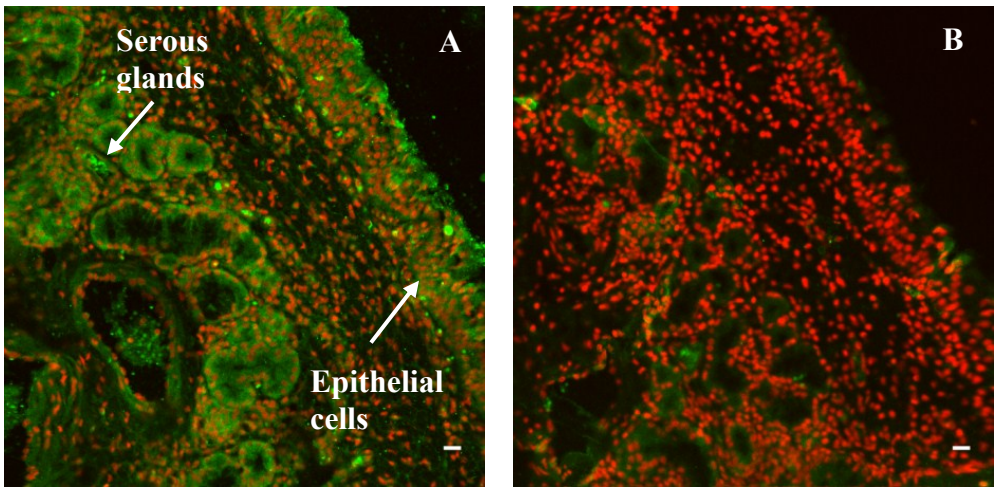

Figure 3-9 Immunohistochemical staining of CYP1A2 in bovine respiratory mucosa. Enzyme immunoreactivity (indicated by green fluorescence) was confined to the pseudostratified columnar epithelial layer and the glandular cells in the submucosal layer. Within the immunopositive tissues, the cellular signal was entirely cytoplasmic, with no immunostaining of the nucleus (seen as To-Pro3 stained red dots). Scale bar: 20 µm. Section thickness: 5 µm.

A: Specimen incubated with the primary antibody: Mouse monoclonal anti-human CYP1A2

B: Negative control: Specimen incubated with mouse IgG

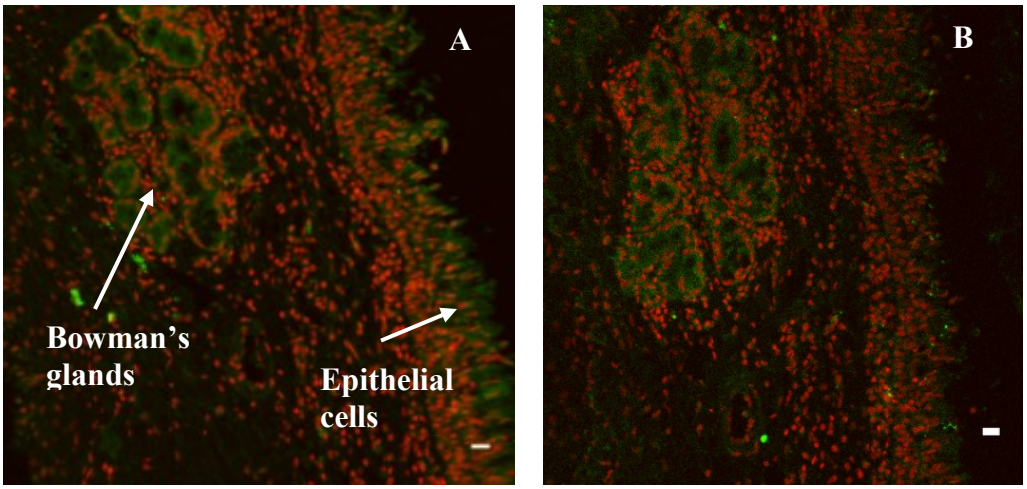

Figure 3-10 Immunohistochemical staining of CYP1A2 in bovine olfactory mucosa. Enzyme immunoreactivity (indicated by green fluorescence) was confined to the pseudostratified columnar epithelial layer and the glandular cells in the submucosal layer. Within the immunopositive tissues, the cellular signal was entirely cytoplasmic, with no immunostaining of the nucleus (seen as To-Pro3 stained red dots). Scale bar: 20 µm. Section thickness: 5 µm.

A: Specimen incubated with the primary antibody: Mouse monoclonal anti-human CYP1A2

B: Negative control: Specimen incubated with mouse IgG

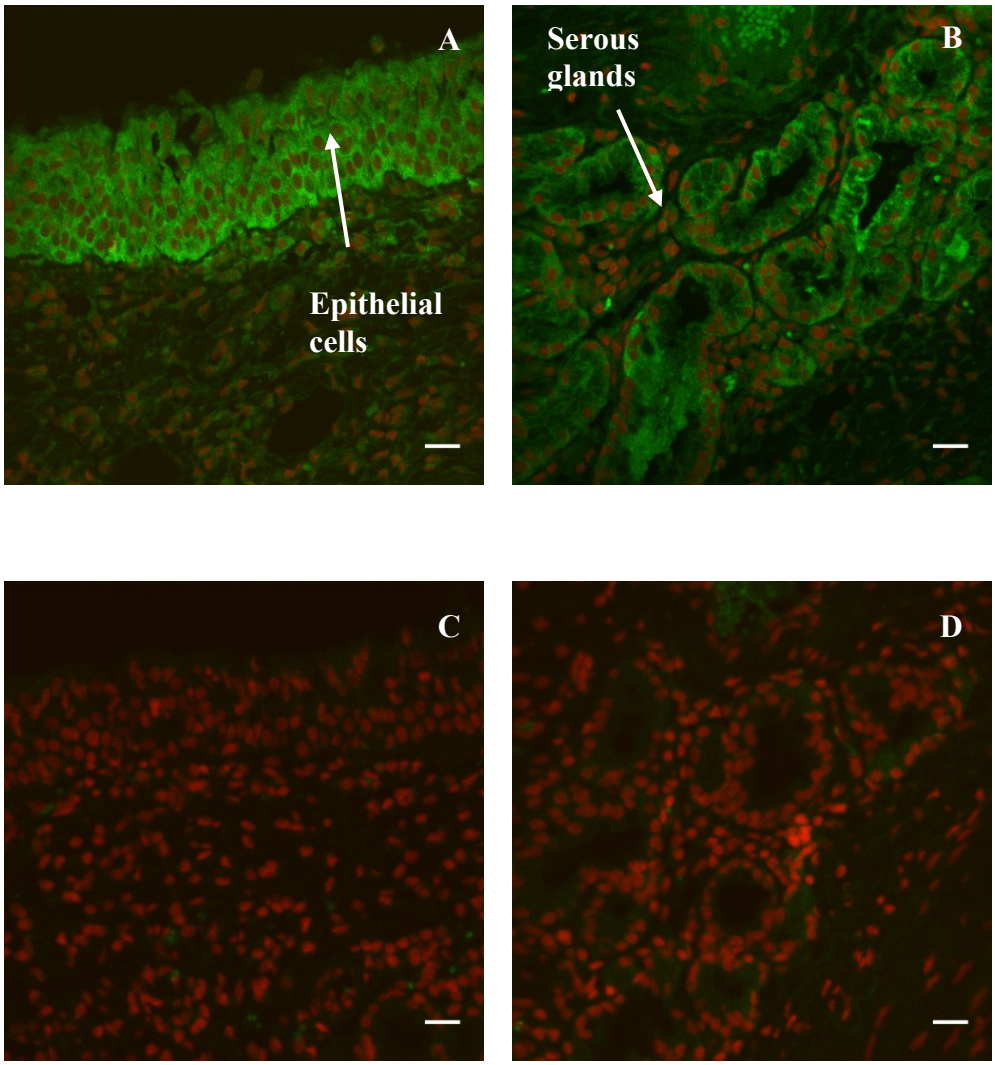

Figure 3-11 Immunohistochemical staining of CYP2A6 in bovine respiratory mucosa. Enzyme immunoreactivity (indicated by green fluorescence) was confined to the pseudostratified columnar epithelial layer and the glandular cells in the submucosal layer. Within the immunopositive tissues, the cellular signal was entirely cytoplasmic, with no immunostaining of the nucleus (seen as To-Pro3 stained red dots). Scale bar: 20 µm. Section thickness: 5 µm.

A,B: Specimen incubated with the primary antibody: Mouse monoclonal anti-human CYP2A6.

C,D: Negative control: Specimen incubated with mouse IgG

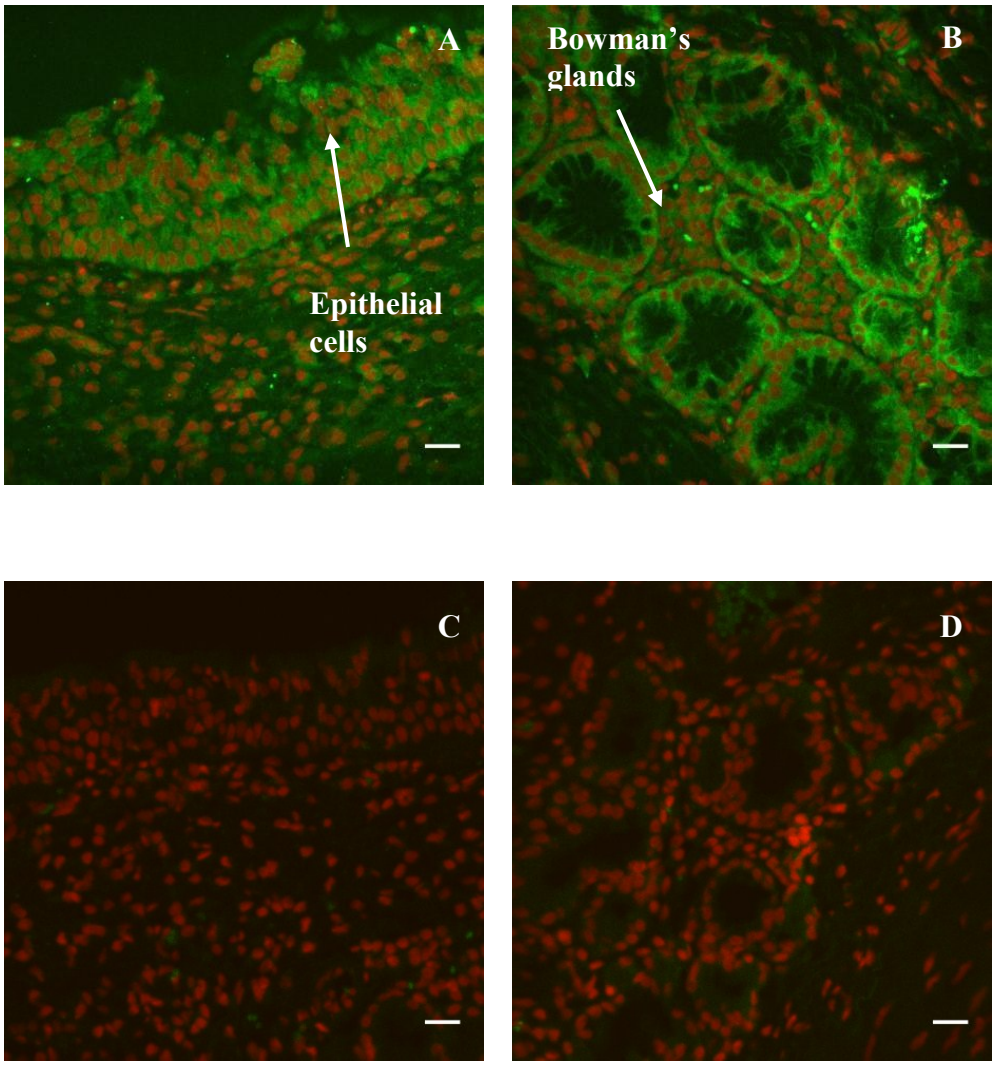

Figure 3-12 Immunohistochemical staining of CYP2A6 in bovine olfactory mucosa. Enzyme immunoreactivity (indicated by green fluorescence) was confined to the pseudostratified columnar epithelial layer and the glandular cells in the submucosal layer. Within the immunopositive tissues, the cellular signal was entirely cytoplasmic, with no immunostaining of the nucleus (seen as To-Pro3 stained red dots). Scale bar: 20 µm. Section thickness: 5 µm.

A,B: Specimen incubated with the primary antibody: Mouse monoclonal anti-human CYP2A6.

C,D: Negative control: Specimen incubated with mouse IgG

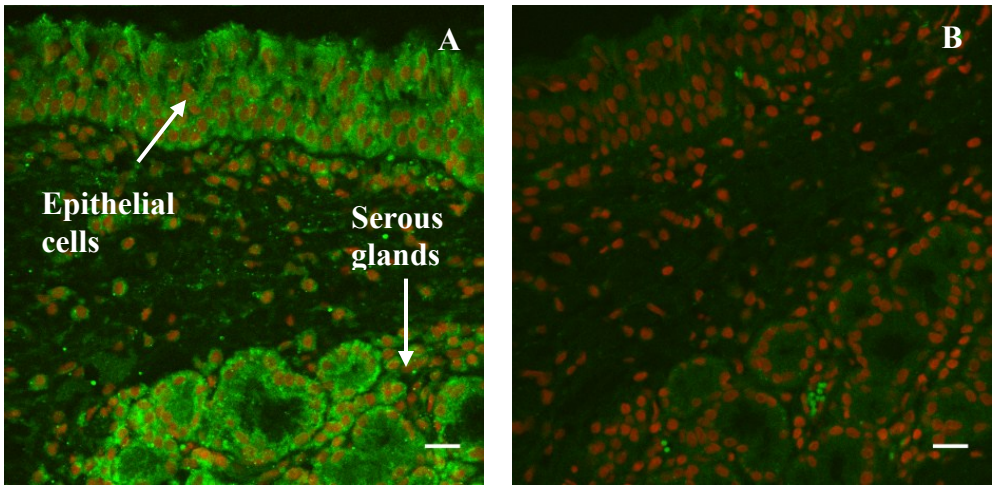

Figure 3-13 Immunohistochemical staining of CYP2C in bovine respiratory mucosa. Enzyme immunoreactivity (indicated by green fluorescence) was confined to the pseudostratified columnar epithelial layer and the glandular cells in the submucosal layer. Within the immunopositive tissues, the cellular signal was entirely cytoplasmic, with no immunostaining of the nucleus (seen as To-Pro3 stained red dots). Scale bar: 20 µm. Section thickness: 5 µm.

A: Specimen incubated with the primary antibody: Rabbit polyclonal anti-human antibody to CYP 2C8, 2C9, and 2C19.

B: Negative control: Specimen incubated with rabbit IgG

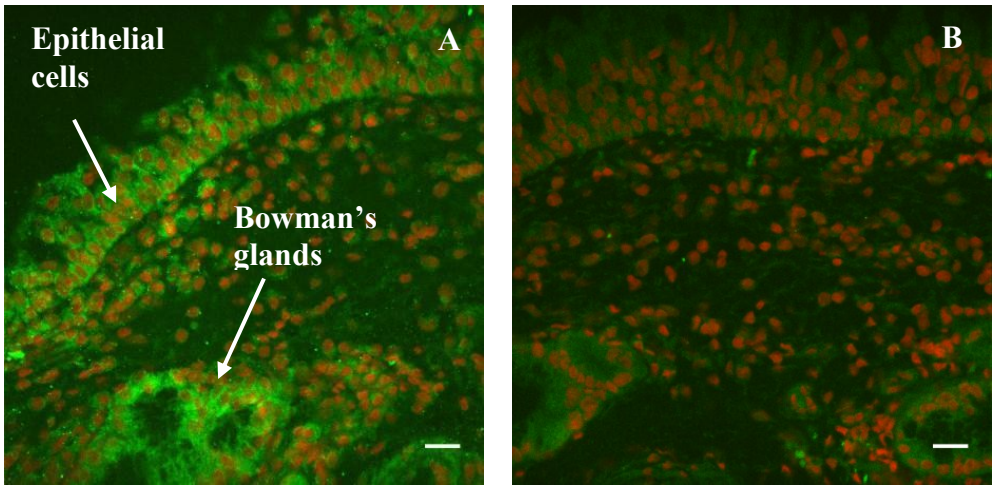

Figure 3-14 Immunohistochemical staining of CYP2C in bovine olfactory mucosa. Enzyme immunoreactivity (indicated by green fluorescence) was confined to the pseudostratified columnar epithelial layer and the glandular cells in the submucosal layer. Within the immunopositive tissues, the cellular signal was entirely cytoplasmic, with no immunostaining of the nucleus (seen as To-Pro3 stained red dots). Scale bar: 20 µm. Section thickness: 5 µm.

A: Specimen incubated with the primary antibody: Rabbit polyclonal anti-human antibody to CYP 2C8, 2C9, and 2C19.

B: Negative control: Specimen incubated with rabbit IgG

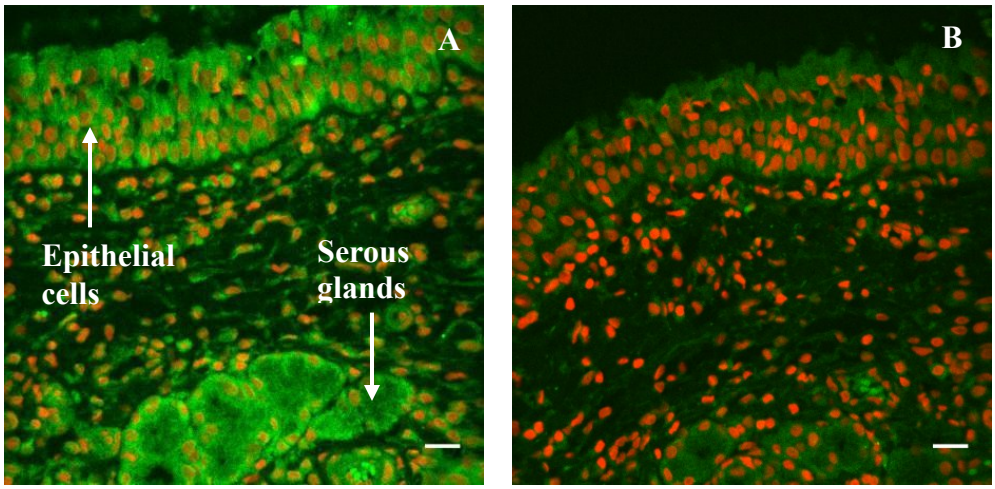

Figure 3-15 Immunohistochemical staining of CYP3A4 in bovine respiratory mucosa. Enzyme immunoreactivity (indicated by green fluorescence) was confined to the pseudostratified columnar epithelial layer and the glandular cells in the submucosal layer. Within the immunopositive tissues, the cellular signal was entirely cytoplasmic, with no immunostaining of the nucleus (seen as To-Pro3 stained red dots). Scale bar: 20 µm. Section thickness: 5 µm.

A: Specimen incubated with the primary antibody: Rabbit monoclonal anti-human CYP3A4.

B: Negative control: Specimen incubated with rabbit IgG

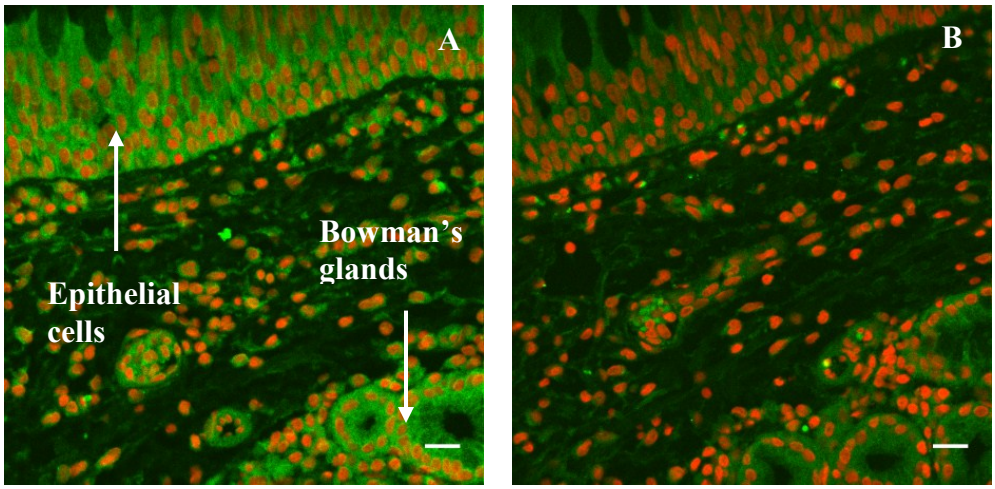

Figure 3-16 Immunohistochemical staining of CYP3A4 in bovine olfactory mucosa. Enzyme immunoreactivity (indicated by green fluorescence) was confined to the pseudostratified columnar epithelial layer and the glandular cells in the submucosal layer. Within the immunopositive tissues, the cellular signal was entirely cytoplasmic, with no immunostaining of the nucleus (seen as To-Pro3 stained red dots). Scale bar: 20 µm. Section thickness: 5 µm.

A: Specimen incubated with the primary antibody: Rabbit monoclonal anti-human CYP3A4.

B: Negative control: Specimen incubated with rabbit IgG

species-matched immunoglobulins (negative control) in the staining protocol resulted in no staining in the tissue sections, including the endothelial cells which are a common site for nonspecific IgG staining.

The enzyme localization pattern obtained for the respiratory mucosa was similar to that obtained with the olfactory mucosa. Strong immunoreactivity was observed in the pseudostratified columnar epithelium and the serous glands in the respiratory mucosa for all the four CYP450 isoforms studies, including 3A4, 2C8/9/19, 2A6, and 1A2.

The CYP1A2 fluorescent signal obtained in the respiratory sections was markedly stronger than that obtained for the olfactory sections (Figure 3-9). The signal obtained in the olfactory sections treated for CYP1A2 immunoflurescence was not visibly different from the signal obtained in the negative control. For comparison of signal intensity of each CYP450 isoform between the olfactory and respiratory mucosae, the nasal explants were matched for animal origin, antibody concentration as well as the staining protocols and the incubations were performed at the same time.

Results from the microarray analysis comparing the relative gene expression levels of various CYP450 isoforms in the nasal mucosa of humans, mice, rats, and cows are summarized in Table 3-2. A distinction between the olfactory and respiratory mucosal CYP450 expression in non-bovine species could not be made due to a lack of adequate information available in the literature about the RNA extraction protocols used to prepare RNA samples from human, rat, and mouse nasal mucosa. Bovine nasal mucosal RNA was extracted individually from the olfactory or the respiratory mucosa and were analyzed on separate microarrays. The expression levels of the selected CYP450 genes were not significantly different between the two nasal mucosal regions (Table 3-2). Rats and mice showed an abundant expression of CYP450 isoforms belonging to the subfamilies 1A, 2A, 2B, 4A, and 4B. Isoforms belong to the 2C subfamily were weakly expressed in mice, whereas in rats, CYP2C18 was highly expressed whereas the other 2C isoforms were not detected. CYP3A4, the major CYP450 drug metabolizing isoform, was

Table 3-2 DNA microarray analysis for CYP450 gene expression levels in the nasal mucosa of humans, mice, rats, and cows.
The olfactory and respiratory mucosal expression levels of CYP450 genes in bovine nasal mucosa were indistinguishable, and hence are grouped in one column. Genes expressed above the 50th percentile were accepted as expressed (Expr), while expression values between the 15th and 50th percentile were termed as weakly expressed (Weak). Absence of genes was indicated by no observable expression (None). "-" represents lack of availability of specific probes on the bovine DNA microarray or data not available for humans, mice, or rats.

Gene	Human	Mouse	Rat	Cow
CYP1A1	Weak	Expr	Expr	Weak
CYP1A2	Expr	Expr	Expr	None
CYP1B1	Expr	Expr	-	-
CYP2A6	Expr	Expr	Weak	-
CYP2A13	Expr	Expr	Expr	-
CYP2B1	Expr	-	-	-
CYP2B6	Expr	Expr	Expr	Expr
CYP2C8	Expr	Weak	None	Weak
CYP2C9	Expr	Weak	None	Weak
CYP2C18	Expr	Weak	Expr	Weak
CYP2C19	Weak	Weak	None	Weak
CYP2D6	Expr	Weak	Expr	Expr
CYP2E1	Expr	Expr	Expr	None
CYP3A4	Weak	Weak	Weak	Expr
CYP3A5	Expr	Weak	Weak	Expr
CYP3A7	Weak	Weak	Weak	Expr
CYP3A43	Weak	Weak	Weak	Expr
CYP4A11	Weak	Expr	Expr	Weak
CYP4B1	Expr	Expr	Expr	Expr
CYP4F2	None	-	-	None
CYP4F3	Expr	-	-	None
CYP4F8	None	-	-	None
CYP4F12	Expr	-	-	-
CYP7A1	Weak	Expr	None	-
CYP7B1	Expr	Expr	Expr	-
CYP8B1	Weak	None	None	-
CYP11A1	None	None	None	Weak
CYP11B1	Weak	Weak	None	None
CYP11B2	None	Weak	None	None

only weakly expressed in the human, rat, and mouse nasal mucosa. The microarray analysis of mRNA samples extracted from bovine nasal mucosa showed strong expression of CYP450 isoforms 2B6, 2D6, 3A4, 3A5, 3A7, 3A43, and 4B1. High expression levels of the CYP3A isoforms obtained from the microarray analysis correlated well with our real time RT-PCR results performed on mRNA extracted from the bovine nasal mucosa. Weak expression of the various CYP2C isoforms detected in the bovine nasal mucosa by the microarray analysis was also in good agreement with our real time RT-PCR results.

Discussion

It is now well accepted that the nasal mucosa contains significant levels of microsomal CYP450 enzymes[15,21,37,42,58,59,61]. Tissue-specific expression of several CYP450 isoforms has been extensively investigated in the nasal mucosa of a number of species[21,42,57,58,64]. In the current study, using a combination of RT-PCR and enzyme immunohistochemistry, we have investigated expression and localization of major CYP450 biotransformative isoforms in bovine nasal olfactory and respiratory mucosae. The large size and ready availability of the nasal cavity can enable quick, inexpensive and convenient use of bovine nasal mucosal explants to elucidate mechanistic information regarding transport, metabolism and absorption of drugs across the nasal mucosa.

Using the real-time RT-PCR technique, mRNA transcripts of major CYP450 isoforms were quantified in bovine olfactory and respiratory mucosae and liver tissues, relative to the expression of GAPDH in the same tissue samples. No statistically significant difference was observed between the gene expression levels obtained in the olfactory and the respiratory mucosa for any of the genes studied. This observation differed strikingly from the previous reports that have claimed that the olfactory mucosa in most species is metabolically more active than the respiratory mucosa[21,42,58]. In rodents

and laboratory animals, the miniscule size of the nasal cavity and the larger surface area coverage of the olfactory mucosa make it virtually impossible to effectively distinguish between the olfactory and respiratory mucosa. In these species, the nasal mucosa has often been interchangeably denoted as the olfactory mucosa[187,188]. However, in cattle, the size of the nasal cavity is large and the organization of the nasal mucosa resembles that in humans, facilitating distinct extraction of separate samples of the olfactory and respiratory mucosa. In a study conducted by Longo et al., the levels of CYP450 protein and cytochrome b5 were higher in bovine olfactory microsomes (four- and seven- fold respectively) than those reported in the respiratory microsomes[189]. Nevertheless, they studied the total CYP450 enzyme amount and activity in homogenized microsomal sub-cellular fractions. In contrast, we investigated the expression of individual genes constituting different isoforms of CYP450 enzymes and compared the olfactory and respiratory expression levels with those obtained in the liver. The seemingly comparable expression of the CYP450 enzymes in bovine olfactory and respiratory nasal mucosa might also be attributed to the large inter-animal variability associated with the expression levels obtained for each isoform in the six animals studied.

Gene expression levels examined by RT-PCR illustrated that CYP2A6-like, CYP3A4-like and CYP3A4 were the dominant CYP450 isoforms in the bovine olfactory and respiratory mucosal tissues. The prominent expression of CYP2A6 in bovine nasal mucosa was expected, as the isoforms of the CYP2A subfamily have been shown to be mainly extra-hepatic, and their nasal mucosal expression and activity has been extensively studied in humans and laboratory animals[73,74,190]. For example, Peng et al. purified the principal CYP450 protein form isolated from rabbit nasal microsomes (NMa)[162] and showed that it consisted of two very similar proteins, CYP2A10 and CYP2A11[191]. Su et al. performed RT-PCR analysis studying the expression of CYP450 isoforms homologous to rabbit CYP2A10/11 in rat, mouse, and human nasal mucosa[73]. They demonstrated that the CYP2A subfamily was present in human nasal mucosa,

however, the mRNA expression levels were much lower than the amount of CYP2A genes expressed in rodent nasal mucosa, when normalized with respect to liver CYP2A content. Expression of CYP2A6 and CYP2A13 mRNA in human adult and fetal nasal mucosa has also been thoroughly investigated by many laboratories[73,74,79,190,192]. Our RT-PCR results indicate that the expression levels of CYP2A6 in bovine olfactory and respiratory mucosa, compared to the liver, were approximately 8 ± 5% and 26 ± 23% respectively. In contrast, however, in humans, the CYP2A6 expression in the nasal mucosa has been reported to be approximately 1-2% that of the liver[192]. In our studies, the olfactory and respiratory mucosal explants were separately isolated and frozen immediately in liquid nitrogen. The literature reported human nasal tissues used for mRNA extraction seemingly contained both olfactory and respiratory epithelium pooled together. In addition, the prolonged post-mortem time for collection of the autopsy samples from human subjects might have caused significant degradation of RNA. These factors could possibly be responsible for the apparent low levels of CYP2A6 reported in human nasal tissues. CYP2A6 polymorphism has been described by many authors[50,193–195] and this might explain the inter-animal variability associated with CYP2A6 gene expression levels. The presence of CYP2A isoforms in the bovine nasal mucosa can potentially have significant toxicological consequences, as the enzymes from this subfamily are involved in the metabolism of many airborne chemicals and carcinogens[196,197] including nicotine[198], coumarin[199], aflatoxin B1[200], 4-(methylnitrosamino)-l-(3-pyridyl)-l-butanone[192,201], and 2,6-dichlorobenzonitrile[202,203].

The isoforms of the CYP3A subfamily play key roles in catalyzing hepatic first pass metabolism of orally administered therapeutic agents. However, information available about the presence and activity of CYP3A enzymes in the nasal mucosa is scarce. CYP3A proteins have been identified in the respiratory and olfactory mucosa of rats, rabbits and humans by immunohistochemistry[42,59,75], but quantitative analysis of nasal mucosal CYP3A expression has not been previously reported in the literature. We

performed real time RT-PCR with bovine primer pairs targeted towards two CYP3A isoforms, CYP3A4 (NCBI accession # NM_001099367) and CYP3A4-like (CYP3A5, CYP3A28, NCBI accession # NM_174531). Both CYP3A4 and CYP3A4-like mRNAs were expressed in the bovine olfactory and respiratory mucosae of the 6 animals studied. The expression levels were approximately 1-12% of the corresponding gene expression levels in the liver. This is the first evidence of the presence of CYP3A4-like mRNA expression in cattle extrahepatic tissues. Insignificant CYP3A4-like expression was reported by Darwish et al. in mRNA samples extracted from bovine mammary glands, lungs, kidneys or tongue[164]. Analysis of CYP450 enzymes in coronary arteries of cattle depicted the presence of CYP1A, 2C, 2E, and 2J subfamilies, but they were devoid of any CYP3A gene expression or catalytic activity[104]. The expression of CYP3A4 mRNA in bovine olfactory and respiratory tissues and immunoreactivity of CYP3A4 proteins obtained in our studies suggest that the bovine nasal mucosa might possess the highest CYP3A4-like catalytic activity among all the extra-hepatic organs in cattle.

CYP1A1-like mRNA was expressed in both the bovine olfactory and respiratory mucosa, but exhibited low expression levels (< 1%) compared to those obtained in bovine hepatic tissue. CYP1A1 is mainly an extra-hepatic enzyme, as its hepatic expression is reported to be very low in rats and humans[58,60,188,204]. However, our results demonstrating the expression of CYP1A1 in bovine liver mRNA are in agreement with previous reports where CYP1A1 has been shown to be highly expressed in bovine liver[105,205]. CYP1A is the most inducible CYP subfamily, and it is induced by many chemicals present in dietary plant components in addition to environmental pollutants like polycyclic aromatic hydrocarbons or by phytochemicals[58,102]. Dietary or environmental CYP1A1 inducers might have played a major role in influencing the apparent expression of CYP1A1 mRNA in the bovine liver. The expression levels of CYP1A1-like mRNA in the bovine nasal mucosa obtained from our studies were comparable to the results of Messina et al.

in pigs where marginal expression of the isoform in olfactory and respiratory mucosa was detected[206].

For the case of CYP1A2-like mRNA amplification by RT-PCR, the liver and the nasal tissues presented notable differences concerning mRNA expression patterns in the six animals studied. The mRNA extracted from the livers of all the six animals exhibited nearly identical expression of the CYP1A2-like isoform. However, amplification of the CYP1A2-like transcript from mRNA extracted from some of the bovine olfactory and respiratory mucosal tissues yielded multiple products. Real time PCR monitoring of one of six olfactory tissues and four of six respiratory tissues resulted in indeterminate C_T values for the desired transcript of CYP1A2 (Figure 3-4). Nucleotide sequences of the unknown CYP1A2 PCR products were partially concordant with bovine CYP1A2 genome and also coincided with nucleotide segments on human CYP1A2 mRNAs [accession # NG_008431: *Homo sapiens* CYP1A1_CYP1A2 locus, having a bidirectional 5' flank promoter of exactly 23,306 bp; accession # AF253322 and DQ022432, *Homo sapiens* CYP1A1 and CYP1A2 genes]. We had ensured selective amplification of the chosen mRNA transcripts for each gene with minimal inter-species cross reactivity by designing *Bos taurus* CYP450 mRNA-specific primer pairs followed by BLAST analysis. The sequencing results suggested the possibility of the expression of a spliced variant of CYP1A2, principally expressed in bovine respiratory mucosa, or the existence of polymorphic forms of the enzyme. The variability in bovine CYP1A2 nasal expression is not entirely surprising, as pronounced inter-individual differences (40-130 fold) have been reported in CYP1A2 activity in humans[204,207]. Examinations of the hepatic mRNA and protein expression levels of CYP1A2 in humans have shown 15- to 40-fold differences[208], and a significant amount of work has been directed towards studying the genetic, epigenetic and environmental factors affecting CYP1A2 expression and catalytic activity in humans and rodents[207–212]. The effect of the CYP1A2 gene variant on regulation of bovine olfactory and respiratory mucosal expression and metabolic activity

of CYP1A2 proteins needs to be determined to establish the significance of CYP1A2 genomic alterations on nasal clearance of CYP1A2-substrates.

The CYP2C subfamily consists of 2C8, 2C9, 2C18, and 2C19 isoforms in humans. The enzymes of this subfamily constitute approximately 20% of total human hepatic CYP450 contents[213], and the expression of CYP2C mRNAs and proteins has been reported in the small intestine and other extrahepatic tissues in humans[214]. Our RT-PCR results showed that the expression of CYP2C9-like gene was mainly confined to bovine hepatic tissues. These findings correlated with previous reports where CYP2C9 was found to be expressed primarily in the liver and kidney of cattle[104,164], with little or no expression in other extra-hepatic tissues including the lungs, spleen, mammary glands, spleen or tongue. CYP2C9-like catalytic activities were also shown to be exhibited only by bovine hepatic microsomes[215]. The expression levels of CYP2C19-like mRNA obtained in both bovine olfactory and respiratory tissues were significantly higher than those obtained for CYP2C9-like mRNA in respective tissues. The expression levels of CYP2C19 in the nasal mucosa (~1- 2%) compared to the liver indicated that CYP2C19 is one of the predominant CYP2C isoforms present in bovine nasal mucosa.

Species specific monoclonal primary antibodies targeted against specific epitopes of bovine CYP450 proteins, required for the immunohistochemical analyses to study the location of major CYP450 isoforms in the bovine nasal mucosa, were not commercially available. Due to the possibility of undesirable cross-reactivity amongst different bovine CYP450 epitopes with the available primary antibodies, only one isoform was selected from each of CYP subfamilies 1A, 2A, 2C, and 3A for investigations of representative protein localization of CYP450 subfamilies in bovine nasal mucosa. The primary antibodies used in the these studies were raised against the human CYP450 antigens and were reported to be cross-reactive with other species. They were immunoreactive to bovine epitopes, as indicated by the green immunofluorescent signal arising from tissue sections incubated with the respective primary antibodies. Such immuno cross-reactivity

does not ensure structural identity between human and bovine proteins, however. The specificity and selectivity of the chosen primary antibodies against individual bovine CYP450 isoforms cannot be confirmed until the bovine proteins have been purified and monoclonal antibodies selectively specific to bovine CYP450 isoforms have been synthesized. Monoclonal antibodies against CYP2C subfamily isoforms were not available, so a polyclonal primary antibody raised against human CYP2C 8/9/19 and rat CYP2C12 was selected.

The enzyme distribution patterns indicated that the major cytochrome P450 isoforms were distributed both in the epithelial layer and in the glandular regions of the bovine nasal mucosa. The cellular localization was identical for all the four isoforms studied for both the olfactory and the respiratory mucosae. These enzyme distribution patterns are consistent with the reported cellular localization of CYP450 isozyme NMa in human nasal mucosa[216] as well as the distribution of CYP2A related proteins in fetal and adult human nasal mucosa[74] and staining patterns obtained for CYP2S1 in human nasal mucosa by in situ hybridization and immunohistochemistry[78]. Yokose et al. carried out immunohistochemical studies of CYP2C and 3A subfamilies on human extrahepatic tissues[75]. Diffuse cellular immunoreactivity for both the subfamilies was observed in the serous cells of nasal glands in non-neoplastic human nasal mucosa; however, they reported a lack of CYP2C and 3A staining in the normal squamous epithelium of the nasal mucosa. Similar observations were also reported by Voigt et al. who observed CYP1A1 immunoreactivity localized in the cells of Bowman's glands in rat olfactory mucosa with minimal staining of the epithelium[188]. Piras et al. investigated olfactory mucosal CYP2A5 expression in mice by in situ hybridization and immunohistochemistry[217]. They observed that the CYP2A5 mRNA and the corresponding protein were co-localized mainly in the sustentacular cells, Bowman's gland, and duct cells in the olfactory region, with extremely minimal expression in the respiratory epithelium. Our findings are also consistent with the observed α-NMa and

α-NMb localization in epithelia, sustentacular cells and Bowman's glands in rat olfactory mucosa[218] as well as CYP2A6/2B6 and CYP3A4 immunohistochemical localization observed in the epithelia and glandular cells of the horse nasal mucosa[68]. In our studies, the signal intensities of CYP2A, 2C, and 3A subfamilies obtained in both bovine olfactory and respiratory epithelium were observed to be comparable upon visual examination. In the case of CYP1A2, the fluorescent signal obtained with the respiratory explants was more intense than that obtained with the olfactory explants. Yet, the signal intensities observed in immunohistochemistry are highly variable and depend greatly on the preparation and staining conditions. Therefore, limited comparisons are able to be made between sections treated with different antibodies.

Results from the microarray analysis showed that the CYP450 subfamilies 1A, 1B, 2A, 2B, 2C, 2D, 2E, 3A, 4B, 4F, and 7B were the predominantly expressed subfamilies in the human nasal mucosa. The human nasal mucosa was observed to express a greater number of CYP450 isoforms than the nasal mucosa of other animals studied. This can partially be attributed to a greater advancement in the development of human genome and human DNA microarray probes as compared to the other species. The microarray results for the expression of various CYP450 isoforms in the human nasal mucosa were consistent with the reported human nasal CYP450 gene expression levels quantified by RT-PCR for CYP450 isoforms 2A6, 2A13, 2B6, 1B1, 2E1, and 4B1[76,79] (Table 3-3). The most prominent CYP450 isoforms observed to be expressed in the nasal mucosa of all the four species studied were CYP1A1, 2B6, 2C18, 2D6, 3A4, 3A5, 3A7, 3A43, 4A11, and 4B1. Interestingly, expression of CYP1A2 was not detected during microarray analysis of RNA extracted from the bovine nasal mucosa, however, the human, mouse, and rat nasal musosae showed an abundant expression of CYP1A2. This observation further strengthened the possibility of the presence of a spliced CYP1A2 variant in the bovine nasal mucosa, as suggested by our real time RT-PCR results. Additionally, the major isoforms belonging to the CYP2A subfamily (2A6 and 2A13) were extensively expressed

Table 3-3 Summary of observations for the CYP450 enzyme expression and localization analysis performed using real time RT-PCR, cDNA microarray, and enzyme immunohistochemistry on bovine nasal mucosa. No significant difference was detected in the olfactory and respiratory mucosal gene expression levels for any of the isoforms studied using real time RT-PCR or cDNA microarray.

CYP450 isoform	Real time RT-PCR	cDNA microarray	Enzyme immunohistochemistry
CYP1A1-like (Bovine CYP1A1)	Weak expression (Nasal levels < 1% hepatic levels)	Weak expression	Not performed
CYP1A2-like (Bovine CYP1A2)	Multiple products following PCR amplification. Possibility of a spliced variant.	Gene not detected	Immunofluorescent epithelial layer and submucosal glands in the respiratory explants. Weak signal in the olfactory explants.
CYP2A6-like (Bovine CYP2A6)	Variable expression levels (Nasal levels: 2-50% hepatic levels)	Not performed	Immunofluorescence detected in the epithelial layer and submucosal glands in both the olfactory and respiratory explants.
CYP2C9-like (Bovine CYP2C87)	Weak expression (Nasal levels < 2% hepatic levels)	Weak expression	Immunofluorescence detected in the epithelial layer and submucosal glands in both the olfactory and respiratory explants.
CYP2C19-like (Bovine CYP2C21)	Weak expression (Nasal levels < 4% hepatic levels)	Weak expression	
CYP3A4-like (Bovine CYP3A28)	Expressed (Nasal levels: 1-12% hepatic levels)	Abundant expression	Immunofluorescence detected in the epithelial layer and submucosal glands in both the olfactory and respiratory explants.
CYP3A4 (Bovine CYP3A4)	Expressed (Nasal levels: 1-10% hepatic levels)	Abundant expression	

in the human, rat, and mouse nasal mucosa, however, they were not detected in the bovine nasal mucosa. Our real time RT-PCR and immunohistochemistry results demonstrated the presence of CYP2A6 coding nucleic acids and proteins in the bovine olfactory and respiratory nasal mucosa. This discrepancy in the expression profiles of bovine nasal CYP2A isoforms detected by microarray and quantitative PCR techniques might arise from the higher threshold limit set during the microarray technique for confirming the gene expression[219]. It has also been reported that that existing microarray screening algorithms may fail to detect many significant differences in the gene expression levels (type II analytic errors) leading to false negative results[220].

In conclusion, our findings show that the nasal olfactory and respiratory mucosae of cattle express many isoforms belonging to the CYP450 superfamily. A summary of our results for the CYP450 gene expression and protein localization analysis is given in Table 3-3. The gene expression levels of the CYP450 enzymes in bovine nasal olfactory and respiratory mucosal tissues were comparable, but were associated with high inter-animal variability. This suggests potentially greater inter-animal and inter-species differences in the extent of drug metabolism in the nasal cavity.

The CYP450 proteins are located both in the epithelial layer as well as in the submucosal glandular regions in bovine nasal explants. This indicates that the submucosal layer plays an important role in the metabolic degradation of intranasally administered compounds, and specific consideration must be given to ensure the permeability and effectiveness of CYP450 inhibitors included in intranasal formulations in both the epithelial as well as the submucosal region. Availability of a bovine genome array can allow for rapid initial screening of gene expression of phase I and phase II enzymes in the bovine nasal mucosa, and further explorations of metabolic barrier properties of bovine nasal mucosa can enable inexpensive and efficient *in vitro* mechanistic investigations of pathways governing the transport and metabolism of drugs across the nasal mucosa.

CHAPTER 4
CHARACTERIZATION OF SUBSTRATE METABOLIZING ACTIVITY OF BOVINE NASAL MICROSOMES

Introduction

As an alternative to oral administration, which is associated with low and variable melatonin bioavailability, intranasal administration of melatonin is being actively investigated for its ability to induce and maintain sleep up to 6-8 hours[149,150,221]. CYP450-mediated enzymatic degradation, a major barrier to oral melatonin delivery[123,144], could potentially also play a critical role in determining the nasal bioavailability of melatonin. The nasal bioavailability of melatonin solution in rabbits is reported to be 55% ± 17%[149]. A possible explanation for this reduced and variable bioavailability could be the metabolic loss of melatonin due to the enzymes present in the rabbit nasal mucosa, which has been shown to possess high expression and activity of various CYP450 isoforms[42,64,162,191]. Measurement of the extent of enzymatic biotransformation of a potential drug molecule intended for intranasal administration using *in vitro* nasal microsomal incubations represents an important experimental approach in nasal drug product development. In these investigations, bovine nasal microsomal metabolism assays were carried out to investigate the capacity of the bovine nasal olfactory and respiratory mucosae to metabolize melatonin.

Microsomes, literally meaning "small bodies" (Hanstein, 1880), are vesicles derived from the disruption of the endoplasmic reticulum[222]. Cytochrome P450 enzymes are membrane-bound proteins located on the endoplasmic reticulum, and these can be isolated in the resulting subcellular microsomal fraction by differential centrifugation[51,223,224]. Microsomes thus represent an enriched source of cytochrome P450 enzymes and are commonly employed as a primary tool for assessing substrate metabolizing capacity of various CYP450 isoforms isolated from a particular organ.

Microsomal fractions provide many advantages for metabolic stability assays including the ability to pool the enzymatic fractions from several animals before assessing the substrate metabolic activity, convenient storage, and stability at -80 ºC for several months. Since microsomes are a subcellular fraction, contributions of other factors in determining the extent of substrate metabolism including cellular uptake, efflux, or inherent drug permeability can be ruled out. However, with microsomes, it is difficult to obtain information regarding the distribution of the enzymes within tissues and cells. Microsomal fractions do not contain enzymes such as monoamine oxidase, sulfotransferase etc., which might play a significant role in *in vivo* drug metabolism. Nevertheless, microsomal assays represent a primary step in the evaluation of the extent of drug metabolism and subsequent drug interactions or toxicity arising due to CYP450-mediated enzymatic activity.

Commercially available hepatocytes and tissue fractions from various species are routinely used for high throughput metabolism and drug interaction screening. They include primary hepatocytes, liver microsomes, hepatic S9 and cytosol fractions, and extra-hepatic microsomes prepared from intestinal, renal and pulmonary tissues (BD Biosciences, San Jose, CA). Nasal microsomes or nasal subcellular fractions are not available commercially; the main reason for this lack of availability is that the role of nasal mucosa as a significant contributor to extra-hepatic metabolism has not received sufficient attention in the past to warrant developing such a product. Expensive and inadequate supplies of human nasal tissues, coupled with the small tissue size and relatively low protein content further complicates the process of manufacturing of human nasal olfactory and respiratory microsomes on a commercial scale. The large size and inexpensive and convenient availability of cattle nasal mucosa in the United States makes it an interesting alternative for assays involving nasal microsomal fractions. Biochemical analyses of the components of the CYP450 electron transport system in the nasal and hepatic microsomes of humans and cattle have been performed by Longo et al. and

Gervasi et al. (Table 4.1)[67,70]. Although the hepatic microsomal concentration of CYP450 was comparable between the two species, the concentrations of CYP450 and cytochrome b5 in bovine nasal respiratory microsomes were reported to be approximately twice that of human respiratory microsomes. Investigations of substrate degradation involving CYP450 monooxygenase activities in the bovine nasal mucosa were performed by Longo et al[189]. Their results indicated that the CYP450 enzymes in cattle olfactory and respiratory nasal mucosa play a major role in detoxication and elimination of odorants in the nasal cavity. In a separate study, the authors isolated three constitutive forms of CYP450 enzymes from the olfactory microsomes of cattle and evaluated their catalytic activity with respect to oxidation of various substrates[14]. They observed that the bovine nasal CYP450 isoforms were more active in the metabolism of xenobiotic compounds (7-ethoxycoumarin, aniline, and hexamethylphosphoramide) than towards endogenous substrates (testosterone and progesterone). In another study by Lazard et al., a protein immunochemically related to the CYP 2A subfamily was isolated from bovine olfactory mucosa[163]. The protein was assigned the name P-45001f2 and was observed to be specific to bovine olfactory epithelium with minimal immunoreactivity observed in bovine respiratory and hepatic microsomes. However, the sequence of these proteins purified from bovine nasal mucosa has not been well established. Literature reports characterizing the CYP450 dependent monooxygenases in bovine nasal microsomes are still scarce. Characterization of the activity of various CYP450 isoforms in bovine olfactory and respiratory microsomal fractions can broaden their application in drug development and toxicology. For the current investigations, we prepared bovine nasal olfactory and respiratory microsomes and examined their activity towards melatonin metabolism compared to bovine hepatic microsomes.

Table 4-1 Components of the human and bovine nasal mucosal and hepatic CYP450 monooxygenase electron transport system[70,189]

Parameter	Amount or specific activity				
	Human		Bovine		
	Nasal (Respiratory)	Liver	Olfactory	Respiratory	Liver
Cytochrome P450 (pmol/mg protein)	24.6	512	250 (± 60)	70 (± 20)	520 (± 130)
Cytochrome b5 (pmol/mg protein)	5.7	357	100 (± 30)	13 (± 2)	230 (± 30)
NADPH-cytochrome c reductase*	23.4	107	49 (± 3.8)	3.7 (± 0.3)	60 (± 3.9)
NADH-cytochrome c reductase*	72	1104	125 (± 6)	105 (± 14)	156 (± 28)
NADH-cytochrome b5 reductase**	2042	2188	7131 (± 852)	3435 (± 480)	5053 (± 1030)

* Units: nmole of cytochrome c reduced/min × mg protein.

** Units: nmole of ferricyanide reduced/min × mg protein.

Materials and Methods

Materials

NADPH Regenerating System Solutions A and B were obtained from BD Bioscience (BD Bioscience, San Jose, CA). Melatonin, 6-hydroxymelatonin, N-acetylserotonin, and TMB (3,3',5,5'-tetramethylbenzidine) were obtained from Sigma-Aldrich® (Sigma-Aldrich® Co., LLC, St. Louis, MO). Pierce® BCA protein assay kit was obtained from Thermo Fisher Scientific (Fisher Scientific Inc., Rockford, IL). Mouse monoclonal anti-human CYP1A2 antibody and horseradish peroxidase (HRP)-conjugated goat anti-mouse IgG were obtained from Abcam (Abcam Inc., Cambridge, MA). Bovine serum albumin standard and Dulbecco's phosphate buffered saline (PBS) were obtained from Molecular Probes® (Life Technologies™, Carlsbad, CA). Glutaraldehyde EM (electron microscopy) grade was obtained from Polysciences (Polysciences Inc., Warrington, PA). All other reagents were obtained from Sigma-Aldrich® (Sigma-Aldrich® Co., LLC, St. Louis, MO). Acrodisc® 13 mm syringe filters with 0.45 μm nylon membrane were obtained from Pall (Pall Gelman Laboratory, Port Washington, NY)

Extraction of bovine nasal olfactory and respiratory mucosa and hepatic tissues

The bovine nasal mucosa was obtained from Bud's Custom Meats Co. (Riverside, IA). A vertical incision from the nostril to the lower eyelids was made along the snout of the cows to expose the nasal cavity. Nasal turbinate mucosae were retrieved by opening the nasal cavity along the septal midline and removing the turbinates from the lateral wall. The olfactory mucosa is located at the roof of the nasal cavity covering two bulb-like projections. The respiratory mucosa, located within the main nasal cavity, was harvested by making vertical incisions along both walls of the nasal cavity and along the

septum with a butchering knife. The cartilage and overlying olfactory or respiratory mucosa were removed by blunt dissection. The olfactory and respiratory mucosal tissue was immediately separated from the underlying cartilage and frozen in liquid nitrogen for subsequent transportation to the lab. For preparing bovine hepatic microsomes, liver samples (approximately 50 g each from each animal) were collected, immediately frozen in liquid nitrogen and transported to the laboratory.

Preparation of microsomes by differential centrifugation

Frozen bovine olfactory or respiratory mucosal tissues or liver samples were individually washed with ice-cold homogenization buffer (0.05M Na_2HPO_4, 0.05M NaH_2PO_4, 1.15% KCl, 0.25M sucrose, pH 7.4) and minced into small pieces with scissors. These cut pieces were homogenized with homogenization buffer in a ceramic mortar and pestle. The volume of the homogenization buffer to the volume of tissue was kept approximately at 3:1. The homogenized tissue pieces were disrupted with a Tissue Tearor™ homogenizer (BioSpec Products Inc., Bartlesville, OK). The crude homogenate was then centrifuged at 15,000× g for 20 min at 4 °C using an Eppendorf 5804R centrifuge (Eppendorf, Hauppauge, NY). The pellet was discarded. The supernatant was centrifuged at 100,000× g for 1 hr at 4 °C using a Sorvall Discovery 90SE ultracentrifuge (Hitachi, Kendro Laboratory Products, Newtown, CT). The resulting supernatant was discarded. To further purify the microsomal fraction, the pellet was re-suspended in the homogenization buffer, and was subjected to ultra-centrifugation at 100,000× g for 1 hr at 4 °C. The resulting pellet represents the microsomal fraction of the tissue, which was re-suspended in microsomal storage buffer (0.05M Na_2HPO_4, 0.05M NaH_2PO_4, 20% glycerol, 0.1 mM EDTA, pH 7.4). The microsomes were kept frozen at -80 °C in cryovials (Sarsted AG & Co., Nümbrecht, Germany) until use. The microsomes prepared from 25 bovine olfactory or respiratory explants and from 6 liver slices were pooled together to obtain the final fractions of bovine olfactory, respiratory or hepatic

microsomes. They were diluted in the microsomal storage buffer to yield a final protein concentration in the range of 10-20 mg/ml. Aliquots (10 µL) were separately withdrawn from the three microsomal fractions and frozen in cryovials for storage at -80 °C. These aliquots were withdrawn to facilitate easy recovery of the microsomal fractions for microsomal incubations in order to avoid repeated freeze-thaw cycling of the entire microsomal pool which can reduce enzyme viability and activity.

Characterization of the microsomal fractions

TEM imaging of microsomes

Bovine respiratory and olfactory microsomal suspension was centrifuged at 20000×g for 30 minutes (Eppendorf 5804R centrifuge) to obtain the respective microsomal pellets. The supernatant was removed and the pellets were rinsed with PBS and fixed in 2.5% glutaraldehyde in 0.1 M sodium cacodylate buffer (pH 7.2) for 1 hour at room temperature. After removing the fixative, the pellets were rinsed with cacodylate buffer and were post-fixed for 1 hour in 1% osmium tetroxide containing 1.5% potassium ferrocyanide in 0.1 M cacodylate buffer (pH 7.2). The pellets were again rinsed in buffer and distilled water. The pellets were en-bloc stained (staining performed on post-fixed pellet without embedding or slicing sections on microscope slides) with 2.5% uranyl acetate solution for 5 minutes. After uranyl acetate treatment, the pellets were dehydrated in increasing concentrations with ethyl alcohol to 100% and embedded in PELCO® Eponate 12™ resin (Ted Pella, Redding, CA). The resin was polymerized overnight in a 60 °C oven. Ultrathin sections (80 nm) were cut on a Leica EM UC6 ultramicrotome (Leica Microsystems Inc, Bannockburn, IL), placed on 300 mesh formvar-coated copper grids, counter-stained with 2% uranyl acetate and lead citrate, and examined under a JEOL 1230 transmission electron microscope (JEOL USA Inc., Peabody, MA) at an accelerating voltage of 120 kV.

Protein content analysis

Protein concentration in the microsomal fractions was assayed using a Pierce® BCA (bicinchoninic acid) protein assay kit. This assay utilizes the biuret reaction involving the reduction of cupric ions to cuprous ions by protein in an alkaline medium. The resulting cuprous ions are chelated by two molecules of BCA, yielding a water soluble complex that exhibits a strong absorbance at 562 nm. The colorimetric reaction is linear with respect to protein concentration over a broad working range (20-2,000 μg/ml). Bovine serum albumin standard provided with the protein assay kit was used for the calibration plots. Protein content analysis was performed on the pooled respiratory, olfactory, or hepatic microsomes. Sequential dilution of the protein samples was performed on a 96 well plate followed by the addition of 50 % of BCA reagent A, 48 % of BCA reagent B and 2% of BCA reagent C to each well and mixed well. A set of calibration standards were prepared similarly using bovine serum albumin (BSA) in the concentration range of 200- 2000 μg/ml. Absorbance of both the samples and standards was measured using a SpectraMax Plus^{384} Microplate Reader (Molecular Devices, Sunnyvale, CA) at 562 nm after incubation at 37 ºC for 2 hours followed by cooling to room temperature. The amount of protein was calculated from the calibration curve from the BSA standards.

CYP1A2 ELISA

Respiratory, olfactory, or hepatic microsomes were diluted in PBS to give a final protein concentration of ~5 μg/ml. Microtiter assay 96 well-plates (Immulon 2HB, Thermo Fischer Scientific Inc. Rockford, IL) were coated with sequential dilutions (protein concentrations covered: 5, 2.5, 1 μg/ml) of olfactory, respiratory, and hepatic microsomal extracts (50 μL). The plate was covered with an adhesive plastic (Cling Wrap, Glad®, Oakland, CA) and incubated overnight at 4 °C. After the incubation period, the wells were washed with 0.05% Tween 20 in PBS. Additional non-specific binding

was minimized by incubating the wells with a blocking buffer (3% bovine serum albumin in PBS, pH 7.4) for 2 hours at room temperature. Mouse monoclonal anti-human CYP1A2 antibody was diluted in blocking buffer (1.25 µg/ml final concentration) and 200 µl were added to each of the wells immediately after removal of the blocking buffer. Negative control wells were incubated with blocking buffer, instead. The incubation with the primary antibody was carried out overnight at 4 °C. Following incubation, the wells were washed five times with 0.05 % Tween 20 in PBS. Secondary antibody, horseradish peroxidase (HRP)-conjugated goat anti-mouse IgG solution diluted in PBS (1:5000) was added to the wells (100 µl) and incubated at room temperature for 1 hour. The plate was washed five times with 0.05% Tween 20 in PBS. The substrate provided for the enzymatic reaction with horseradish peroxidase was hydrogen peroxide. In the ELISA, cleavage of hydrogen peroxide was coupled to oxidation of the hydrogen donor TMB. Prior to the reaction of hydrogen peroxide and horseradish peroxidase, the TMB substrate solution is colorless. After an approximately 15-20 minute incubation with peroxidase and hydrogen peroxide, the substrate system develops a blue reaction product which has strong absorption maxima at 370 and 655 nm. The colorimetric reaction was halted by acidifying the well (addition of 2M sulfuric acid or 1M hydrochloric acid), to yield a yellow complex that has an absorption maximum at 450 nm. The absorbance of the substrate-HRP complex resulting from CYP1A2 immunoassay reaction in different wells of the 96-well plate was measured at 370 nm using a SpectraMax Plus^{384} Microplate Reader (Molecular Devices, Sunnyvale, CA). A well containing 3% BSA (negative control) was treated in the same way to rule out any non-specific binding of the primary or secondary antibody with the blocking agent. The CYP1A2 signal was normalized with respect to total microsomal protein (mg) for the respiratory, olfactory, and hepatic microsomal fractions and the relative CYP1A2 ELISA signal intensities for each microsomal fraction were compared.

Microsomal protein binding analysis

Aliquots (1 ml) of melatonin, 6-hydroxymelatonin and N-acetylserotonin (50 µM each) in 0.05 M phosphate buffer containing 3 mM $MgCl_2$ (pH 7.4) were individually mixed with bovine respiratory, olfactory and hepatic microsomal fractions (1 ml), each at 10 mg/ml protein concentration. The solutions (2 ml) were individually injected into pre-conditioned dialysis-membrane tubes (Spectra-Por #4, molecular weight cutoff 12–14 kDa, Spectrum Laboratories Inc., Rancho Dominguez, CA). Both ends of the membrane tube were tied and the tube was placed in a beaker containing 500 ml of the phosphate buffer/magnesium chloride solution maintained at 37 °C for 2 hours with constant stirring. After the incubation period, aliquots (1 ml) of the dialysate were mixed 1:1 with the melatonin internal standard melatonin D7 (MTd7, deuterated melatonin where seven hydrogen atoms in melatonin are replaced with deuterium) solution at 50 ng/ml. The dialysate was sampled in triplicate for each dialysis experiment. These sample solutions were subjected to solid phase extraction and LCMS analysis for the detection of each compound (melatonin, 6-hydroxymelatonin or N-acetylserotonin). The ratio of the total amount of the compound in the dialysate divided by the total amount of the compound added initially to the microsomal solutions represents the unbound fraction of each compound for each microsomal fraction.

The extent of protein binding was calculated as the percent bound to microsomal proteins as shown in Equation 4-1.

$$\% \text{ bound} = \left(1 - \frac{\text{Amount in dialysate}}{\text{Total amount added initially}}\right) \times 100 \qquad \text{Equation 4-1}$$

For all the three compounds, the percent bound to the microsomal proteins was determined to be less that 5% for bovine hepatic, respiratory, and olfactory microsomal fractions.

Microsomal assays

Aliquots of bovine olfactory, respiratory or hepatic microsomes were thawed to 37 °C immediately before use. The microsomal suspension (50 µL) was added to 950 µL of melatonin solution dissolved in 0.1 M phosphate buffer (pH 7.4). The solution was pre-equilibrated to 37 °C for 5 minutes. The reaction was initiated by adding NADPH regenerating system solutions A (50 µL) and B (10 µL). The final concentrations of the components of the NADPH regenerating system in the microsomal incubation mixture were: 1.3 mM $NADP^+$, 3.3 mM glucose-6-phosphate, 0.4 U/ml glucose-6-phosphate dehydrogenase and 3.3 mM magnesium chloride. Appropriate conditions to allow data treatment using initial rate reaction kinetics for the microsomal assay were verified by conducting a preliminary assay with bovine hepatic microsomes at 39 µM melatonin initial concentration and measuring the degradation of melatonin along with the formation of 6-hydroxymelatonin and N-acetylserotonin over a 2 hour incubation period at 37 °C. The final incubation time for studying the kinetics of melatonin 6-hydroxylation for all of the microsomal assays was selected to be 15 minutes, such that the conversion of melatonin to 6-hydroxymelatonin increased in a linear fashion with time, and the net loss of melatonin from the incubation system at the end of the assay was less than 10%. Following an incubation period of 15 minutes at 37 °C, the metabolism reaction was terminated by addition of 100 µl acetonitrile and placement of the tubes in an ice bath for 30 minutes. The ice-cooled tubes were vortex-mixed for 30 seconds and centrifuged at 20,000× g for 20 minutes using an Eppendorf 5804R centrifuge to precipitate the microsomal proteins. The supernatant was filtered through Acrodisc® 13 mm syringe filters with 0.45 µm nylon membrane and diluted 10 times with phosphate buffer for

subsequent solid phase extraction (SPE) and liquid chromatography-mass spectroscopy (LCMS) analysis. Incubations without NADPH were separately performed to verify that the formation of the observed metabolic products required microsomal enzymes as well as a source of NADPH.

SPE and LCMS analysis

Sample preparation

To each of the diluted filtered supernatant aliquots (200 μL), an equal volume (200 μL) of internal standard (deuterated melatonin, melatonin D7) diluted to 50 ng/ml in water) was added. The resulting samples were vortex-mixed for 30 seconds and subjected to SPE and LCMS analysis. Fresh standards were prepared for melatonin, 6-hydroxymelatonin, and N-acetylserotonin on each day of the analysis and subjected to the same SPE-LCMS procedure that was used to treat the samples obtained from the microsomal studies. The efficiency of melatonin, 6-hydroxymelatonin, and N-acetylserotonin extraction from the microsomal solutions was determined by comparing the recovery of the three compounds extracted from the 0-minute microsomal incubations (microsomes and test compounds pre-equilibrated at 37 °C for 5 minutes without addition of the cofactors) to the standard solutions of the three compounds.

The % recovery for the extracted compounds was calculated as follows:

$$\%\ \text{Recovery} = \frac{\text{Concentration extracted from microsomal suspension after incubation } (\mu M)}{\text{Measured concentration for the standard solution } (\mu M)} \times 100 \qquad \text{Equation 4-2}$$

Solid phase extraction (SPE)

EVOLUTE® ABN solid phase extraction cartridges (25 mg-1 ml capacity) (Biotage, Charlotte, NC) were used for SPE. The cartridges were conditioned with 1ml methanol followed by equilibration with 1ml water. Samples (400 µL) were loaded on the cartridge. The cartridges were washed with 1 ml of 5% methanol and the analytes were eluted with 200 µL of acetonitrile. Water (200 µL) was added to the eluted samples followed by vortexing for 30 seconds. The tubes were centrifuged at 2500 ×g for 5 minutes and the supernatant samples (50 µL) were transferred to autosampler vials.

Liquid chromatography-mass spectroscopy (LCMS)

The HPLC system used for the analysis of melatonin and its metabolites was a Shimadzu LC-10AD HPLC system with an autosampler (SIL-HTC) (Shimadzu Scientific Instruments, Columbia, MD). The HPLC was coupled to a Shimadzu LCMS-2010A system with single quadrupole mass spectrometer with an atmospheric-pressure chemical ionization (APCI) interface. Chromatographic separation was carried out at room temperature (22 °C) on a Phenomenex Gemini-NX C18 (150 mm × 2.0 mm, 5 µm particle size, 110°A pore size) column (Phenomenex Inc., Torrance, CA). The mobile phase consisted of a gradient of methanol-water, both with 0.04 % glacial acetic acid, from 20:80 v/v to 85:15 v/v over 4 minutes. The flow rate was 0.2 mL/min. The APCI source was set in the positive ionization mode. A selected ion monitoring (SIM) setting was used with $[M + H]^+$, m/z of 233.25, 249.25, 219.15, and 240.25 as the detecting ions for melatonin, 6-hydroxymelatonin, N-acetylserotonin, and melatonin D7, respectively. The total run time for the LCMS analysis was 10 minutes. The concentrations were calculated from a calibration curve obtained from fresh melatonin, 6-hydroxymelatonin, and N-acetylserotonin standard solutions subjected to identical SPE and LCMS analysis as that of sample solutions during every run.

The operating conditions for the LCMS were as follows:

Interface: APCI

Interface temperature: 400 °C

Curved desolvation line (CDL) temperature: 200 °C

Nebulizing gas flow: 2.5 L/min

Heat block: 200 °C

The limit of quantification of melatonin, 6-hydroxymelatonin, and N-acetylserotonin with the SPE-LCMS method was 5 ng/ml, 18 ng/ml, and 4 ng/ml respectively at a signal-to-noise ratio of ~10-12. A representative LCMS chromatogram and ion plot are shown in Figure 4-1. Examples of melatonin, 6-hydroxymelatonin, and N-acetylserotonin calibration plots are shown in Figures 4-2, 4-3, and 4-4, respectively.

Calculations and statistical analysis

For each initial melatonin concentration used in the reaction, reaction velocity was calculated as the amount of 6-hydroxymelatonin formed per unit incubation time (15 minute) per gram of protein in the microsomal incubation mixture. A typical (hyperbolic) Michaelis - Menten kinetics model[225] (Equation 4-3) was used to fit the experimentally obtained 6-hydroxymelatonin formation velocity at each melatonin initial concentration.

$$V=\frac{V_{max}C}{K_M+C} \qquad \text{Equation 4-3}$$

Where, C is the initial melatonin concentration, V_{max} is the apparent maximal velocity of substrate-to-metabolite conversion reaction and K_M is the substrate concentration at which the reaction velocity is equal to 50% of V_{max}.

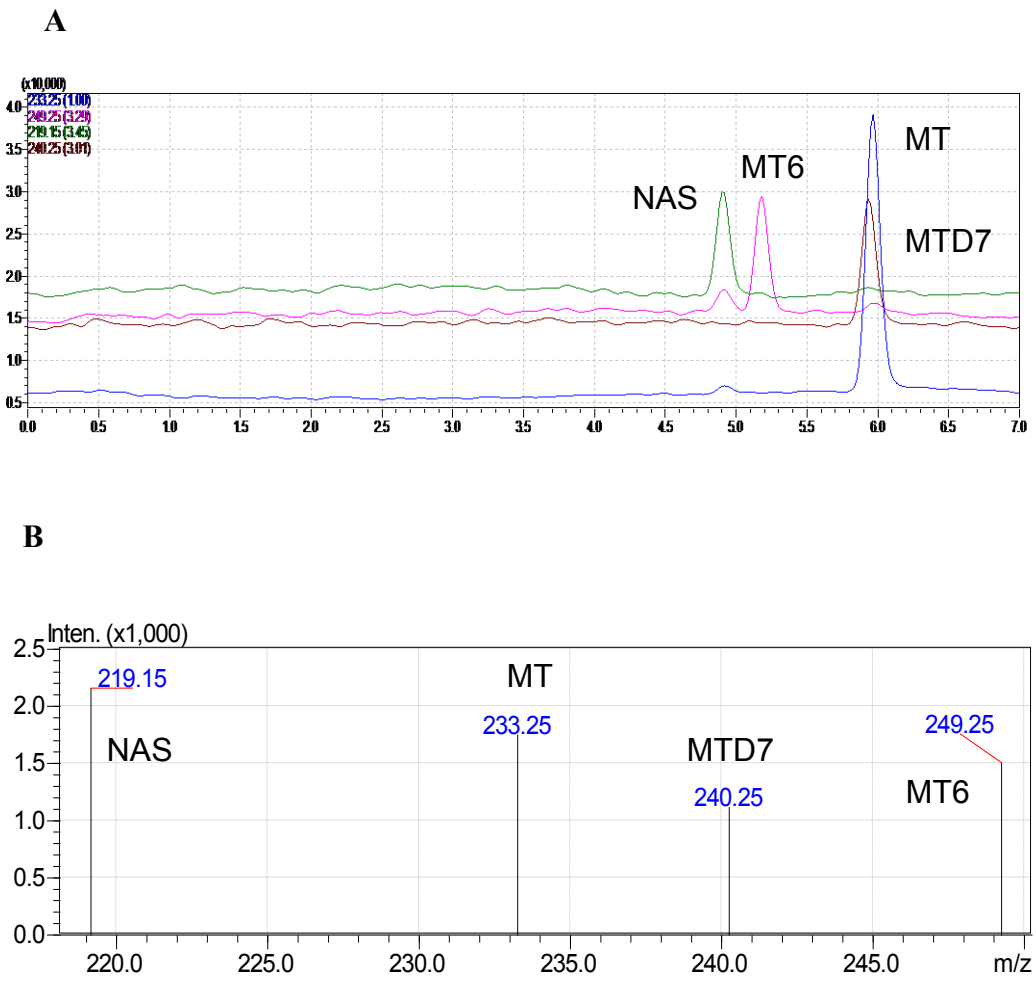

Figure 4-1 A representative LCMS chromatogram (A) and ion plot (B) for the detection of melatonin (MT, 5.8 min, m/z of 233.25); 6-hydroxymelatonin (MT6, 5.1 min, m/z of 249.25); N-acetylserotonin (NAS, 4.8 min, m/z of 219.15); and the internal standard deuterated melatonin (MTD7, 5.8 min, m/z of 240.25).

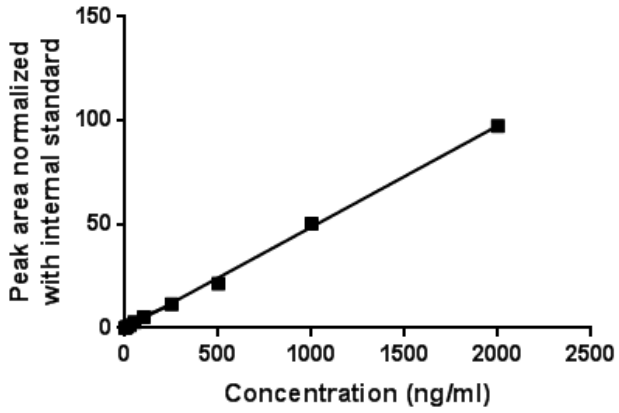

Figure 4-2 A representative calibration curve for melatonin in Kreb's Ringer buffer (KRB) after SPE-LCMS analysis. Peak area for melatonin was divided by the peak area of internal standard (deuterated melatonin) to yield normalized peak area. Linear regression of data results in the following equation: $y = 0.04 x - 0.14$, $r^2 = 0.99$.

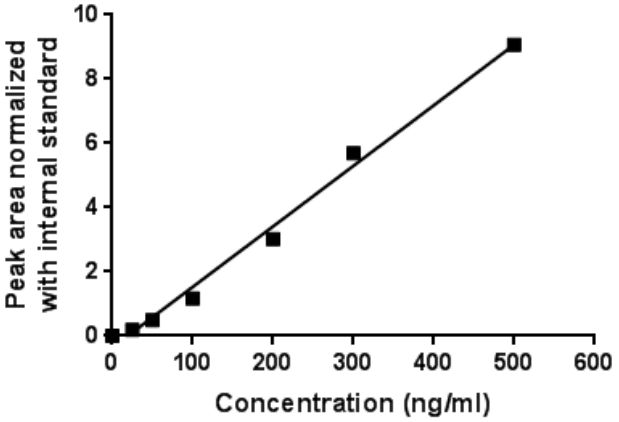

Figure 4-3 A representative calibration curve for 6-hydroxymelatonin in Kreb's Ringer buffer (KRB) after SPE-LCMS analysis. Peak area for 6-hydroxymelatonin was divided by the peak area of internal standard (deuterated melatonin) to yield normalized peak area. Linear regression of data results in the following equation: $y = 0.02 x - 0.37$, $r^2 = 0.99$.

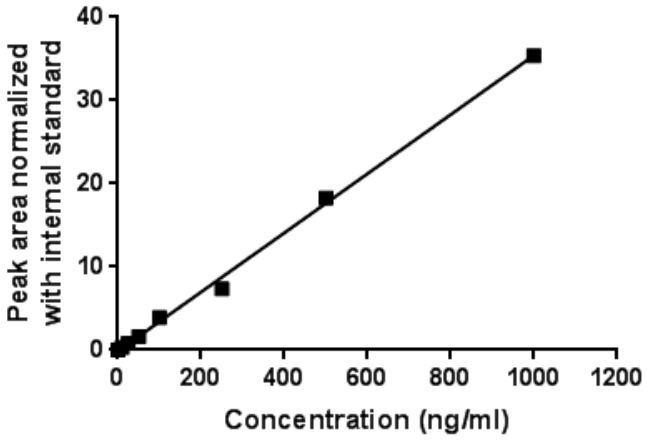

Figure 4-4 A representative calibration curve for N-acetylserotonin in Kreb's Ringer buffer (KRB) after SPE-LCMS analysis. Peak area for N-acetylserotonin was divided by the peak area of internal standard (deuterated melatonin) to yield normalized peak area. Linear regression of data results in the following equation: $y = 0.04 x - 0.14$, $r^2 = 0.99$.

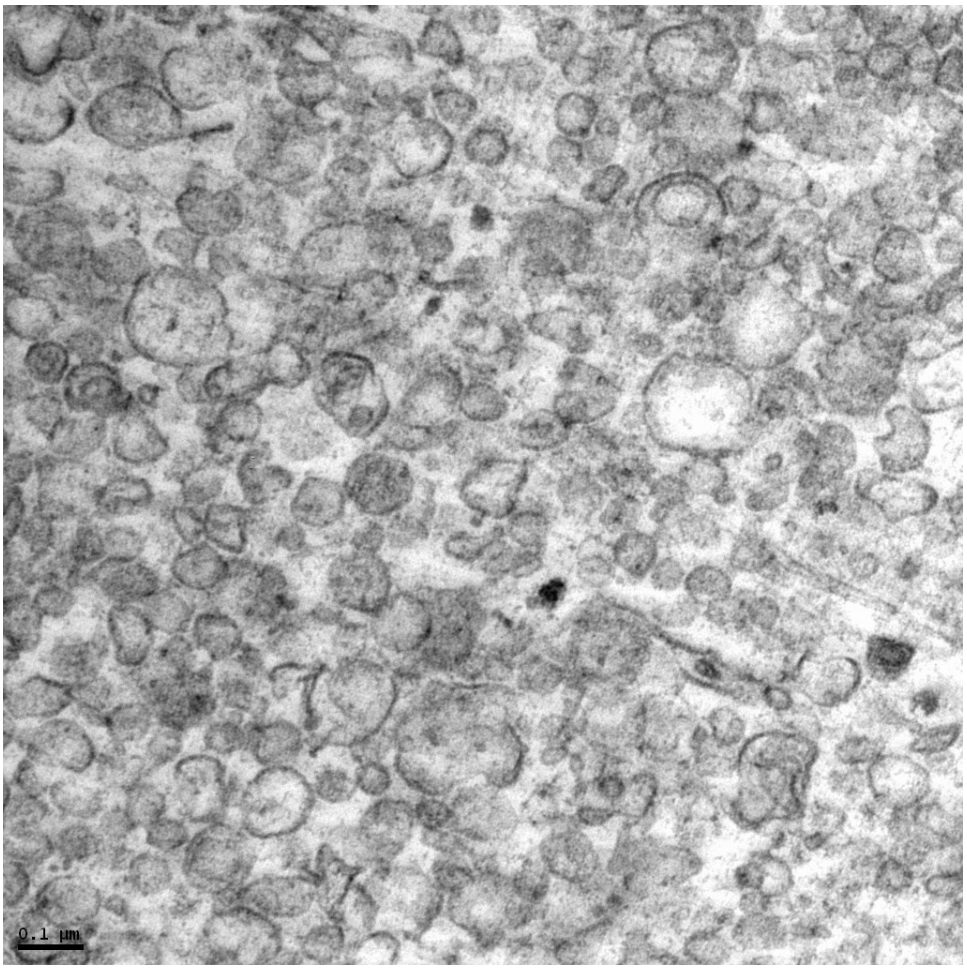

Figure 4-5 Transmission electron micrograph showing uranyl acetate stained bovine respiratory microsomes. Scale bar: 0.1 µm.

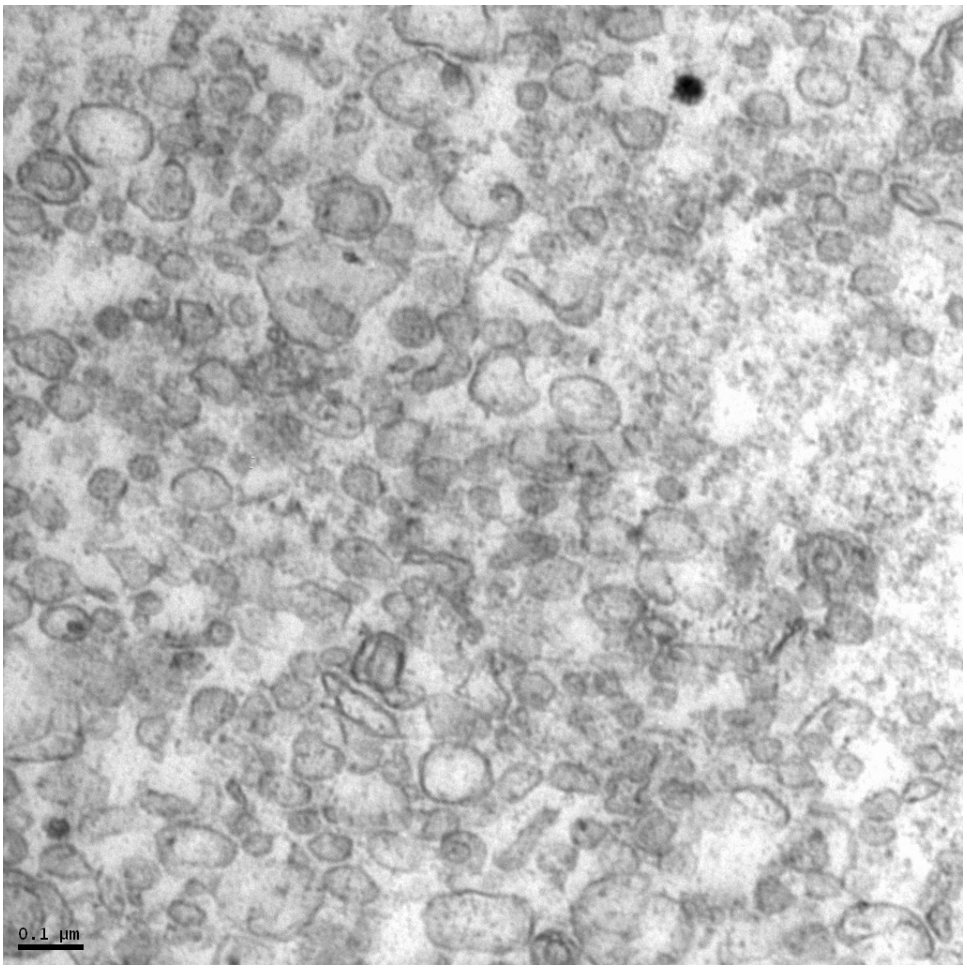

Figure 4-6 Transmission electron micrograph showing uranyl acetate stained bovine olfactory microsomes. Scale bar: 0.1 µm.

Non-linear regression was performed using GraphPad Prism version 6.00 for Windows (GraphPad Software Inc., La Jolla CA, www.graphpad.com). Statistical significance between the maximum apparent reaction velocities between the three microsomal fractions was evaluated using ANOVA and Student's t-test with a Bonferroni correction. A p-value less than 0.05 was considered to be significant.

Results

Transmission electron micrographs of bovine respiratory and olfactory microsomal fractions (Figures 4-5 and 4-6) showed smooth, round-shaped vesicles with diameters ranging roughly from 0.05 to 0.1 μm, presumably consisting of smooth endoplasmic reticulum. The final protein concentrations in the respiratory, olfactory, and hepatic microsomal fractions were 16.9 mg/ml, 13.5 mg/ml, and 14.0 mg/ml, respectively. To semi-quantitatively analyze the CYP1A2 enzyme content of the microsomal protein, an indirect ELISA (enzyme linked immuno-sorbent assay) was performed on the respiratory, olfactory, and hepatic microsomal fractions.

The "indirect" ELISA relies on the binding between a primary antibody (mouse anti-CYP1A2) targeted towards the specific antigen, and a secondary antibody conjugated to a chromophore or a chemi-luminescent substrate (HRP-conjugated goat anti-mouse IgG) to yield a measureable colored complex. Microsomal protein extracts probed with anti-CYP1A2 antibody showed that the immunoassay absorbance signal resulting from the conjugation of the HRP-colorimetric complex of the secondary antibody was the stronger in the hepatic microsomal fraction than the signal in the olfactory and respiratory microsomal fractions (Figure 4-7). As standardized microsomal CYP1A2 protein solutions from bovine sources were not available, a statistically significant difference between the concentration of CYP1A2 present in bovine respiratory, olfactory and hepatic microsomal fractions could not be established from the data generated by this semi-quantitative ELISA.

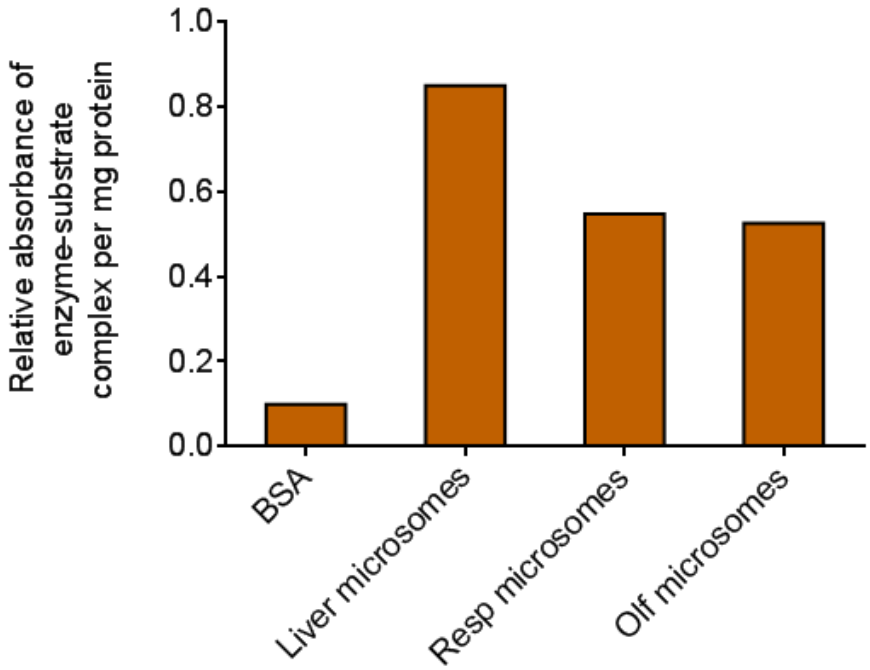

Figure 4-7 CYP1A2 signal intensity per mg of microsomal proteins analyzed using CYP1A2 ELISA in microsomal fractions prepared from bovine liver, bovine olfactory mucosa (Olf), and bovine respiratory mucosa (Resp). Bovine serum albumin (BSA) was used as the negative control.

Validation of the maintenance of initial rate substrate metabolism kinetics during the microsomal assays was performed with bovine hepatic microsomes to examine melatonin degradation and metabolite appearance kinetics over a longer incubation period (2 hours). As shown in Figure 4-8, the amount of melatonin in the incubation mixture decreased with time, apparently due to metabolism of melatonin to 6-hydroxymelatonin and N-acetylserotonin. The amounts of both the metabolites in the incubation mixture increased with time. The amounts of N-acetylserotonin quantified during the two-hour incubation were insignificant when compared to those of 6-hydroxymelatonin. This indicated that melatonin was primarily converted to 6-hydroxymelatonin as a result of bovine hepatic microsomal CYP1A2-mediated 6-hydroxylation.

The total melatonin loss during the initial 15 minute incubation period was less than 10% of the initial amount, thus confirming the initial rate assay conditions were met. Additional primary and secondary metabolites of melatonin were not detected during the two hour incubation with bovine hepatic microsomes. The total mass balance of melatonin and its detected metabolites at the end of 15 minutes was 95.6% ± 3.4% of the initial melatonin amount added in the assay. However, at the end of the 2-hour microsomal incubation, the net mass balance for melatonin and its metabolites was 79.4% ± 2.3% of the original melatonin amount in the incubation mixture. The total mass unaccounted for (~20%) might represent these fractional amounts of minor or secondary melatonin metabolites which were either lost during the SPE-LCMS analysis or were undetectable under the LCMS assay conditions. The limit of quantification of melatonin, 6-hydroxymelatonin, and N-acetylserotonin with the SPE-LCMS method was 5 ng/ml, 18 ng/ml, and 4 ng/ml, respectively, at a signal-to-noise ratio of ~10-12. The recoveries of melatonin, 6-hydroxymelatonin and N-acetylserotonin extracted from the microsomal solutions were each greater than 95%, confirming the efficiency of protein precipitation, solid phase extraction, and LCMS method for the detection of melatonin along with its

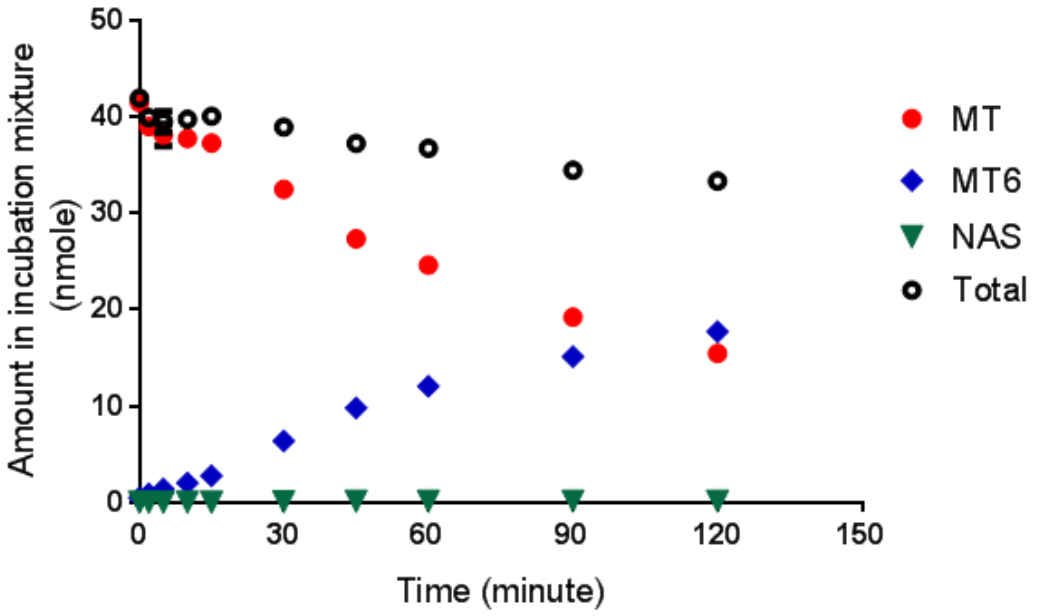

Figure 4-8 Disappearance of melatonin (MT) and appearance of 6-hydroxymelatonin (MT6) and N-acetylserotonin (NAS) in incubation mixture containing bovine hepatic microsomes over 120 minutes. Results indicate <10% loss of melatonin over first 15 minute incubation interval. Recovery of all species (total) at 120 minutes was ~80% of the initial melatonin concentration. Results are presented as the mean of 3 replicates ± standard deviation (error bars included within the symbols).

two metabolites, 6-hydroxymelatonin and N-acetylserotonin. The control solution incubated without NADPH regenerating solution resulted in <1% of total melatonin loss over a 60 minute incubation period at 37 °C using the identical 39 μM melatonin initial concentration, thus verifying the necessity of microsomal enzymes and NADPH for the degradation of melatonin to 6-hydroxymelatonin or N-acetylserotonin.

Figure 4-9 shows the results for Michaelis-Menten curve fit to the experimental data of the microsomal melatonin 6-hydroxylation rate by bovine hepatic microsomes. In Figure 4-10, the Michaelis-Menten plots for the velocities of melatonin to 6-hydroxymelatonin metabolism by bovine nasal olfactory and respiratory microsomes are displayed.

Melatonin conversion to N-acetylserotonin during the microsomal incubations was monitored as well, but bovine nasal and hepatic microsomes did not yield quantifiable amounts of N-acetylserotonin during the 15 minute incubation period at 37 °C. (The amount of N-acetylserotonin quantified at the end of 120 minutes using a melatonin initial concentration of 39 nM in bovine hepatic microsomes was approximately about 0.15 nmoles). The K_M and V_{max} values obtained for melatonin 6-hydroxylation in the three different microsomal preparations are tabulated in Table 4-2. The apparent average V_{max} values obtained for the conversion of melatonin to 6-hydroxymelatonin by bovine hepatic microsomes (734.6 pmol min^{-1} mg^{-1} microsomal protein), respiratory microsomes (205.2 pmol min^{-1} mg^{-1} microsomal protein) and olfactory microsomes (80.5 pmol min^{-1} mg^{-1} microsomal protein) were significantly different from each other when compared using the Student's t test with Bonferroni correction at $p < 0.05$.

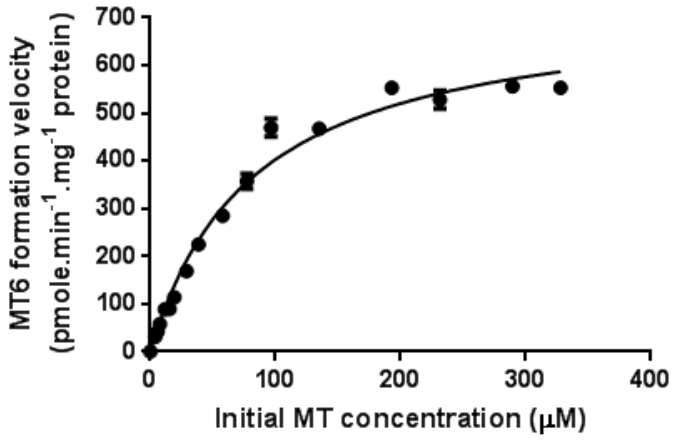

Figure 4-9 Rate of 6-hydroxymelatonin formation in bovine hepatic microsomal incubations at varying initial melatonin concentrations. Results are presented as the mean of 3 replicates ± standard deviation (error bars included within the symbols). Curve represents the fit of Michaelis-Menten kinetics (Equation 4-3) to the data.

Estimated enzyme kinetics parameters were as follows ($r^2 = 0.98$):

$V_{max} = 734.6 \pm 20.8$ pmol. min^{-1}. mg^{-1} of microsomal proteins,

$K_M = 82.5 \pm 6.2$ μM.

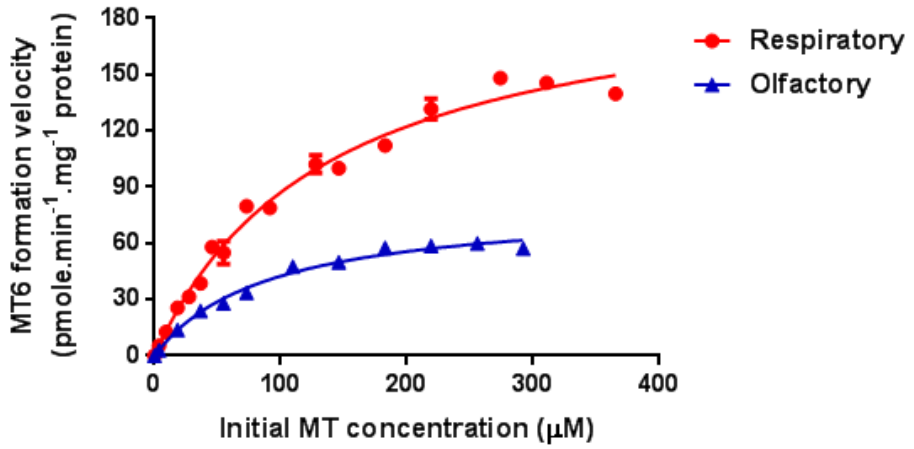

Figure 4-10 Rate of 6-hydroxymelatonin formation in bovine nasal olfactory and respiratory microsomal incubations at varying initial melatonin concentrations. Results are presented as the mean of 3 replicates ± standard deviation (error bars included within the symbols). Curve represents the fit of Michaelis-Menten kinetics (Equation 4-3) to the data.

Estimated enzyme kinetics parameters were as follows:

Olfactory ($r^2 = 0.98$):

$V_{max} = 80.5 \pm 2.7$ pmol. min^{-1}. mg^{-1} of microsomal proteins,

$K_M = 89.7 \pm 8.1$ µM

Respiratory ($r^2 = 0.98$):

$V_{max} = 205.2 \pm 6.6$ pmol. min^{-1}. mg^{-1} of microsomal proteins,

$K_M = 135.7 \pm 9.9$ µM

Table 4-2 Comparison of fitted values for the apparent V_{max} and K_M for melatonin 6-hydroxylation by bovine hepatic, respiratory, and olfactory microsomes.

Parameter	Hepatic	Respiratory	Olfactory
Apparent V_{max} (pmole/min/mg microsomal protein) (mean ± standard error)	734.6 ± 20.8	205.2 ± 6.6	80.5 ± 2.7
Apparent K_M (μM) (mean ± standard error)	82.5 ± 6.2	135.7 ± 9.9	89.9 ± 8.1
Coefficient of determination (r^2)	0.98	0.98	0.98

Discussion

Significant enzymatic activity was exhibited by bovine hepatic and nasal microsomes towards the conversion of melatonin to 6-hydroxymelatonin, and this was in good agreement with literature reports suggesting that 6-hydroxylation is the principal metabolic pathway of melatonin[127,130]. The typical Michaelis-Menten kinetics (Equation 4-3) fit the data for the three microsomal fractions studied (coefficient of determination (r^2) > 0.98, Figures 4-9 and 4-10). The average apparent V_{max} for conversion of melatonin to 6-hydroxymelatonin using bovine hepatic microsomes was approximately 3.5 times higher than that obtained with respiratory microsomes and approximately 9-fold higher than that obtained with olfactory microsomes. In contrast, measureable conversion of melatonin to N-acetylserotonin was not observed in the bovine nasal or hepatic microsomal fractions.

Several researchers have investigated the identity of CYP450 isoforms responsible for melatonin metabolism[127,129,130,134]. In studies with human liver microsomes, 6-hydroxymelatonin (75%) and N-acetylserotonin (10-15%) have been reported to be the major melatonin metabolites[129,134]. The primary metabolite,

6-hydroxymelatonin, is further conjugated with sulfuric (~75%) or glucuronic (~25%) acid. Ma et al. investigated melatonin 6-hydroxylation and O-demethylation with a panel of 11 recombinant human P450 isozymes and demonstrated that CYP1A1, CYP1A2, and CYP1B1, along with a minor contribution from CYP2C19 were involved in the 6-hydroxylation of melatonin, whereas CYP2C19 was responsible for melatonin O-demethylation with minimal involvement from CYP1A2[127]. With a thorough comparison of V_{max} and K_M values, they concluded that CYP1A2 was the most important isoform responsible for the conversion of melatonin to 6-hydroxymelatonin. Similar observations have been reported by Facciola et al.[129] and Skene et al.[130] in studies with human liver microsomes and rat liver microsomes, respectively. With the assistance of molecular modeling, Skene et al. demonstrated that melatonin is a planar substrate with an area-to-depth ratio of 3.97. It is expected to readily be accommodated within the human CYP1A2 substrate binding site in a position that favors 6-hydroxylation[130]. These results strongly suggest that CYP1A2 is the foremost high affinity enzyme involved in the 6-hydroxylation of melatonin, and CYP2C19 is responsible for the minor metabolic pathway leading to O-demethylation of melatonin in the liver.

The relative gene expression levels of CYP1A2 and 2C19 isoforms in bovine olfactory and respiratory mucosae and hepatic tissues using quantitative reverse transcriptase-polymerase chain reaction (RT-PCR) were described in Chapter 3. The CYP2C19-like genes were expressed in bovine olfactory and respiratory mucosa and exhibited lower expression levels (<4%) than those obtained in bovine hepatic tissues. Amplification of CYP1A2-like genes indicated the possibility of expression of a spliced variant of CYP1A2 in bovine olfactory and respiratory mucosa, which was different from the variant detected in the bovine hepatic tissues. The expression of CYP1A2 and CYP2C19 proteins in bovine nasal olfactory and respiratory explants was confirmed using immunohistochemical analyses (Figures 3-9, 3-10, 3-13, 3-14). The appearance of 6-hydroxymelatonin in microsomal incubations involving all the three microsomal

fractions indicates that bovine olfactory, respiratory, and hepatic CYP450 proteins were active towards melatonin biotransformation to 6-hydroxymelatonin.

Based on our results, it is also clear that bovine respiratory microsomes were metabolically more active than bovine olfactory microsomes towards melatonin 6-hydroxylation. Since the respiratory mucosa accounts more than 90% of the surface area of the nasal cavity in humans[20], these results can translate into considerable loss of intranasally administered melatonin due to enzymatic degradation. Since the amount of nasal mucosal tissues is smaller than liver tissues, and the protein content per mg of tissue in the nasal olfactory and respiratory mucosa is significantly lower than that of the hepatic tissues, the extent of pre-systemic loss of melatonin due to CYP450-mediated enzymatic activity upon intranasal administration is expected to be significantly lower than the fraction lost due to hepatic first-pass effect following oral administration. Nevertheless, the reduction in the bioavailable fraction of intranasally administered melatonin by the action of CYP450 enzymes located in the nasal cavity needs to be critically examined to improve the systemic absorption of melatonin after intranasal administration.

CHAPTER 5
ANALYSIS OF *IN VITRO* DIFFUSION AND CONCURRENT METABOLISM OF MELATONIN ACROSS BOVINE NASAL EXPLANTS

Introduction

In vitro diffusion experiments have been widely used to obtain mechanistic information which needs to be evaluated in tissues rather than at the cellular or subcellular level, regarding drug uptake, metabolism, and other physiological factors that potentially affect drug absorption. Permeability of a metabolically labile substrate across a viable biological membrane is influenced by both its diffusion and metabolic parameters. Mechanistic examinations of melatonin permeability across the nasal olfactory and respiratory mucosa were carried out to determine the metabolic limitation the nasal route may contribute in the evaluation of nasal delivery as a promising alternative route for the systemic delivery of melatonin.

Investigations of the *in vitro* permeability of melatonin have been reported in the literature; the permeability coefficient of melatonin across a Caco-2 cell monolayer (human cell line derived from heterogenous colon carcinoma cells) was calculated to be 1.26×10^{-6} cm/s[139]. Additionally, Costa et al. showed that melatonin can easily pass through multilamellar lipid vesicles[148]. Melatonin has been postulated to permeate across biomembranes via transcellular passive diffusion, owing to its low molecular weight and lipophilicity arising from an unionizable indole amide moiety.

In this work, we characterized the *in vitro* diffusion and concurrent metabolism of melatonin during its transport across bovine olfactory and respiratory explants. The major CYP450 isoforms responsible for the metabolism of melatonin in human liver are CY1A2 and CYP2C19[127,129]. Real time RT-PCR and enzyme immunohistochemistry results have demonstrated that CYP1A2 and CYP2C19 coding genes and corresponding

proteins are expressed in the bovine nasal mucosa, and microsomal degradation of melatonin to 6-hydroxymelatonin enabled a quantitative measurement of the relevant metabolic activity of the CYP450 isoforms in the bovine respiratory and olfactory mucosa. The purpose of the current investigations was to further understand the activity of nasal CYP450 enzymes in metabolizing melatonin during its diffusion across bovine nasal mucosa explants and to correlate the enzyme activity with the observed enzyme distribution patterns to identify the extent of pre-systemic loss of melatonin in bovine respiratory and olfactory tissues.

Materials and Methods

Materials

Melatonin, 6-hydroxymelatonin, N-acetylserotonin, polyoxyethylene-9-1auryl ether (laureth-9), trypsin-EDTA solution (10-fold concentrated; 5 g porcine trypsin and 2 g sodium EDTA per liter of 0.9% sodium chloride), fluvoxamine maleate, and Kreb's Ringer's buffer (KRB) components were obtained from Sigma-Aldrich® (Sigma-Aldrich® Co. LLC, St. Louis, MO). T-PER® protein extraction reagent was obtained from Thermo Fisher (Thermo Fisher Scientific Inc., Rockford, IL). Chemicals and stains used in microscopy were obtained from the Central Microscopy Research Facility, University of Iowa. Solvent 100 mounting medium was obtained from IMEB (IMEB Inc., San Macros, CA).

Preparation of mucosal tissues

The bovine nasal mucosa was obtained from Bud's Custom Meats Co. (Riverside, IA). A vertical incision from the nostril to the lower eyelids was made along the snout of the cows to expose the nasal cavity. Nasal turbinate mucosae were retrieved by opening the nasal cavity along the septal midline and removing the turbinates from the lateral wall. The olfactory mucosa is located at the roof of the nasal cavity covering two

bulb-like projections. The respiratory mucosa, located within the main nasal cavity, was harvested by making vertical incisions along both walls of the nasal cavity and along the septum with a butchering knife. The cartilage and overlying olfactory or respiratory mucosae were removed by blunt dissection. The tissues were placed in cold KRB maintained on ice and transported to the lab.

The thickness of bovine respiratory and olfactory epithelial, as well as the submucosal layer was measured by examining formalin-fixed, paraffin-embedded, hematoxylin and eosin stained bovine olfactory and respiratory mucosal sections under Olympus BX-51 light microscope (Olympus America Inc., Center Valley, PA) equipped with a DP-71 digital camera with measurement of the thickness accomplished using ImageJ software[180,181] (U.S. National Institutes of Health, Bethesda, MD). The mean of 10 measurements was taken as the average thickness value for the epithelial and submucosal layers of bovine respiratory and olfactory mucosa.

In vitro diffusion experiments

Krebs Ringer's buffer solution (KRB) (1.67 mM $MgCl_2$, 4.56 mM KCl, 119.78 mM NaCl, 1.5 mM NaH_2PO_4, 0.83 mM Na_2HPO_4 and 10 mM D-glucose, 15 mM $NaHCO_3$ and 1.2 mM $CaCl_2$) was used as the physiological buffer for all diffusion experiments. It was prepared by dissolving the salts, except calcium chloride, in 900 ml of deionized water. Carbogen (95% O_2 + 5% CO_2) was bubbled through the solution for ~15 minutes and then calcium chloride was added. The volume of the solution was made up to 2000 ml by adding deionized water, and the pH was adjusted to 7.4 using either 1N HCl or NaOH. Melatonin donor solutions were prepared by dissolving the required amount of melatonin in KRB at room temperature.

Fresh mucosal membranes were carefully stripped from the underlying cartilage using dissecting forceps and used immediately for transport studies. Navicyte® Diffusion Chambers™ (1 ml) (Harvard Apparatus, Holliston, MA) were used to study the diffusion

of melatonin across bovine nasal mucosa. Bovine respiratory or olfactory mucosal explants were mounted between the donor and receiver compartments of the diffusion chambers. The chambers were maintained at 37 °C using a Lauda RM6 circulating water bath (Brinkmann Instruments Co., New York, NY) and aerated with carbogen gas (95% O_2 + 5% CO_2) at a rate of 2-4 bubbles/second throughout the experiment. The gas improves the viability of the tissues by supplying oxygen and also stirs the content of the chambers. The mucosal explants were equilibrated with 1 ml of pre-warmed KRB in both donor and receiver compartments for 20 minutes. After equilibration, the buffer was replaced with 1 ml of melatonin solution in the donor chamber and 1 ml of fresh KRB in the receiver chamber. The transport of melatonin across the mucosal membrane was measured by withdrawing aliquots (200 µl) at regular intervals (30, 45, 60, 75, 90, and 120 minutes). The aliquots removed were replaced with fresh buffer to keep the volume in the receiver cell constant. At the end of the 2-hour permeability experiment, 200 µl were withdrawn from the donor compartment and analyzed for the concentration of melatonin and its metabolites. The mucosal integrity of the tissues was checked by measuring the transepithelial electrical resistance. TEER was measured before and after the diffusion experiment using an EVOM volt-ohmmeter (Model: EVOM^2; World Precision Instruments Inc., Sarasota, FL). TEER values above 100 Ω*cm^2 were considered to be indicative of an intact mucosal explant.

To each of the withdrawn aliquots (200 µL), a fixed volume (200 µL) of internal standard (deuterated melatonin, melatonin D7 diluted to 50 ng/ml in water) was added. The resulting samples were vortex-mixed for 30 seconds and subjected to SPE and LCMS analysis. Fresh standards were prepared for melatonin, 6-hydroxymelatonin, and N-acetylserotonin on each day of the analysis and subjected to the same SPE-LCMS procedure that was used to treat the samples obtained from the diffusion studies. The procedure for SPE and LCMS has been described in Chapter 4. To isolate and identify all the possible melatonin metabolites formed during its diffusion across the bovine

respiratory and olfactory explants, aliquots withdrawn from the receiver and donor chambers at the end of the 2 hour permeability study using a melatonin donor concentration of 431 μM were subjected to solid phase extraction. The extracted solution was directly injected on the APCI mass spectrometer (without separation on column) to detect the protonated molecular ions $[M + H]^+$ present in the solution following SPE. The compounds that yielded a signal on the mass spectrometer were identified as melatonin, 6-hydroxymelatonin, and N-acetylserotonin with a mass-to-charge (m/z) ratio of 233.25, 249.25, and 219.15, respectively. A representative LCMS chromatogram and ion plot are shown in Figure 4-1. Examples of melatonin, 6-hydroxymelatonin, and N-acetylserotonin calibration plots are shown in Figure 4-2, 4-3, and 4-4, respectively.

6-hydroxymelatonin and N-acetylserotonin diffusion across bovine nasal explants

To measure the permeability of the two primary metabolites of melatonin, 6-hydroxymelatonin, and N-acetylserotonin across the bovine nasal explants, additional sets of diffusion experiments were performed with either 6-hydroxymelatonin or N-acetylserotonin solutions in the donor compartment. The experimental procedure for these permeability experiments was identical to that described for melatonin diffusion, however, instead of melatonin, the donor compartment contained 6-hydroxymelatonin (202 μM) or N-acetylserotonin (229 μM) solutions prepared in KRB. The receiver solution contained fresh, pre-warmed KRB from which aliquots were removed at the specified time points and analyzed for the concentration of either 6-hydroxymelatonin or N-acetylserotonin.

Flux calculations and statistical comparison

The amount of melatonin present in the receiver chamber, as well as the accumulation of the metabolites, 6-hydroxymelatonin and N-acetylserotonin, were measured at each time point during a typical transport study. The amounts of melatonin,

6-hydroxymelatonin, and N-acetylserotonin withdrawn from the receiver chamber at each time point were added to the calculated amount transported at the next time point to obtain the cumulative amount of melatonin, 6-hydroxymelatonin, or N-acetylserotonin transported into the receiver chamber. The cumulative amount of melatonin permeated across each mucosal explant was plotted against time, as shown in Figure 5-1.

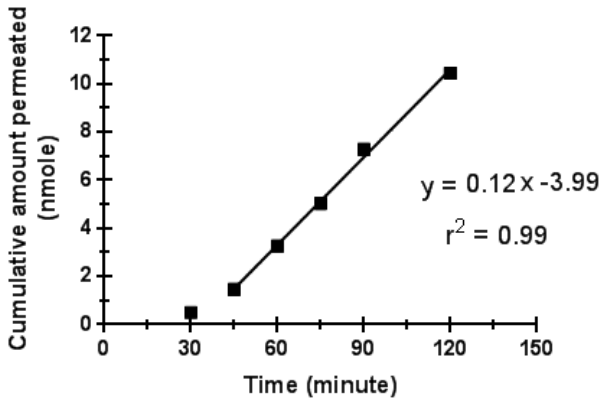

Figure 5-1 A representative plot of the cumulative amount of melatonin transported across a bovine respiratory tissue explant as a function of time (30, 45, 60, 75, 90, and 120 minutes) at 323 μM donor melatonin concentration. Linear regression of the steady state region of data (post 30- minutes) gave the equation: $y = 0.12x - 3.99$, $r^2 = 0.99$.

Melatonin flux (*J*) in the mucosal-to-submucosal direction was calculated by dividing the slope of the steady-state portion (post-30 minutes) of the plot (GraphPad Prism version 6.00 for Windows, GraphPad Software Inc., La Jolla CA, www.graphpad.com) by the tissue cross-sectional area (0.64 cm^2) exposed to the donor and receiver compartments (Equation 5-1)[226]. The effective permeability coefficient value was calculated by dividing the flux by the initial melatonin donor concentration. Each experiment was performed in triplicate. The Student's *t*-test with Bonferroni correction

was performed to compare the mean flux and permeability values at each concentration. A value of $p < 0.05$ was considered statistically significant.

$$J = \frac{1}{A}\frac{dM_R}{dt} = P_e \times C_D \qquad \text{Equation 5-1}$$

Where,

J = flux of substrate in mucosal-to-submucosal direction

dM_R/dt = slope of cumulative amount of drug transported in the receiver versus time plot

A = the diffusional cross-sectional area of the mucosal membrane (0.64 cm^2)

C_D = initial donor concentration

P_e = effective permeability of substrate in the mucosal-to-submucosal (m-s) direction

Analysis of total protein and CYP1A2 enzyme content in bovine nasal explants

In order to estimate the relative abundance of the CYP1A2 isoform in the bovine olfactory and respiratory explants, the proteins were extracted from full thickness mucosal explants. Fixed surface areas of bovine olfactory and respiratory mucosal explants were individually homogenized using T-PER® tissue protein extraction reagent (a proprietary detergent in 25 mM bicine buffered saline, pH 7.6) at 4 ºC. The protein extract was separated from the tissue debris after centrifuging the homogenate at 10,000×g at 4 ºC for 20 min. The protein content in the olfactory and respiratory homogenate was quantified using the BCA assay. The CYP1A2 enzyme content in each protein extract was semi-quantitatively determined using ELISA. The procedures for BCA assay and ELISA are described in Chapter 4.

Melatonin diffusion studies with CYP1A2 inhibition

The effect of fluvoxamine, a potent and selective CYP1A2 inhibitor, on melatonin metabolism during transport across bovine nasal mucosae was studied by equilibrating explants with fluvoxamine (216 μM) dissolved in KRB both donor and receiver chambers for 30 minutes prior to the initiation of transport studies. After the equilibration, the buffer was replaced by 1 ml of melatonin (216 μM) dissolved in KRB containing fluvoxamine (216 μM) in the donor chamber and 1 ml of fresh KRB containing dissolved fluvoxamine (216 μM) in the receiver chamber. Samples (200 μl) were withdrawn at 15 min intervals and replaced with fresh, pre-warmed buffer containing dissolved fluvoxamine (216 μM) at regular intervals (30, 45, 60, 75, 90, and 120 minutes). The withdrawn samples were analyzed for parent drug and metabolite content by SPE-LCMS.

Melatonin diffusion studies with de-epithelized nasal explants

The nasal mucosal explants are composed of both an epithelial layer and a submucosal region. In order to determine the flux and metabolism of melatonin in the isolated submucosal tissues, the epithelial cell layer was chemically removed from the full thickness tissue. Previous studies from our lab have indicated that the de-epithelization of bovine nasal mucosa with trypsin-EDTA solution takes 2 hours for complete epithelial removal[227]. For experiments designed to estimate the role of submucosal enzymes in metabolizing melatonin, shorter de-epithelization incubation times were desired, due to the limited viability of the submucosal enzymes during the 2 hour permeability experiments following a 2-hour de-epithelization incubation period at 37 ºC.

To perform the process of de-epithelization, bovine olfactory and respiratory nasal explants were mounted between the donor and receiver compartments of the

diffusion chambers. The chambers were maintained at 37 °C and aerated with carbogen gas (95% O_2 + 5% CO_2) at a rate of 2-4 bubbles/second throughout the incubation time. Laureth-9 solution (1% laureth-9 in KRB; 1 ml) was added to the donor compartment and 1 ml of fresh KRB was added to the receiver compartment. After 30 minute incubation, the laureth-9 solution in the donor compartment was replaced with 0.5% trypsin 0.2% sodium EDTA solution in KRB (manufacturer's stock diluted 1:9 in KRB) for additional 30 minute incubation.

To ensure that the treatment resulted in complete removal of the epithelial layer, following the 1 hour de-epithlization treatment, control explants were rinsed 3 times with fresh KRB in the diffusion chamber at 1 minute intervals, de-mounted from the diffusion chambers and fixed in zinc formalin (1% zinc sulfate in 3.7% unbuffered formalin prepared from a commerically available 37-40% concentrated formaldehyde solution) for 48 hours at 4 °C with continuous stirring. Fixed nasal mucosal explants were dehydrated and embedded in low melting- temperature paraffin using an RMC 1530 paraffin tissue processor (Kroslak Enterprises Inc., Midland, ON, Canada). For histological examination, 5 μm thick sections were cut using a Leica UC6 ultramicrotome (Leica Microsystems Inc, Bannockburn, IL), dehydrated overnight, deparaffinized and stained with hematoxylin and eosin using a DRS-601 Sakura Diversified Stainer (GMI Inc., Ramsey, MN). Finally, the sections were coverslipped using Solvent 100 mounting medium and examined under a Olympus BX-61 light microscope (Olympus America Inc., Center Valley, PA).

To perform diffusion experiments following de-epithelization, tissues were incubated with laureth-9 and trypsin-EDTA as described above. The donor and the receiver compartments were emptied and filled with fresh KRB for a 10 minute equilibration. Then the donor compartment was replaced with a melatonin solution dissolved in KRB and the receiver compartment was replaced with fresh KRB.

Results

Melatonin diffusion across bovine nasal mucosa

The flux of melatonin across bovine olfactory and respiratory explants in the mucosal-to-submucosal directions along with the appearance of metabolites was studied for melatonin donor concentrations ranging between 108 μM - 431 μM. The lowest melatonin donor concentration (108 μM) used for the diffusion experiments was determined by the sensitivity of the SPE-LCMS analysis to accurately detect the concentrations of melatonin, 6-hydroxymelatonin and N-acetylserotonin during the course of the permeability experiments. The limit of quantification of melatonin, 6-hydroxymelatonin, and N-acetylserotonin with the SPE-LCMS method was 5 ng/ml, 18 ng/ml, and 4 ng/ml, respectively, at a signal-to-noise ratio of ~10-12. The maximum melatonin donor concentration (431 μM) used during the permeability experiments was the saturation solubility of melatonin in the KRB at room temperature. The steady state melatonin flux across bovine respiratory and olfactory explants did not increase linearly with increasing donor melatonin concentration over this concentration range (108 μM - 431 μM) (Figure 5-2 and Figure 5-3). An apparent proportionality in melatonin flux to donor concentration between 216 μM - 431 μM suggested the saturation of melatonin metabolism in the nasal mucosa above ~ 200 μM melatonin donor concentration. The resulting concentration-dependent increase in flux is primarily due to passive diffusion of the remaining unmetabolized fraction of melatonin.

The thickness of the bovine respiratory mucosa has been observed to be ~1.6 times greater than that of the olfactory mucosa (average thickness of bovine respiratory mucosa: 0.096 cm, average thickness of bovine olfactory mucosa: 0.059 cm). To compare the magnitude of melatonin flux across bovine olfactory and respiratory explants, the flux of melatonin across the respiratory mucosa was scaled to the thickness of the olfactory mucosa, as shown in Equation 5-2.

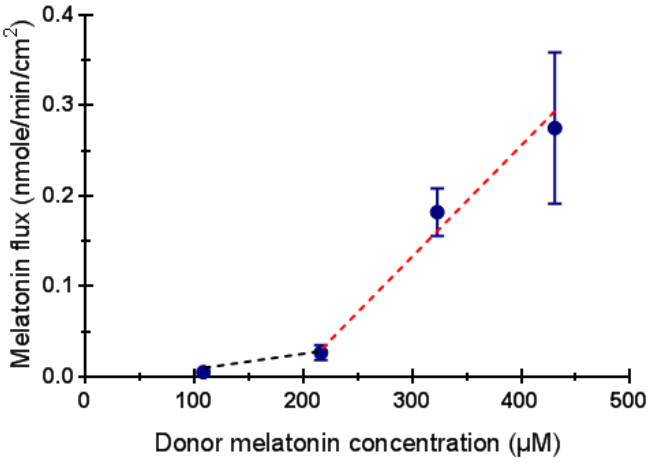

Figure 5-2 Concentration dependence of melatonin flux across bovine respiratory explants in the mucosal to submucosal (M-S) direction. Results are presented as the mean of 3 replicates ± standard deviation. Points are connected with dotted lines to highlight a change in slope of melatonin flux with increasing melatonin donor concentration.

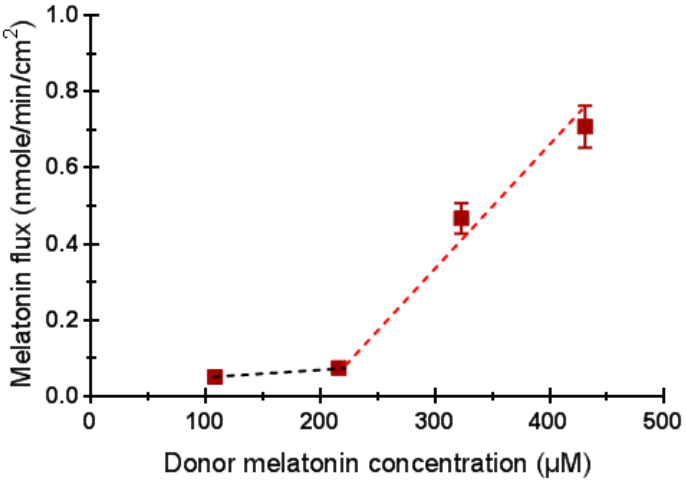

Figure 5-3 Concentration dependence of melatonin flux across bovine olfactory explants in the mucosal to submucosal (M-S) direction. Results are presented as the mean of 3 replicates ± standard deviation. Points are connected with dotted lines to highlight a change in slope of melatonin flux with increasing melatonin donor concentration.

$$\text{thickness normalized flux across respiratory mucosa} = \text{flux across the respiratory mucosa} \times 1.6 \qquad \text{Equation 5-2}$$

A comparison of the thickness normalized melatonin flux across the two tissues is shown in Figure 5-4.

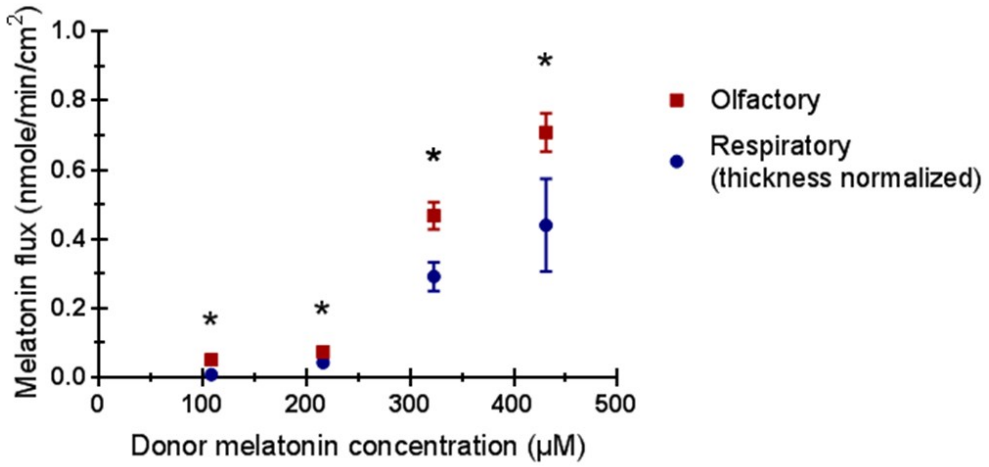

Figure 5-4 Comparison of thickness normalized flux of melatonin across bovine respiratory and olfactory explants in the mucosal to submucosal direction. Results are presented as the mean of 3 replicates ± standard deviation. * indicates statistically significant difference ($p < 0.05$) in thickness normalized flux of melatonin between bovine respiratory and olfactory explants.

Melatonin flux values across bovine nasal olfactory and respiratory explants and the thickness corrected flux values across bovine respiratory explants are summarized in Table 5-1. Following correction for differences in tissue thickness, the flux of melatonin across the olfactory explants was significantly higher than the thickness normalized flux of melatonin across the respiratory explants. This observation implies that the difference in tissue thickness was not the only factor responsible for the reduced flux of melatonin across the respiratory mucosa when compared to the flux across the olfactory mucosa.

Higher enzymatic activity in the respiratory tissues might be a significant factor responsible for the considerable reduction in the net mass transfer of unmetabolized melatonin across the respiratory explants. Histological differences (more nerves and glands in the olfactory mucosa, thicker submucosal layer in the respiratory mucosa) in the two mucosal tissues might also contribute towards the apparent differences in melatonin flux across the two mucosal explants.

Table 5-1 Melatonin flux across bovine olfactory and respiratory explants in the mucosal to submucosal direction. (n=3)

Melatonin donor concentration (μM)	Flux across bovine olfactory explants (nmole/min/cm^2) (mean ± std dev)	Flux across bovine respiratory explants (nmole/min/cm^2) (mean ± std dev)	Thickness normalized flux across bovine respiratory explants (nmole/min/cm^2) (mean ± std dev)
108	0.051 ± 0.003	0.005 ± 0.001	0.008 ± 0.002
216	0.074 ± 0.007	0.027 ± 0.009	0.043 ± 0.014
323	0.467 ± 0.040	0.182 ± 0.026	0.291 ± 0.042
431	0.708 ± 0.055	0.275 ± 0.084	0.440 ± 0.134

For simple passive diffusion of a drug governed by its concentration gradient across a membrane with no metabolic reaction, the effective permeability coefficient is independent of the drug's concentration. Comparison of effective permeability coefficients (P_e) of melatonin across bovine nasal explants (Table 5-2, Figures 5-5 and 5-6) showed an increase in apparent permeability with increasing donor melatonin concentration between 108 μM to 323 μM, however no significant difference in melatonin effective permeability values was observed at 323 μM and 431 μM donor concentrations. This apparent change in effective permeability coefficients is likely the result of enzyme saturation at high donor melatonin concentration. This results in a

constant concentration gradient for parent melatonin within the mucosal explants and thus, an increase in flux and net permeability.

Table 5-2 Melatonin effective permeability coefficients (P_e) across bovine olfactory and respiratory explants in the mucosal to submucosal direction. (n=3)

Melatonin donor concentration (μM)	P_e: Olfactory (cm/sec) (mean ± std dev)	P_e: Respiratory (cm/sec) (mean ± std dev)
108	$7.89\times10^{-6} \pm 4.82\times10^{-7}$	$8.10\times10^{-7} \pm 1.67\times10^{-7}$
216	$5.72\times10^{-6} \pm 5.37\times10^{-7}$	$2.07\times10^{-6} \pm 6.57\times10^{-7}$
323	$2.41\times10^{-5} \pm 2.04\times10^{-6}$	$9.39\times10^{-6} \pm 1.35\times10^{-6}$
431	$2.74\times10^{-5} \pm 2.13\times10^{-6}$	$1.06\times10^{-5} \pm 3.24\times10^{-6}$

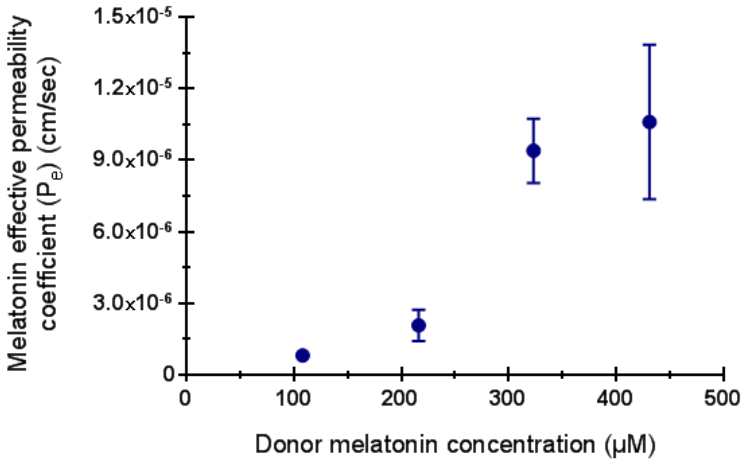

Figure 5-5 Effective permeability coefficients (P_e) for melatonin flux across bovine respiratory explants as a function of melatonin donor concentrations. Results are the mean of 3 replicates ± standard deviation.

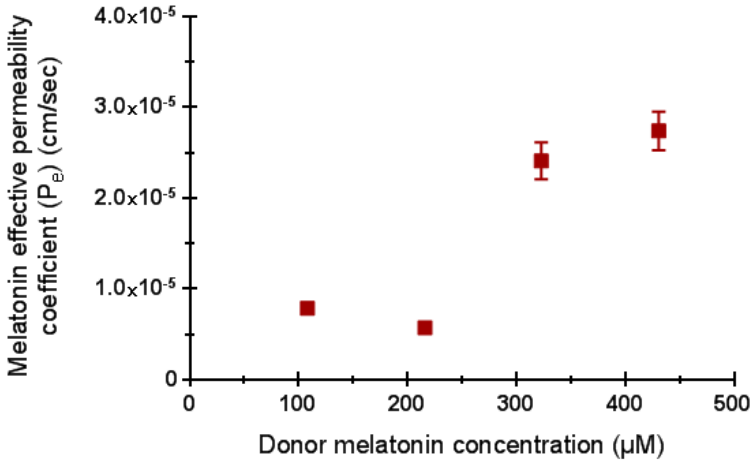

Figure 5-6 Effective permeability coefficients (P_e) for melatonin flux across bovine olfactory explants as a function of melatonin donor concentrations. Results are the mean of 3 replicates ± standard deviation.

Table 5-3 Cumulative amounts of melatonin and 6-hydroxymelatonin after 120 minute transport experiments across bovine olfactory explants. (n = 3)

Melatonin donor concentration (µM)	Melatonin (nmole) (mean ± std dev)	6-hydroxymelatonin (nmole) (mean ± std dev)
108	3.08 ± 0.57	0.78 ± 0.35
216	4.94 ± 1.07	1.32 ± 0.74
323	31.44 ± 5.90	0.98 ± 0.38
431	43.95 ± 3.03	2.26 ± 1.27

Table 5-4 Cumulative amounts of melatonin and 6-hydroxymelatonin after 120 minute transport experiments across bovine respiratory explants. (n = 3)

Melatonin donor concentration (µM)	Melatonin (nmole) (mean ± std dev)	6-hydroxymelatonin (nmole) (mean ± std dev)
108	0.28 ± 0.06	0.35 ± 0.29
216	1.31 ± 0.24	0.97 ± 0.43
323	10.63 ± 1.13	3.12 ± 0.53
431	16.49 ± 4.08	1.52 ± 1.29

The activity of bovine nasal CYP1A2 was demonstrated by the formation of 6-hydroxymelatonin, the primary metabolite of melatonin, during diffusion of melatonin across both bovine olfactory and respiratory explants. Conversion of melatonin to N-acetylserotonin was also monitored, but the cumulative amounts of N-acetylserotonin detected at the end of the 120 minute transport study using a 431 μM melatonin donor concentration were less than 0.1 nmole, indicating insignificant de-methylation of melatonin in the bovine nasal explants. Cumulative amounts of melatonin and 6-hydroxymelatonin permeated across bovine olfactory and respiratory explants are tabulated in Tables 5-3 and 5-4.

The cumulative amounts of 6-hydroxymelatonin measured during the diffusion of melatonin across bovine respiratory explants at lower donor concentrations (108 μM and 216 μM) were not significantly different from the cumulative amounts of melatonin permeated (Figure 5-7), suggesting a near 50% conversion of melatonin to 6-hydroxymelatonin during diffusion. At higher donor concentrations (323 μM and 431 μM), however, the cumulative amounts of melatonin measured were significantly higher than those of 6-hydroxymelatonin, indicating saturation of melatonin 6-hydroxylation activity and increasing flux of unmetabolized substrate. In the case of transport across bovine olfactory explants, the cumulative amounts of melatonin that permeated across the explants were greater than the amounts of 6-hydroxymelatonin quantified for all the four donor concentrations studied (Figure 5-8).

No statistically significant differences were observed in the amounts of 6-hydroxymelatonin quantified between the respiratory or the olfactory explants for the range of melatonin donor concentrations studied (Figure 5-9), except the results obtained at 323 μM donor concentration which show differences in 6-hydroxymelatonin formation between the two tissues. The observed increase in the amounts of 6-hydroxymelatonin quantified during transport experiments performed using 323 μM melatonin donor

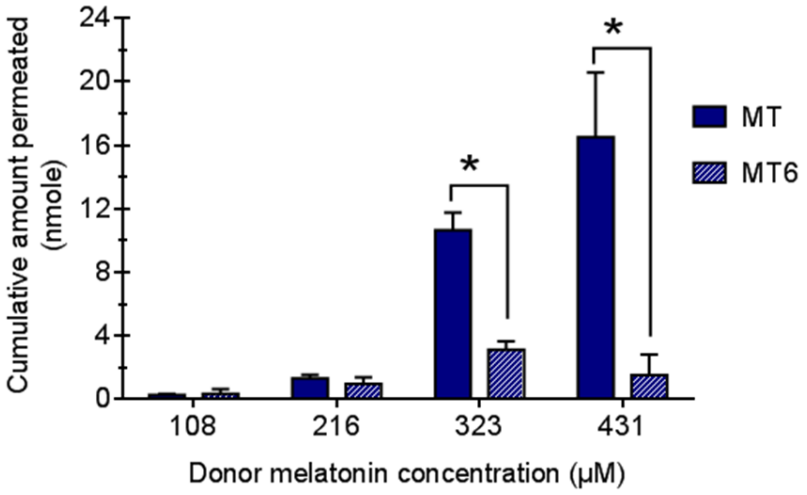

Figure 5-7 Comparison of cumulative amounts of melatonin (MT) and 6-hydroxymelatonin (MT6) in the receiver chamber following flux measurements across bovine respiratory explants at various donor melatonin concentrations after 120 minute permeability experiments. Results are the mean of 3 replicates ± standard deviation. The mean cumulative melatonin and 6-hydroxymelatonin amounts at each donor concentration were compared using an unpaired, two-tailed t-test. * indicates a statistically significant difference ($p < 0.05$) in the quantified cumulative amounts of melatonin and 6-hydroxymelatonin at each donor concentration.

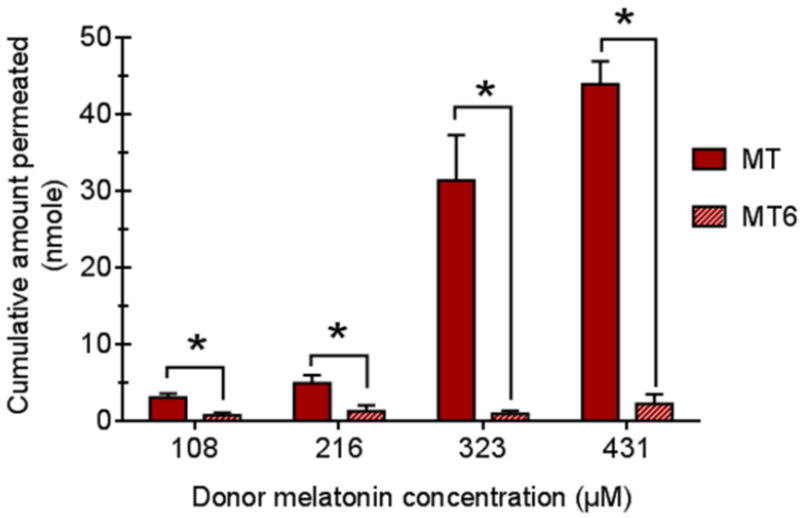

Figure 5-8 Comparison of cumulative amounts of melatonin (MT) and 6-hydroxymelatonin (MT6) in the receiver chamber following flux measurements across bovine olfactory explants at various donor melatonin concentrations after 120 minute permeability experiments. Results are the mean of 3 replicates ± standard deviation. The mean cumulative melatonin and 6-hydroxymelatonin amounts at each donor concentration were compared using an unpaired, two-tailed t-test. * indicates a statistically significant difference ($p < 0.05$) in the quantified cumulative amounts of melatonin and 6-hydroxymelatonin at each donor concentration.

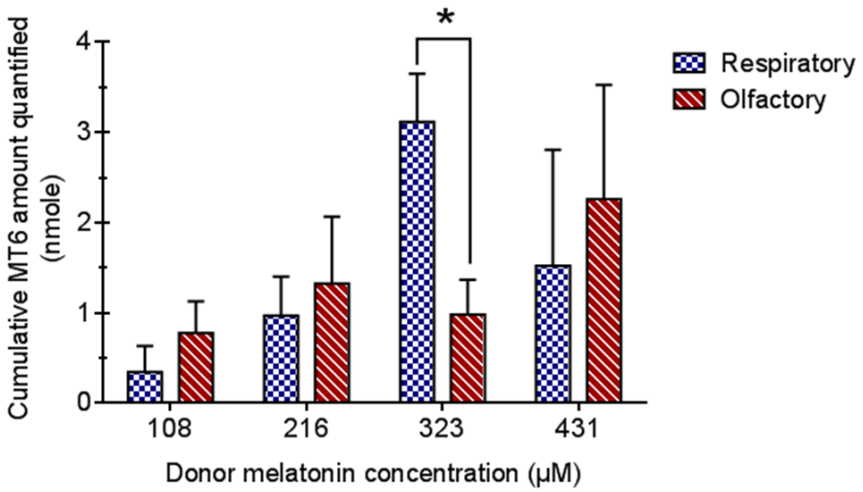

Figure 5-9 Comparison of cumulative amounts of 6-hydroxymelatonin (MT6) in the receiver chamber following flux measurements across bovine respiratory and olfactory explants at various donor melatonin concentrations after 120 minute permeability experiments. Results are the mean of 3 replicates ± standard deviation. The mean cumulative MT6 amounts measured across bovine respiratory and olfactory explants at each donor concentration were compared using an unpaired, two-tailed t-test. * indicates statistically significant difference ($p < 0.05$) in the quantified cumulative MT6 amounts between bovine respiratory and olfactory explants at 323 µM melatonin donor concentration.

concentration might be due to inter-animal differences in respiratory mucosal metabolic capacity towards melatonin 6-hydroxylation.

To compare the relative metabolic capacities of bovine respiratory and olfactory explants, the cumulative amounts of 6-hydroxymelatonin were normalized with respect to the cumulative amounts of melatonin permeated across the nasal explants at each donor concentration as shown in Equation 5-3.

$$\frac{MT6}{MT}\text{ ratio} = \frac{\text{Cumulative 6-hydroxymelatonin amount in receiver at the end of diffusion study}}{\text{Cumulative melatonin amount in receiver at the end of diffusion study}} \qquad \text{Equation 5-3}$$

The amounts of 6-hydroxymelatonin produced relative to the amounts of melatonin permeated were significantly higher for melatonin diffusion across the respiratory explants than those quantified across the olfactory explants at 216 μM and 323 μM donor concentrations (Figure 5-10). This indicates that the bovine respiratory mucosa was metabolically more active towards melatonin 6-hydroxylation than the olfactory mucosa. No significant difference in MT6/MT ratio observed at 431 μM melatonin donor concentrations further demonstrates metabolic saturation in the tissue

6-hydroxymelatonin and N-acetylserotonin diffusion across bovine nasal explants

Comparisons of 6-hydroxymelatonin and N-acetylserotonin effective permeability coefficients across bovine nasal explants are shown in Table 5-5. The permeability values of both the metabolites were expected to be lower than the flux of melatonin, as metabolism was expected to increase the hydrophilicity of melatonin metabolites, thereby lowering their flux and effective permeability coefficients across the nasal mucosa. The effective permeability coefficient value of melatonin used for this comparison was

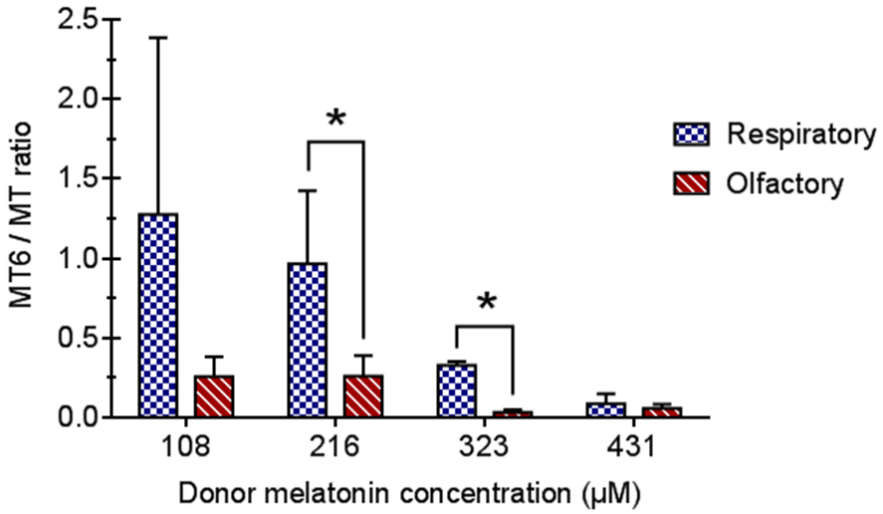

Figure 5-10 Comparison of cumulative amounts of 6-hydroxymelatonin quantified relative to the cumulative amounts of melatonin (MT6 / MT ratio, Equation 5-3) permeated across bovine respiratory or olfactory explants at various donor melatonin concentrations after 120 minute permeability experiments. Results are presented as the mean MT6/MT ratio of 3 replicates ± standard deviation. The mean MT6/MT ratio values obtained during melatonin diffusion across the two mucosal tissues were compared using an unpaired, two-tailed t-test. * indicates statistically significant difference ($p < 0.05$) in the MT6/MT ratio between bovine respiratory and olfactory explants at 216 µM and 323 µM melatonin donor concentrations.

.

obtained by averaging the permeability coefficient values obtained using 323 μM and 431 μM donor concentrations, presumably corresponding to enzyme saturation in the nasal mucosa.

Analysis of total protein and CYP1A2 enzyme content in bovine nasal explants

The amount of total proteins per unit area extracted from bovine respiratory explants was significantly higher than that extracted from the olfactory explants ($p < 0.05$) (Figure 5-11). This was expected, as the bovine respiratory mucosa contains a thicker submucosal layer than the olfactory mucosa. Thus, on a unit surface area basis, the respiratory explants contain more proteins than the olfactory explants.

A higher total protein content in the respiratory mucosa than the olfactory mucosa does not necessarily indicate a similar trend in the CYP1A2 enzyme content in these two tissues. A classical indirect ELISA was adapted for estimating the relative concentration of the CYP1A2 isoform in the olfactory and respiratory mucosal explants. Protein extracts probed with anti-CYP1A2 antibody showed that the immunoassay absorbance signal was more intense in the respiratory protein extract than the olfactory protein extract (Figure 5-12). With a semi-quantitative ELISA, a statistically significant difference in the CYP1A2 enzyme levels in these two tissues could not established. However, higher amounts of protein extracted per unit area of bovine respiratory explants coupled with a stronger CYP1A2 signal obtained in the ELISA (normalized with respect to the total protein content), suggest that bovine respiratory mucosa expresses higher levels of CYP1A2 proteins than bovine olfactory mucosa per unit area.

Table 5-5 Comparison of effective permeability coefficients (P_e) of melatonin (MT), 6-hydroxymelatonin (MT6) and N-acetylserotonin (NAS) across bovine respiratory and olfactory explants in the mucosal to submucosal direction. (n=3)

Donor solution	P_e across bovine olfactory explants (cm/sec) (mean ± std dev)	P_e across bovine respiratory explants (cm/sec) (mean ± std dev)
Melatonin	$2.57\times10^{-5} \pm 2.59\times10^{-6}$	$1.00\times10^{-5} \pm 2.32\times10^{-6}$
6-Hydroxymelatonin	$4.90\times10^{-6} \pm 1.29\times10^{-6}$	$1.68\times10^{-6} \pm 5.13\times10^{-7}$
N-acetylserotonin	$8.07\times10^{-6} \pm 5.96\times10^{-7}$	$3.86\times10^{-6} \pm 6.09\times10^{-7}$

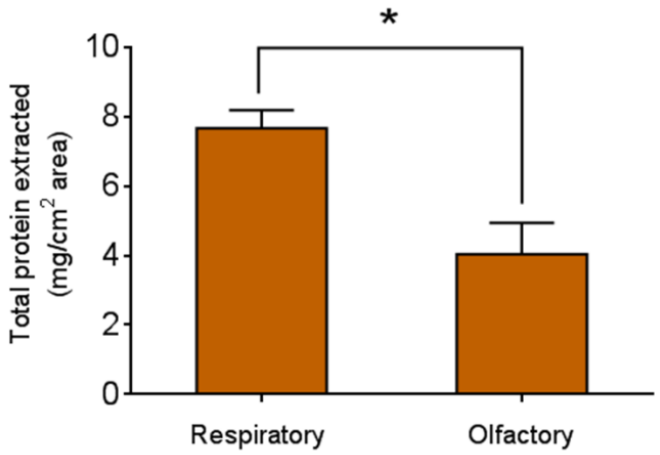

Figure 5-11 Amounts of total proteins extracted from an equivalent surface area of bovine respiratory and olfactory mucosal tissues and analyzed using the BCA assay. Results are presented as the mean of 3 replicates ± standard deviation. The mean protein values extracted from bovine respiratory and olfactory explants were compared using an unpaired, two-tailed t-test. * indicates statistically significant difference ($p < 0.05$) in the total protein quantities extracted from bovine respiratory and olfactory mucosa.

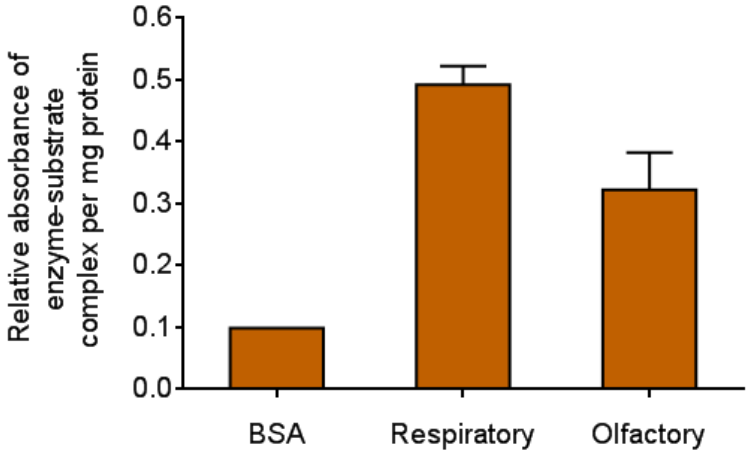

Figure 5-12 Relative CYP1A2 ELISA expression (absorbance intensity) per mg of total proteins extracted from bovine respiratory and olfactory mucosa. Bovine serum albumin (BSA) was used as the negative control.

Melatonin diffusion studies with CYP1A2 inhibition

In these experiments, fluvoxamine was used as a competitive inhibitor of CYP1A2 to investigate the effects of CYP1A2 inhibition on melatonin permeability across the nasal mucosa. Fluvoxamine has been reported to inhibit melatonin 6-hydroxylation, yielding approximately 50% inhibition at 1 μM concentration in a human liver microsomal incubation with 50 μM melatonin[129]. A comparison of melatonin flux across the bovine nasal explants with and without CYP1A2 inhibition is given in Table 5-6. CYP1A2 inhibition using fluvoxamine significantly increased the flux of melatonin across the olfactory and respiratory explants (Figure 5-13).

No difference was observed in the cumulative amounts of 6-hydroxymelatonin quantified in the receiver compartment during diffusion studies performed with or without CYP1A2 inhibition, however (Figure 5-14). A possible explanation for this could be that during diffusion studies performed with 216 μM melatonin donor concentration without CYP1A2 inhibition, the action of epithelial CYP1A2 enzymes decreases the fraction of parent melatonin reaching the submucosal region and thus, the submucosal CYP1A2 enzymes are not acting at their saturation level towards melatonin to 6-hydroxymelatonin conversion. During diffusion studies performed with fluvoxamine, the fraction of parent melatonin reaching the submucosal layer is expected to be higher than the fraction reaching during diffusion without CYP1A2 inhibition. With a higher concentration of melatonin present in the submucosal layer available to be metabolized by the submucosal CYP1A2 enzymes, there is considerable 6-hydroxymelatonin generation in spite of competitive CYP1A2 inhibition. Alternatively, no change in the cumulative amounts of 6-hydroxymelatonin quantified in the receiver compartment during diffusion studies could also be reflective of possible accumulation of 6-hydroxymelatonin in the mucosal explants limiting its appearance in the receiver chamber.

Table 5-6 Melatonin flux across bovine olfactory and respiratory explants in the mucosal to submucosal direction with and without CYP1A2 inhibition (n=3)

Donor solution	Flux across bovine olfactory explants (nmole/min/cm^2) (mean ± std dev)	Flux across bovine respiratory explants (nmole/min/cm^2) (mean ± std dev)
Melatonin (216 μM)	0.074 ± 0.007	0.027 ± 0.009
Melatonin (216 μM) + fluvoxamine (216 μM)	0.255 ± 0.046	0.114 ± 0.011

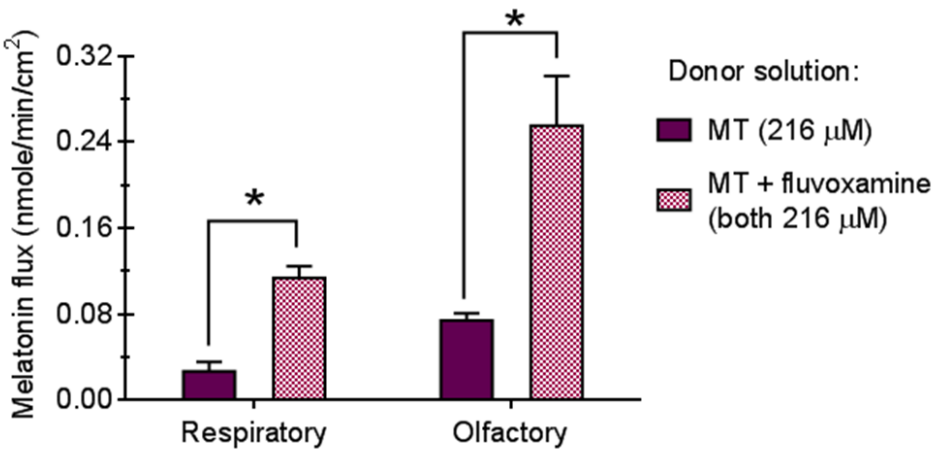

Figure 5-13 Effect of fluvoxamine, a CYP1A2 inhibitor, on melatonin transport across bovine respiratory and olfactory explants in the mucosal-to-submucosal direction after 120 minute permeability experiments. Results are presented as the mean of 3 replicates ± standard deviation. Unpaired, two-tailed t-test was performed to compare the mean flux values with or without CYP1A2 inhibition. * indicates statistically significant increase ($p < 0.05$) in melatonin flux following CYP1A2 inhibition across bovine respiratory and olfactory mucosae.

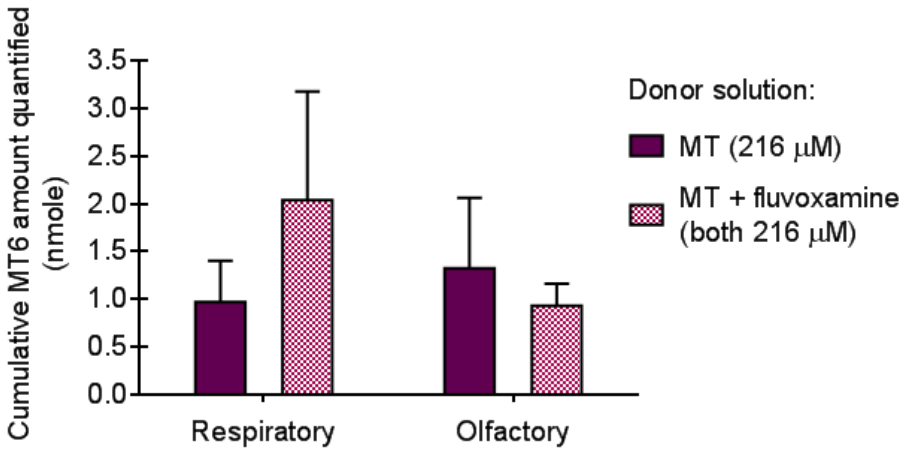

Figure 5-14 Effect of fluvoxamine, a CYP1A2 inhibitor, on cumulative amounts of 6-hydroxymelatonin (MT6) quantified across bovine respiratory and olfactory explants after 120 minute permeability experiments. Results are presented as the mean of 3 replicates ± standard deviation. The mean cumulative 6-hydroxymelatonin values with or without CYP1A2 inhibition were compared using unpaired, two-tailed t-test. No statistically significant difference in the amounts of 6-hydroxymelatonin quantified with or without CYP1A2 inhibition was observed during melatonin diffusion across both bovine respiratory and olfactory mucosa.

When scaled with respect to the cumulative amounts of parent melatonin permeated across the nasal explants (Equation 5-3), the relative reduction in MT6/MT ratio with CYP1A2 inhibition during diffusion across both the olfactory and respiratory explants was more obvious (Figure 5-15).

The decrease in MT6/MT ratio following CYP1A2 inhibition using fluvoxamine was approximately 3 fold for diffusion across the respiratory explants and approximately 5 fold for diffusion across the olfactory explants. The respiratory mucosa is thicker and contains a higher population of enzymes, thus concentration of fluvoxamine available within the tissue to compete with melatonin for CYP1A2 enzymatic activity is expected to be lower in the respiratory explants than the olfactory explants. This would reduce the MT6/MT fold change in the respiratory explants by reducing both total melatonin permeated due to the increased tissue thickness and increase the 6-hydroxymelatonin produced due to lower tissue concentration of the inhibitor.

Melatonin diffusion studies with de-epithelized nasal explants

The effectiveness of the de-epithelization treatment on bovine olfactory and respiratory mucosal explants was confirmed with brightfield microscopy. As seen in the hematoxylin and eosin stained images (Figure 5-16 and 5-17), the epithelial layer was completely removed after a 30 minute treatment with laureth-9 followed by a 30 minute treatment with trypsin-EDTA. As seen in Figure 5-18, the flux of melatonin across the respiratory and olfactory explants was not significantly altered after de-epithelization (Table 5-7). This result was unusual, as the removal of epithelial layer and loss of the epithelial CYP1A2 enzymatic activity was expected to result in a significant increase in melatonin flux across the de-epithelized explants.

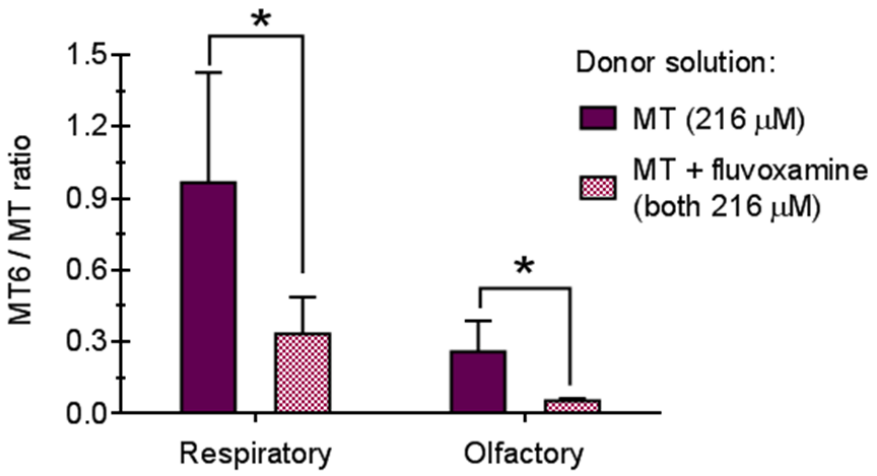

Figure 5-15 Effect of fluvoxamine, a CYP1A2 inhibitor, on the cumulative amounts of 6-hydroxymelatonin relative to the cumulative amounts of melatonin permeated (MT6/MT ratio, Equation 5-3) permeated across bovine respiratory and olfactory explants after 120 minute permeability experiments. Results are presented as the mean MT6/MT ratio of 3 replicates ± standard deviation. The mean MT6/MT ratios obtained during melatonin diffusion with or without CYP1A2 inhibition across the two mucosal tissues were compared using unpaired, two-tailed t-test. * indicates statistically significant decrease ($p < 0.05$) in MT6/MT ratio following CYP1A2 inhibition across both bovine respiratory and olfactory mucosa.

The significant activity of submucosal CYP1A2 was clearly demonstrated by the appearance of 6-hydroxymelatonin during melatonin diffusion across these de-epithelized nasal explants. Both bovine olfactory and respiratory submucosal regions exhibited significant CYP1A2-mediated melatonin 6-hydroxylation, thus confirming the role of the submucosal region in contributing to the metabolic barrier properties of the nasal mucosa.

As seen in Figure 5-19, when the amounts of 6-hydroxymelatonin permeated were expressed relative to the amounts of parent melatonin permeated (MT6/MT ratio), a significant reduction in MT6/MT ratio was observed following de-epithelization of bovine respiratory mucosa.

Discussion

Passive diffusion across a permeable membrane is characterized by concentration independence of permeability coefficients. Apparent increase in the effective permeability coefficient values obtained during melatonin diffusion studies with increasing melatonin donor concentration is likely the result of enzyme saturation in the presence of high substrate (unmetabolized melatonin) concentrations within the mucosal tissues. The extent of melatonin metabolism during diffusion at lower melatonin donor concentrations showed a significant fraction of the parent compound lost due to metabolism, resulting in a significant reduction in net mass transfer of unmetabolized melatonin across the nasal mucosa. The identification of 6-hydroxymelatonin formed during the diffusion studies correlated well with our immunohistochemistry and PCR results, which confirmed that CYP1A2 coding genes and proteins were expressed in the bovine nasal mucosa. The bovine respiratory mucosa, being approximately 1.6-times thicker than the olfactory mucosa, transported lower amounts of melatonin across the mucosal explants than the olfactory mucosa; yet the amounts of the primary metabolite quantified during melatonin diffusion across bovine respiratory and olfactory explants were comparable. These observations suggest a lower CYP1A2-mediated enzymatic

Table 5-7 Calculated melatonin flux across full thickness and de-epithelized bovine olfactory and respiratory explants in the mucosal to submucosal direction at 323 μM donor melatonin concentration (n=3)

Tissue	Flux across bovine olfactory explants (nmole/min/cm^2) (mean ± std dev)	Flux across bovine respiratory explants (nmole/min/cm^2) (mean ± std dev)
Full thickness	0.467 ± 0.040	0.182 ± 0.026
De-epithelized	0.595 ± 0.167	0.267 ± 0.067

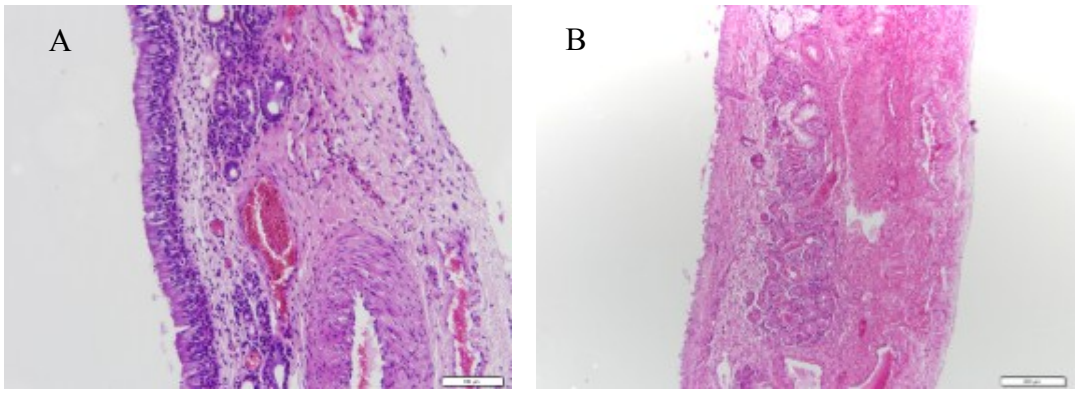

Figure 5-16 Effectiveness of de-epithelization treatment on bovine respiratory explants using 1% laureth-9 and 0.5% trypsin - 0.2% EDTA solution (30 minute incubation each). Scale bar: 200 µm. Section thickness: 5 µm.

(A): Brightfield image of a formalin fixed, paraffin embedded, and hematoxylin and eosin stained bovine respiratory explants containing the epithelial layer.

(B) Brightfield image of a formalin fixed, paraffin embedded, and hematoxylin and eosin stained bovine respiratory explants treated with laureth-9 and trypsin-EDTA solutions.

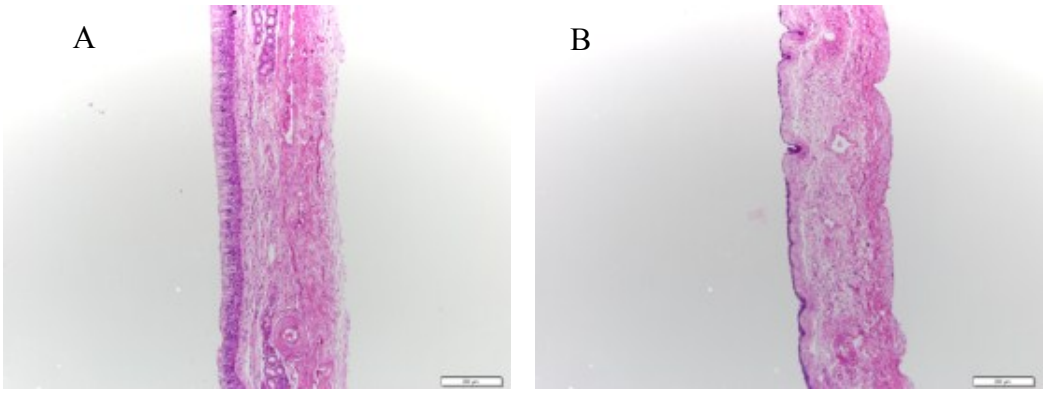

Figure 5-17 Effectiveness of de-epithelization treatment on bovine olfactory explants using 1% laureth-9 and 0.5% trypsin - 0.2% EDTA solutions (30 minute incubation each). Scale bar: 200 µm. Section thickness: 5 µm.

(A): Brightfield image of a formalin fixed, paraffin embedded, and hematoxylin and eosin stained bovine olfactory explants containing the epithelial layer.

(B) Brightfield image of a formalin fixed, paraffin embedded, and hematoxylin and eosin stained bovine olfactory explants treated with laureth-9 and trypsin-EDTA solutions.

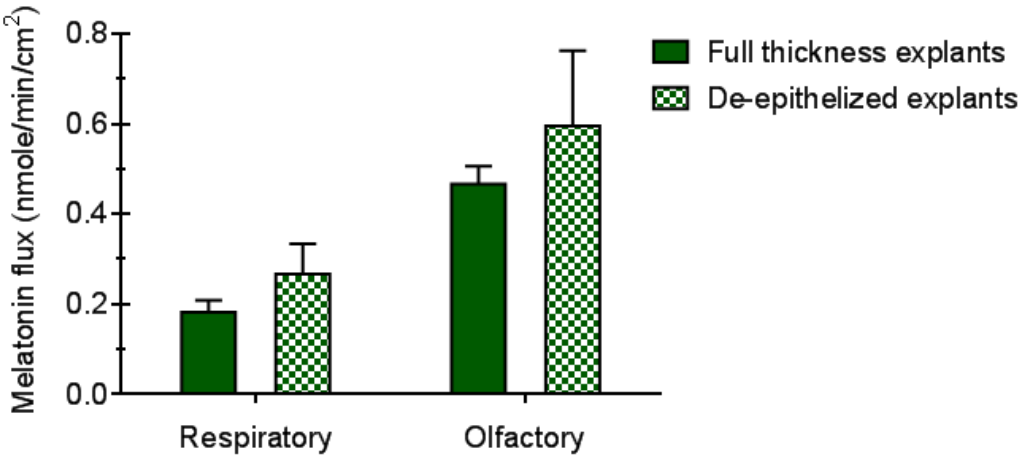

Figure 5-18 Effect of de-epithelization on melatonin transport across bovine respiratory and olfactory explants in the mucosal-to-submucosal direction at 323 µM donor melatonin concentration after 120 minute permeability experiments. Results are presented as the mean of 3 replicates ± standard deviation. Unpaired two tailed t-test was performed to compare the mean flux values across full thickness and de-epithelized bovine nasal explants. No statistically significant difference in melatonin flux was observed following de-epithelization of bovine respiratory or olfactory mucosa.

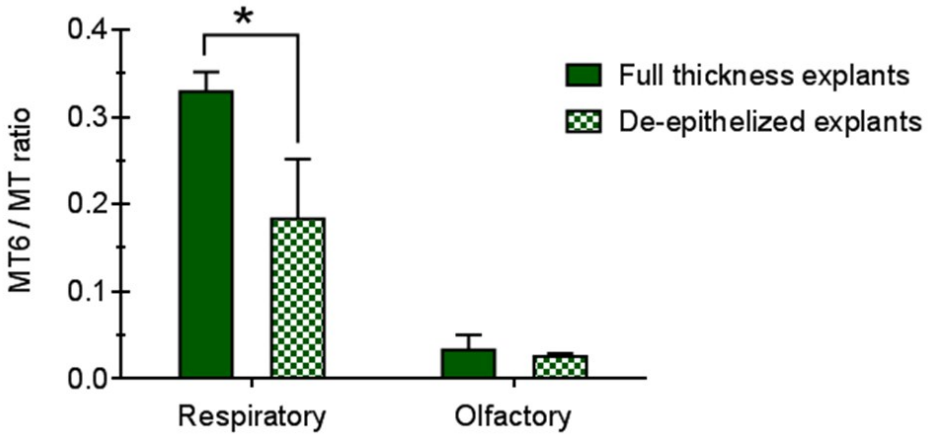

Figure 5-19 Confirmation of CYP1A2-mediated enzymatic activity of bovine respiratory and olfactory submucosal layers: effect of de-epithelization on the cumulative amounts of 6-hydroxymelatonin relative to the cumulative amounts of melatonin (MT6/MT ratio, Equation 5-3) permeated across bovine respiratory and olfactory explants at 323 μM donor melatonin concentration after 120 minute permeability experiments. Results are presented as the mean MT6/MT ratio of 3 replicates ± standard deviation. Unpaired, two-tailed t-test was used to compare the mean MT6/MT ratios obtained during melatonin diffusion with or without de-epithelization the two mucosal tissues. * indicates statistically significant decrease ($p < 0.05$) in MT6/MT ratio following de-epithelization of bovine respiratory mucosa.

activity in the bovine olfactory mucosa than for the respiratory mucosa. The ELISA results indicated higher CYP1A2 protein expression per mg of total proteins extracted from bovine respiratory mucosa, and this correlated well with the observation that the bovine respiratory explants exhibited higher melatonin 6-hydroxylation capacity than bovine olfactory mucosa. These results are in good agreement with our microsomal melatonin diffusion results which showed that the maximum melatonin 6-hydroxylation velocity (V_{max}) of bovine respiratory microsomes was significantly higher than that of bovine olfactory microsomes.

In our experiments, fluvoxamine was used as a competitive inhibitor of CYP1A2 to investigate the effects of CYP1A2 inhibition on melatonin permeability across the nasal mucosa. The classical CYP1A2 inhibitors used in most metabolism assays are caffeine and theophylline. However, melatonin, being a potent substrate for CYP1A2, strongly competes with other CYP1A2 substrates, rendering them ineffective competitive inhibitors. Caffeine and theophylline (200 μM each) have been reported to result in less than 30% inhibition of melatonin 6-hydroxylation at 50 μM melatonin concentration during *in vitro* incubations with human liver microsomes[129]. Other *in vivo* studies have demonstrated that a single dose of the selective serotonin re-uptake inhibitor fluvoxamine increased serum melatonin concentrations significantly, but this effect was not seen with the intake of other SSRIs including paroxetin or citalopram[133,228,229]. Fluvoxamine undergoes CYP1A2 mediated metabolism to form an O-demethylated metabolite[230] (Figure 5-20). It was determined that fluvoxamine, being a substrate for CYP1A2, was able to compete with melatonin for phase I metabolism, thereby increasing the serum levels of the later. Facciola et al. reported that efficient inhibition of melatonin 6-hydroxylation can be achieved with furafylline and fluvoxamine. Their studies confirmed that fluvoxamine was a potent inhibitor of 6-hydroxymelatonin formation, giving approximately 50% inhibition at 1 μM concentration in human liver microsomal

incubation with 50 μM melatonin[129]. It exhibits good lipophilicity (logP of 2.89)[231], and its MDRI-MDCKII cell monolayer permeability is reported to be 3.2×10^{-7} cm/s[232].

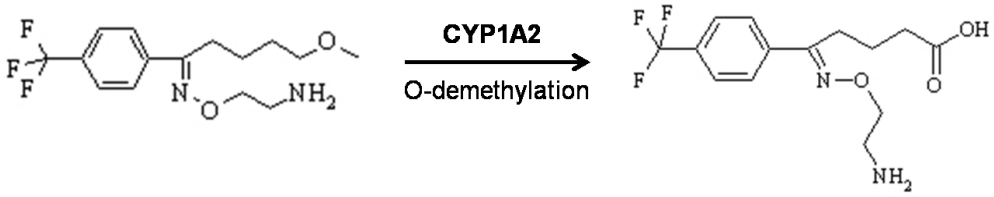

Fluvoxamine **Fluvoxamine acid**

Figure 5-20 CYP1A2 mediated O-demethylation of fluvoxamine to fluvoxamine acid[228]

The results of CYP1A2 inhibition during melatonin diffusion studies suggests that CYP1A2-mediated metabolism significantly reduced the flux of melatonin across the bovine respiratory and olfactory mucosa and the net mass transfer of melatonin across the mucosal tissues could be significantly improved by inclusion of a potent and selective CYP1A2 inhibitor.

Traditionally, nasal enzymatic activity is considered to limited to the epithelial region of the nasal mucosa[54,60,62,67,197,233,234]. Our enzyme immunohistochemistry results have demonstrated that CYP1A2 protein to be located in the epithelial region as well as in the submucosal glandular region of the bovine nasal respiratory and olfactory mucosa (Figures 3-9 to 3-10). The role of the submucosal CYP1A2 enzymes during melatonin transfer across the nasal explants was investigated in de-epithelized tissues. To shorten the duration of de-epithelization, the mucosal explants were pre-treated with laureth-9 for the initial 30 minutes. Polyoxyethylene-9-1auryl ether (laureth-9) has been reported to cause severe degeneration of the nasal epithelium at a concentration of 1%[235]. Incubation with laureth-9 followed by subsequent incubation with trypsin-EDTA shortened the

de-epithelization treatment time period to one hour. The confirmed viability and activity of the submucosal CYP1A2 enzymes was demonstrated by the appearance of 6-hydroxymelatonin during diffusion of melatonin across both the bovine respiratory and olfactory explants.

In summary, affirmation of melatonin 6-hydroxylation during diffusion experiments performed with bovine nasal olfactory and respiratory (full-thickness as well as de-epithelized) explants confirmed that the drug molecule encounters metabolic barriers in the epithelial layer as well in the submucosal region during its transport across the nasal mucosa into the systemic circulation. Both permeability and microsomal studies demonstrated a higher activity of the bovine respiratory mucosa towards melatonin metabolism than that of the bovine olfactory mucosa. The respiratory mucosa covers greater than 90% of the total surface area of human nasal cavity. The higher metabolic capacity of respiratory CYP1A2 enzymes towards melatonin metabolism could translate into significant metabolic loss of melatonin after intranasal administration. Thus, the role of nasal epithelial and submucosal enzymes in limiting the nasal bioavailability of melatonin needs to be carefully investigated, and particular attention need to be paid to ensure the permeability of metabolic inhibitors across the epithelium into the submucosal region, where a significant fraction of nasal CYP450 isoforms are located.

CHAPTER 6
SIMULATION OF PASSIVE DIFFUSION AND CONCURRENT ENZYMATIC METABOLISM OF DRUGS ACROSS THE NASAL MUCOSA

Introduction

Multiple metabolic barriers may be encountered by a drug molecule administered intranasally prior to its transfer to the systemic circulation, thus reducing the net drug transfer into the systemic circulation. As a result, flux of an intact substrate penetrating the nasal mucosa is influenced by both mass transport and metabolism parameters. Evaluation of melatonin permeability across bovine nasal olfactory and respiratory explants demonstrated that melatonin was metabolized to 6-hydroxymelatonin during its diffusion across the nasal mucosa. In order to examine diffusion and concurrent metabolism of drugs across the nasal mucosa, we developed a kinetic model evaluating the extent of degradation that a drug molecule undergoes as it diffuses across the layers of the nasal mucosa. The model was used to predict the *in vitro* transport of melatonin, 6-hydroxymelatonin, and N-acetylserotonin across bovine nasal olfactory and respiratory explants, which was experimentally measured and described in Chapter 5. For the purpose of this model development, we focused on passive transcellular diffusion of drugs undergoing saturable intracellular enzymatic metabolism. The model can also be expanded to incorporate other transport pathways mediating drug permeation across the nasal mucosa.

Mechanisms of membrane diffusion have been described in the pharmaceutical literature to elucidate the physical, anatomical, and physiological factors that influence molecular transport processes across bio-membranes[236–241]. Initial biophysical models examining flux and metabolism were based on Fickian diffusion coupled with first-order degradation kinetics of drug substrates[242–244]. Although it can be argued that first-order

enzymatic reaction kinetics accurately describes degradation rates for low substrate concentrations, a more complex treatment of metabolism was necessary for the higher substrate concentrations used in drug formulations permeating across a viable membrane exhibiting saturable enzymatic activity. A preliminary approach to model steady-state membrane diffusion with Michaelis-Menten metabolism was provided by Fox et al. using an *in vitro* diffusion system for a prodrug undergoing enzymatic cleavage to the active drug, followed by further metabolism to inactive metabolites during transport through the skin[245]. These investigators used a 'shooting method' to solve the non-linear, boundary-value differential equations aided by a computer algorithm to numerically generate steady-state prodrug, drug, and metabolite concentration profiles in the dermis layer of the skin. Guy et al. and Sugibayashi et al. investigated *in vitro* cutaneous absorption of drugs by combining flux governed by Fick's laws and metabolism described using Michaelis-Menten kinetics and solving the resultant differential equations using Laplace's transforms[246,247]. Effects of various factors (partition coefficient, diffusion coefficient, extent of metabolism, enzyme distribution) on membrane diffusion and concurrent metabolic degradation of drugs following transdermal or buccal administration have been extensively examined by many researchers[248–252].

When compared to other alternative sites of drug administration, such as buccal or transdermal, kinetic analysis of drug absorption from the nasal cavity raises some additional concerns. Anatomically, the nasal cavity consists of multiple regions with variable disposition and permeability characteristics (Figure 1-1)[12,18]. The kinetics of deposition and disposition of inhaled vapors, solutions, and other nasally administered dosage forms is an extensive area of research and many investigators have developed mathematical models to evaluate the rate processes involved in the clearance of drugs and formulations from various regions in the nasal cavity[253–256].

Absorption of drugs from the nasal cavity into the systemic circulation occurs primarily in the nasal turbinate regions, also referred to as the respiratory (inferior and middle turbinates) and olfactory mucosal regions (superior turbinate). These sites possess an absorptive epithelial layer and a highly vascular submucosal layer[17,19]. Biotransformation of a metabolically-labile substrate can occur during transfer across the metabolically active cell layers within the nasal mucosa, however significantly reducing its net flux and bioavailability. In this project, we report an *in vitro* simulation model to study passive diffusion of drugs in combination with saturable enzymatic metabolism within the nasal mucosa. The primary objective was to estimate the effect of metabolism on limiting the net mass transfer of drugs across the nasal mucosa into the systemic circulation.

Theoretical

Bovine nasal mucosal explants were used as *in vitro* models for nasal permeability studies. The bovine nasal mucosa can be divided into a number of diffusional barriers connected in series, as shown schematically in Figure 6-1.

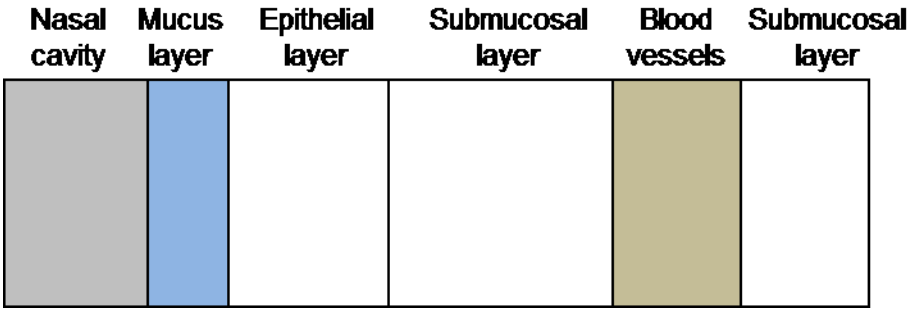

Figure 6-1 Barriers encountered during the transport of drugs across the nasal mucosa into the systemic circulation. The systemic circulation is modeled as a distinct compartment within the submucosal layer.

Drugs administered into the nasal cavity need to first diffuse through an aqueous-like mucus layer. The effective thickness of the mucus layer is influenced by the rate of secretion of mucus by the goblet glands and the hydrodynamic conditions imposed by ciliary activity on the respiratory epithelial surface. The partitioning of the drug substance at the mucus/nasal epithelial interface is followed by diffusion through the pseudostratified columnar epithelial layer via transcellular and paracellular pathways. This is followed by partitioning into the submucosal layer and diffusion through the cellular and connective tissue matrix. These layers represent the major volume of the nasal mucosa. Partitioning into the endothelial cells of the submucosal blood vessels marks the entry of the drug into the systemic circulation.

In a typical diffusion experiment, a segment of excised bovine nasal olfactory or respiratory mucosa is mounted between the donor (D) and receiver (R) compartments of the diffusion chamber. A schematic representation of the *in vitro* diffusion-metabolism model is given in Figure 6-2.

Consider a nasal explant of thickness h. It can be anatomically divided into an apical epithelial layer (thickness h_E) and an underlying submucosal layer (thickness h_S). Position x = 0 represents the epithelial-submucosal interface. At the donor-tissue interface ($x = -h_E$), the tissue is in contact with a well-stirred donor solution of a defined substrate concentration ($C_{S,D}$) through a defined cross-sectional area, denoted by A. At the tissue-receiver interface ($x = h_S$), the tissue is in contact with a well-stirred buffer solution, initially containing no drug. The drug partitions into the epithelial layer and travels across the mucosal layer by passive diffusion. During passage across the metabolically active tissue, degradation of substrate (S) to one or more metabolites (M) can occur. Based on the concentration gradient and the permeability parameters of the metabolites, after formation they can diffuse into the donor or the receiver compartments.

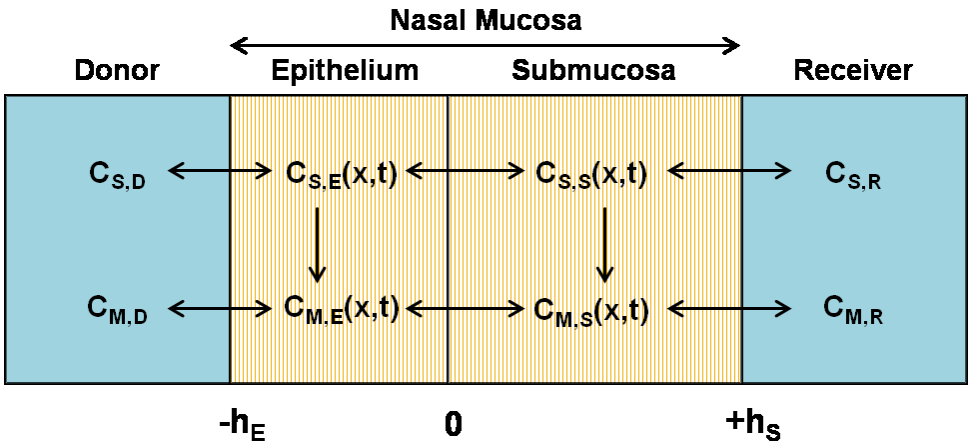

Figure 6-2 Schematic diagram of an *in vitro* diffusion experiment across the nasal mucosa. Term C_S represents the concentration of the substrate, and C_M represents the concentration of the metabolite. Subscripts D, E, S and R correspond to the donor chamber, epithelial layer, submucosal layer, and the receiver chamber respectively. The thickness of the mucosal tissue is divided into h_E, epithelial layer thickness, and h_S, submucosal layer thickness.

Assumptions

The following assumptions were made:

1. Diffusion occurs by transcellular passive diffusion only.
2. Mass transport is one-dimensional and restricted to the x-coordinate with constant diffusivity in each layer of the tissue.
3. Metabolism occurs in the tissue only (in the epithelial and submucosal regions) and follows Michaelis-Menten kinetics.
4. Diffusion in the unstirred water layer (aqueous boundary layer, ABL) was not considered as a contribution to the overall diffusional resistance.
5. A constant dose condition is assumed for the substrate in the donor compartment, which means that the donor concentration of substrate is constant throughout the duration of the experiment.
6. Perfect sink conditions are assumed in the receiver compartment for both the substrate and metabolite concentrations.

Diffusive transport

According to Fick's First Law, the flux (J_S) of a substrate (S) at concentration (C_S) across a membrane of unit area, in a predefined plane, is proportional to the concentration gradient across that plane (dC_S/dx) with the diffusion coefficient (D_S) being a proportionality constant[226]. This can be mathematically expressed as shown in Equation 6-1.

$$J_S = - D_S \frac{dC_S}{dx} \qquad \text{Equation 6-1}$$

Where J_S is the flux of substrate in mucosal-to-submucosal direction, D_S is the diffusion coefficient of substrate across the nasal mucosa, C_S is the concentration of substrate, and x is the distance within the mucosal explants.

Changes in concentration of the substrate (C_S) in the tissue as a function of time t and distance x can be given by Fick's Second Law[226]:

$$\frac{dC_S}{dt} = D_S \frac{d^2C_S}{dx^2} \qquad \text{Equation 6-2}$$

Fick's second law (Equation 6-2) was used in the model to calculate the concentration gradient of the substrate and metabolites within the nasal mucosa at any given time t.

Enzymatic degradation governed by

Michaelis-Menten kinetics

The Michaelis-Menten enzymatic reaction kinetics assumes that the enzyme (E) combines reversibly with the substrate (S) in a relatively fast reaction to form an enzyme-substrate complex (ES), which then undergoes a relatively slow breakdown to the enzyme and product (P)[225].

$$E + S \underset{k_{-1}}{\overset{k_1}{\rightleftharpoons}} ES \overset{k_2}{\rightleftharpoons} E + P \qquad \text{Equation 6-3}$$

The key assumption in Michaelis-Menten kinetics is that the initial substrate concentration is much greater than the total enzyme concentration in the tissue (quasi-steady state assumption). Thus, the concentration of the substrate-bound enzyme complex ([ES]) changes much more slowly than that of the product ([P]) or the substrate ([S]).

The rate of the reaction for the degradation of the substrate into the metabolite can be given by[225]:

$$V = \frac{V_{max} \times C_S}{K_M + C_S} \qquad \text{Equation 6-4}$$

Where V is the apparent rate of the enzymatic reaction, V_{max} is the maximum rate of the reaction, C_S is concentration of substrate, and K_M is the Michaelis constant. The Michaelis-Menten enzymatic reaction rate equation (Equation 6-4) was used in the model to calculate the rate of substrate degradation and metabolite generation within the tissue at any given time t.

Diffusion with enzymatic degradation

Combining Fickian diffusion (Equation 6-2) and Michaelis-Menten biotransformation (Equation 6-4), changes in the concentration of substrate (C_S) in the tissue as a function of time t can be expressed by the partial differential equation:

$$\frac{dC_S}{dt} = D_S \frac{d^2C_S}{dx^2} - \frac{V_{max} \times C_S}{K_M + C_S} \qquad \text{Equation 6-5}$$

Assuming a 1:1 molar conversion of substrate to metabolite, the rate of change of metabolite concentration within the tissue as a function of time can be described by Equation 6-6.

$$\frac{dC_M}{dt} = D_M \frac{d^2C_M}{dx^2} + \frac{V_{max} \times C_S}{K_M + C_S} \qquad \text{Equation 6-6}$$

Where D_M is the metabolite diffusion coefficient across the nasal mucosa and C_M is the metabolite concentration within the tissue.

The concentration gradients of substrate and metabolite within the nasal mucosa at any time (t) can be numerically generated by solving Equations 6-5 and 6-6, respectively. The method of lines[257] was used to solve these differential equations. A spatial grid was defined by discretizing the partial differential equations with respect to distance within the mucosal explants, as shown schematically in Figure 6-3.

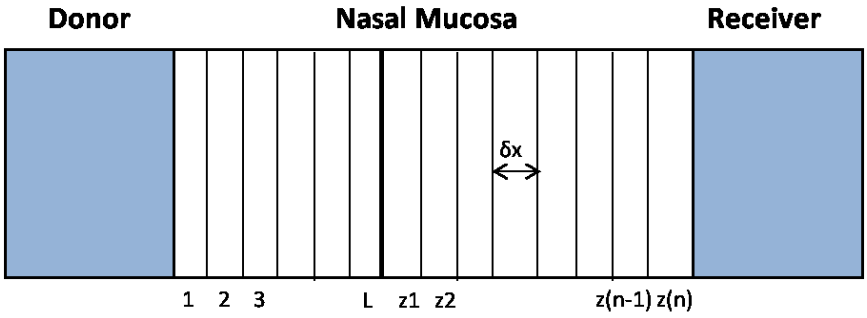

Figure 6-3 Schematic representation of the space grid used for discretization of the partial differential equation in the model. The full thickness mucosa was divided into a total of N discrete space elements, comprised of L epithelial boxes, and z(n) submucosal boxes, each of length δx (cm).

The full-thickness mucosal tissue was divided into N number of discrete space elements, called “boxes”, with δx being the thickness of each box. The length of the epithelial layer was divided into ‘1 to L’ (total L) boxes, whereas the length of the submucosal layer was divided into ‘z(1) to z(n)’ (total n) boxes as shown in Figure 6-3.

The total number of boxes used in the simulation was kept constant at 128, such that the total number of boxes in the full thickness mucosa (N) was equal to the sum of epithelial boxes (L) and submucosal boxes (n). The number of epithelial boxes (L) was calculated by dividing the thickness of the epithelial layer (h_E) by the thickness of each box (δx), and rounding up the number to the next integer. The procedure for measuring the thickness of the epithelial and the submucosal layer is described in the experimental section. The number of submucosal boxes (n) was calculated by subtracting the number of epithelial boxes (L) from the total number of boxes (N=128). The concentration of the substrate and metabolite within the tissue was expressed as $C_S(x_i,t)$, namely the substrate concentration in the i^{th} box at time t; or $C_M(x_i,t)$, namely the metabolite concentration in the i^{th} box at time t.

The first-order differential (dC/dx) can be replaced by a central difference[258] as shown in Equation 6-7.

$$\frac{dC(x,t)}{dx} = \frac{C\,(x_{i+1},t) - C(x_{i-1},t)}{2\delta x} \qquad \text{Equation 6-7}$$

The second-order differential for change in concentration with respect to time can also be replaced by a central difference[258] as shown in Equation 6-8.

$$\frac{d^2C(x_i,t)}{dx^2} = \frac{1}{\delta x^2}[C(x_{i+1},t) - 2C(x_i,t) + C(x_{i-1},t)]$$

$$\text{for boxes } 2 \le i \le (L-1) \text{ and } z(2) \le i \le z(n-1) \qquad \text{Equation 6-8}$$

The rate of change of substrate and metabolite with respect to time can now be expressed as a series of ordinary differential equations using the method of lines[257] as shown in Equation 6-9 and Equation 6-10, respectively.

$$\frac{dC_S(x_i,t)}{dt} = \frac{D_S}{\delta x^2}[C_S(x_{i+1},t) - 2C_S(x_i,t) + C_S(x_{i-1},t)] - \frac{V_{max} \times C_S(x_i,t)}{K_M + C_S(x_i,t)}$$

for boxes $2 \le i \le (L-1)$ and $z(2) \le i \le z(n-1)$ Equation 6-9

$$\frac{dC_M(x_i,t)}{dt} = \frac{D_M}{\delta x^2}[C_M(x_{i+1},t) - 2C_M(x_i,t) + C_M(x_{i-1},t)] + \frac{V_{max} \times C_s(x_i,t)}{K_M + C_s(x_i,t)}$$

for boxes $2 \le i \le (L-1)$ and $z(2) \le i \le z(n-1)$ Equation 6-10

Identification of boundary conditions

Donor-epithelial boundary

At time = 0, the tissue is free of any drug or metabolites. Hence, the initial condition can be expressed as:

$$C_S(x,0) = C_M(x,0) = 0 \quad \text{at time } 0$$ Equation 6-11

The first epithelial box (box 1 at $x = -h_E$) is in direct contact with the donor solution over a cross-sectional area A. Assuming partitioning equilibrium between the donor solution and the first epithelial box, the substrate concentration in the first epithelial box is the substrate concentration in the donor compartment $C_{S,D}$, multiplied by the apparent tissue/buffer partition coefficient for the substrate (PC_S).

$$C_S(1,t) = PC_S \times C_{S,D}$$ Equation 6-12

However, partitioning of the drug from the donor compartment into the epithelial layer might not be an instantaneous process. If a drug's chemical properties limit its instantaneous partitioning into the tissue at the start of diffusion experiments (t=0) owing to the interfacial barrier between the donor solution and the epithelial layer (this can also

account for the aqueous boundary layer), the time lag for partitioning of the drug into the first epithelial box needs to be accounted for in the model. Here, we introduce a factor α_S_{DE} at $x = -h_E$ (factor α for substrate (S) at the donor (D) – epithelial (E) interface) to account for a delay in the partitioning of the substrate into the epithelial layer from the donor compartment owing to an interfacial barrier between the two layers. The boundary condition for partitioning of the substrate from donor compartment into the epithelial layer can now be modified as shown in Equation 6-13. This indicates that at partition equilibrium (when substrate concentration in the first box is equal to the substrate concentration in the donor compartment, $C_{S,D}$, multiplied by the apparent tissue/buffer partition coefficient for the substrate, PC_S), the substrate concentration in the first epithelial box has reached its steady state; the rate of change in substrate concentration in the first epithelial box with time is zero.

$$D_S \frac{dC_S(1,t)}{dx} + \alpha\_S_{DE}\left(C_{S,D} - \frac{C_S(1,t)}{PC_S}\right) = 0 \text{ at } x = -h_E \qquad \text{Equation 6-13}$$

The term α_S_{DE} decides the lag-time to reach partition equilibrium for the substrate from the donor compartment into the first epithelial box at $x = -h_E$. At a high α_S_{DE} value, partition equilibrium between the donor compartment and the first epithelial box is instantaneous. As the α_S_{DE} value gets smaller, there is more resistance at the boundary to partition equilibrium.

Rearranging Equation 6-13, we obtain:

$$D_S \frac{dC_S(1,t)}{dx} = -\alpha\_S_{DE}\left(C_{S,D} - \frac{C_S(1,t)}{PC_S}\right) \text{ at } x = -h_E$$

For our simulation model, the first box is designated as "1", the second box is designated as "2", and so on. The concentration of substrate in the first box at time t is $C_S(1,t)$. The concentration of substrate in the second box at time t is $C_S(2,t)$. We need to define the value for dC_S/dx for entry of substrate from donor compartment into the first box. To obtain that value, a fictitious box was introduced in the donor compartment (box "-1"), such that the substrate concentration in this fictitious box can now be denoted as $C_S(-1,t)$.

The first order differential for the rate of change of substrate concentration with distance in the first box can be replaced by a central difference (Equation 6-14).

$$\frac{dC_S(1,t)}{dx} = \frac{C_S(2,t) - C_S(-1,t)}{2\delta x} \qquad \text{Equation 6-14}$$

The boundary condition can be used to solve for the fictitious concentration of substrate in box -1.

$$\frac{C_S(2,t) - C_S(-1,t)}{2\delta x} = - \frac{\alpha\_S_{DE}}{D_S} \left(C_{S,D} - \frac{C_S(1,t)}{PC}\right) \qquad \text{Equation 6-15}$$

$$C_S(-1,t) = C_S(2,t) + \frac{\alpha\_S_{DE} 2\,\delta x}{D_S} \left(C_{S,D} - \frac{C_S(1,t)}{PC}\right) \qquad \text{Equation 6-16}$$

The rate of change of substrate concentration with time in the first epithelial box can be written using Equation 6-5.

$$\frac{dC_S(1,t)}{dt} = D_S \frac{d^2C_S(1,t)}{dx^2} - V_1 \qquad \text{Equation 6-17}$$

Where V_1 is for the rate of enzymatic reaction in the first box.

The second-order differential in Equation 6-17 can be replaced by a central difference[258] as shown in Equation 6-18.

$$\frac{dC_S(1,t)}{dt} = D_S \frac{C_S(2,t) - 2C_S(1,t) + C_S(-1,t)}{\delta x^2} - V_1 \qquad \text{Equation 6-18}$$

Substituting the value of fictitious concentration of substrate in box -1 ($C_S(-1,t)$) from Equation 6-16 into Equation 6-18, we obtain:

$$\frac{dC_S(1,t)}{dt} = D_S \frac{C_S(2,t) - 2C_S(1,t) + \frac{\alpha\_S_{DE}\, 2\,\delta x}{D_S}\left(C_{S,D} - \frac{C_S(1,t)}{PC_s}\right) + C_S(2,t)}{\delta x^2} - V_1$$

Equation 6-19

$$\frac{dC_S(1,t)}{dt} = D_S \frac{2(C_S(2,t) - C_S(1,t)) + \frac{\alpha\_S_{DE}\, 2\,\delta x}{D_S}\left(C_{S,D} - \frac{C_S(1,t)}{PC_s}\right)}{\delta x^2} - V_1 \qquad \text{Equation 6-20}$$

$$\frac{dC_S(1,t)}{dt} = \frac{2D_S}{\delta x^2}\left[(C_S(2,t) - C_S(1,t)) + \alpha\_S_{DE}\frac{\delta x}{D_S}\left(C_{S,D} - \frac{C_S(1,t)}{PC_S}\right)\right] - V_1 \qquad \text{Equation 6-21}$$

Equation 6-21 gives the boundary condition for partitioning of the substrate from the donor compartment into the first epithelial box.

Along similar lines, the boundary condition for the back-flux of metabolite from the first epithelial box ($x = -h_E$) into the donor compartment can be written as shown in Equation 6-22.

$$\frac{dC_M(1,t)}{dt} = \frac{2D_M}{\delta x^2}\left[(C_M(2,t) - C_M(1,t)) - \beta\_M_{ED}\frac{\delta x}{D_M}\left(C_{M,D} - \frac{C_M(1,t)}{PC_M}\right)\right] + V_1$$

Equation 6-22

Where β_M_{ED} is the factor accounting for the interfacial barrier to partitioning of the metabolite from the epithelial layer into the donor compartment. The derivation for Equation 6-22 is given in Appendix B.

Epithelial-submucosal boundary

The interior boundary between the epithelial and submucosal layers can be evaluated to take into account the epithelial-submucosal partition coefficients of the drug and the metabolites. The treatment of the epithelial-submucosal boundary condition is given in Appendix B.

For these simulations, the epithelial-to-submucosal partition coefficient of the substrate and the metabolite was assumed to be unity, due to lack of availability of sufficient information about the partitioning behavior of drugs in these two tissue layers. The model was developed to take into account the partitioning and diffusivity differences of the substrate and the metabolite in the epithelial and submucosal regions to enable better prediction of drug transport across the nasal mucosa if such information is available.

Submucosal-receiver boundary

Partitioning of the substrate or metabolite at the boundary between the last submucosal box (box z(n)) and the receiver compartment can be treated similarly. The derived boundary equations for partitioning of the substrate and metabolite from the submucosal layer into the receiver compartment ($x = h_S$) are expressed as Equations 6-23 and Equation 6-24, respectively. The related derivations for obtaining the boundary conditions are given in Appendix B.

For the substrate:

$$\frac{dC_S(z(n),t)}{dt} = \frac{2D_S}{\delta x^2}\left[(C_S(z(n-1),t) - C_S(z(n),t)) - \alpha\_S_{SR}\frac{\delta x}{D_S}\left(\frac{C_S(z(n),t)}{PC_s} - C_{S,R}\right)\right] - V_{z(n)}$$

Equation 6-23

Where, α_S_{SR} is the factor accounting for the interfacial barrier against partitioning of the substrate from the submucosal layer into the receiver compartment.

For the metabolite:

$$\frac{dC_M(z(n),t)}{dt} = \frac{2D_M}{\delta x^2}\left[(C_M(z(n-1),t) - C_M(z(n),t)) - \alpha\_M_{SR}\frac{\delta x}{D_M}\left(\frac{C_M(z(n),t)}{PC_M} - C_{M,R}\right)\right] + V_{z(n)}$$

Equation 6-24

Where α_M_{SR} is the factor accounting for the interfacial barrier against partitioning of the metabolite from the submucosal layer into the receiver compartment.

The model was developed to account for the partitioning and contact resistance to partitioning of the substrate and the metabolite at each interface, namely the donor-epithelial interface and the submucosal-receiver interface. However, while performing simulations and optimization routines for the current project, partitioning at each interface was assumed to be instantaneous.

Calculation of flux and amounts permeated across the nasal mucosa

The flux of the substrate and metabolite into the receiver compartment were calculated using Equation 6-25 and Equation 6-26, respectively, at the submucosal-receiver interface:

$$J_{S,R} = -D_S \left.\frac{dC_S(z(n),t)}{dx}\right|_{x = h_S}$$

Equation 6-25

$$J_{M,R} = -D_M \left. \frac{dC_M(z(n),t)}{dx} \right|_{x = h_S} \qquad \text{Equation 6-26}$$

Where, $J_{S,R}$ is the flux of the substrate into the receiver compartment and $J_{M,R}$ is the flux of the metabolite into the receiver compartment.

The cumulative amounts of the substrate ($Q_{S,R}$) and the metabolite ($Q_{M,R}$) permeated across the mucosal explants into the receiver chamber in time, t, were then calculated by the using Equation 6-27 and Equation 6-28 respectively.

$$Q_{S,R}(t) = -A\, D_S \int_0^t \left. \frac{dC_S(z(n),t)}{dx} \right|_{x = h_S} dt \qquad \text{Equation 6-27}$$

$$Q_{M,R}(t) = -A\, D_M \int_0^t \left. \frac{dC_M(z(n),t)}{dx} \right|_{x = h_S} dt \qquad \text{Equation 6-28}$$

Distribution of CYP450 enzymes in the nasal mucosa

Many previously reported diffusion-metabolism models have assumed homogeneous distribution of drug metabolizing enzymes within the tissue of interest[239,248]. However, the nasal olfactory and respiratory mucosal tissues exhibit distinct differences in enzyme expression within the different regions. Our immunohistochemistry results have shown that the distribution of CYP450 enzymes within the nasal mucosa is not entirely homogeneous (Chapter 3). CYP450 enzyme immunohistochemical analyses performed on bovine nasal olfactory and respiratory explants demonstrated that the apical epithelial layer exhibits a strong, uniform CYP450 immunoreactivity. However, in the submucosal layer, the immunoreactive signal was

scattered. Intense immunoreactivity was observed in the middle glandular section, whereas little to no immunofluorescence signal was detected in the lamina propria and basal connective tissue layers. To simulate this enzyme localization pattern, the value of the V_{max} parameter was altered by position in the nasal mucosa (Figure 6-4). The enzyme distribution was assumed to be homogeneous in the epithelial layer, and a constant V_{max} value was assigned for each of the epithelial boxes in the model. For the submucosal layer, a Gaussian distribution was used with a mean V_{max} at the mid-point of the submucosal layer and a standard deviation appropriate to retain 90% of the area under the V_{max}-distance curve in the middle one-third region of the submucosal layer. The representative distribution of V_{max} within bovine nasal epithelial and submucosal layers is given in Figure 6-4. The Gaussian distribution mimicked the observed CYP450 protein localization patterns, where the maximum localization was observed in the middle region within glandular cells of the submucosal layer, and the immunoreactivity gradually diminished on either side.

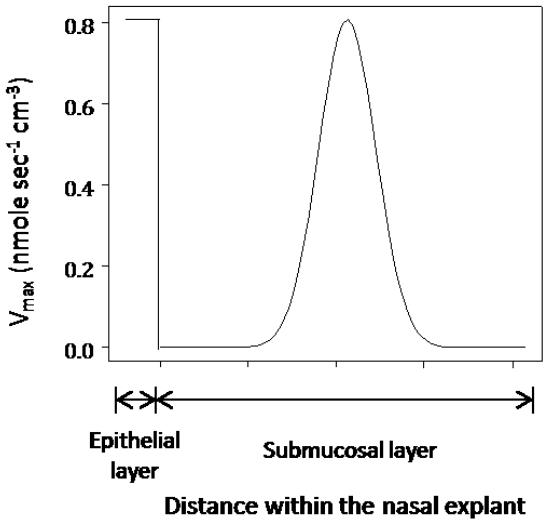

Figure 6-4 Proposed distribution of V_{max} values with respect to distance within bovine mucosal epithelial and submucosal regions.

Experimental analysis of diffusion of melatonin, 6-hydroxymelatonin, and N-acetylserotonin across bovine nasal explants

In the present study, melatonin was used as a model drug to examine nasal CYP450-mediated enzymatic activity and its effects on melatonin flux across bovine nasal explants. The procedure for studying *in vitro* diffusion and metabolism of melatonin is described in Chapter 5. Diffusion experiments were also performed with either 6-hydroxymelatonin or N-acetylserotonin in the donor chamber to study flux and net mass transfer of these two compounds with no apparent metabolism within the mucosal tissues.

The thickness values of the bovine respiratory and olfactory epithelia, as well as the submucosal layers were measured by examining formalin-fixed, paraffin-embedded, hematoxylin and eosin stained bovine olfactory and respiratory mucosal sections with an Olympus BX-51 light microscope (Olympus America Inc, Center Valley, PA) equipped with a DP-71 digital camera. The thickness was measured using ImageJ software[180,181] (U.S. National Institutes of Health, Bethesda, MD). The mean of 10 measurements on separate sections was taken as the average thickness value for the epithelial and submucosal layers.

Numerical computations

The experimentally determined melatonin flux and the appearance of 6-hydroxymelatonin were used to probe the ability of our model to estimate the net mass transfer and metabolism of melatonin across the nasal mucosa. The experimentally obtained effective permeability values for melatonin, 6-hydroxymelatonin, or N-acetylserotonin across bovine nasal olfactory or respiratory explants (Chapter 5) were used in the model as fixed parameters. For melatonin diffusion and concurrent metabolism to 6-hydroxymelatonin, the values of V_{max} and K_M were optimized within the

model to best describe the experimental results. The cumulative amounts of substrate and metabolite in the receiver compartment were calculated using Equations 6-28 and 6-29 respectively, and were compared with the experimentally measured amounts in the receiver chamber at each sampling time point.

Numerical simulations and non-linear regressions were performed using the R Software Environment for Statistical Computing and Graphics, version 2.14.1[259]. The FME[260] package built in R was used for performing theoretical simulations, and weighted least squares regression was used to fit experimental data for melatonin, 6-hydroxymelatonin and N-acetylserotonin diffusion. The R package, deSolve[261], was used to solve the differential equations using the LSODA solver with relative and absolute tolerances set at 10^{-8} and the maximum number of steps per output interval set at 10000.

Since 6-hydroxymelatonin and N-acetylserotonin undergo minimal metabolic transformations, the model predictions for 6-hydroxymelatonin (substrate) and N-acetylserotonin (substrate) diffusion across the bovine respiratory and olfactory explants were optimized using the Port optimization algorithm assuming no metabolic degradation during diffusion. For evaluating melatonin diffusion and simultaneous metabolism to 6-hydroxymelatonin, weighted least squares regression was used to fit the model predictions to the experimentally measured cumulative amounts of melatonin (substrate) and 6-hydroxymelatonin (metabolite) quantified during diffusion. Weighting of $1/y_{obs}$ was used for all data points (substrate (j= 1) or metabolite (j = 2)), as shown in Equation 6-29.

$$\text{weight}_{(j,t)} = \frac{1}{\text{Experimentally measured cumulative amount of substrate or metabolite permeated at time t } (y_{obs(j,t)})} \qquad \text{Equation 6-29}$$

The weighted residuals (wRes) for the substrate (j = 1) or metabolite (j = 2) at time = t were calculated as shown in Equation 6-30.

$$wRes_{(j,t)} = \left[\text{amount measured } \left(y_{obs\ (j,t)}\right) - \text{amount predicted } (y_{pred(j,t)})\right] \times weight_{(j,t)}$$

Equation 6-30

The optimization routine was set to minimize the sum of the squared, weighted residuals (SSwR) for the substrate (j= 1) or metabolite (j = 2) amount predictions at each time point of measurement for each melatonin donor concentration.

$$SSwR = \sum_{j=1}^{2} \sum_{t=1}^{\text{total time points}} \left(wRes_{(i,t)}\right)^2$$

Equation 6-31

Finally, the simulation and optimization output was exported to comma separated value (csv) files (Microsoft Office 2010, Microsoft Corp., Redmond, WA) and plotted using GraphPad Prism version 6.00 for Windows (GraphPad Software Inc., La Jolla, CA). The values and ranges of fixed and variable parameters used for simulation and optimization routines are given in Tables 6-1 to 6-4.

Table 6-1 Fixed and variable parameter values used for simulations and optimization routines (part 1)

Parameter	Unit	Initial estimate	Range	Comments
h_E	cm	Resp: 0.011 Olf: 0.008	Fixed	Thickness of epithelial layer, measured microscopically. (Resp: respiratory, Olf: olfactory)
h_S	cm	Resp: 0.085 Olf: 0.051	Variable Resp: 0.077-0.094 Olf: 0.046-0.056	Thickness of submucosal layer, measured microscopically. (Resp: respiratory, Olf: olfactory)
A	cm^2	0.64	Fixed	Cross-sectional area for diffusion, diffusion cell dimensions.
V_{max}	nmol cm^{-3} sec^{-1}	0.5	Variable 0.1-5.0	Max velocity for metabolite formation, value optimized using simulations. (Fixed value for the epithelial layer, Gaussian distribution for the submucosal layer)
K_M_E	nmol cm^{-3}	Resp: 135 Olf: 90	Fixed	K_M, Michaelis-Menten constant for the epithelial layer, melatonin microsomal metabolism value. (Resp: respiratory, Olf: olfactory)
K_M_S	nmol cm^{-3}	Resp: 135 Olf: 90	Fixed	K_M, Michaelis-Menten constant for the submucosal layer, melatonin microsomal metabolism value. (Resp: respiratory, Olf: olfactory)

Table 6-2 Parameter values used for simulations and optimization (part 2)

Parameter	Initial estimate	Range	Unit	Comments
f	1	Fixed		Scale factor for the mean V_{max} in the submucosal layer with respect to V_{max} in epithelial layer, assuming maximum metabolic activity in the submucosal layer is equal to the maximum metabolic activity in the epithelial layer.
μ (mu)	Resp: 0.0425 Olf: 0.0255	Fixed	cm	Mean of the V_{max} normal distribution (location of the maximum V_{max}: center of the submucosal layer) (Resp: respiratory, Olf: olfactory)
σ (sigma)	0.0065	Fixed	cm	Standard deviation of V_{max} normal distribution, to generate a normal V_{max} distribution in the submucosal layer.

Table 6-3 Effective permeability coefficient (P_e) and maximum metabolic velocity (V_{max}) values used for theoretical simulations based on experimentally determined values and permeability range reported in Chapter 5.

Range	Effective permeability (P_e) (cm/sec)	Maximum metabolic rate (V_{max}) (nmole $cm^{-3}.sec^{-1}$)
Low	P1: 2.5×10^{-6}	V1: 0.25
Medium	P2: 5×10^{-6}	V2: 0.5
High	P3: 10×10^{-6}	V3: 1

Table 6-4 Initial estimates and ranges of parameters representing the physicochemical properties of the compounds used during optimization of the model predictions to fit the experimental diffusion data

Parameter	Unit	Initial estimate ± range	Comments
Melatonin (MT)			
logPC		1.04 ± 0.80	Initial estimate: octanol-water partition coefficient
P_e_Resp	cm/sec	1.00×10^{-5} ± 2.32×10^{-6}	Experimentally determined from *in vitro* diffusion experiments: the plateau mean ± standard deviation of P_e values at donor concentrations of 323 μM and 416 μM
P_e_Olf	cm/sec	2.57×10^{-5} ± 2.59×10^{-6}	
6-Hydroxymelatonin (MT6)			
logPC		0.91 ± 0.80	Initial estimate: octanol-water partition coefficient
P_e_Resp	cm/sec	1.68×10^{-6} ± 5.13×10^{-7}	Experimentally determined from *in vitro* diffusion experiments: the mean ± standard deviation of P_e values at donor concentration = 201 μM
P_e_Olf	cm/sec	4.90×10^{-6} ± 1.29×10^{-6}	
N-acetylserotonin (NAS)			
logPC		0.27 ± 0.80	Initial estimate: octanol-water partition coefficient
P_e_Resp	cm/sec	3.86×10^{-6} ± 6.09×10^{-7}	Experimentally determined from *in vitro* diffusion experiments: the mean ± standard deviation of P_e values at donor concentration = 229 μM
P_e_Olf	cm/sec	8.07×10^{-6} ± 5.96×10^{-7}	

Results and discussion

Influence of kinetic parameters on substrate mass transfer across the nasal mucosa

This model was developed for the evaluation of *in vitro*, metabolism-limited, mass transport of drugs across nasal mucosal explants where the nasal mucosa is anatomically viewed as two distinct diffusional barriers connected in series, namely the epithelial and submucosal layers. The primary goal was to understand the relative contributions of drug permeability and metabolic susceptibility on net drug mass transfer across the mucosal explants. The simulation results for cumulative amounts of drug permeated across the bovine nasal mucosal explants for selected diffusion and metabolism parameters are summarized in Figures 6-5 to 6-9. Figure 6-5 demonstrates the effects of changes in effective permeability coefficient on drug diffusion across bovine respiratory mucosa for both metabolically susceptible and non-susceptible drugs. As seen from the curves, as little as a 2- to 4- fold difference in effective permeability coefficient notably altered the cumulative amounts of un-metabolized drug permeating across the nasal explants, and the effect was evident at both high and low levels of metabolism of the parent drug. It can thus be inferred that irrespective of metabolic susceptibility of the drug or the enzymatic activity within the nasal mucosa, the effective permeability coefficient of drugs strongly affects the net mass transfer across the nasal mucosa into the systemic circulation. The effective permeability coefficient of a drug takes into account the effects of its diffusion coefficient (D), partition coefficient (PC) and the membrane thickness (h) on the net mass transfer.

$$P_e = D\frac{PC}{h} \qquad \text{Equation 6-32}$$

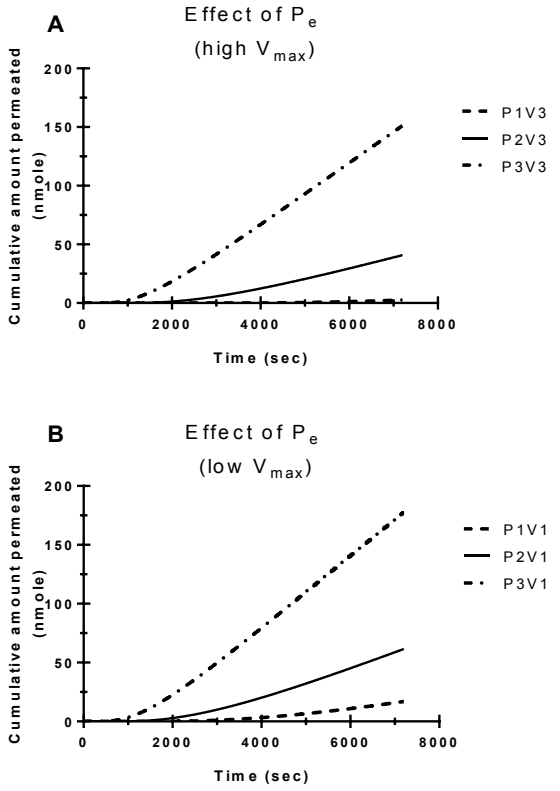

Figure 6-5 Effect of changes in effective permeability coefficients on flux of metabolically susceptible (A, high V_{max}) and non-susceptible (B, low V_{max}) drugs. The effective permeability (P_e) and V_{max} values used for these simulations are listed in Table 6-3.

A high partition coefficient corresponds to favorable tissue partitioning, thus yielding higher drug concentrations at position $x = -h_E$ in the epithelial layer, than that in the donor compartment or on the external mucosal surface. This effectively increases the input and concentration gradient of a drug across the nasal mucosa. Higher drug concentrations in the epithelial layer could lead to saturation of the epithelial enzymatic activity thereby reducing the impact of metabolic degradation and increasing the net flux of drugs across the mucosal explants. Highly diffusible drugs travel faster across the mucosal cell layers, and have a shorter retention time in the nasal mucosa. In addition, for highly permeable drugs, even if the concentration gradient in the tissue is reduced due to

enzymatic degradation, the drug's inherent partitioning and diffusive properties result in a constant influx of the substrate from the donor compartment into the tissue. Representative concentration-distance profiles for metabolically-susceptible drug substrates exhibiting high or low permeability across the nasal explants are demonstrated in Figure 6-6.

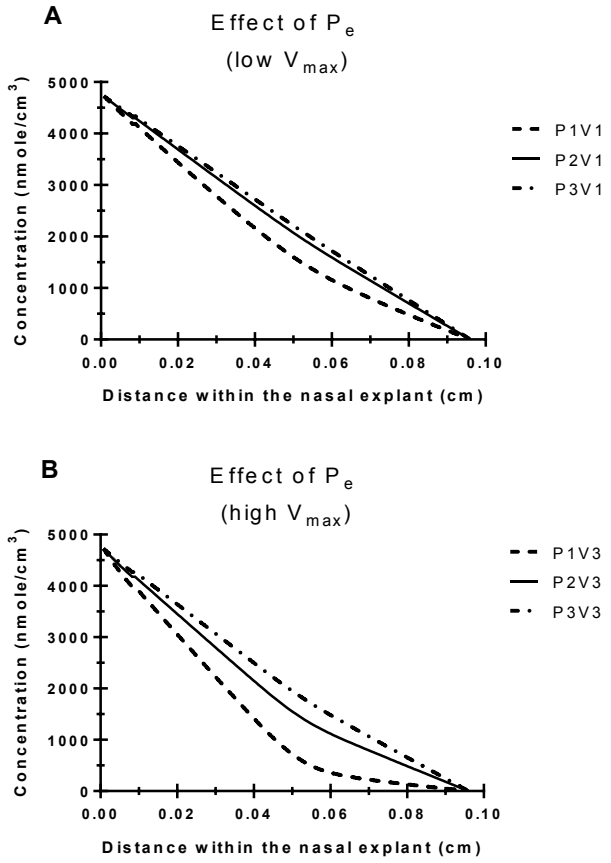

Figure 6-6 Representative steady state concentration-distance profiles within the nasal tissues demonstrating the effect of changes in effective permeability coefficient on the concentration gradient of substrates undergoing metabolism in the nasal mucosa. At a constant V_{max}, the steady state profile for substrates with high P_e (A) is nearly linear, whereas the profile for a substrate with low P_e (B) is non-linear. The effective permeability (P_e) and V_{max} values used for simulations are listed in Table 6-3.

At a constant V_{max} value, drugs with high permeability exhibit an almost linear concentration gradient across the nasal explants. In contrast, for simulations depicting diffusion of a drug exhibiting low permeability, the effective steady-state concentration gradient was observed to be non-linear, indicating the effect of metabolism in reducing the net mass transfer across the nasal mucosa into the systemic circulation. Figure 6-7 shows the effects of a 2- or 4- fold changes in V_{max} on net transfer of drugs exhibiting high or low permeability across the nasal mucosa.

It can be inferred that for drugs exhibiting relatively high permeability across bovine respiratory explants (P_e equivalent to 10^{-5} cm/sec), apparent changes in V_{max} values did not influence the net mass transfer across the nasal mucosa. The significance of enzymatic degradation in limiting the mass transport of drugs was more pronounced in the case of poorly diffusible substrates. The effect of metabolism in reducing the concentration gradient of substrates across the nasal mucosa was more evident from the concentration-distance profiles simulated for substrates with a range of permeability and metabolism characteristics (Figure 6-8).

Figure 6-8 (A) shows that for highly permeable compounds, a linear concentration-distance profile is obtained within the tissue for a range of V_{max} values. Consequently, the flux of highly permeable compounds is not affected by the metabolic activity within the tissue. However, for compounds exhibiting low permeability across the nasal mucosa (Figure 6-8, B) the concentration-distance profiles at steady state for moderate-to-high levels of metabolism were non-linear, suggesting a reduction in flux and net mass transfer across the nasal mucosa. It can be concluded that enzymatic degradation decreases the concentration gradient and limits the transport of drugs across the nasal mucosa. However, its relative contribution as a mass transport barrier is significantly reduced for highly permeable/ high partitioning drugs.

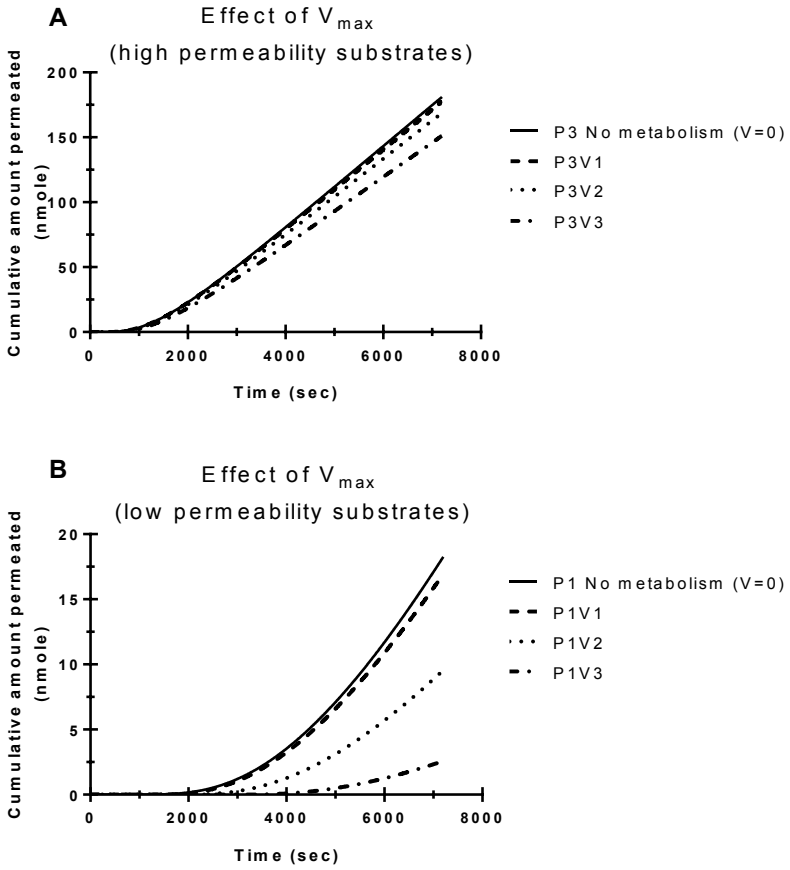

Figure 6-7 Effect of changes in maximum metabolism rate (V_{max}) on diffusion of drugs with high (A) or low (B) permeability coefficients across the nasal mucosa. The effective permeability (P_e) and V_{max} values used for simulations are listed in Table 6-3.

Differences in the morphology and total thickness of the bovine respiratory and olfactory mucosa contribute to significant differences in the net mass transfer of drugs across the different nasal regions. The thickness of the respiratory epithelium was measured as 0.096 cm, while the thickness of the olfactory epithelium was measured as 0.059 cm. The bovine olfactory mucosa also possesses more submucosal glandular cells than does the respiratory mucosa. While simulating the net mass transfer across the olfactory and respiratory mucosa, the thickness was set to the measured thickness of the tissue, and a V_{max} distribution was set to match the enzyme distribution within the nasal mucosa, as shown in Figure 6-4. Figure 6-9 demonstrates the effect of the thickness differences between these two tissues on the net mass transfer of a poorly permeable ($P_e = 2.5 \times 10^{-6}$ cm/sec) drug across bovine olfactory and respiratory mucosa with high levels of metabolic degradation rate. The transit time of compounds within the mucosal explants is longer during diffusion across the respiratory mucosa owing to its greater thickness than the olfactory mucosa, thus, the net mass transfer across the respiratory mucosa is lower than that across the olfactory mucosa over equal time intervals.

Comparison of model predictions to experimental data

To validate the ability of the simulation model to predict net substrate and metabolite mass transfer across the nasal mucosa, the model predictions for the diffusion of melatonin, 6-hydroxymelatonin and N-acetylserotonin across bovine respiratory and olfactory mucosa were compared with the experimental data obtained during *in vitro* diffusion experiments. The transport of 6-hydroxymelatonin and N-acetylserotonin across bovine nasal olfactory and respiratory explants was modeled assuming passive Fickian diffusion with no metabolic reaction ($V_{max} = 0$). The simulations were performed using the experimentally determined values of effective permeability. The optimized parameter values obtained from fitting the permeation experiment data for N-acetylserotonin

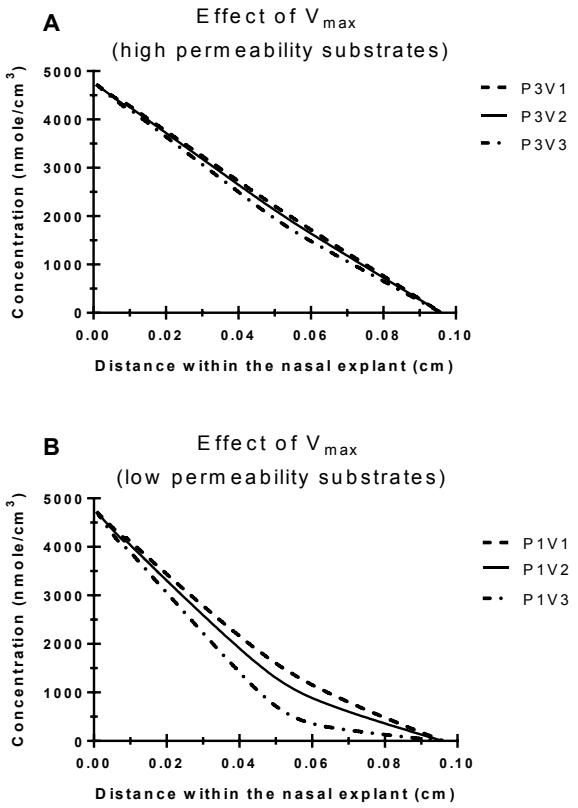

Figure 6-8 Representative steady state concentration-distance profiles within the nasal tissues demonstrating the effect of changes in maximum metabolism rate (V_{max}) on the concentration gradient of substrates undergoing metabolism in the nasal mucosa. Changes in V_{max} have negligible effect on the substrate concentration gradient within the tissue for highly permeable compounds (A).The effect of V_{max} in lowering the concentration gradient of the substrate in the nasal mucosa is more pronounced for drugs with low permeability across the nasal mucosa (B). The effective permeability (P_e) and V_{max} values used for simulations are listed in Table 6-3.

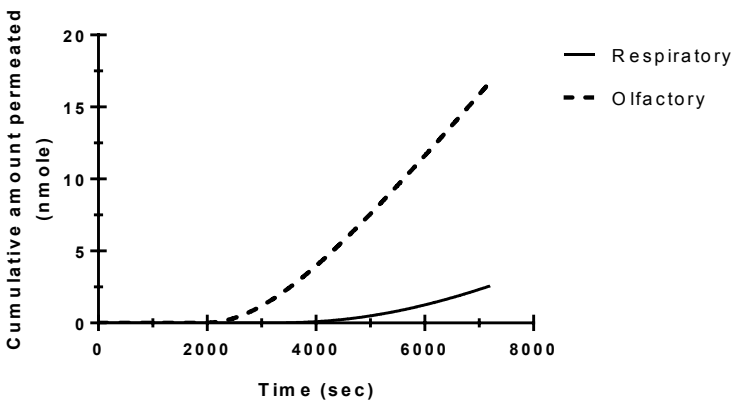

Figure 6-9 Effect of tissue thickness on net mass transfer of a poorly permeable drug (P_e 2.5×10^{-6} cm/sec) with high levels of metabolic degradation (V_{max}: 1 nmoles-cm^{-3}-sec^{-1}) within the nasal mucosa

(NAS), 6-hydroxymelatonin (MT6) and melatonin (MT) across bovine respiratory and olfactory explants are listed in Table 6-5 and Table 6-6, respectively.

Figure 6-10 demonstrates the comparison between the experimental and simulated values for N-acetylserotonin diffusion across bovine respiratory and olfactory explants. Figure 6-11 demonstrates the comparison between the experimental and simulated values for 6-hydroxymelatonin diffusion across bovine respiratory and olfactory explants. As seen from the plots, the experimental and the simulated cumulative amount vs. time profiles for N-acetylserotonin or 6-hydroxymelatonin permeation across bovine nasal explants were in close approximation, assuming no metabolic activity of nasal enzymes towards biotransformation of N-acetylserotonin or 6-hydroxymelatonin during transport.

Diffusion of melatonin across bovine nasal olfactory and respiratory explants was modeled assuming passive Fickian diffusion with Michaelis-Menten enzymatic reaction kinetics. The experimentally determined values of effective permeability for melatonin diffusion across bovine respiratory and olfactory explants were significantly lower at the low donor concentrations of 108 μM and 216 μM compared to the values obtained for higher donor concentrations of 323 μM and 431 μM (Figure 5-5 and Figure 5-6), presumably due to saturation of the nasal enzymatic activity. The simulations were performed using the plateau effective permeability coefficient values (mean of permeability coefficient values at 323 μM and 431 μM donor melatonin concentrations) for melatonin diffusion across bovine respiratory and olfactory explants.

Figure 6-12 demonstrates the comparison of the experimental data to simulated values for melatonin diffusion across bovine respiratory mucosa with concurrent metabolism to 6-hydroxymelatonin for the four donor concentrations studied. Each concentration was tested individually using the model and the predicted parameter values for melatonin diffusion across the respiratory mucosa for each melatonin donor concentration are given in Table 6-5.

Table 6-5 Numerically obtained optimized parameter values from fits of the experimental results for N-acetylserotonin (NAS), 6-hydroxymelatonin (MT6) and melatonin (MT) permeation across bovine respiratory explants.

Substrate	Donor concentration (μM)	P_e (cm/sec) Mean (SE)	h_S (cm) Mean (SE)	logPC Mean (SE)	V_{max} (nmol $cm^{-3}sec^{-1}$) Mean (SE)
NAS	229	4.31×10^{-6} (7.72×10^{1})	0.077 (0.416)	0.101 (0.516)	Not applicable
MT6	201	2.23×10^{-6} (4.65×10^{4})	0.077 (0.082)	0.339 (0.835)	Not applicable
MT	108	7.72×10^{-6} (4.54×10^{2})	0.094 (0.076)	0.300 (1.172)	0.814 (3.827)
MT	216	7.72×10^{-6} (7.72×10^{1})	0.094 (0.111)	0.300 (2.033)	0.900 (4.063)
MT	323	7.72×10^{-6} (1.68×10^{1})	0.083 (0.020)	0.300 (0.251)	0.484 (0.460)
MT	431	7.72×10^{-6} (1.37×10^{1})	0.085 (0.016)	0.300 (0.31)	0.218 (0.197)

Table 6-6 Numerically obtained optimized parameter values from fits of the experimental results for N-acetylserotonin (NAS), 6-hydroxymelatonin (MT6) and melatonin (MT) permeation across bovine olfactory explants.

Substrate	Donor concentration (μM)	P_e (cm/sec) Mean (SE)	h_S (cm) Mean (SE)	logPC Mean (SE)	V_{max} (nmol $cm^{-3}sec^{-1}$) Mean (SE)
NAS	229	7.23×10^{-6} (8.793×10^{3})	0.056 (0.204)	0.100 (1.339)	Not applicable
MT6	201	4.91×10^{-6} (2.51×10^{1})	0.054 (0.001)	0.150 (0.201)	Not applicable
MT	108	1.11×10^{-5} (9.38×10^{3})	0.056 (0.031)	0.150 (3.036)	0.200 (0.595)
MT	216	1.11×10^{-5} (8.49×10^{1})	0.056 (0.049)	0.150 (0.748)	0.297 (0.516)
MT	323	1.56×10^{-5} (3.87×10^{1})	0.046 (0.011)	0.200 (0.372)	0.378 (0.017)
MT	431	1.56×10^{-5} (4.20×10^{1})	0.046 (0.011)	0.200 (0.402)	0.801 (0.034)

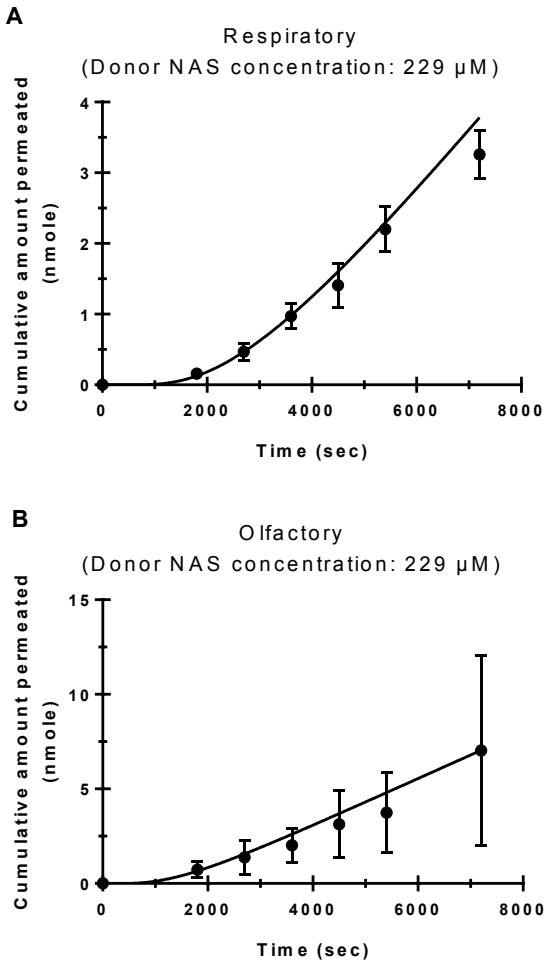

Figure 6-10 Comparison of experimental data and model prediction for diffusion of N-acetylserotonin across bovine respiratory (A) and olfactory (B) explants. Data points represent the cumulative amount of N-acetylserotonin transported across bovine respiratory (A) and olfactory (B) explants as a function of time at 229 µM donor concentration. Results are presented as the mean of 3 replicates ± standard deviation. Curves represent numerical simulations for N-acetylserotonin diffusion across bovine nasal explants with no metabolic degradation. The optimized parameters for the respiratory and olfactory mucosal simulations are listed in Table 6-5 and Table 6-6, respectively.

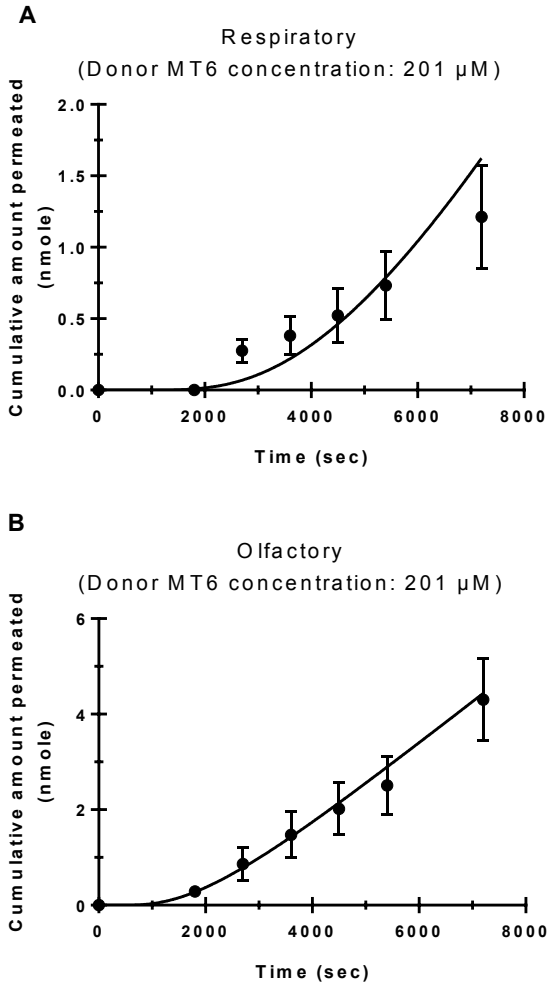

Figure 6-11 Comparison of experimental data and model prediction for diffusion of 6-hydroxymelatonin across bovine respiratory (A) and olfactory (B) explants. Data points represent the cumulative amount of 6-hydroxymelatonin transported across bovine respiratory (A) and olfactory (B) explants as a function of time at 201 µM donor concentration. Results are presented as the mean of 3 replicates ± standard deviation. Curves represent numerical simulations for 6-hydroxymelatonin diffusion across bovine nasal explants with no metabolic degradation. The optimized parameters for the respiratory and olfactory mucosal simulations are listed in Table 6-5 and Table 6-6, respectively.

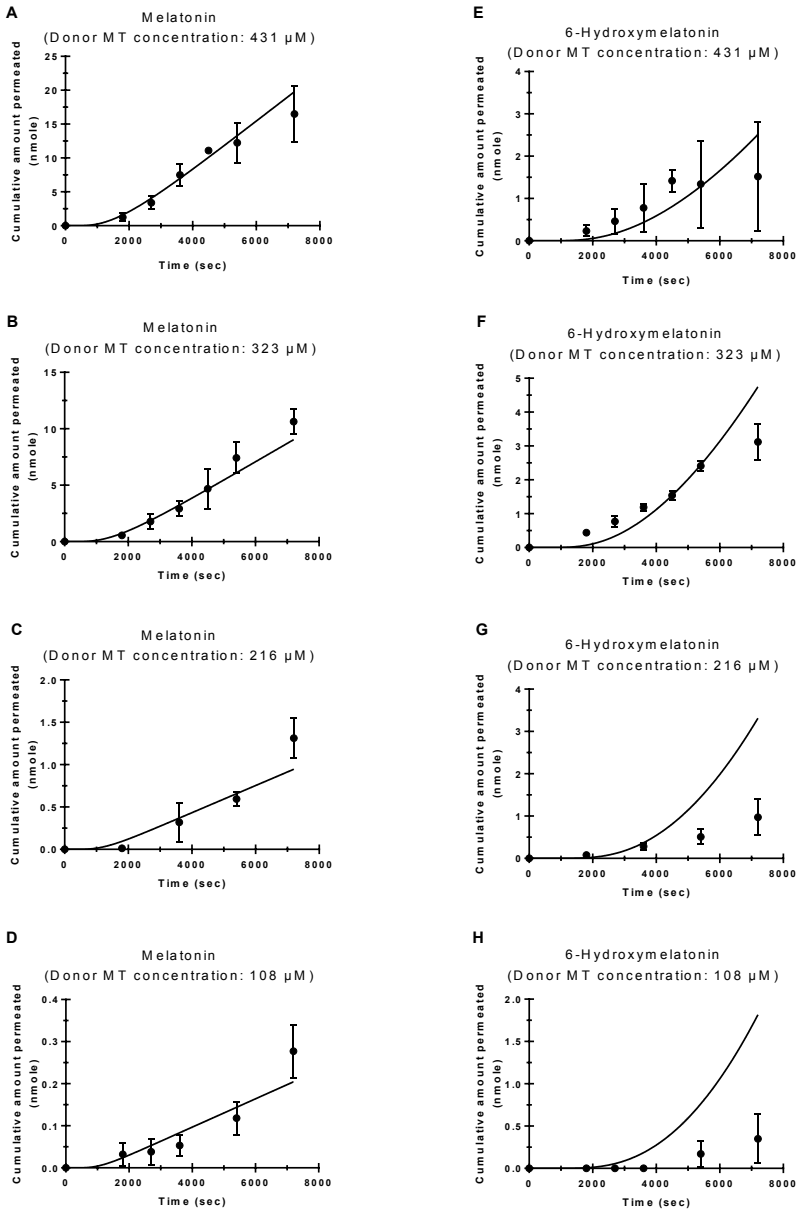

Figure 6-12 Comparison of experimental data and model prediction for melatonin diffusion and concurrent metabolism to 6-hydroxymelatonin across bovine respiratory explants at four donor concentrations. Data points represent the cumulative amount of melatonin (A-D) and 6-hydroxymelatonin (E-H) transported across bovine respiratory explants as a function of time at 108 µM, 216 µM, 323 µM, and 431 µM donor concentrations. Results are presented as the mean of 3 replicates ± standard deviation. Curves represent numerical simulations for melatonin and 6-hydroxymelatonin diffusion across bovine respiratory explants. The optimized parameters for the respiratory mucosal simulations are listed in Table 6-5.

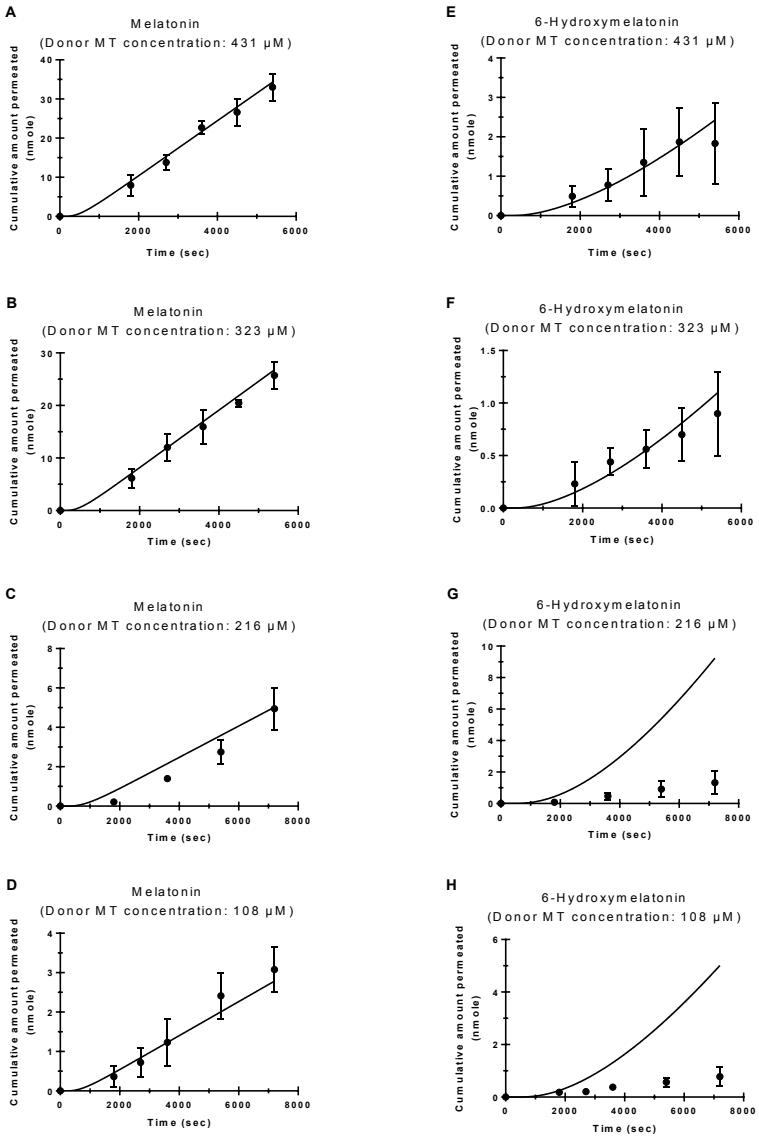

Figure 6-13 Comparison of experimental data and model prediction for melatonin diffusion and concurrent metabolism to 6-hydroxymelatonin across bovine olfactory explants at four donor concentrations. Data points represent the cumulative amount of melatonin (A-D) and 6-hydroxymelatonin (E-H) transported across bovine olfactory explants as a function of time at 108 µM, 216 µM, 323 µM, and 431 µM donor concentrations. Experiments with 323 µM and 431 µM donor concentrations were stopped after 90 minutes (5400 seconds) as sink conditionds for melatonin in receiver chamber were exceeded. Results are presented as the mean of 3 replicates ± standard deviation. Curves represent numerical simulations for melatonin and 6-hydroxymelatonin diffusion across bovine olfactory explants. The optimized parameters for the olfactory mucosal simulations are listed in Table 6-6.

It can be seen that the model performed better in predicting the permeation of substrate and metabolite at higher melatonin donor concentrations than at lower melatonin donor concentrations. At lower donor concentrations (108 μM and 216 μM), the values of metabolite generated during the diffusion were over-predicted at the longer time points. A similar trend was observed while comparing the model-predicted and experimentally-determined values for melatonin diffusion and metabolism to 6-hydroxymelatonin across bovine olfactory mucosa (Figure 6-13). The extent of melatonin biotransformation during its diffusion across bovine olfactory explants was over-predicted by the model, and the effect was more evident at lower donor concentrations of melatonin.

The model was unable to simultaneously optimize the parameters to fit the substrate and metabolite diffusion data (melatonin and 6-hydroxymelatonin quantified values) for all the four donor melatonin concentrations studied during diffusion across either bovine respiratory or the olfactory explants. Differences between simulated and experimental data for the diffusion of melatonin across the nasal mucosa at lower donor concentrations can be attributed to a variety of factors, along with consideration of some of the model assumptions. The permeability coefficients of melatonin and its metabolites used in the model were the apparent permeability coefficients obtained from the experimental data at higher donor concentrations. Differences in the permeability through the epithelial and the submucosal regions within the nasal mucosa were not considered, and the full-thickness permeability was assumed to be constant throughout the nasal mucosa. Differences in the effective permeability coefficients of compounds in the nasal epithelial and submucosal regions can subsequently change the mass transfer across the nasal mucosa. The partition coefficient between the epithelial and the submucosal regions was assumed to be 1. Any deviations from the unit partition coefficient between the two regions could also contribute to significantly altering the mass transfer across the nasal mucosa. For example, an epithelial-to-submucosal partition coefficient value of lower

than one can result in lower concentrations in the submucosal region than those predicted by assuming an equal partitioning in these two regions, resulting in a decrease in the net mass transfer of the substrate or the metabolite diffusing across the submucosal region in the receiver compartment.

For the treatment of metabolism within the nasal mucosa, the apparent V_{max} and K_M values obtained from bovine microsomal experiments for metabolism of melatonin to 6-hydroxymelatonin should be appropriately scaled to match the metabolic activity in the full thickness mucosa. For bovine nasal olfactory and respiratory mucosa, such a scaling factor has not been reported in the literature. Hence the value of K_M was fixed to the microsomal level and the value of V_{max} was optimized to simulate the experimental data. As an alternative, simultaneous optimization of V_{max} and K_M was performed, but the model was unable to fit the experimental data due to a strong correlation between these parameters.

A delay in partitioning at any of the diffusion interfaces (donor-epithelial, epithelial-submucosal, and submucosal-receiver interface) could result in a reduction in the net mass transfer of substrate and its metabolites. To improve the performance of our model at lower donor melatonin concentrations (108 μM and 216 μM), simulations were performed with the inclusion of a few additional variable parameters, including interfacial barriers that delay substrate partitioning at the donor-epithelial interface (α_S_{DE}) and the interfacial barriers to substrate (α_S_{SR}) and metabolite (α_M_{SR}) partitioning at the submucosal-receiver interface. The results of these simulations for melatonin diffusion across bovine respiratory and olfactory explants are given in Figures 6-14 and 6-15, respectively. The corresponding parameter estimates are given in Tables 6-7 and 6-8, respectively. The standard errors for these parameter estimates were infinity, indicating that the fit was not unique and the amount of information provided in the experimental results was insufficient for accurate estimation of the strongly correlated parameters, such as the interfacial barrier resistances. As seen in Figures 6-14 and 6-15,

when the interfacial barriers delayed substrate partitioning at the donor-epithelial interface and substrate and metabolite partitioning at the submucosal-receiver interface, the extent of substrate and metabolite mass transfer across the nasal mucosa was reduced, and the net substrate and metabolite mass transfer was better predicted by the model. However, the physiological significance and validity of these interfacial barriers against partitioning of drugs at tissue-buffer interfaces needs to be established to justify the over-parameterization of the model at lower melatonin donor concentrations (108 μM and 216 μM).

Accurate prediction of model parameters for melatonin diffusion and metabolism results could also be limited by the inadequate information available from the experimental data. The viability of nasal enzymes and integration of nasal mucosa are compromised after the two-hour diffusion experiments performed at 37 ºC. Hence, the diffusion experiments could not be continued for longer duration of times, which otherwise could have helped to understand the deviation of the model predictions from the experimental data. The time period of sampling was set at every 15 minutes to be able to quantify the changes in substrate and metabolite concentrations in the receiver chamber at each sampling interval. This results in a limited the number of data points available for fitting. A more extensive data set (diffusion studies performed with multiple substrate or metabolite donor concentrations) could help to elucidate the root causes for the deviations in fitting the model predictions to experimental data of diffusion and concurrent metabolism.

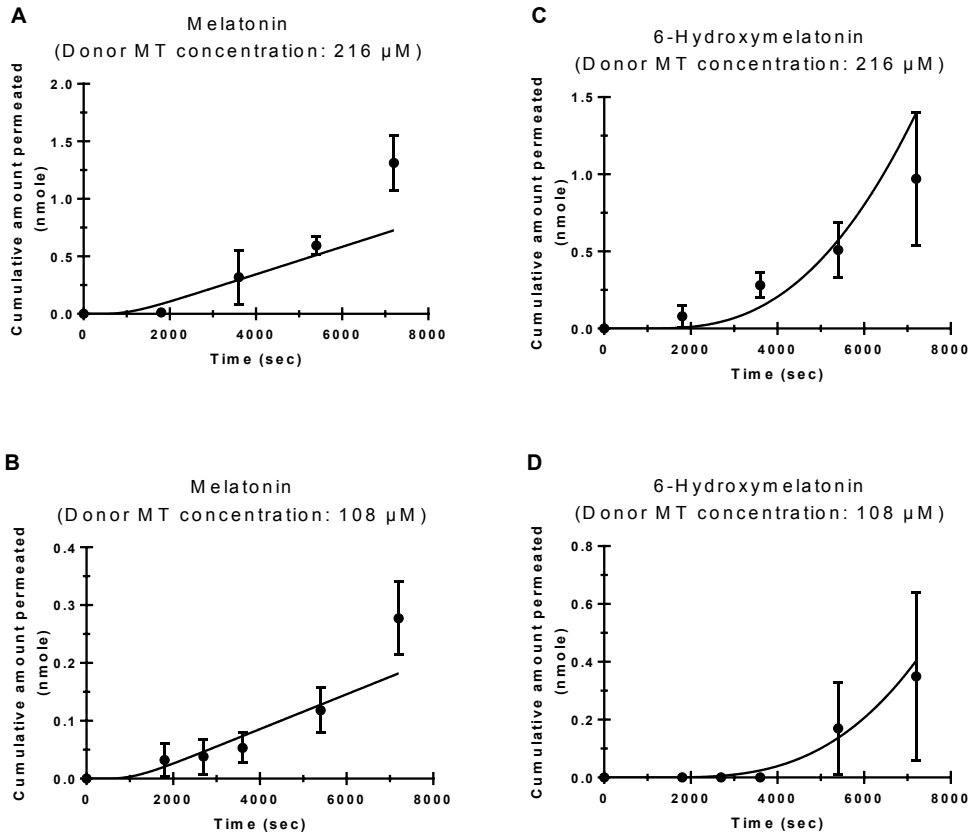

Figure 6-14 Comparison of experimental data and model prediction for melatonin diffusion and concurrent metabolism to 6-hydroxymelatonin across bovine respiratory explants at 108 µM and 216 µM donor melatonin concentrations. Data points represent the cumulative amount of melatonin (A-B) and 6-hydroxymelatonin (C-D) transported across bovine respiratory explants as a function of time. Results are presented as the mean of 3 replicates ± standard deviation. Curves represent numerical simulations for melatonin and 6-hydroxymelatonin diffusion across bovine respiratory explants with the inclusion of interfacial barrier against substrate and metabolite partitioning at donor-epithelial and submucosal-receiver boundaries. The optimized parameters for the respiratory mucosal simulations are listed in Table 6-7.

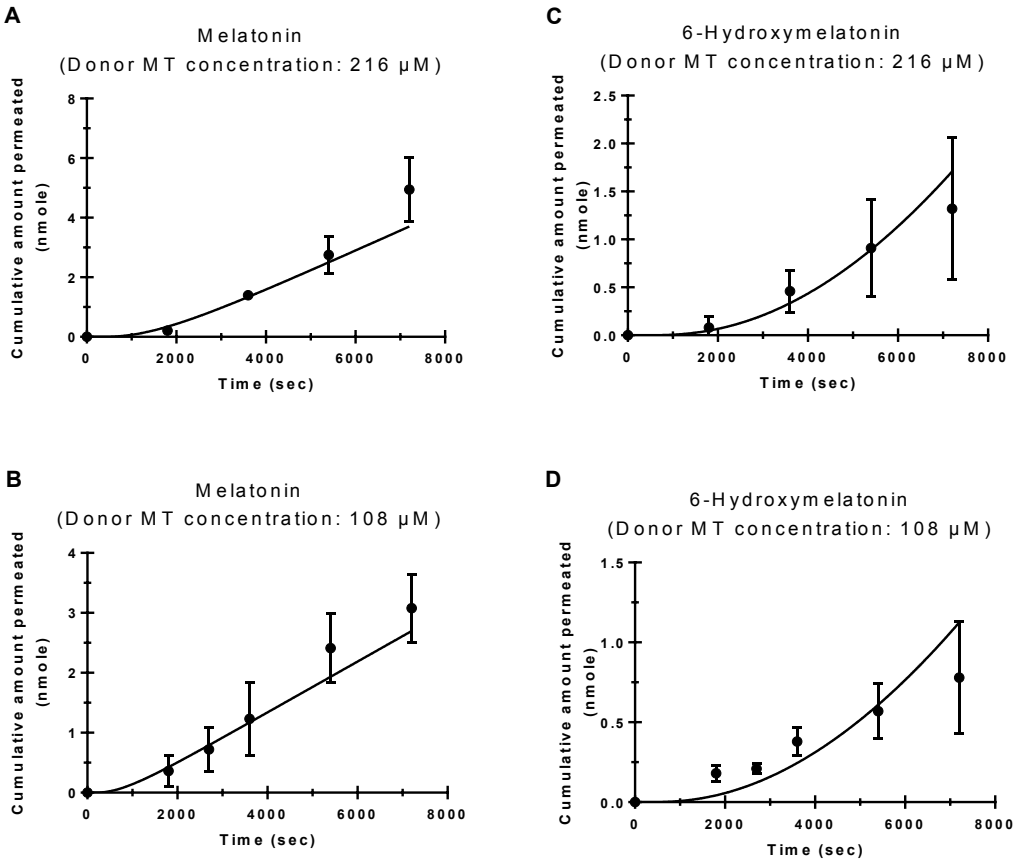

Figure 6-15 Comparison of experimental data and model prediction for melatonin diffusion and concurrent metabolism to 6-hydroxymelatonin across bovine olfactory explants at 108 µM and 216 µM donor melatonin concentrations. Data points represent the cumulative amount of melatonin (A-B) and 6-hydroxymelatonin (C-D) transported across bovine olfactory explants as a function of time. Results are presented as the mean of 3 replicates ± standard deviation. Curves represent numerical simulations for melatonin and 6-hydroxymelatonin diffusion across bovine olfactory explants with the inclusion of interfacial barrier against substrate and metabolite partitioning at donor-epithelial and submucosal-receiver boundaries. The optimized parameters for the olfactory mucosal simulations are listed in Table 6-8.

Table 6-7 Numerically obtained optimized parameter values from fits of the experimental results for melatonin (MT) permeation across bovine respiratory explants with the inclusion of interfacial barrier to partitioning of substrate and metabolite at donor-epithelial and submucosal-receiver interface.

Parameter	Melatonin donor concentration 216 μM	Melatonin donor concentration 108 μM
P_e (cm/sec)	7.72×10^{-6}	7.72×10^{-6}
h_S (cm)	0.085	0.094
logPC	0.300	0.300
V_{max} (nmol $cm^{-3}sec^{-1}$)	1.000	1.000
$\log(\alpha\_S_{DE})$	-2.000	-2.000
$\log(\alpha\_S_{SR})$	-0.020	-0.950
$\log(\alpha\_M_{SR})$	-6.000	-5.910

Table 6-8 Numerically obtained optimized parameter values from fits of the experimental results for melatonin (MT) permeation across bovine olfactory explants with the inclusion of interfacial barrier to partitioning of substrate and metabolite at donor-epithelial and submucosal-receiver interface.

Parameter	Melatonin donor concentration 216 μM	Melatonin donor concentration 108 μM
P_e (cm/sec)	1.73×10^{-5}	1.73×10^{-5}
h_S (cm)	0.056	0.046
logPC	0.170	0.100
V_{max} (nmol $cm^{-3}sec^{-1}$)	0.200	0.200
$\log(\alpha\_S_{DE})$	-4.000	-4.970
$\log(\alpha\_S_{SR})$	-5.000	-5.000
$\log(\alpha\_M_{SR})$	-5.690	-5.750

Limitations of the model

The current simulation model was aimed at understanding the relative significance of permeability and metabolic degradation in reducing the net mass transfer of drugs across nasal mucosal explants. One of the major limitations of the model is that it assumes Fickian passive diffusion for the substrate and metabolites, along with Michaelis-Menten-like enzymatic metabolism within the nasal mucosa. The permeation of drugs across the nasal mucosa is a complex process and can involve interplay between various influx or efflux transporters, enzymes, and a combination of transport pathways including the paracellular, transcellular, or transneuronal pathways. This model also does not take conjugation or phase II metabolism of the oxidized metabolites into account. A more complicated treatment of metabolism would also be necessary for drugs that exhibit "atypical" enzymatic kinetics *in vitro*, such as sigmoidal kinetics (auto-activation), biphasic kinetics, substrate inhibition kinetics, or heterotropic cooperativity (activation)[262]. Inter-subject variability in the nasal permeation of drugs resulting from genetic polymorphism, mutation, induction and inhibition of nasal enzymes has not been addressed in the present model.

Conclusions

We have presented a numerical simulation model to simultaneously examine passive diffusion and saturable enzymatic metabolism of drugs in the nasal mucosa. The model contains an apical epithelial layer and a basal submucosal layer exhibiting non-uniform enzyme distribution. Cellular distribution of CYP450 enzymes in the nasal mucosa was accounted for in the model by relative scaling of the maximum biotransformation velocity (V_{max}) in different regions within the nasal mucosa. Simulated substrate concentration-distance profiles were used to calculate the resulting substrate fluxes for various mass transport and metabolism parameters at steady state. These simulations can be used for predicting the net flux of unmetabolized drugs across the nasal mucosa into

the systemic circulation. The simulated concentration-distance profiles can allow for the estimation of the concentrations of a drug and its metabolites within different regions in the nasal mucosa at various times and can evaluate the relative order of the enzymatic reaction within the tissue based on the drug's permeability coefficient (P_e), maximum metabolic velocity (V_{max}) in different regions, and the Michaelis constant (K_M) for the reaction. Rapid screening of metabolically susceptible drug candidates for intranasal delivery can be performed and drugs exhibiting low tissue concentrations ($\leq K_M$ value) can be identified for potential bioavailability concerns. Moreover, the concentration of metabolites generated within the mucosal tissue can be simulated to predict the toxicological, therapeutic, or physiological consequences of metabolite production or accumulation following intranasal administration of drugs.

In the case of diffusion across the bovine nasal olfactory and respiratory explants, the net mass transfer of drugs exhibiting low permeability values ($<10^{-7}$ cm/sec) are expected to be affected by low-to-moderate enzymatic activity within the nasal mucosa (V_{max}: 0.25-0.5 nmoles-sec^{-1}-cm^{-3} tissue volume). Although a more detailed treatment of permeation and metabolism within the epithelial and submucosal layers of the nasal mucosa is needed to accurately predict the substrate and metabolite mass transfer across the nasal mucosa, the mathematical treatment of diffusion and concurrent metabolism provided in this model can be used for assessing the metabolic barrier properties of the nasal mucosa and for predicting the bioavailability limitations arising from nasal enzymatic metabolism.

CHAPTER 7

CONCLUSIONS

Despite many advantages, the efficacy and broader use of the nasal route as an alternative drug delivery site is mainly limited by bioavailability restrictions arising from the anatomical and physiological characteristics of the nasal cavity. Regional deposition and distribution of administered formulations, local clearance processes, and differences in cellular barrier properties in various regions within the nasal cavity may have a potential impact on nasal drug permeation and absorption. Mucociliary clearance has been shown to significantly reduce the net residence time and bioavailability of formulations in the nasal cavity, and approaches to improve contact between the applied formulations and the mucus layer covering the permeable mucosal membranes are being actively investigated[23,24,263]. In contrast, the role of enzymatic metabolism in limiting the bioavailability of intranasally administered drugs has been long overlooked. Even though the nasal route circumvents hepatic first-pass metabolism, multiple metabolic barriers can be encountered by a drug molecule administered intranasally prior to its transfer to the systemic circulation. Critical evaluation of enzymatic biotransformation processes involved in clearance, activation, or inactivation of drugs in the nasal cavity can help improve the design and systemic bioavailability of intranasal formulations.

Cytochrome P450 isoforms are important drug metabolizing enzymes in the nasal mucosa. Our first objective was aimed at studying CYP450 enzyme expression and distribution in excised bovine nasal mucosa to investigate the possibility of utilizing this model to examine *in vitro* metabolic clearance of CYP450 substrates. Amplification of specific genes through real time RT-PCR confirmed the expression of several CYP450 isoforms (1A1, 1A2, 2A6, 2C9, 2C19, and 3A4) in bovine liver tissues and the nasal mucosa. While bovine liver expressed significantly higher levels of all CYP450 isoforms, the nasal olfactory and respiratory mucosa showed abundant expression of CYP 2A6 and

3A4 whereas 1A1, 1A2, 2C9, and 2C19 isoforms were expressed at marginal levels in the nasal tissues. Greater inter-animal variability was observed in the olfactory and respiratory expression levels of CYP450 isoforms as compared to the hepatic expression levels, suggesting potential inter-individual differences in the extent of metabolism and nasal bioavailability of CYP450 substrates upon intranasal administration. Analysis of CYP450 protein localization in bovine nasal olfactory and respiratory explants indicated that the biotransformation in the nasal mucosa can occur in both the epithelial layer as well as the submucosal layer.

Melatonin was selected as a model compound for our second objective of examining the activity of bovine olfactory and respiratory CYP450 isoforms in microsomal incubations and during *in vitro* diffusion across the nasal explants. Nasal melatonin delivery is currently being investigated to provide a fast-acting, efficient, and daily-use medication for sleep improvement[154,221]. The bioavailability of melatonin nasal solution in rabbits was reported to be 55±17%[149]. Pre-systemic loss of melatonin following intranasal administration has been attributed to mucociliary clearance and reduced residence time of formulations in the nasal mucosa. However, the significance of enzymatic metabolism in limiting melatonin's nasal bioavailability has not received sufficient attention. With our microsomal and diffusion studies, we confirmed that bovine nasal olfactory and respiratory mucosal CYP450 isoforms were capable of metabolizing significant amounts of melatonin to 6-hydroxymelatonin, its principal metabolite. The action of biotransformative enzymes in the nasal epithelial and submucosal layers significantly reduced the flux of melatonin across the nasal explants. Enzyme saturation at higher melatonin donor concentrations and CYP1A2 inhibition resulted in the ability to transfer significant amounts of melatonin across the nasal mucosa, and these results indicate that the contribution of nasal CYP450 enzymes in limiting the nasal bioavailability of melatonin needs to be carefully evaluated in addition to mucociliary clearance, to minimize the pre-systemic loss of this drug following intranasal delivery.

Our third objective was to develop a simulation model for prediction of the extent of drug metabolism during transport across the nasal mucosa. Numerical simulations combining Fickian passive diffusion of drugs with saturable enzymatic degradation illustrated that the concentration gradient and resulting flux of a drug molecule across the nasal mucosa are primarily governed by its permeability coefficient. Enzymatic degradation reduces the net flux of drugs across the nasal mucosa and has the greatest impact on low permeability compounds ($P_e < 10^{-6}$ cm/sec across bovine nasal explants). For these low permeability compounds, enzymatic activity with maximum bioconversion velocity (V_{max}) in the range of 0.25 to 1 nmoles-sec^{-1}-cm^{-3} tissue volume resulted in significant reductions (~50-75%) in flux across the nasal mucosa, and the effect was more pronounced at lower substrate donor concentrations. Some reduction in bioavailability can also be observed with moderate and high permeability compounds. In the case of melatonin, a high permeability compound ($P_e > 5\times10^{-6}$ cm/sec across bovine olfactory and respiratory explants), the numerically obtained apparent maximum bioconversion velocity (V_{max}) values for melatonin 6-hydroxylation were in the range of 0.2-0.9 nmoles-sec^{-1}-cm^{-3} tissue volume. Experimentally it was determined that the flux of melatonin at lower donor concentrations could be significantly reduced (up to ~ 50%) due to the enzymatic activity in the bovine nasal mucosa. CYP450-mediated enzymatic activity in the nasal mucosa can thus help to account for the significant reduction in melatonin bioavailability following the nasal administration. With further enhancements to the current model, including carrier-mediated uptake and efflux activities and improved characterization of the diffusional differences between the epithelial and submucosal regions, the simulation model can allow for the initial estimation of the reduction in mass transfer and resulting bioavailability limitations which may occur for metabolically-labile compounds.

APPENDIX A

DNA SEQUENCING RESULTS

For DNA sequencing, the PCR products were extracted from the agarose gel using a procedure described in Chapter 3. The extracted products were sequenced by the DNA sequencing facility at the University of Iowa to identify the nucleotide sequence of the PCR products. The nucleotide sequence was then matched with the bovine CYP1A2-like mRNA (NCBI accession number NM_001099364) to identify sequence homology between the PCR products and the bovine CYP1A2-like gene.

The results from DNA sequencing can be described as follows:

1. Sequence homology was observed between the heavier PCR product (top band, Figure 3-3) obtained from respiratory mucosa of animal 3, when sequenced with sense CYP1A2-like primer (Table 3-1).

```
Query  838  CTGCAGTTCGTGCGGAAAACGGTCCAGGAGCACTACCAGGACTTTGACAAG  888
            |||||||||||||||||| ||||||||||||||||||||||||||||||||
Sbjct  5    CTGCAGTTCGTGCGGAAA-CGGTCCAGGAGCACTACCAGGACTTTGACAAG  54


Query  434  ACCCAGACTCT  444
            ||||||||||| 
Sbjct  99   ACCCAGACTCT  89
```

2. Sequence homology was observed between the heavier PCR product (top band, Figure 3-3) obtained from respiratory mucosa of animal 3, when sequenced with anti-sense CYP1A2-like primer (Table 3-1).

```
Query  887  AGAACAGCATCCAGGACATCATAGGCGCCCTGTTCAAGCACAGTGAGGATAACTCCCGAG  946
            ||||||||||||||||||||||||| ||||||||||||||||||||||||||||||||
Sbjct  94   AGAACAGCATCCAGGACATCATAGGCACCCTGTTCAAGCACAGTGAGGATAACTCCCGAG  35

Query  947  CCAGCAGTCGCCTCATCTCCCAGGAGAAGACTGTCA  982
            ||||||||||||||| || |||||||||||| ||||
Sbjct  34   CCAGCAGTCGCCTCA-CTGCCAGGAGAAGAC-GTCA  1

Query  97   CTTCTCCTGGC  107
            ||||||||||| 
Sbjct  7    CTTCTCCTGGC  17
```

3. Sequence homology was observed between the lighter PCR product (bottom band, Figure 3-3) obtained from respiratory mucosa of animal 3, when sequenced with sense CYP1A2-like primer (Table 3-1).

```
Query  838  CTGCAGTTCGTGCGGAAAACGGTCCAGGAGCACTACCAGGACTTTGACAAG  888
            |||||||||||||||||| ||||||||||||||||||||||||||||||||
Sbjct  5    CTGCAGTTCGTGCGGAAA-CGGTCCAGGAGCACTACCAGGACTTTGACAAG  54


Query  434  ACCCAGACTCT  444
            ||||||||||| 
Sbjct  99   ACCCAGACTCT  89
```

4. No sequence homology was observed between the lighter PCR product (bottom band, Figure 3-3) obtained from respiratory mucosa of animal 3, when sequenced with anti-sense CYP1A2-like primer (Table 3-1).

APPENDIX B

IDENTIFICATION OF BOUNDARY CONDITIONS FOR DIFFUSION AND METABOLISM MODELING

Boundary condition for substrate and metabolite partitioning from the submucosal layer into receiver chamber

In our diffusion-metabolism model (Chapter 6), the last box is designated as $z(n)^{th}$ box. Compounds are diffusing from $z(n-1)^{th}$ box to $z(n)^{th}$ box and finally partitioning into the receiver. The concentration of the substrate in the receiver compartment is denoted as $C_{S,R}$.

$$PC_S\ (tissue/buffer\ partition\ coefficient)\ =\ \frac{C_S(z(n))}{C_{S,R}} \qquad \text{Equation B-1}$$

At partitioning equilibrium between the last submucosal box ($z(n)^{th}$ box) and the receiver compartment, the substrate concentration in the receiver ($C_{S,R}$) is expected to be equal to the substrate concentration in the last submucosal box ($C_S(z(n),t)$), corrected by the apparent tissue/buffer partition coefficient for the substrate (PC_S).

$$C_{S,R} = \frac{C_S(z(n),t)}{PC_S} \qquad \text{Equation B-2}$$

If there is an interfacial barrier against the partitioning of the drug from the last submucosal box into the receiver compartment, the boundary condition at the submucosal-receiver interface (at $x = +h_S$) can be modified as shown in Equation B-3.

$$\frac{dC_S(z(n),t)}{dx} = -\frac{\alpha\_S_{SR}}{D_S}\left(\frac{C_S(z(n),t)}{PC_S} - C_{S,R}\right) \quad \text{Equation B-3}$$

Where α_S_{SR} at $x = +h_S$ is the partitioning delay factor for substrate (S) at the submucosal-receiver (SR) interface to account for interfacial barrier between the two layers.

To evaluate this boundary for partitioning of the substrate from last submucosal box into the receiver compartment, we introduce a fictitious box in the receiver compartment, the $z(n+1)^{th}$ box.

Using central difference, the first order differential of rate of change of concentration of substrate with distance in the last submucosal box can now be expressed as shown in Equation B-4.

$$\frac{dC_S(z(n),t)}{dx} = \frac{C_S(z(n+1),t) - C_S(z(n-1),t)}{2\delta x} \quad \text{Equation B-4}$$

Substituting Equation A-3 into Equation B-4, we get:

$$\frac{C_S(z(n+1),t) - C_S(z(n-1),t)}{2\delta x} = -\frac{\alpha\_S_{SR}}{D_S}\left(\frac{C_S(z(n),t)}{PC_S} - C_{S,R}\right) \quad \text{Equation B-5}$$

$$C_S(z(n+1),t) = C_S(z(n-1),t) - \frac{\alpha\_S_{SR}\ 2\delta x}{D_S}\left(\frac{C_S(z(n),t)}{PC_S} - C_{S,R}\right) \quad \text{Equation B-6}$$

The rate of change of substrate concentration with time in the first epithelial box can be written using Equation 6-5.

$$\frac{dC_S(z(n),t)}{dt} = D_S\frac{d^2C}{dx^2} - V_{z(n)}$$ Equation B-7

Where $V_{z(n)}$ is for the rate of enzymatic reaction in the last submucosal box.

The second order differential can be replaced by a central difference.

$$\frac{dC_S(z(n),t)}{dt} = D_S\frac{C_S(z(n-1),t) - 2C_S(z(n),t) + C_S(z(n+1),t)}{\delta x^2} - V_{z(n)}$$

Equation B-8

Substituting the value of fictitious concentration of substrate in box z(n+1) (C_S(z(n+1),t)) from Equation B-6 into Equation B-8, we get:

$$\frac{dC_S(z(n),t)}{dt} = \frac{D_S}{\delta x^2}\left[C_S(z(n-1),t) - 2C_S(z(n),t) + C_S(z(n-1),t) - \frac{\alpha\_S_{SR}\ 2\delta x}{D_S}\ (\frac{C_S(z(n),t)}{PC_S} - C_{S,R})\right] - V_{z(n)}$$

Equation B-9

The boundary condition for the partitioning of the substrate from the last submucosal box into the receiver compartment is given by Equation B-10.

$$\frac{dC_S(z(n),t)}{dt} = \frac{2D_S}{\delta x^2}\left[C_S(z(n-1),t) - C_S(z(n),t) - \frac{\alpha\_S_{SR}\ \delta x}{D_S}\ (\frac{C_S(z(n),t)}{PC_S} - C_{S,R})\right] - V_{z(n)}$$

Equation B-10

Assuming a 1:1 molar conversion of the substrate into the metabolite, the boundary condition for the partitioning of the metabolite from the last submucosal box into the receiver compartment is given by Equation B-11.

$$\frac{dC_M(z(n),t)}{dt} = \frac{2D_M}{\delta x^2}\left[C_M(z(n-1),t) - C_M(z(n),t) - \frac{\alpha\_M_{SR}\,\delta x}{D_M}\left(\frac{C_M(z(n),t)}{PC_M} - C_{M,R}\right)\right] + V_{z(n)}$$

Equation B-11

Boundary condition for metabolite backflux from the epithelial layer the donor compartment

Metabolite concentration in the donor compartment due to its backflux from the epithelial first box ($x = -h_E$) is expected to be equal to the metabolite concentration in the first box, corrected by the apparent tissue/buffer partition coefficient for the metabolite PC_M.

$$C_{M,D} = \frac{C_M(1,t)}{PC_M} \quad at\ x = -h_E$$

Equation B-12

However, partitioning of the metabolite from the epithelial layer into the donor compartment might not be an instantaneous process. If a drug's chemical properties limit its immediate partitioning into the donor, the time lag for partitioning of the metabolite from the first epithelial box into donor compartment needs to be accounted for in the model. Here, we introduce a term β_M_{ED} at $x = -h_E$ (the donor-epithelial interface) to account for the interfacial barrier against partitioning of the metabolite from the first epithelial box into the donor compartment. The boundary epithelial-donor boundary

condition for the backflux of metabolite can now be expressed as shown in Equation B-13.

$$D_M \frac{dC_M(1,t)}{dx} = \beta\_M_{ED}\left(C_{M,D} - \frac{C_M(1,t)}{PC_M}\right) \quad \text{Equation B-13}$$

For our simulation model, first box is designated at "1", second box is designated at "2" The concentration of the metabolite in the first box is $C_M(1,t)$. The concentration in the second box is $C_M(2,t)$. We need dC_M/dx for the backflux of the metabolite from the epithelial layer into the donor compartment. To get that value, we introduce a fictitious box in the donor compartment, such that concentration of the metabolite in this fictitious box can now be denoted as $C_M(-1,t)$.

Using central difference, the first order differential (dC_M/dx) for metabolite backflux from the epithelial layer into the donor compartment can now be replaced as:

$$\frac{dC_M(1,t)}{dx} = \frac{C_M(-1,t) - C_M(2,t)}{2\delta x} \quad \text{Equation B-14}$$

Combining Equation B-13 and Equation B-14, we get:

$$D_M \frac{C_M(2,t) - C_M(-1,t)}{2 \times \delta x} = \beta\_M_{ED}\left(C_{M,D} - \frac{C_M(1,t)}{PC_M}\right) \quad \text{Equation B-15}$$

$$C_M(-1,t) = C_M(2,t)$$

$$-\frac{2 \times \delta x \times \beta\_M_{ED}}{D_M}\left(C_{M,D} - \frac{C_M(1,t)}{PC_M}\right) \quad \text{Equation B-16}$$

We need to eliminate the metabolite concentration in the fictitious box ($C_M(-1,t)$) from Equation B-16.

The rate of change of substrate concentration with time in the first epithelial box can be written using Equation 6-5.

$$\frac{dC_M(1,t)}{dt} = D_M \frac{d^2C_M(1,t)}{dx^2} + V_1 \qquad \text{Equation B-17}$$

Where V_1 is for the rate of enzymatic reaction in the first epithelial box.

Using central difference, the second order differential for metabolite backflux from the epithelial layer into the donor compartment can now be replaced as shown in Equation B-18.

$$\frac{dC_M(1,t)}{dt} = D_M \frac{C_M(2,t) - 2C_M(1,t) + C_M(-1,t)}{\delta x^2} + V_1 \qquad \text{Equation B-18}$$

Substituting the value of fictitious concentration of the metabolite in box -1 ($C_M(-1,t)$) from Equation B-16 into Equation A-18, we get:

$$\frac{dC_M(1,t)}{dt} = \frac{D_M}{\delta x^2}\left[C_M(2,t) - 2C_M(1,t) + C_M(2,t) - \frac{2 \times \delta x \times \beta\_M_{ED}}{D_M}\left(C_{M,D} - \frac{C_M(1,t)}{PC_M}\right)\right] + V_1$$

Equation B-19

The boundary condition for the metabolite backflux from the first epithelial box into the receiver compartment can be expressed as shown in Equation B-20.

$$\frac{dC_M(1,t)}{dt} = \frac{2D_M}{\delta x^2}\left[(C_M(2,t) - C_M(1,t)) - \frac{\delta x \times \beta\_M_{ED}}{D_M}\left(C_{M,D} - \frac{C_M(1,t)}{PC_M}\right)\right] + V_1$$

Equation B-20

Boundary condition at the epithelial-submucosal boundary

The interior boundary between the epithelial and submucosal layers must satisfy a common flux to maintain diffusion continuity at the boundary.

The last epithelial box is the L^{th} box. The first box in the submucosal region is the $z(1)^{st}$ box. We assume that there is some partitioning between the two layers, with PC_{S_EtoS} and PC_{M_EtoS} being the epithelial-to-submucosal partition coefficient of the substrate and the metabolite respectively.

$$PC_{S\_EtoS} = \frac{C_S(z(1),t)}{C_S(L,t)}$$

Equation B-21

Mathematically, we can write the flux expression for the substrate at the epithelial-submucosal boundary as shown in Equation B-22:

$$D_{S\_E}\frac{dC_S(L,t)}{dx}\bigg|_{x=0^+} = -D_{S\_S}\frac{dC_S(z(1),t)}{dx}\bigg|_{x=0^-} = F = -\gamma_S\left(C_S(L,t) - \frac{C_S(z(1),t)}{PC_{S\_EtoS}}\right)$$

Equation B-22

Where F is an unknown function of the concentration at the boundary. D_{S_E} is the diffusion coefficient of the substrate in the epithelial layer and D_{S_E} is the diffusion coefficient of the substrate in the submucosal layer Factor γ_S accounts for the interfacial barrier at the epithelial-submucosal boundary for partitioning of the substrate from the epithelial layer into the submucosal region. If γ_S is 0, it represents an impermeable boundary. A high value of γ_S represents an instantaneous equilibrium. As γ_S gets smaller,

the barrier to partitioning equilibrium for the substrate between the last epithelial box and the first submucosal box increases.

We can now express the boundary condition using a central difference. To use central difference, we introduce a fictitious box in both the epithelial and submucosal layers. On the epithelial layer box (L+1) and on the submucosal layer, box (z(-1)).

$$D_{S\_E} \cdot \frac{C_S(L+1,t) - C_S(L-1,t)}{2\delta x} = -D_{sS} \cdot \frac{C_S(z(-1),t) - C_S(z(2),t}{2\delta x} = F$$
$$= -\gamma_S \left(C_S(L,t) - \frac{C_S(z(1),t)}{PC_{S\_EtoS}} \right)$$

Equation B-23

For the epithelial layer,

$$C_S(L+1,t) = \frac{-2\delta x \gamma_S \left(C_S(L,t) - \frac{C_S(z(1),t)}{PC_{S\_EtoS}} \right)}{D_{S\_E}} + C_S(L-1,t)$$

Equation B-24

The overall equation for the first order differential of the rate of change in substrate concentration with distance at the epithelial-submucosal boundary is given by using central difference.

$$\frac{dC_S(L,t)}{dt} = D_{S\_E} \left[\frac{C_S(L-1,t) - 2C_S(L,t) + C_S(L+1,t)}{\delta x^2} \right] - V_L$$

Equation B-25

Where V_L is for the rate of enzymatic reaction in the last epithelial box.

Combining Equation B-24 and Equation B-25, we obtain Equation B-26.

$$\frac{dC_S(L,t)}{dt} = D_{S\_E}\left[\frac{C_S(L-1,t) - 2C_S(L,t) + \frac{-2\delta x\gamma_S\left(C_S(L,t) - \frac{C_S(z(1),t)}{PC_{S\_EtoS}}\right)}{D_{S\_E}} + C_S(L-1,t)}{\delta x^2}\right] - V_L$$

Equation B-26

Simplifying Equation A-26 results in:

$$\frac{dC_S(L,t)}{dt} + V_L = \frac{D_{S\_E}}{\delta x^2}\left[2C_S(L-1,t) - 2C_S(L,t) + \frac{-2\delta x}{D_{S\_E}}\gamma_S\left(C_S(L,t) - \frac{C_S(z(1),t)}{PC_{S\_EtoS}}\right)\right]$$

Equation B-27

$$\frac{dC_S(L,t)}{dt} = \frac{2D_{S\_E}}{\delta x^2}(C_S(L-1,t) - C_S(L,t)) - \frac{2}{\delta x}\gamma_S\left(C_S(L,t) - \frac{C_S(z(1),t)}{PC_{S\_EtoS}}\right) - V_L$$

Equation B-28

Equation B-28 gives the boundary condition for substrate in the last epithelial box. Assuming a 1:1 molar conversion of substrate to metabolite, the boundary condition for the metabolite in the last epithelial box can be expressed as shown in EquationB-29.

$$\frac{dC_M(L,t)}{dt} = \frac{2D_{M\_E}}{\delta x^2}(C_M(L-1,t) - C_M(L,t)) - \frac{2}{\delta x}\gamma_M\left(C_M(L,t) - \frac{C_M(z(1),t)}{PC_{M\_EtoS}}\right) + V_L$$

Equation B-29

Similar boundary equations can be derived for the rate of change in concentration of substrate with time in the first submucosal box as shown in Equation B-30 to Equation B-35.

$$D_{S\_S} \cdot \frac{C_S(z(2),t) - C_S(z(-1),t)}{2\delta x} = -\gamma_S\left(C_S(L,t) - \frac{C_S(z(1),t)}{PC_{S\_EtoS}}\right)$$

Equation B-30

$$C_S(z(2),t) + \frac{2\delta x}{D_{S\_S}}\gamma_S\left(C_S(L,t) - \frac{C_S(z(1),t)}{PC_{S\_EtoS}}\right) = C_S(z(-1),t$$

Equation B-31

$$\frac{dC_S(z(1),t)}{dt} = D_{S\_S}\left[\frac{C_S(z(2),t) - 2C_S(z(1),t) + C_S(z(-1),t)}{\delta x^2}\right] - V_{z(1)}$$

Equation B-32

$$\frac{dC_S(z(1),t)}{dt} = \frac{D_{S\_S}}{\delta x^2}\Big[C_S(z(2),t) - 2C_S(z(1),t) + C_S(z(2),t) + \frac{2\delta x}{D_{S\_S}}\gamma_S\left(C_S(L,t) - \frac{C_S(z(1),t)}{PC_{S\_EtoS}}\right)\Big] - V_{z(1)}$$

Equation B-33

$$\frac{dC_S(z(1),t)}{dt} = \frac{2D_{S\_S}}{\delta x^2}\left[C_S(z(2),t) - C_S(z(1),t) + \frac{\delta x}{D_{sS}}\gamma_S\left(C_S(L,t) - \frac{C_S(z(1),t)}{PC_{S\_EtoS}}\right)\right] - V_{z(1)}$$

Equation B-34

$$\frac{dC_S(z(1),t)}{dt} = \frac{2D_{S\_S}}{\delta x^2}\left(C_S(z(2),t) - C_S(z(1),t)\right) + \frac{2}{\delta x}\gamma_S\left(C_S(L,t) - \frac{C_S(z(1),t)}{PC_{S\_EtoS}}\right) - V_{z(1)}$$

Equation B-35

Assuming a 1:1 molar conversion of substrate to metabolite, the boundary condition for the metabolite in the first submucosal box can be expressed as shown in Equation B-36.

$$\frac{dC_M(z(1),t)}{dt} = \frac{2D_{M\_S}}{\delta x^2}(C_M(z(2),t) - C_M(z(1),t)) + \frac{2}{\delta x}\gamma_{MS}\left(C_M(L,t) - \frac{C_M(z(1),t)}{PC_{M\_EtoS}}\right) + V_{z(1)}$$

Equation B-36

APPENDIX C

RECIPE OF BUFFERS AND REAGENT KITS

Real time RT-PCR

- SuperScript™ III Reverse Transcriptase

SuperScript™ III RT	200 Units/µl
Dithiothreitol (DTT)	0.1M
5X First-Strand Buffer	250 mM Tris-HCl (pH 8.3)
	375 mM KCl
	15 mM MgCl2

- 10X dNTP mix

dATP	10 mM
dCTP	10 mM
dGTP	10 mM
dTTP	10 mM

- SYBR® Advantage® qPCR Premix

  SYBR® Advantage® Premix (2X) containing:

  full-length *Taq polymerase*,

  hot-start *Taq* antibody

  dNTP mixture

  Mg^{2+}

  SYBR Green I

  ROX Reference Dye (50X)

Immunohistochemistry

- Zinc formalin

  Zinc sulfate 1%

  Formalin 3.7% (unbuffered)

- HIER- citrate buffer (pH 6)

  $Na_3C_6H_5O_7$ 10 mM

  Tween 20 0.05%

  HCl (1N) To adjust pH

- Dulbecco's phosphate buffered saline (PBS) (pH 7.4)

  KCl 2.67 mM

  NaCl 137.93 mM

  Na_2HPO_4 8.06 mM

  KH_2PO_4 1.47 mM

  NaOH (1N) To adjust pH

- Blocking solution (in PBS pH 7.4)

  Normal goat serum 10% v/v

  Bovine serum albumin 1% w/v

Microsomal assays

- Homogenization buffer (in 0.1 M phosphate buffer pH 7.4)

  Sucrose 0.25 M

  EDTA 1 mM

- Microsomal storage buffer (in 0.1 M phosphate buffer pH 7.4)

  Glycerol 20%

- NADPH regenerating system Solution A

  $NADP^+$ 31 mM

  Glucose-6-phosphate 66 mM

  $MgCl_2$ 66 mM

- NADPH regenerating system Solution B (in 5 mM sodium citrate)

  Glucose-6-phosphate dehydrogenase 40 U/ml

BCA assay

- Reagent A (in 0.1M NaOH)

  Sodium carbonate

  Sodium bicarbonate

  Sodium tartrate

  Bicinchoninic acid

- Reagent B

  Cupric sulfate 4% w/v

ELISA

- Wash buffer (in PBS, pH 7.4)

  Tween 20 0.05% w/v

- Blocking solution (in PBS pH 7.4)

  Bovine serum albumin 3% w/v

TEM imaging of microsomes

- Cacodylate buffer (in water, pH 7.2)

  Sodium cacodylate 0.1 M

In vitro diffusion studies

- KRB buffer (pH 7.4)

$MgCl_2$	1.67 mM
NaCl	119.76 mM
KCl	4.56 mM
Na_2HPO_4	0.83 mM
NaH_2PO_4	1.5 mM
$NaHCO_3$	15 mM
$CaCl_2$	1.2 mM
Glucose	10 mM

APPENDIX D

LIST OF ABBREVIATIONS

ABL: Aqueous boundary layer

ALDH: Aldehyde dehydrogenase

AMP: Adenosine 5′-monophosphate

ANOVA: Analysis of variance

APCI: Atmospheric pressure chemical ionization

ATP: adenosine 5′-triphosphate

BCA: Bicinchoninic acid

BSA: Bovine serum albumin

cDNA: complementary DNA

CMC: Carboxymethyl cellulose

CoA: Coenzyme A

CYP450: Cytochrome P450

dATP: 2-Deoxyadenosine-5´-triphosphate

dCTP: 2-Deoxycytidine-5´-triphosphate

dGTP: 2-Deoxyguanosine-5´-triphosphate

DNA: Deoxyribonucleic acid

dsDNA: Double stranded deoxyribonucleic acid

dNTP: 2-Deoxynucleoside-5´-triphosphate

DTT: Dithiothreitol

dTTP: 2-Deoxythymidine -5´-triphosphate

EDTA: Ethylenediaminetetraacetic acid

ELISA: Enzyme linked immune-sorbent assay

EM: Electron microscopy

Expr: Expressed

FMO: Flavin-containing monooxygenases

GAPDH: Glyceraldehyde 3-phosphate dehydrogenase

GSH: Glutathione

GST: Glutathione S-transferases

H and E: Hematoxylin and Eosin

HIER: Heat induced epitope retrieval

HPLC: High performance (pressure) liquid chromatography.

HRP: Horseradish peroxidase

IgG: Immunoglobulin G

IHC: Immunohistochemistry

KRB: Krebs-Ringer bicarbonate buffer

LC-MS: Liquid chromatography mass spectroscopy

MAO: Monoamine oxidase

m-s: mucosal-to-submucosal

Min: Minutes

MT: Melatonin

MT6: 6-hydroxymelatonin

mRNA: Messenger ribonucleic acid

$NADP^+$: Nicotinamide adenine dinucleotide phosphate

NADPH: Reduced form of nicotinamide adenine dinucleotide phosphate

NAS: N-acetylserotonin

NGS: Normal goat serum

Olf: Olfactory

PAPS: 3′-phosphoadenosine 5′-phosphosulfate

PBS: Phosphate buffered saline

PEG: Polyethylene glycol

PC: Partition coefficient

PCR: Polymerase chain reaction

RBC: Red blood cell

Resp: Respiratory

REM: Rapid eye movement

RIN: RNA integrity number

RNA: Ribonucleic acid

RT-PCR: Reverse transcriptase polymerase chain reaction

SPE: Solid phase extraction

SSwR: Sum of squared weighted residuals

SULT: Sulfotransferase

TEER: Transepithelial electrical resistance

TEM: Transmission electron microscopy

TMB: 3,3’,5,5’-tetramethylbenzidine

UGT: Uridine diphosphate glucuronosyltransferases

wRes: Weighted residuals

REFERENCES

(1) Chien, Y. W.; Chang, S. F. Intranasal drug delivery for systemic medications. *Critical Reviews in Therapeutic Drug Carrier Systems* **1987**, *4*, 67–194.

(2) Hussain, A. A. Intranasal drug delivery. *Advanced Drug Delivery Reviews* **1998**, *29*, 39–49.

(3) Pires, A.; Fortuna, A.; Alves, G.; Falcão, A. Intranasal drug delivery: how, why and what for? *Journal of Pharmacy & Pharmaceutical Sciences* **2009**, *12*, 288–311.

(4) Illum, L. Nasal drug delivery: possibilities, problems and solutions. *Journal of Controlled Release* **2003**, *87*, 187–198.

(5) Illum, L. Nasal drug delivery: new developments and strategies. *Drug Discovery Today* **2002**, *7*, 1184–1189.

(6) Callenbach, P. M. C.; Pels, L. P. M.; Mulder, P. G. H.; Linssen, W. H. J. P.; Gooskens, R. H. J. M.; Van der Zwan, J. L.; Brouwer, O. F. Sumatriptan nasal spray in the acute treatment of migraine in adolescents and children. *European Journal of Paediatric Neurology* **2007**, *11*, 325–330.

(7) Plosker, G. L.; McTavish, D. Intranasal salcatonin (salmon calcitonin). A review of its pharmacological properties and role in the management of postmenopausal osteoporosis. *Drugs & Aging* **1996**, *8*, 378–400.

(8) Pisal, S. S.; Paradkar, A. R.; Mahadik, K. R.; Kadam, S. S. Pluronic gels for nasal delivery of Vitamin B12. Part I: preformulation study. *International Journal of Pharmaceutics* **2004**, *270*, 37–45.

(9) Robson, W. L. M.; Leung, A. K. C.; Norgaard, J. P. The comparative safety of oral versus intranasal desmopressin for the treatment of children with nocturnal enuresis. *The Journal of Urology* **2007**, *178*, 24–30.

(10) Stead, L. F.; Perera, R.; Bullen, C.; Mant, D.; Hartmann-Boyce, J.; Cahill, K.; Lancaster, T. Nicotine replacement therapy for smoking cessation. *Cochrane database of systematic reviews (Online)* **2012**, *11*, CD000146.

(11) Global Industry Analysts Inc. Expanding Therapeutic Applications to Drive the US Intranasal Drug Delivery Market. *"Intranasal Drug Delivery: A US Market Report"* **2012**.

(12) Mygind, N.; Dahl, R. Anatomy, physiology and function of the nasal cavities in health and disease. *Advanced Drug Delivery Reviews* **1998**, *29*, 3–12.

(13) Illum, L. Is nose-to-brain transport of drugs in man a reality? *Journal of Pharmacy and Pharmacology* **2004**, *56*, 3–17.

(14) Wu, H.; Hu, K.; Jiang, X. From nose to brain: understanding transport capacity and transport rate of drugs. *Expert Opinion on Drug Delivery* **2008**, *5*, 1159–1168.

(15) Wong, Y. C.; Zuo, Z. Intranasal delivery-modification of drug metabolism and brain disposition. *Pharmaceutical Research* **2010**, *27*, 1208–1223.

(16) Graff, C. L.; Pollack, G. M. Nasal drug administration: potential for targeted central nervous system delivery. *Journal of Pharmaceutical Sciences* **2005**, *94*, 1187–1195.

(17) Arora, P.; Sharma, S.; Garg, S. Permeability issues in nasal drug delivery. *Drug Discovery Today* **2002**, *7*, 967–975.

(18) Jones, N. The nose and paranasal sinuses physiology and anatomy. *Advanced Drug Delivery Reviews* **2001**, *51*, 5–19.

(19) Corbo, D. C.; Liu, J. C.; Chien, Y. W. Characterization of the barrier properties of mucosal membranes. *Journal of Pharmaceutical Sciences* **1990**, *79*, 202–206.

(20) Smith, T. D.; Bhatnagar, K. P. Microsmatic primates: reconsidering how and when size matters. *The Anatomical Record Part B: The New Anatomist* **2004**, *279*, 24–31.

(21) Sarkar, M. A. Drug metabolism in the nasal mucosa. *Pharmaceutical Research* **1992**, *9*, 1–9.

(22) McMartin, C.; Hutchinson, L. E.; Hyde, R.; Peters, G. E. Analysis of structural requirements for the absorption of drugs and macromolecules from the nasal cavity. *Journal of Pharmaceutical Sciences* **1987**, *76*, 535–540.

(23) Marttin, E.; Schipper, N. G. M.; Verhoef, J.; Merkus, F. W. H. M. Nasal mucociliary clearance as a factor in nasal drug delivery. *Advanced Drug Delivery Reviews* **1998**, *29*, 13–38.

(24) Lansley, A. Mucociliary clearance and drug delivery via the respiratory tract. *Advanced Drug Delivery Reviews* **1993**, *11*, 299–327.

(25) Wilkinson, G. R. The dynamics of drug absorption, distribution, and elimination. In *Goodman and Gilman's the Pharmacological Basis of Therapeutics*; Hardman, J. G.; Limbird, L. E., Eds.; McGraw Hill, New York, 2001; pp. 3–29.

(26) Shuster, L. Metabolism of drugs and toxic substances. *Annual Review of Biochemistry* **1964**, *33*, 571–596.

(27) Iyanagi, T. Molecular mechanism of phase I and phase II drug-metabolizing enzymes: implications for detoxification. *International Review of Cytology* **2007**, *260*, 35–112.

(28) Lee, M.-Y.; Dordick, J. S. High-throughput human metabolism and toxicity analysis. *Current Opinion in Biotechnology* **2006**, *17*, 619–27.

(29) Gonzales, F.J., Tukey, R. H. Drug metabolism. In *Goodman and Gilman's The Pharmacological Basis of Therapeutics*; Brunton, L.L., Lazo, J.S., Parker, K. L., Ed.; McGraw-Hill, New York, United States, 2005.

(30) DeWitt, R. C.; Kudsk, K. A. The gut's role in metabolism, mucosal barrier function, and gut immunology. *Infectious Disease Clinics of North America* **1999**, *13*, 465–481.

(31) Doherty, M. M.; Charman, W. N. The mucosa of the small intestine: how clinically relevant as an organ of drug metabolism? *Clinical Pharmacokinetics* **2002**, *41*, 235–253.

(32) Beaumont, K. The Importance of Gut Wall Metabolism in Determining Drug Bioavailability. In *Drug Bioavailability*; Wiley-VCH Verlag GmbH & Co. KGaA, 2004; pp. 311–328.

(33) Zhang, J.; Wang, Y. F. Xenobiotic-metabolizing enzymes in human lung. *Current Drug Metabolism* **2006**, *7*, 939–948.

(34) Mace, K.; Bowman, E.; Vautravers, P.; Shields, P.; Harris, C.; Pfeifer, A. M. A. Characterisation of xenobiotic-metabolising enzyme expression in human bronchial mucosa and peripheral lung tissues. *European Journal of Cancer* **1998**, *34*, 914–920.

(35) Bernauer, U.; Heinrich-Hirsch, B.; Tönnies, M.; Peter-Matthias, W.; Gundert-Remy, U. Characterisation of the xenobiotic-metabolizing Cytochrome P450 expression pattern in human lung tissue by immunochemical and activity determination. *Toxicology Letters* **2006**, *164*, 278–288.

(36) Zhao, X.; Imig, J. D. Kidney CYP450 enzymes: biological actions beyond drug metabolism. *Current Drug Metabolism* **2003**, *4*, 73–84.

(37) Hadley, W. M.; Dahl, A. R. Cytochrome P-450-dependent monooxygenase activity in nasal membranes of six species. *Drug Metabolism and Disposition* **1983**, *11*, 275–276.

(38) Hikima, T.; Tojo, K.; Maibach, H. Skin metabolism in transdermal therapeutic systems. *Skin Pharmacology and Physiology* **2005**, *18*, 153–159.

(39) Baron, J. M.; Merk, H. F. Drug metabolism in the skin. *Current Opinion in Allergy and Clinical Immunology* **2001**, *1*, 287–291.

(40) Syme, M. R.; Paxton, J. W.; Keelan, J. A. Drug transfer and metabolism by the human placenta. *Clinical Pharmacokinetics* **2004**, *43*, 487–514.

(41) Hua, X.; Wan, L. Comparison of enzyme activities of tissues lining portals of absorption of drugs : Species differences. *Drug Delivery* **1991**, *70*, 271–283.

(42) Thornton-Manning, J. Metabolic capacity of nasal tissue:: interspecies comparisons of xenobiotic-metabolizing enzymes. *Mutation Research* **1997**, *380*, 43–59.

(43) Yamahara, H.; Lee, V. H. L. Drug metabolism in the oral cavity. *Advanced Drug Delivery Reviews* **1993**, *12*, 25–39.

(44) Rosa, C. G.; Velardo, J. T. Histochemical localization of vaginal oxidative enzymes and mucins in rats treated with estradiol and progesterone. *Annals of the New York Academy of Sciences* **1959**, *83*, 122–44.

(45) Nebert, D. W.; Russell, D. W. Clinical importance of the cytochromes P450. *Lancet* **2002**, *360*, 1155–1162.

(46) Coon, M. J. Cytochrome P450: nature's most versatile biological catalyst. *Annual Review of Pharmacology and Toxicology* **2005**, *45*, 1–25.

(47) Cytochrome P450 Homepage http://drnelson.uthsc.edu/CytochromeP450.html.

(48) Rendic, S.; Di Carlo, F. Human cytochrome P450 enzymes: a status report summarizing their reactions, substrates, inducers, and inhibitors. *Drug Metabolism Reviews* **1997**, *29*, 413.

(49) Bertz, R. J.; Granneman, G. R. Use of in vitro and in vivo data to estimate the likelihood of metabolic pharmacokinetic interactions. *Clinical Pharmacokinetics* **1997**, *32*, 210–258.

(50) Zhou, S.-F.; Liu, J.-P.; Chowbay, B. Polymorphism of human cytochrome P450 enzymes and its clinical impact. *Drug Metabolism Reviews* **2009**, *41*, 89–295.

(51) Meunier, B.; De Visser, S. P.; Shaik, S.; Visser, S. P. Mechanism of oxidation reactions catalyzed by cytochrome p450 enzymes. *Chemical Reviews* **2004**, *104*, 3947–3980.

(52) Dahl, A.; Briner, T. Biological fate of a representative lipophilic metal compound (ferrocene) deposited by inhalation in the respiratory tract of rats. *Toxicology and Applied Pharmacology* **1980**, *56*, 232–239.

(53) Brittebo, E.; Lofberg, B.; Tjalve, H. Sites of metabolism of N-nitrosodiethylamine in mice. *Chemico-Biological Interactions* **1981**, *34*, 209–221.

(54) Dahl, A. R.; Hadley, W. M.; Hahn, F. F.; Benson, J. M.; McClellan, R. O. Cytochrome P-450-dependent monooxygenases in olfactory epithelium of dogs: possible role in tumorigenicity. *Science* **1982**, *216*, 57.

(55) Reznik, G.; Stinson, S. F. *Nasal Tumors in Animals and Man*; Reznik, G., Ed.; CRC Press, 1983; p. 288.

(56) Ding, X. X.; Koop, D. R.; Crump, B. L.; Coon, M. J. Immunochemical identification of cytochrome P-450 isozyme 3a (P-450ALC) in rabbit nasal and kidney microsomes and evidence for differential induction by alcohol. *Molecular Pharmacology* **1986**, *30*, 370–378.

(57) Minn, A.; Pelczar, H.; Denizot, C.; Martinet, M.; Heydel, J. J. M.; Walther, B.; Goudonnet, H.; Artur, Y.; Poincare, H. Characterization of microsomal cytochrome P450-dependent monooxygenases in the rat olfactory mucosa. *Drug Metabolism and Disposition* **2005**, *33*, 1229–1237.

(58) Ling, G.; Gu, J.; Genter, M. B.; Zhuo, X.; Ding, X. Regulation of cytochrome P450 gene expression in the olfactory mucosa. *Chemico-Biological Interactions* **2004**, *147*, 247–258.

(59) Ding, X.; Kaminsky, L. S. Human extrahepatic cytochromes P450: function in xenobiotic metabolism and tissue-selective chemical toxicity in the respiratory and gastrointestinal tracts. *Annual Review of Pharmacology and Toxicology* **2003**, *43*, 149–173.

(60) Hadley, W. Cytochrome P-450 dependent monooxygenase activity in rat nasal epithelial membranes. *Toxicology Letters* **1982**, *10*, 417–422.

(61) Reed, C. J. Drug metabolism in the nasal cavity: relevance to toxicology. *Drug Metabolism Reviews* **1993**, *25*, 173–205.

(62) Reed, C.; Lock, E. A.; De Matteis, F. NADPH: cytochrome P-450 reductase in olfactory epithelium. Relevance to cytochrome P-450-dependent reactions. *Biochemical Journal* **1986**, *240*, 585.

(63) Miwa, G.; West, S. Studies on the rate-limiting enzyme component in the microsomal monooxygenase system. Incorporation of purified NADPH-cytochrome c reductase and cytochrome P-450 into rat liver microsomes. *Journal of Biological Chemistry* **1978**, *253*, 1921–1929.

(64) Ding, X. X.; Coon, M. J. Immunochemical characterization of multiple forms of cytochrome P-450 in rabbit nasal microsomes and evidence for tissue-specific expression of P-450s NMa and NMb. *Molecular Pharmacology* **1990**, *37*, 489–496.

(65) Dahl, A. R. Possible consequences of cytochrome P450-dependent monooxygenases in nasal tissues. In *Toxicology of The Nasal Passages*; Barroe, C. S., Ed.; Hemisphere, New York, NY, 1986; pp. 263–273.

(66) Marini, S.; Longo, V.; Mazzaccaro, A.; Gervasi, P. G. Xenobiotic-metabolizing enzymes in pig nasal and hepatic tissues. *Xenobiotica* **1998**, *28*, 923–935.

(67) Longo, V.; Amato, G.; Santucci, A.; Gervasi, P. G. Purification and characterization of three constitutive cytochrome P-450 isoforms from bovine olfactory epithelium. *Biochemical Journal* **1997**, *323*, 65.

(68) Larsson, P. Cell-specific activation of aflatoxin B1 correlates with presence of some cytochrome P450 enzymes in olfactory and respiratory tissues in horse. *Research in Veterinary Science* **2003**, *74*, 227–233.

(69) Longo, V.; Mazzaccaro, A.; Ventura, P.; Gervasi, P. G. Drug-metabolizing enzymes in respiratory nasal mucosa and liver of cynomolgus monkey. *Xenobiotica* **1992**, *22*, 427–431.

(70) Gervasi, P. G.; Longo, V.; Naldi, F.; Panattoni, G.; Ursino, F. Xenobiotic-metabolizing enzymes in human respiratory nasal mucosa. *Biochemical Pharmacology* **1991**, *41*, 177–184.

(71) Longo, V.; Pacifici, G. M.; Panattoni, G.; Ursino, F.; Gervasi, P. G. Metabolism of diethylnitrosamine by microsomes of human respiratory nasal mucosa and liver. *Biochemical Pharmacology* **1989**, *38*, 1867–1869.

(72) Venter, J. C.; Adams, M. D.; Myers, E. W.; Li, P. W.; Mural, R. J.; Sutton, G. G.; Smith, H. O.; Yandell, M.; Evans, C. a; Holt, R. a; Gocayne, J. D.; Amanatides, P.; Ballew, R. M.; Huson, D. H.; Wortman, J. R.; Zhang, Q.; Kodira, C. D.; Zheng, X. H.; Chen, L.; Skupski, M.; Subramanian, G.; Thomas, P. D.; Zhang, J.; Gabor Miklos, G. L.; Nelson, C.; Broder, S.; Clark, a G.; Nadeau, J.; McKusick, V. a; Zinder, N.; Levine, a J.; Roberts, R. J.; Simon, M.; Slayman, C.; Hunkapiller, M.; Bolanos, R.; Delcher, A.; Dew, I.; Fasulo, D.; Flanigan, M.; Florea, L.; Halpern, A.; Hannenhalli, S.; Kravitz, S.; Levy, S.; Mobarry, C.; Reinert, K.; Remington, K.; Abu-Threideh, J.; Beasley, E.; Biddick, K.; Bonazzi, V.; Brandon, R.; Cargill, M.; Chandramouliswaran, I.; Charlab, R.; Chaturvedi, K.; Deng, Z.; Di Francesco, V.; Dunn, P.; Eilbeck, K.; Evangelista, C.; Gabrielian, a E.; Gan, W.; Ge, W.; Gong, F.; Gu, Z.; Guan, P.; Heiman, T. J.; Higgins, M. E.; Ji, R. R.; Ke, Z.; Ketchum, K. a; Lai, Z.; Lei, Y.; Li, Z.; Li, J.; Liang, Y.; Lin, X.; Lu, F.; Merkulov, G. V; Milshina, N.; Moore, H. M.; Naik, a K.; Narayan, V. a; Neelam, B.; Nusskern, D.; Rusch, D. B.; Salzberg, S.; Shao, W.; Shue, B.; Sun, J.; Wang, Z.; Wang, A.; Wang, X.; Wang, J.; Wei, M.; Wides, R.; Xiao, C.; Yan, C.; Yao, A.; Ye, J.; Zhan, M.; Zhang, W.; Zhang, H.; Zhao, Q.; Zheng, L.; Zhong, F.; Zhong, W.; Zhu, S.; Zhao, S.; Gilbert, D.; Baumhueter, S.; Spier, G.; Carter, C.; Cravchik, A.; Woodage, T.; Ali, F.; An, H.; Awe, A.; Baldwin, D.; Baden, H.; Barnstead, M.; Barrow, I.; Beeson, K.; Busam, D.; Carver, A.; Center, A.; Cheng, M. L.; Curry, L.; Danaher, S.; Davenport, L.; Desilets, R.; Dietz, S.; Dodson, K.; Doup, L.; Ferriera, S.; Garg, N.; Gluecksmann, A.; Hart, B.; Haynes, J.; Haynes, C.; Heiner, C.; Hladun, S.; Hostin, D.; Houck, J.; Howland, T.; Ibegwam, C.; Johnson, J.; Kalush, F.; Kline, L.; Koduru, S.; Love, A.; Mann, F.; May, D.; McCawley, S.; McIntosh, T.; McMullen, I.; Moy, M.; Moy, L.; Murphy, B.; Nelson, K.; Pfannkoch, C.; Pratts, E.; Puri, V.; Qureshi, H.; Reardon, M.; Rodriguez, R.; Rogers, Y. H.; Romblad, D.; Ruhfel, B.; Scott, R.; Sitter, C.; Smallwood, M.; Stewart, E.; Strong, R.; Suh, E.; Thomas, R.; Tint, N. N.; Tse, S.; Vech, C.; Wang, G.; Wetter, J.; Williams, S.; Williams, M.; Windsor, S.; Winn-Deen, E.; Wolfe, K.; Zaveri, J.; Zaveri, K.; Abril, J. F.; Guigó, R.; Campbell, M. J.; Sjolander, K. V; Karlak, B.; Kejariwal, A.; Mi, H.; Lazareva, B.; Hatton, T.; Narechania, A.; Diemer, K.; Muruganujan, A.; Guo, N.; Sato, S.; Bafna, V.; Istrail, S.; Lippert, R.; Schwartz, R.; Walenz, B.; Yooseph, S.; Allen, D.; Basu, A.; Baxendale, J.; Blick, L.; Caminha, M.; Carnes-Stine, J.; Caulk, P.; Chiang, Y. H.; Coyne, M.; Dahlke, C.; Mays, A.; Dombroski, M.; Donnelly, M.; Ely, D.; Esparham, S.; Fosler, C.; Gire, H.; Glanowski, S.; Glasser, K.; Glodek, A.; Gorokhov, M.; Graham, K.; Gropman, B.; Harris, M.; Heil, J.; Henderson, S.; Hoover, J.; Jennings, D.; Jordan, C.; Jordan, J.; Kasha, J.; Kagan, L.; Kraft, C.; Levitsky, A.; Lewis, M.; Liu, X.; Lopez, J.; Ma, D.; Majoros, W.; McDaniel, J.; Murphy, S.; Newman, M.; Nguyen, T.; Nguyen, N.; Nodell, M.; Pan, S.; Peck, J.; Peterson, M.; Rowe, W.; Sanders, R.; Scott, J.; Simpson, M.; Smith, T.; Sprague, A.; Stockwell, T.; Turner, R.; Venter, E.; Wang, M.; Wen, M.; Wu, D.; Wu, M.; Xia, A.; Zandieh, A.; Zhu, X. The sequence of the human genome. *Science* **2001**, *291*, 1304–51.

(73) Su, T.; Sheng, J. J.; Lipinskas, T. W.; Ding, X. Expression of CYP2A genes in rodent and human nasal mucosa. *Drug Metabolism and Disposition* **1996**, *24*, 884–890.

(74) Chen, Y. Immunoblot analysis and immunohistochemical characterization of CYP2A expression in human olfactory mucosa. *Biochemical Pharmacology* **2003**, *66*, 1245–1251.

(75) Yokose, T.; Doy, M.; Taniguchi, T.; Shimada, T.; Kakiki, M.; Horie, T.; Matsuzaki, Y.; Mukai, K. Immunohistochemical study of cytochrome P450 2C and 3A in human non-neoplastic and neoplastic tissues. *Virchows Archiv* **1999**, *434*, 401–411.

(76) Zhang, X.; Zhang, Q. Y.; Liu, D.; Su, T.; Weng, Y.; Ling, G.; Chen, Y.; Gu, J.; Schilling, B.; Ding, X. Expression of cytochrome p450 and other biotransformation genes in fetal and adult human nasal mucosa. *Drug Metabolism and Disposition* **2005**, *33*, 1423–1428.

(77) Sheng, J.; Ding, X. Identification of human genes related to olfactory-specific CYP2G1. *Biochemical and Biophysical Research Communications* **1996**, *218*, 570–574.

(78) Saarikoski, S. T.; Wikman, H. a-L.; Smith, G.; Wolff, C. H. J.; Husgafvel-Pursiainen, K. Localization of cytochrome P450 CYP2S1 expression in human tissues by in situ hybridization and immunohistochemistry. *The Journal of Histochemistry and Cytochemistry* **2005**, *53*, 549–556.

(79) Gu, J.; Su, T.; Chen, Y.; Zhang, Q. Y.; Ding, X. Expression of biotransformation enzymes in human fetal olfactory mucosa: potential roles in developmental toxicity. *Toxicology and Applied Pharmacology* **2000**, *165*, 158–162.

(80) Andersen, M. E.; Green, T.; Frederick, C. B.; Bogdanffy, M. S. Physiologically Based Pharmacokinetic (PBPK) Models for Nasal Tissue Dosimetry of Organic Esters: Assessing the State-of-Knowledge and Risk Assessment Applications with Methyl Methacrylate and Vinyl Acetate. *Regulatory Toxicology and Pharmacology* **2002**, *36*, 234–245.

(81) Sasagawa, T.; Yamada, T.; Nakagawa, T.; Tsujioka, T.; Takahashi, Y.; Kawakita, N.; Nonaka, K.; Nakamura, A. In vitro metabolism of dexamethasone cipecilate, a novel synthetic corticosteroid, in human liver and nasal mucosa. *Xenobiotica* **2011**, *41*, 874–884.

(82) Sato, H.; Nave, R.; Nonaka, T.; Mochizuki, T.; Takahama, S.; Kondo, S. In vitro metabolism of ciclesonide in human nasal epithelial cells. *Biopharmaceutics and Drug Disposition* **2007**, *28*, 43–50.

(83) Nave, R.; McCracken, N. Metabolism of ciclesonide in the upper and lower airways: review of available data. *Journal of Asthma and Allergy* **2008**, *1*, 11–8.

(84) Chemuturi, N. V. N. V.; Donovan, M. D. M. D. Metabolism of dopamine by the nasal mucosa. *Journal of Pharmaceutical Sciences* **2006**, *95*, 2507–2515.

(85) Pontiroli, A. E. Peptide hormones: review of current and emerging uses by nasal delivery. *Advanced Drug Delivery Reviews* **1998**, *29*, 81–87.

(86) Agu, R. U.; Vu Dang, H.; Jorissen, M.; Willems, T.; Kinget, R.; Verbeke, N. Nasal absorption enhancement strategies for therapeutic peptides: an in vitro study using cultured human nasal epithelium. *International Journal of Pharmaceutics* **2002**, *237*, 179–191.

(87) Harris, A. S. Review: clinical opportunities provided by the nasal administration of peptides. *Journal of Drug Targeting* **1993**, *1*, 101–16.

(88) Ohkubo, K.; Baraniuk, J. N.; Hohman, R.; Merida, M.; Hersh, L. B.; Kaliner, M. a Aminopeptidase activity in human nasal mucosa. *The Journal of Allergy and Clinical Immunology* **1998**, *102*, 741–750.

(89) Agu, R. U.; Obimah, D. U.; Lyzenga, W. J.; Jorissen, M.; Massoud, E.; Verbeke, N. Specific aminopeptidases of excised human nasal epithelium and primary culture: a comparison of functional characteristics and gene transcripts expression. *The Journal of Pharmacy and Pharmacology* **2009**, *61*, 599–606.

(90) Ohkubo, K.; Baraniuk, J. N.; Merida, M.; Hausfeld, J. N.; Okada, H.; Kaliner, M. a Human nasal mucosal carboxypeptidase: activity, location, and release. *The Journal of Alergy and Clinical Immunology* **1995**, *96*, 924–931.

(91) Schorn, K.; Hochstrasser, K. Biochemical investigations of nasal secretions. *Acta oto-rhino-laryngologica Belgica* **1979**, *33*, 603–606.

(92) Chung, F. Y.; Donovan, M. D. Bradykinin metabolism in rat and sheep nasal secretions. *Journal of Pharmaceutical Sciences* **1995**, *84*, 829–834.

(93) Schmidt, M.; Peter, H.; Lang, S.; Ditzinger, G. In vitro cell models to study nasal mucosal permeability and metabolism. *Advanced Drug Delivery Reviews* **1998**, *29*, 51–79.

(94) Schmidt, M. C.; Simmen, D.; Hilbe, M.; Boderke, P.; Ditzinger, G.; Sandow, J.; Lang, S.; Rubas, W.; Merkle, H. P. Validation of excised bovine nasal mucosa as in vitro model to study drug transport and metabolic pathways in nasal epithelium. *Journal of Pharmaceutical Sciences* **2000**, *89*, 396–407.

(95) Wadell, C.; Björk, E.; Camber, O. Permeability of porcine nasal mucosa correlated with human nasal absorption. *European Journal of Pharmaceutical Sciences* **2003**, *18*, 47–53.

(96) Lee, T. C.; Wu, R.; Brody, A. R.; Barrett, J. C.; Nettesheim, P. Growth and differentiation of hamster tracheal epithelial cells in culture. *Experimental Lung Research* **1984**, *6*, 27–45.

(97) Steele, V. E.; Arnold, J. T. Isolation and long-term culture of rat, rabbit, and human nasal turbinate epithelial cells. *In vitro Cellular & Developmental Biology* **1985**, *21*, 681–687.

(98) Lee, M.-K.; Yoo, J.-W.; Lin, H.; Kim, Y.-S.; Kim, D.-D.; Choi, Y.-M.; Park, S.-K.; Lee, C.-H.; Roh, H.-J. Air-liquid interface culture of serially passaged human nasal epithelial cell monolayer for in vitro drug transport studies. *Drug Delivery* **2005**, *12*, 305–311.

(99) Chemuturi, N. V; Hayden, P.; Klausner, M.; Donovan, M. D. Comparison of human tracheal/bronchial epithelial cell culture and bovine nasal respiratory explants for nasal drug transport studies. *Journal of Pharmaceutical Sciences* **2005**, *94*, 1976–1985.

(100) Aklillu, E.; Carrillo, J. A.; Makonnen, E.; Hellman, K.; Pitarque, M.; Bertilsson, L.; Ingelman-Sundberg, M. Genetic polymorphism of CYP1A2 in Ethiopians affecting induction and expression: characterization of novel haplotypes with single-nucleotide polymorphisms in intron 1. *Molecular Pharmacology* **2003**, *64*, 659–669.

(101) Brockmöller, J.; Kirchheiner, J.; Schmider, J.; Walter, S.; Sachse, C.; Müller-Oerlinghausen, B.; Roots, I. The impact of the CYP2D6 polymorphism on haloperidol pharmacokinetics and on the outcome of haloperidol treatment. *Clinical Pharmacology and Therapeutics* **2002**, *72*, 438–452.

(102) Ioannides, C. Effect of diet and nutrition on the expression of cytochromes P450. *Xenobiotica* **1999**, *29*, 109–154.

(103) Yang, S.-P.; Medling, T.; Raner, G. M. Cytochrome P450 expression and activities in rat, rabbit and bovine tongue. *Comparative Biochemistry and Physiology Part C: Toxicology and Pharmacology* **2003**, *136*, 297–308.

(104) Grasso, E.; Longo, V.; Coceani, F.; Giovanni Gervasi, P. Cytochrome P450 expression and catalytic activity in coronary arteries and liver of cattle. *Biochimica et biophysica acta* **2005**, *1722*, 116–23.

(105) Darwish, W. S.; Ikenaka, Y.; Eldaly, E. A.; Ohno, M.; Sakamoto, K. Q.; Fujita, S.; Ishizuka, M. Cytochrome P450 1A-dependent activities in deer, cattle and horses. *Journal of Veterinary Medical Science* **2010**, *72*, 561–566.

(106) Virkel, G.; Carletti, M.; Cantiello, M.; Della Donna, L.; Gardini, G.; Girolami, F.; Nebbia, C. Characterization of xenobiotic metabolizing enzymes in bovine small intestinal mucosa. *Journal of Veterinary Pharmacology and Therapeutics* **2010**, *33*, 295–303.

(107) Lerner, A. B.; Nordlund, J. J. Melatonin: clinical pharmacology. *Journal of Neural Transmission. Supplementum* **1978**, 339–347.

(108) Karasek, M. Melatonin in humans-where we are 40 years after its discovery. *Neuro Endocrinology Letters* **1999**, *20*, 179–188.

(109) Macchi, M. M.; Bruce, J. N. Human pineal physiology and functional significance of melatonin. *Frontiers in Neuroendocrinology* **2004**, *25*, 177–195.

(110) Pandi-Perumal, S. R.; Srinivasan, V.; Maestroni, G. J. M.; Cardinali, D. P.; Poeggeler, B.; Hardeland, R. Melatonin: Nature's most versatile biological signal? *The FEBS Journal* **2006**, *273*, 2813–2838.

(111) Dollins, A. B.; Zhdanova, I. V; Wurtman, R. J.; Lynch, H. J.; Deng, M. H. Effect of inducing nocturnal serum melatonin concentrations in daytime on sleep, mood, body temperature, and performance. *Proceedings of the National Academy of Sciences of the United States of America* **1994**, *91*, 1824–1828.

(112) Tzischinsky, O.; Lavie, P. Melatonin possesses time-dependent hypnotic effects. *Sleep* **1994**, *17*, 638–45.

(113) Barrenetxe, J.; Delagrange, P.; Martínez, J. A. Physiological and metabolic functions of melatonin. *Journal of Physiology and Biochemistry* **2004**, *60*, 61–72.

(114) Dubocovich, M. L.; Markowska, M. Functional MT1 and MT2 melatonin receptors in mammals. *Endocrine* **2005**, *27*, 101–110.

(115) Arendt, J.; Middleton, B.; Stone, B.; Skene, D. Complex effects of melatonin: evidence for photoperiodic responses in humans? *Sleep* **1999**, *22*, 625–635.

(116) Nishida, S. Metabolic effects of melatonin on oxidative stress and diabetes mellitus. *Endocrine* **2005**, *27*, 131–136.

(117) Panzer, A.; Viljoen, M. The validity of melatonin as an oncostatic agent. *Journal of Pineal Research* **1997**, *22*, 184–202.

(118) Reiter, R. J.; Tan, D. X.; Osuna, C.; Gitto, E. Actions of melatonin in the reduction of oxidative stress. A review. *Journal of Biomedical Science* **2000**, *7*, 444–458.

(119) Carpentieri, a; Díaz de Barboza, G.; Areco, V.; Peralta López, M.; Tolosa de Talamoni, N. New perspectives in melatonin uses. *Pharmacological Research* **2012**, *65*, 437–444.

(120) Dubocovich, M. L. Melatonin receptors: role on sleep and circadian rhythm regulation. *Sleep Medicine* **2007**, *8 Suppl 3*, 34–42.

(121) Mathes, A. M. Hepatoprotective actions of melatonin: possible mediation by melatonin receptors. *World Journal of Gastroenterology* **2010**, *16*, 6087–6097.

(122) Yeleswaram, K.; McLaughlin, L. G.; Knipe, J. O.; Schabdach, D. Pharmacokinetics and oral bioavailability of exogenous melatonin in preclinical animal models and clinical implications. *Journal of Pineal Research* **1997**, *22*, 45–51.

(123) Lane, E. A.; Moss, H. B. Pharmacokinetics of melatonin in man: first pass hepatic metabolism. *The Journal of Clinical Endocrinology and Metabolism* **1985**, *61*, 1214–1216.

(124) Waldhauser, F.; Waldhauser, M.; Lieberman, H. R.; Deng, M. H.; Lynch, H. J.; Wurtman, R. J. Bioavailability of oral melatonin in humans. *Neuroendocrinology* **1984**, *39*, 307–313.

(125) Kopin, I. J.; Pare, C. M.; Axelrod, J.; Weissbach, H. The fate of melatonin in animals. *The Journal of Biological Chemistry* **1961**, *236*, 3072–3075.

(126) Leone, A. M.; Francis, P. L.; Silman, R. E. The isolation, purification, and characterisation of the principal urinary metabolites of melatonin. *Journal of Pineal Research* **1987**, *4*, 253–66.

(127) Ma, X.; Idle, J. R. J. J. R.; Krausz, K. W. K. K. W.; Gonzalez, F. J. Metabolism of melatonin by human cytochromes P450. *Drug Metabolism and Disposition* **2005**, *33*, 489–494.

(128) Semak, I.; Korik, E.; Antonova, M.; Wortsman, J.; Slominski, A. Metabolism of melatonin by cytochrome P450s in rat liver mitochondria and microsomes. *Journal of Pineal Research* **2008**, *45*, 515–523.

(129) Facciolá, G.; Hidestrand, M.; Von Bahr, C.; Tybring, G. Cytochrome P450 isoforms involved in melatonin metabolism in human liver microsomes. *European Journal of Clinical Pharmacology* **2001**, *56*, 881–888.

(130) Skene, D. J.; Papagiannidou, E.; Hashemi, E.; Snelling, J.; Lewis, D. F.; Fernandez, M.; Ioannides, C. Contribution of CYP1A2 in the hepatic metabolism of melatonin: studies with isolated microsomal preparations and liver slices. *Journal of Pineal Research* **2001**, *31*, 333–342.

(131) Härtter, S.; Ursing, C.; Morita, S.; Tybring, G.; Von Bahr, C.; Christensen, M.; Röjdmark, S.; Bertilsson, L. Orally given melatonin may serve as a probe drug for cytochrome P450 1A2 activity in vivo: a pilot study. *Clinical Pharmacology and Therapeutics* **2001**, *70*, 10–16.

(132) Yeleswaram, K.; Vachharajani, N.; Santone, K. Involvement of cytochrome P-450 isozymes in melatonin metabolism and clinical implications. *Journal of Pineal Research* **1999**, *26*, 190–191.

(133) Von Bahr, C.; Ursing, C.; Yasui, N.; Tybring, G.; Bertilsson, L.; Röjdmark, S. Fluvoxamine but not citalopram increases serum melatonin in healthy subjects-- an indication that cytochrome P450 CYP1A2 and CYP2C19 hydroxylate melatonin. *European Journal of Clinical Pharmacology* **2000**, *56*, 123–127.

(134) Young, I. M.; Leone, R. M.; Francis, P.; Stovell, P.; Silman, R. E. Melatonin is metabolized to N-acetyl serotonin and 6-hydroxymelatonin in man. *The Journal of Clinical Endocrinology and Metabolism* **1985**, *60*, 114–119.

(135) Chang, T. K. H.; Chen, J.; Yang, G.; Yeung, E. Y. H. Inhibition of procarcinogen-bioactivating human CYP1A1, CYP1A2 and CYP1B1 enzymes by melatonin. *Journal of Pineal Research* **2010**, *48*, 55–64.

(136) Härtter, S.; Wang, X.; Weigmann, H.; Friedberg, T.; Arand, M.; Oesch, F.; Hiemke, C. Differential effects of fluvoxamine and other antidepressants on the biotransformation of melatonin. *Journal of Clinical Psychopharmacology* **2001**, *21*, 167–174.

(137) Ma, X.; Idle, J.; Krausz, K. Metabolism of melatonin by human cytochromes p450. *Drug metabolism and disposition* **2005**, *33*, 489–494.

(138) Hardeland, R. Melatonin metabolism in the central nervous system. *Current Neuropharmacology* **2010**, *8*, 168–181.

(139) Hughes, R. J.; Badia, P. Sleep-promoting and hypothermic effects of daytime melatonin administration in humans. *Sleep* **1997**, *20*, 124–131.

(140) Dowling, G. A.; Mastick, J.; Colling, E.; Carter, J. H.; Singer, C. M.; Aminoff, M. J. Melatonin for sleep disturbances in Parkinson's disease. *Sleep Medicine* **2005**, *6*, 459–466.

(141) Singer, C.; Tractenberg, R. E.; Kaye, J.; Schafer, K.; Gamst, A.; Grundman, M.; Thomas, R.; Thal, L. J. A multicenter, placebo-controlled trial of melatonin for sleep disturbance in Alzheimer's disease. *Sleep* **2003**, *26*, 893–901.

(142) Van der Heijden, K. B.; Smits, M. G.; Van Someren, E. J. W.; Ridderinkhof, K. R.; Gunning, W. B. Effect of melatonin on sleep, behavior, and cognition in ADHD and chronic sleep-onset insomnia. *Journal of the American Academy of Child and Adolescent Psychiatry* **2007**, *46*, 233–241.

(143) Riemersma-van der Lek, R. F.; Swaab, D. F.; Twisk, J.; Hol, E. M.; Hoogendijk, W. J. G.; Van Someren, E. J. W. Effect of bright light and melatonin on cognitive and noncognitive function in elderly residents of group care facilities: a randomized controlled trial. *The Journal of the American Medical Association* **2008**, *299*, 2642–55.

(144) DeMuro, R. L.; Nafziger, A. N.; Blask, D. E.; Menhinick, A. M.; Bertino, J. S. The absolute bioavailability of oral melatonin. *Journal of Clinical Pharmacology* **2000**, *40*, 781–784.

(145) Bénès, L.; Claustrat, B.; Horrière, F.; Geoffriau, M.; Konsil, J.; Parrott, K. a; DeGrande, G.; McQuinn, R. L.; Ayres, J. W. Transmucosal, oral controlled-release, and transdermal drug administration in human subjects: a crossover study with melatonin. *Journal of Pharmaceutical Sciences* **1997**, *86*, 1115–1119.

(146) Lee, B. Oral controlled release of melatonin using polymer-reinforced and coated alginate beads. *International Journal of Pharmaceutics* **1996**, *144*, 37–46.

(147) Lee, B.-J.; Parrott, K. A.; Ayres, J. W.; Sack, R. L. Design and evaluation of an oral controlled release delivery system for melatonin in human subjects. *International Journal of Pharmaceutics* **1995**, *124*, 119–127.

(148) Costa, E. J.; Lopes, R. H.; Lamy-Freund, M. T. Permeability of pure lipid bilayers to melatonin. *Journal of Pineal Research* **1995**, *19*, 123–6.

(149) Bechgaard, E.; Lindhardt, K.; Martinsen, L. Intranasal absorption of melatonin in vivo bioavailability study. *International Journal of Pharmaceutics* **1999**, *182*, 1–5.

(150) Mao, S.; Chen, J.; Wei, Z.; Liu, H.; Bi, D. Intranasal administration of melatonin starch microspheres. *International Journal of Pharmaceutics* **2004**, *272*, 37–43.

(151) Merkus, F. W. H. M. Nasal melatonin composition. *Patent, United States* **1999**, 1–14.

(152) Baker, M. T.; Attala, M. N. Melatonin Analogue Prodrugs. *wipo.int* **2008**, *405*, 1–7.

(153) Merkus, P.; Guchelaar, H.-J.; Bosch, D. A.; Merkus, F. W. H. M. Direct access of drugs to the human brain after intranasal drug administration? *Neurology* **2003**, *60*, 1669–1671.

(154) Van den Berg, M. P.; Merkus, P.; Romeijn, S. G.; Verhoef, J. C.; Merkus, F. W. H. M. Uptake of melatonin into the cerebrospinal fluid after nasal and intravenous delivery: studies in rats and comparison with a human study. *Pharmaceutical Research* **2004**, *21*, 799–802.

(155) Jayachandra Babu, R.; Dayal, P. P.; Pawar, K.; Singh, M. Nose-to-brain transport of melatonin from polymer gel suspensions: a microdialysis study in rats. *Journal of Drug Targeting* **2011**, *19*, 731–740.

(156) Fischer, T. W.; Greif, C.; Fluhr, J. W.; Wigger-Alberti, W.; Elsner, P. Percutaneous penetration of topically applied melatonin in a cream and an alcoholic solution. *Skin Pharmacology and Physiology 17*, 190–194.

(157) Priano, L.; Esposti, D.; Esposti, R.; Castagna, G.; De Medici, C.; Fraschini, F.; Gasco, M. R.; Mauro, A. Solid lipid nanoparticles incorporating melatonin as new model for sustained oral and transdermal delivery systems. *Journal of Nanoscience and Nanotechnology* **2007**, *7*, 3596–601.

(158) Dubey, V.; Mishra, D.; Asthana, A.; Jain, N. K. Transdermal delivery of a pineal hormone: melatonin via elastic liposomes. *Biomaterials* **2006**, *27*, 3491–3496.

(159) Dubey, V.; Mishra, D.; Jain, N. K. Melatonin loaded ethanolic liposomes: physicochemical characterization and enhanced transdermal delivery. *European Journal of Pharmaceutics and Biopharmaceutics* **2007**, *67*, 398–405.

(160) Lemoine, P.; Zisapel, N. Prolonged-release formulation of melatonin (Circadin) for the treatment of insomnia. *Expert Opinion on Pharmacotherapy* **2012**, *13*, 895–905.

(161) Bonn, D. Melatonin's multifarious marvels: miracle or myth? *The Lancet* **1996**, *347*, 184.

(162) Ding, X. X.; Coon, M. J. Purification and characterization of two unique forms of cytochrome P-450 from rabbit nasal microsomes. *Biochemistry* **1988**, *27*, 8330–8337.

(163) Lazard, D.; Tal, N.; Rubinstein, M.; Khen, M.; Lancet, D.; Zupko, K. Identification and biochemical analysis of novel olfactory-specific cytochrome P-450IIA and UDP-glucuronosyl transferase. *Biochemistry* **1990**, *29*, 7433–40.

(164) Darwish, W. S.; Ikenaka, Y.; El-Ghareeb, W. R.; Ishizuka, M. High expression of the mRNA of cytochrome P450 and phase II enzymes in the lung and kidney tissues of cattle. *Animal* **2010**, *4*, 2023–2029.

(165) Williams, J. A.; Hyland, R.; Jones, B. C.; Smith, D. A.; Hurst, S.; Goosen, T. C.; Peterkin, V.; Koup, J. R.; Ball, S. E. Drug-drug interactions for UDP-glucuronosyltransferase substrates: a pharmacokinetic explanation for typically observed low exposure (AUCi/AUC) ratios. *Drug Metabolism and Disposition* **2004**, *32*, 1201–8.

(166) Bustin, S. a Absolute quantification of mRNA using real-time reverse transcription polymerase chain reaction assays. *Journal of Molecular Endocrinology* **2000**, *25*, 169–93.

(167) Bustin, S. a Quantification of mRNA using real-time reverse transcription PCR (RT-PCR): trends and problems. *Journal of Molecular Endocrinology* **2002**, *29*, 23–39.

(168) White, T. J.; Arnheim, N.; Erlich, H. A. The polymerase chain reaction. *Trends in Genetics* **1989**, *5*, 185–189.

(169) Lynch, J. R.; Brown, J. M. The polymerase chain reaction: current and future clinical applications. *Journal of Medical Genetics* **1990**, *27*, 2–7.

(170) Higuchi, R.; Dollinger, G.; Walsh, P. S.; Griffith, R. Simultaneous amplification and detection of specific DNA sequences. *Biotechnology (Nature Publishing Company)* **1992**, *10*, 413–7.

(171) Higuchi, R.; Fockler, C.; Dollinger, G.; Watson, R. Kinetic PCR analysis: real-time monitoring of DNA amplification reactions. *Biotechnology (Nature Publishing Company)* **1993**, *11*, 1026–30.

(172) Morrison, T.; Weis, J.; Wittwer, C. Quantification of low-copy transcripts by continuous SYBR Green I monitoring during amplification. *BioTechniques* **1998**, *24*, 954–962.

(173) Schmittgen, T. D.; Livak, K. J. Analyzing real-time PCR data by the comparative CT method. *Nature Protocols* **2008**, *3*, 1101–1108.

(174) Schmittgen, T. D.; Zakrajsek, B. a Effect of experimental treatment on housekeeping gene expression: validation by real-time, quantitative RT-PCR. *Journal of Biochemical and Biophysical Methods* **2000**, *46*, 69–81.

(175) Dheda, K.; Huggett, J. F.; Bustin, S. a; Johnson, M. a; Rook, G.; Zumla, A. Validation of housekeeping genes for normalizing RNA expression in real-time PCR. *BioTechniques* **2004**, *37*, 112–4, 116, 118–9.

(176) Javois, L. Immunocytochemical Methods and Protocols. In *Methods in Molecular Biology*; Humana Press Inc., 1999.

(177) Derisi, J. Overview of nucleic acid arrays. In *Current Protocols in Molecular Biology*; Ausubel, F. M., Ed.; 2001; Vol. Chapter 22, p. Unit 22.1.

(178) Butte, A. The use and analysis of microarray data. *Nature Reviews. Drug Discovery* **2002**, *1*, 951–960.

(179) Giantin, M.; Carletti, M.; Capolongo, F.; Pegolo, S. Effect of breed upon cytochromes P450 and phase II enzyme expression in cattle liver. *Drug Metabolism and Disposition* **2008**, *36*, 885–893.

(180) Abramoff, M. D.; Magalhaes, P. J.; Ram, S. J. Image Processing with ImageJ. *Biophotonics International* **2004**, *11*, 36–42.

(181) Schneider, C. A.; Rasband, W. S.; Eliceiri, K. W. NIH Image to ImageJ: 25 years of image analysis. *Nature Methods* **2012**, *9*, 671–675.

(182) Edgar, R.; Domrachev, M.; Lash, A. E. Gene Expression Omnibus: NCBI gene expression and hybridization array data repository. *Nucleic Acids Research* **2002**, *30*, 207–210.

(183) Hubbell, E.; Liu, W.-M.; Mei, R. Robust estimators for expression analysis. *Bioinformatics* **2002**, *18*, 1585–92.

(184) Flicek, P.; Amode, M. R.; Barrell, D.; Beal, K.; Brent, S.; Carvalho-Silva, D.; Clapham, P.; Coates, G.; Fairley, S.; Fitzgerald, S.; Gil, L.; Gordon, L.; Hendrix, M.; Hourlier, T.; Johnson, N.; Kähäri, A. K.; Keefe, D.; Keenan, S.; Kinsella, R.; Komorowska, M.; Koscielny, G.; Kulesha, E.; Larsson, P.; Longden, I.; McLaren, W.; Muffato, M.; Overduin, B.; Pignatelli, M.; Pritchard, B.; Riat, H. S.; Ritchie, G. R. S.; Ruffier, M.; Schuster, M.; Sobral, D.; Tang, Y. A.; Taylor, K.; Trevanion, S.; Vandrovcova, J.; White, S.; Wilson, M.; Wilder, S. P.; Aken, B. L.; Birney, E.; Cunningham, F.; Dunham, I.; Durbin, R.; Fernández-Suarez, X. M.; Harrow, J.; Herrero, J.; Hubbard, T. J. P.; Parker, A.; Proctor, G.; Spudich, G.; Vogel, J.; Yates, A.; Zadissa, A.; Searle, S. M. J. Ensembl 2012. *Nucleic Acids Research* **2012**, *40*, D84–90.

(185) Takahashi, S.; Iwanaga, T.; Takahashi, Y.; Nakano, Y.; Fujita, T. Neuron-specific enolase, neurofilament protein and S-100 protein in the olfactory mucosa of human fetuses. An immunohistochemical study. *Cell and Tissue Research* **1984**, *238*, 231–234.

(186) Weiler, E.; Benali, A. Olfactory epithelia differentially express neuronal markers. *Journal of Neurocytology* **2005**, *34*, 217–240.

(187) Zhou, X.; Li Wan Po, A. Comparison of enzymic activities of tissues lining portals of drug absorption, using the rat as a model. *International Journal of Pharmaceutics* **1990**, *62*, 259–267.

(188) Voigt, J. M.; Guengerich, F. P.; Baron, J. Localization and induction of cytochrome P450 1A1 and aryl hydrocarbon hydroxylase activity in rat nasal mucosa. *The Journal of Histochemistry and Cytochemistry* **1993**, *41*, 877–885.

(189) Longo, V.; Mazzaccaro, A.; Naldi, F. Drug metabolizing enzymes in liver, olfactory, and respiratory epithelium of cattle. *Journal of Biochemical Toxicology* **1991**, *6*, 123–128.

(190) Koskela, S.; Hakkola, J.; Hukkanen, J.; Pelkonen, O.; Sorri, M.; Saranen, A.; Anttila, S.; Fernandez-Salguero, P.; Gonzalez, F.; Raunio, H. Expression of CYP2A genes in human liver and extrahepatic tissues. *Biochemical Pharmacology* **1999**, *57*, 1407–1413.

(191) Peng, H. M.; Ding, X.; Coon, M. J. Isolation and heterologous expression of cloned cDNAs for two rabbit nasal microsomal proteins, CYP2A10 and CYP2A11, that are related to nasal microsomal cytochrome P450 form a. *The Journal of Biological Chemistry* **1993**, *268*, 17253–17260.

(192) Su, T.; Bao, Z.; Zhang, Q.; Smith, T.; Hong, J.; Ding, X. Human cytochrome P450 CYP2A13: predominant expression in the respiratory tract and its high efficiency metabolic activation of a tobacco-specific carcinogen, 4-(methylnitrosamino)-1-(3-pyridyl)-1-butanone. *Cancer Research* **2000**, *60*, 5074–5079.

(193) Fernandez-Salguero, P.; Hoffman, S. M.; Cholerton, S.; Mohrenweiser, H.; Raunio, H.; Rautio, A.; Pelkonen, O.; Huang, J. D.; Evans, W. E.; Idle, J. R. A genetic polymorphism in coumarin 7-hydroxylation: sequence of the human CYP2A genes and identification of variant CYP2A6 alleles. *American Journal of Human Genetics* **1995**, *57*, 651–660.

(194) Yun, C.; Shimada, T.; Guengerich, F. P. Purification and characterization of human liver microsomal cytochrome P-450 2A6. *Molecular pharmacology* **1991**, *40*, 679–685.

(195) Ding, S.; Lake, B. G.; Friedberg, T.; Wolf, C. R. Expression and alternative splicing of the cytochrome P-450 CYP2A7. *The Biochemical Journal* **1995**, *306 (Pt 1)*, 161–166.

(196) Le Gal, a Diversity of selective environmental substrates for human cytochrome P450 2A6: alkoxyethers, nicotine, coumarin, N-nitrosodiethylamine, and N-nitrosobenzylmethylamine. *Toxicology Letters* **2003**, *144*, 77–91.

(197) Béréziat, J. C.; Raffalli, F.; Schmezer, P.; Frei, E.; Geneste, O.; Lang, M. A. Cytochrome P450 2A of nasal epithelium: regulation and role in carcinogen metabolism. *Molecular Carcinogenesis* **1995**, *14*, 130–139.

(198) Messina, E. S.; Tyndale, R. F.; Sellers, E. M. A major role for CYP2A6 in nicotine C-oxidation by human liver microsomes. *The Journal of Pharmacology and Experimental Therapeutics* **1997**, *282*, 1608–1614.

(199) Pelkonen, O.; Rautio, A.; Raunio, H.; Pasanen, M. CYP2A6: a human coumarin 7-hydroxylase. *Toxicology* **2000**, *144*, 139–147.

(200) Gallagher, E. P.; Kunze, K. L.; Stapleton, P. L.; Eaton, D. L. The kinetics of aflatoxin B1 oxidation by human cDNA-expressed and human liver microsomal cytochromes P450 1A2 and 3A4. *Toxicology and Applied Pharmacology* **1996**, *141*, 595–606.

(201) Jalas, J. R.; Hecht, S. S.; Murphy, S. E. Cytochrome P450 enzymes as catalysts of metabolism of 4-(methylnitrosamino)-1-(3-pyridyl)-1-butanone, a tobacco specific carcinogen. *Chemical Research in Toxicology* **2005**, *18*, 95–110.

(202) Xie, F.; Zhou, X.; Behr, M.; Fang, C.; Horii, Y.; Gu, J.; Kannan, K.; Ding, X. Mechanisms of olfactory toxicity of the herbicide 2,6-dichlorobenzonitrile: essential roles of CYP2A5 and target-tissue metabolic activation. *Toxicology and Applied Pharmacology* **2010**, *249*, 101–106.

(203) Ding, X.; Spink, D.; Bhama, J.; Sheng, J.; Vaz, A. D. N.; Coon, M. J. Metabolic activation of 2, 6-dichlorobenzonitrile, an olfactory-specific toxicant, by rat, rabbit, and human cytochromes P450. *Molecular Pharmacology* **1996**, *49*, 1113–1121.

(204) Zhou, S.-F.; Wang, B.; Yang, L.-P.; Liu, J.-P. Structure, function, regulation and polymorphism and the clinical significance of human cytochrome P450 1A2. *Drug Metabolism Reviews* **2010**, *42*, 268–354.

(205) Sivapathasundaram, S.; Magnisali, P.; Coldham, N. G.; Howells, L. C.; Sauer, M. J.; Ioannides, C. A study of the expression of the xenobiotic-metabolising cytochrome P450 proteins and of testosterone metabolism in bovine liver. *Biochemical Pharmacology* **2001**, *62*, 635–645.

(206) Messina, a; Nannelli, a; Fiorio, R.; Longo, V.; Gervasi, P. G. Expression and inducibility of CYP1A1, 1A2, 1B1 by beta-naphthoflavone and CYP2B22, 3A22, 3A29, 3A46 by rifampicin in the respiratory and olfactory mucosa of pig. *Toxicology* **2009**, *260*, 47–52.

(207) Gunes, A.; Dahl, M.-L. Variation in CYP1A2 activity and its clinical implications: influence of environmental factors and genetic polymorphisms. *Pharmacogenomics* **2008**, *9*, 625–37.

(208) Ikeya, K.; Jaiswal, A. K.; Owens, R. A.; Jones, J. E.; Nebert, D. W.; Kimura, S. Human CYP1A2: sequence, gene structure, comparison with the mouse and rat orthologous gene, and differences in liver 1A2 mRNA expression. *Molecular Endocrinology* **1989**, *3*, 1399–1408.

(209) Eaton, D. L.; Gallagher, E. P.; Bammler, T. K.; Kunze, K. L. Role of cytochrome P4501A2 in chemical carcinogenesis: implications for human variability in expression and enzyme activity. *Pharmacogenetics* **1995**, *5*, 259–274.

(210) Landi, M. T.; Sinha, R.; Lang, N. P.; Kadlubar, F. F. Human cytochrome P4501A2. *IARC Scientific Publications* **1999**, 173–195.

(211) Rajkumar, A. P.; Poonkuzhali, B.; Kuruvilla, A.; Srivastava, A.; Jacob, M.; Jacob, K. S. Association between CYP1A2 gene single nucleotide polymorphisms and clinical responses to clozapine in patients with treatment-resistant schizophrenia. *Acta Neuropsychiatrica* **2012**, 1–10.

(212) Zhou, S.-F.; Yang, L.-P.; Zhou, Z.-W.; Liu, Y.-H.; Chan, E. Insights into the substrate specificity, inhibitors, regulation, and polymorphisms and the clinical impact of human cytochrome P450 1A2. *The AAPS Journal* **2009**, *11*, 481–494.

(213) Shimada, T.; Yamazaki, H.; Mimura, M.; Inui, Y.; Guengerich, F. P. Interindividual variations in human liver cytochrome P-450 enzymes involved in the oxidation of drugs, carcinogens and toxic chemicals: studies with liver microsomes of 30 Japanese and 30 Caucasians. *The Journal of Pharmacology and Experimental Therapeutics* **1994**, *270*, 414–423.

(214) Klose, T. S.; Blaisdell, J. a; Goldstein, J. a Gene structure of CYP2C8 and extrahepatic distribution of the human CYP2Cs. *Journal of Biochemical and Molecular Toxicology* **1999**, *13*, 289–295.

(215) Pegolo, S.; Merlanti, R.; Giantin, M.; Dacasto, M.; Montesissa, C.; Capolongo, F. High performance liquid chromatography determination of cytochrome P450 1A and 2C activities in bovine liver microsomes. *The Veterinary Journal* **2010**, *183*, 81–88.

(216) Getchell, M.; Chen, Y.; Xinxin, D.; Sparks, D.; Getchell, T. Immunohistochemical localization of a cytochrome P-450 isozyme in human nasal mucosa: age-related trends. *The Annals of Otology, Rhinology & Laryngology* **1993**, *102*, 368–374.

(217) Piras, E.; Franzen, a.; Fernandez, E. L.; Bergstrom, U.; Raffalli-Mathieu, F.; Lang, M.; Brittebo, E. B. Cell-specific Expression of CYP2A5 in the Mouse Respiratory Tract: Effects of Olfactory Toxicants. *Journal of Histochemistry & Cytochemistry* **2003**, *51*, 1545–1555.

(218) Chen, Y.; Getchell, M.; Ding, X.; Getchell, T. Immunolocalization of two cytochrome P450 isozymes in rat nasal chemosensory tissue. *Neuroreport* **1992**, *3*, 749–752.

(219) Wu, J.; Lenchik, N. I.; Gerling, I. C. Approaches to reduce false positives and false negatives in the analysis of microarray data: applications in type 1 diabetes research. *BMC Genomics* **2008**, *9 Suppl 2*, S12.

(220) Cole, S. W.; Galic, Z.; Zack, J. A. Controlling false-negative errors in microarray differential expression analysis: a PRIM approach. *Bioinformatics* **2003**, *19*, 1808–1816.

(221) Babu, R. J.; Dayal, P.; Singh, M. Effect of cyclodextrins on the complexation and nasal permeation of melatonin. *Drug Delivery* **2008**, *15*, 381–388.

(222) Claude, A. The constitution of protoplasm. *Science* **1943**, *97*, 451–456.

(223) Omura, T.; Sato, R. The carbon monoxide-binding pigment of liver microsomes. I. Evidence for its hemoprotein nature. *The Journal of Biological Chemistry* **1964**, *239*, 2370–2378.

(224) Omura, T.; Sato, R. The carbon monoxide-binding pigment of liver microsomes. II. Solubilization, purification and properties. *The Journal of Biological Chemistry* **1964**, *239*, 2379–2385.

(225) Nelson, D. L.; Cox, Michael, M. Enzymes. In *Lehninger Principles of Biochemistry*; W. H. Freeman Publishers, 2004; pp. 257–260.

(226) Crank, J. The diffusion equations. In *The Mathematics of Diffusion*; 2, Ed.; Oxford University Press Inc.: New York, 1975; pp. 1–10.

(227) Zhang, H. PhD thesis, The University of Iowa, 2009, p. 26.

(228) Hiemke, C.; Härtter, S. Pharmacokinetics of selective serotonin reuptake inhibitors. *Pharmacology & Therapeutics* **2000**, *85*, 11–28.

(229) Grözinger, M.; Härtter, S.; Wang, X.; Röschke, J.; Hiemke, C.; Rose, D. M. Fluvoxamine strongly inhibits melatonin metabolism in a patient with low-amplitude melatonin profile. *Archives of General Psychiatry* **2000**, *57*, 812–813.

(230) Overmars, H.; Scherpenisse, P. M.; Post, L. C. Fluvoxamine maleate: metabolism in man. *European Journal of Drug Metabolism and Pharmacokinetics* **1983**, *8*, 269–80.

(231) Kwon, J.-W.; Armbrust, K. L. Aqueous solubility, n-octanol-water partition coefficient, and sorption of five selective serotonin reuptake inhibitors to sediments and soils. *Bulletin of Environmental Contamination and Toxicology* **2008**, *81*, 128–135.

(232) Mahar Doan, K. M.; Humphreys, J. E.; Webster, L. O.; Wring, S. A.; Shampine, L. J.; Serabjit-Singh, C. J.; Adkison, K. K.; Polli, J. W. Passive permeability and P-glycoprotein-mediated efflux differentiate central nervous system (CNS) and non-CNS marketed drugs. *The Journal of Pharmacology and Experimental Therapeutics* **2002**, *303*, 1029–1037.

(233) Aceto, A.; Sacchetta, P.; Dragani, B.; Bucciarelli, T.; Angelucci, S.; Longo, V.; Gervasi, G. P.; Martini, F.; Di Ilio, C. Glutathione transferase isoenzymes in olfactory and respiratory epithelium of cattle. *Biochemical Pharmacology* **1993**, *46*, 2127–2133.

(234) Banger, K. K.; Lock, E. a; Reed, C. J. The characterization of glutathione S-transferases from rat olfactory epithelium. *The Biochemical Journal* **1993**, *290 (Pt 1)*, 199–204.

(235) Zhou, M.; Donovan, M. D. Recovery of the nasal mucosa following laureth-9 induced damage. *International Journal of Pharmaceutics* **1996**, *130*, 93–102.

(236) Suzuki, A.; Higuchi, W. I.; Ho, N. F. Theoretical model studies of drug absorption and transport in the gastrointestinal tract.I. *Journal of Pharmaceutical Sciences* **1970**, *59*, 644–651.

(237) Suzuki, A.; Higuchi, W. I.; Ho, N. F. Theoretical model studies of drug absorption and transport in the gastrointestinal tract. II. *Journal of Pharmaceutical Sciences* **1970**, *59*, 651–659.

(238) Ho, N. F.; Higuchi, W. I.; Turi, J. Theoretical model studies of drug absorption and transport in the GI tract. III. *Journal of Pharmaceutical Sciences* **1972**, *61*, 192–197.

(239) Vora, K. R.; Higuchi, W. I.; Ho, N. F. Analysis of human buccal absorption of drugs by physical model approach. *Journal of Pharmaceutical Sciences* **1972**, *61*, 1785–1791.

(240) Amidon, G. L.; Lee, P. I.; Topp, E. M. *Transport Processes in Pharmaceutical Systems*; Mercel Dekker, Inc., 2000.

(241) Ho, N. F.; Burton, P. S.; Conradi, R. A.; Barsuhn, C. L. A biophysical model of passive and polarized active transport processes in Caco-2 cells: approaches to uncoupling apical and basolateral membrane events in the intact cell. *Journal of Pharmaceutical Sciences* **1995**, *84*, 21–27.

(242) Ho, N. F.; Park, J.; Morozowich, W.; Higuchi, W. I. A physical model for the simultaneous membrane transport and metabolism of drugs. *Journal of Theoretical Biology* **1976**, *61*, 185–193.

(243) Yu, C. D.; Fox, J. L.; Ho, N. F.; Higuchi, W. I. Physical model evaluation of topical prodrug delivery-simultaneous transport and bioconversion of vidarabine-5'-valerate I: Physical model development. *Journal of Pharmaceutical Sciences* **1979**, *68*, 1341–1346.

(244) Yu, C. Der; Fox, J. L.; Ho, N. F. H.; Higuchi, W. I. Physical model evaluation of topical prodrug delivery—simultaneous transport and biocnversion of vidarabine-5′-valerate II: Parameter determinations. *Journal of Pharmaceutical Sciences* **1979**, *68*, 1347–1357.

(245) Fox, J. L.; Cheng-Der, Y.; Higuchi, W. I.; Ho, N. F. H. General physical model for simultaneous diffusion and metabolism in biological membranes. The computational approach for the steady-state case. *International Journal of Pharmaceutics* **1979**, *2*, 41–57.

(246) Guy, R. H.; Hadgraft, J. Percutaneous metabolism with saturable enzyme kinetics. *International Journal of Pharmaceutics* **1982**, *11*, 187–197.

(247) Sugibayashi, K.; Hayashi, T.; Hatanaka, T.; Ogihara, M.; Morimoto, Y. Analysis of simultaneous transport and metabolism of ethyl nicotinate in hairless rat skin. *Pharmaceutical Research* **1996**, *13*, 855–860.

(248) Boderke, P.; Schittkowski, K.; Wolf, M.; Merkle, H. P. Modeling of diffusion and concurrent metabolism in cutaneous tissue. *Journal of Theoretical Biology* **2000**, *204*, 393–407.

(249) Sugibayashi, K.; Hayashi, T.; Morimoto, Y. Simultaneous transport and metabolism of ethyl nicotinate in hairless rat skin after its topical application: the effect of enzyme distribution in skin. *Journal of Controlled Release* **1999**, *62*, 201–208.

(250) Anissimov, Y. G.; Roberts, M. S. Diffusion modeling of percutaneous absorption kinetics: 3. Variable diffusion and partition coefficients, consequences for stratum corneum depth profiles and desorption kinetics. *Journal of Pharmaceutical Sciences* **2004**, *93*, 470–487.

(251) Rougier, A.; Rallis, M.; Krien, P.; Lotte, C. In vivo percutaneous absorption: a key role for stratum corneum/vehicle partitioning. *Archives of Dermatological Research* **1990**, *282*, 498–505.

(252) Ho, N. F. H. Biophysical kinetic modeling of buccal absorption. *Advanced Drug Delivery Reviews* **1993**, *12*, 61–97.

(253) Franks, S. J. A mathematical model for the absorption and metabolism of formaldehyde vapour by humans. *Toxicology and Applied Pharmacology* **2005**, *206*, 309–320.

(254) Andersen, M. E.; Sarangapani, R. Clearance concepts applied to the metabolism of inhaled vapors in tissues lining the nasal cavity. *Inhalation Toxicology* **1999**, *11*, 873–897.

(255) Gonda, I. Mathematical modeling of deposition and disposition of drugs administered via the nose. *Advanced Drug Delivery Reviews* **1998**, *29*, 179–184.

(256) Gonda, I.; Gipps, E. Model of disposition of drugs administered into the human nasal cavity. *Pharmaceutical Research* **1990**, *7*, 69–75.

(257) Schiesser, W. E. *The Numerical Method of Lines*; Academic Press: San Diego, CA, 1991.

(258) Levy, H.; Lessman, F. *Finite difference equations*; Dover Publications: Mineola, NY, 1992.

(259) R Development Core Team, R. R: A Language and Environment for Statistical Computing. *R Foundation for Statistical Computing* **2011**, *1*, 409.

(260) Soetaert, K.; Petzoldt, T. Inverse modelling, sensitivity and monte carlo analysis in R using package FME. *Journal of Statistical Software* **2010**, *33*, 1–28.

(261) Soetaert, K.; Petzoldt, T.; Woodrow, S. R. Solving Differential Equations in R: Package deSolve. *Journal of Statistical Software* **2010**, *33*, 1–23.

(262) Tracy, T. S.; Hummel, M. A. Modeling kinetic data from in vitro drug metabolism enzyme experiments. *Drug Metabolism Reviews* **2004**, *36*, 231–242.

(263) Rusznak, C.; Devalia, J.; Lozewicz, S.; Davies, R. The assessment of nasal mucociliary clearance and the effect of drugs. *Respiratory Medicine* **1994**, *88*, 89–101.